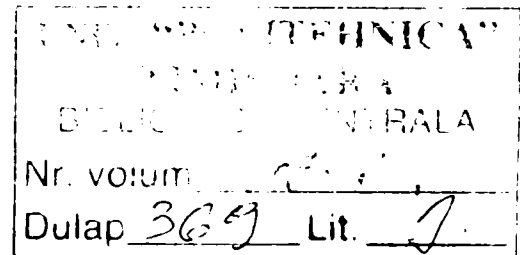


**A PERMANENT MAGNETS ASSISTED
RELUCTANCE SYNCHRONOUS MACHINE
FOR MILD HYBRID VEHICLES**

Ph.D. Thesis



El.Eng. Cristian Ilie Pitic

Supervisor: Prof. Dr.-Eng. Ion Boldea, IEEE Fellow

**Timisoara
2005**

Abstract

This thesis is presenting a high performance drive – starting with the motor design, prototype and latest control strategy for hybrid (mild hybrid) vehicles applications. This is a complete solution of design and control for reluctance synchronous motor assisted by permanent magnets backed up by strong experimental results.

Increased demand for better performance, higher vehicle fuel economy and reduced emissions of environmental pollutants has spurred research within the automotive industry in alternative vehicle architectures. To meet these demands, car manufacturers are investigating features such as electromechanical valves, all electric power steering, active suspension system, and electrically heated system. This dramatic increase requires substantial change in automotive electrical generation and distribution systems.

Electric and hybrid vehicle are two systems receiving attention in the recent years.

EV and HEV have the unique advantage over conventional vehicle as their architecture can be adapted to operating environment to maximize the energy efficiency and emission reduction (until zero emission). In the urban traffic, due to their beneficial effect on environment, electric vehicles are an important factor for improvement of traffic and more particularly for a healthier living environment.

The main goal of the thesis is to offer new solutions for the electrical system in a hybrid vehicle – area that is growing every year.

Index terms / Keyword

Hybrid Vehicle, Permanent Magnet, Reluctance Synchronous Machine, Synchronous Motor, Sensorless, Position Estimation, DTFC-SVM, Signal Injection, Rotor Position Estimation.

Preface

This thesis represents an approach, based on permanent magnets assisted reluctance synchronous motor with a 48 V inverter fed by a battery stand, to electrical systems for traction applications in mild hybrid vehicle technology.

Study motivation

Far from being a modern conception, electric cars were among the first vehicles on the road. In the formative days of the automobile, a third of cars were electric, and they challenged internal combustion engine vehicles for primacy. Economic and environmental concerns have periodically revived widespread interest in electric and hybrid vehicles, and the quest for a non- or less-polluting vehicle that meets consumer's performance demands continues today. The story of the electric car is a long one, and it is still being written.

The release of the first hybrid electric vehicles in the United States marks the start of a revolution. Hybrid vehicles are electric cars that utilize small internal-combustion engines and an electric generator. The advantages of this concept are clear: increased fuel efficiency and reduced levels of pollution without the complications and maintenance requirements of a purely electrically powered vehicle. This article provides some history on the hybrid concept as well as a survey of the innovative systems that have been developed in hybrid science.

The target of this thesis is to offer a concrete alternative to the electric motor, driven by an advanced and robust control, for this very demanding application.

A very important part of the thesis was the development of a simulation model and the first implementation on a dSpace system of a sensorless direct torque and flux control for interior permanent magnet synchronous machine (Chapter 4). This was done within the Institute of Energy Technology, Aalborg University, Aalborg, Denmark.

The design of the machine, the prototyping and the experimental work - on the permanent magnet assisted reluctance synchronous machine - were carried out in the Intelligent Motion Control Laboratory of the Faculty of Electrical Engineering, University "Politehnica" of Timisoara, Timisoara, Romania.

Objectives of the thesis

The main objectives of the thesis are:

- To present an overview of the hybrid systems and the vehicles in which were implemented, including the manufacturing companies, their vehicles configurations, type of electrical motors, the storage systems, the starter – alternator functionality.
- To choose the best electric motor for the traction applications, including the characteristics of the mild hybrid vehicles.
- To develop, after the specifications were fixed, a designing program for the chosen electrical machine.
- After the dimensions of the machine are set, finite elements simulations should be done to validate and correct the analytical program.
- Then, the building of a prototype for the decided type of electric machine and conception of a setup to validate the analytical and finite element simulated models.
- The first step for validations is to prove the standstill and generating characteristics of the machine – an important feature in the implementation of a robust control.
- Then, having the permanent magnets assisted reluctance synchronous machine well known, the need of a control is very important.
- By getting to know the laboratory setups and especially the dSpace system, we should be able to implement a robust control - with the 48 V Sauer Danfoss inverter.
- With the generator results and all the parameters known, a very robust control is needed. As the direct torque and flux control (DTFC) without motion sensors with space vector modulation (SVM) of induction machine has been proven very successful from very low speed in a rather dynamically robust implementation, we are now trying to employ the DTFC – SVM for the PM – RSM as starter – alternators, where specifications are much tougher than for industrial drives – the safety of the vehicles being the first issue.

Outline (organization) of the thesis

The thesis is organized in 6 chapters following the above-presented objectives.

In the *first chapter*, a state of the art in hybrid and electric vehicles is presented. In the beginning, the topologies of the hybrid electric vehicles are presented, followed by the latest hybrids on the market, then a characterization of the electrical system in hybrids and at the end, the start of the thesis, by choosing a proper type of motor for the application.

In the *second chapter*, a specified design program - after the specifications are determined, assisted by a finite element simulation is presented. Then, the results obtain by FEM are shown – with the torque capability validation. At the end, a sample design for PM-RSM is revealed.

In the *third chapter* a series of tests for parameters and efficiency determination of a PM - assisted RSM in the generator mode are introduced. The testing methods consist in standstill tests (dc decay), generator no load testing with capacitor and on load ac and diode-rectifier dc tests.

The *forth chapter* presents a comprehensive implementation of a wide speed motion-sensorless control of IPMSM drives via direct torque and flux control (DTFC) with space vector modulation (SVM). Signal injection with a modified D-module filter and phase-locked loop (PLL) observer is used at low speeds to observe the rotor position and speed, to be used in the flux observer and, respectively, as speed feedback. A combined voltage-current model flux observer suits the whole speed range while the current model fades away as speed increases. PWM and inverter nonlinearities compensation provide for a smooth current waveform even at very low speeds.

The *fifth chapter* introduces PM-RSM direct torque and flux control (DTFC) with space vector modulation (SVM) for the motion sensorless control from zero speed with initial position identification for nonhesitant starting. The proposed control system is described as implemented on a dSpace with a 350 A MOSFET-PWM converter connected to a 48 V dc, 55Ah battery, and a PM-RSM with a peak torque of 140 Nm. Ample experimental results at various speeds for motoring and generating seem very encouraging. The *sixth chapter* summarizes the conclusion and the contributions.

Acknowledgements

I wish to thank to my supervisor Prof. Ion Boldea from Politehnica University of Timisoara, Roamania. His guidance and support made this work possible.

I would like to thank also Prof. Frede Blaabjerg from the Institute of Energy Technology, Aalborg University, Denmark for his support and for the discussions during and after my three months researching period in Aalborg.

Many thanks to Prof. Gheorghe Daniel Andreescu from Faculty of Automation and Computers, Timisoara, Romania. His numerous inputs during the experimental work were invaluable.

Thanks also to Per Sandholdt from Sauer-Danfoss, Denmark for his support concerning the 48 V inverter, without whom, the control part of this thesis (the last chapter) would not be so valuable.

I want to thank to all of those who contributed to my engineering education and also to my colleagues from Intelligent Motion Control Laboratory at Faculty of Electrical Engineering, Timisoara; Dr. Eng. Ioan Serban, Assoc. Prof. Lucian Tutelea and Assist. Prof. Cristian Lascu deserves my special gratitude.

Finally, and most of all, I want to thank and express my love to my family. Their love and support was priceless during all this period. This thesis is dedicated to them.

Timisoara, September 15th, 2005

Cristian Ilie Pitic

Table of contents

Abstract	3
Index terms / Keyword	3
Preface	4
Objectives of the thesis	5
Outline (organization) of the thesis	6
Acknowledgements	7
Table of contents	8
Nomenclature	12
Chapter I	
Starter-alternators for mild hybrid vehicles – a review	15
Abstract	15
1.1 Introduction: Why hybrid and electrical vehicles?	15
1.2 Hybrid (HEV) and electric (EV) vehicle topologies	16
1.2.1 Series hybrid configuration	17
1.2.2 Parallel hybrid configuration	18
1.2.3 Series – parallel hybrid configuration	19
1.3 Hybrids on the market: Brief state of the art in HEV	20
1.3.1 Toyota Hybrids	20
A. THS – Toyota Hybrid System - Prius	20
B. THS-C–Toyota Hybrid System-CVT (4-Wheel Drive)–Toyota Estima	22
C. THS-M – Toyota Mild Hybrid System – Toyota Crown	23
D. FCHV-4 – Fuel Cell Hybrid Vehicle	24
1.3.2 Honda Hybrid - Honda Insight	25
1.3.3 Daimler Chrysler hybrids	27
A. Smart hyper HEV	27
B. M-Class HEV	28
C. Mercedes S-Class Hybrids	30
1.3.4 Ford Escape Hybrid	30
1.3.5 Hybrid Mileage Tips	34
1.3.6 What's Next for HEVs?	35
1.4 Characterization of electrical systems in Hybrid Vehicles	35

1.4.1	42 V PowerNet in HEVs	36
1.4.2	Storage systems in HEV	41
1.4.3	Integrated starter generator	47
1.5	Choosing an electric machine for traction application	52
	Specifications and typical performance / costs for ISA systems	52
	Comparison of four types of motors for EV and HEV	52
	Motor comparison	55
	Flux weakening capability and control laws	56
	Compared motor performances	56
	Electronic power converter and related losses	60
1.6	Conclusion	64
1.7	References	65
Chapter II		
	PM assisted starter/generator – conceptual design and FEM analysis	71
	Abstract	71
2.1.	Introduction: considered specifications & constraints	71
2.2.	The practical configuration and conceptual design aspect	73
2.2.1.	Selecting a suitable PM-SM configuration	74
2.2.2.	Rotor design with FEA assistance	79
2.2.3.	Stator winding design	82
2.2.4.	Inductances, resistances and PM flux linkage	83
2.2.5.	Simplified core loss model	86
2.2.6.	Torque & turns / stator coil nc	87
2.3.	Sample numerical analysis (FEM)	89
2.4.	Sample design program for PM - RSM	97
2.5.	Conclusion	106
2.6.	References	107
Chapter III		
	The PM –RSM: generator experimental characterization	111
	Abstract	111
3.1.	Introduction	111
3.2.	PM-RSM prototype specifications	112

3.2.1. Model description:	113
3.2.2. Permanent magnets flux (Ψ_{PM}):	114
3.2.3. Testing methods	115
3.3. Standstill testing	115
3.4. No load and shortcircuit testing	120
3.5. Capacitor – only load tests	122
3.6. On load a.c. testing with capacitor excitation	123
3.7. On load testing with diode rectifier	126
3.8. Conclusion	128
3.9. References	129

Chapter IV

Interior Permanent Magnet Synchronous Machine: Motion-Sensorless Direct Torque and Flux Control

Abstract	133
4.1. Introduction	133
4.2. Implemented motion-sensorless DTFC-SVM system	135
4.3. Digital simulation sample results	138
4.4. Experimental system	144
Simovert MasterDrive	145
Danfoss VLT 5005:	148
The interior permanent magnets synchronous machine	149
4.5. Sample results	150
4.6. Conclusion	155
4.7. References:	156

Chapter V

DTFC – SVM motion – sensorless control of PM –RSM	159
5.1. Introduction	159
5.2. Typical ISA (integrated starter – alternator) specifications	160
5.3. Flux reference	161
A. PM-RSM Model	162
B. Flux Reference	163
5.4. Sensorless DTFC-SVM of PM-RSM: The observers	166

A. Stator Flux Observers	166
B. Speed and Position Observers with Signal Injection	167
C. Speed Estimation from Stator Flux	169
D. DTFC-SVM Motion-Sensorless Control System	170
5.5. Experimental setup	172
5.5.1. dSpace DS 1103	173
5.6. Experimental Results	175
5.7. Conclusion	181
5.8. References	182
Chapter VI	
Conclusion and contributions	187
5.1. Conclusion	187
5.2. Original contributions	188
Appendix	191
Summary in Romanian	197
Author's CV	203
Author's papers related to the Ph. D. thesis	205

Nomenclature

Abbreviations

AC	Alternating current
ALA	Axially laminated anisotropic
DC	Direct current
DSP	Digital signal processor
EMF	Electromotive force
HPF	High-pass filter
HV AC	Heating, ventilating and air conditioning
IPMSM	Interior magnets type permanent-magnet synchronous machine
LPF	Low-pass filter
PI	Proportional-Integral control
PM	Permanent magnets
PLL	Phase-locked loop
PWM	Pulse width modulation
RSM	Reluctance synchronous machine
SM	Synchronous machine
SPMSM	Surface magnets type permanent-magnet synchronous machine
SVM	Space vector modulation
VSI	Voltage source inverter

Symbols

B	Viscous friction coefficient;
E_m	Magnitude of the rotor permanent-magnet flux induced voltage vector in steady state;
E_s	Magnitude of the stator flux linkage induced voltage vector in steady state;
$i_{as}; i_{bs}; i_{cs}$	Instantaneous stator a, b, c phase currents;
$i_{ds}; i_{qs}$	Instantaneous stator currents in rotor fixed d, q frame
$I_{ds}; I_{qs}$	Steady state stator currents in rotor fixed d, q frame
I_s	Magnitude of the stator current vector in steady state

I_{dc}	DC-link current
i_{abcs}	Stator current vector in stationary reference frame
i_{rqds}	Stator current vector in rotor fixed d,q frame
J	Inertia of the motor shaft and the load system
$L_d; L_q$	Rotor d- and q- axis inductances
L_{ls}	Leakage inductance
$L_{md}; L_{mq}$	Rotor d- and q- axis magnetizing inductances
p_l	Pole pairs of the motor
P_e	Steady state power input to the motor
R_s	Stator resistance per phase
s	Laplace operator
T_s	Sampling period
T_L	Load torque
T_e	Electromagnetic torque produced by the motor
$v_{as}; v_{bs}; v_{cs}$	Instantaneous stator a,b,c phase voltages
$v_{ds}^r; v_{qs}^r$	Instantaneous stator voltages in rotor fixed d, q frame
$V_{ds}^r; V_{qs}^r$	Steady state stator voltages in rotor fixed d, q frame
V_s	Magnitude of the stator voltage vector in steady state
V_{dc}	DC-link voltage
v_{abcs}	Stator voltage vector in stationary reference frame
v_{qds}^r	Stator voltage vector in rotor fixed d,q frame
α	Torque angle
δ	Load angle
θ_r	Electrical rotor position
$\lambda_{as}; \lambda_{bs}; \lambda_{cs}$	Stator a,b,c phase flux linkage
$\lambda_{ds}^r; \lambda_{qs}^r$	Stator flux linkage in rotor fixed d,q frame
λ_s	Magnitude of the stator flux linkage vector
λ_{abcs}	Stator flux linkage vector in stationary reference frame
λ_{qds}^r	Stator flux linkage vector in rotor fixed d,q frame
λ_{PM}	Rotor permanent-magnet flux which linkages with stator
ω_r	Electrical rotor speed
ω_e	Electrical speed of the applied voltage vector to the machine

Subscripts

$a; b; c$	Stator a,b,c phases
n	Normalized quantity
s	Stator quantity
r	Rotor quantity
0	Steady state quantity

Superscripts

*	Reference quantity
^	Estimated quantity

Chapter I

Starter-alternators for mild hybrid vehicles – a review

Abstract

In this chapter, a state of the art in hybrid and electric vehicles is presented. In the beginning, the topologies of the hybrid electric vehicles are presented, followed by the latest hybrids on the market, then a characterization of the electrical system in hybrids and at the end, the start of the thesis, by choosing a proper type of motor for the application.

1.1 Introduction: Why hybrid and electrical vehicles?

Increased demand for better performance, higher vehicle fuel economy and reduced emissions of environmental pollutants has spurred research within the automotive industry in alternative vehicle architectures. To meet these demands, car manufacturers are investigating features such as electromechanical valves, all electric power steering, active suspension system, and electrically heated system. The average electrical power load on the alternator is between 0.75 and 1 kW. In luxury cars in 2005 – 2010, this is expected to increase to 4 – 6 kW. This dramatic increase requires substantial change in automotive electrical generation and distribution systems. [1-11]

Electric and hybrid vehicle are two systems receiving attention in recent years.

EV and HEV has the unique advantage over conventional vehicle as their architecture can be adapted to operating environment to maximize the energy efficiency and emission reduction (until zero emission). In urban traffic, due to their beneficial effect on environment, electric vehicles are an important factor for improvement of traffic and more particularly for a healthier living environment.

A hybrid vehicle has a powertrain in which propulsion energy can be transmitted to the wheels by at least two different energy conversion devices (e.g. ICE, gas turbine, Stirling engine, electric motor, hydraulic motor, fuel cell) drawing energy from at least two different energy storage devices (e.g. fuel tank, battery, flywheel, ultracapacitor, pressure tank etc.). At least one of the paths along which

energy can flow from an energy storage device to the wheels is reversible, while at least one path is irreversible. In a hybrid-electric vehicle the reversible energy storage device supplies electric energy.

Hybrid electric vehicles (HEVs) combine the internal combustion engine of a conventional vehicle with the battery and electric motor of an electric vehicle, resulting in twice the fuel economy of conventional vehicles. This combination offers the extended range and rapid refueling that consumers expect from a conventional vehicle, with a significant portion of the energy and environmental benefits of an electric vehicle. The practical benefits of HEVs include improved fuel economy and lower emissions compared to conventional vehicles. [12-19]

HEVs have several advantages over conventional vehicles:

- Regenerative braking capability helps minimize energy loss and recover the energy used to slow down or stop a vehicle.
- Engines can be sized to accommodate average load, not peak load, which reduces the engine's weight.
- Fuel efficiency is greatly increased (hybrids consume significantly less fuel than vehicles powered by gasoline alone).
- Emissions are greatly decreased.
- HEVs can reduce dependency on fossil fuels because they can run on alternative fuels.
- Special lightweight materials are used to reduce the overall vehicle weight of HEVs.

1.2 Hybrid (HEV) and electric (EV) vehicle topologies

In order to improve the quality in vehicles – from all points of view – the car manufacturers combined the classical configurations vehicles – internal combustion engine (Figure 1.1.a) and electric vehicle (Figure 1.1.b) and obtained 3 main configurations [20]:

- series hybrid configuration;
- parallel hybrid configuration;
- series – parallel hybrid configuraion.

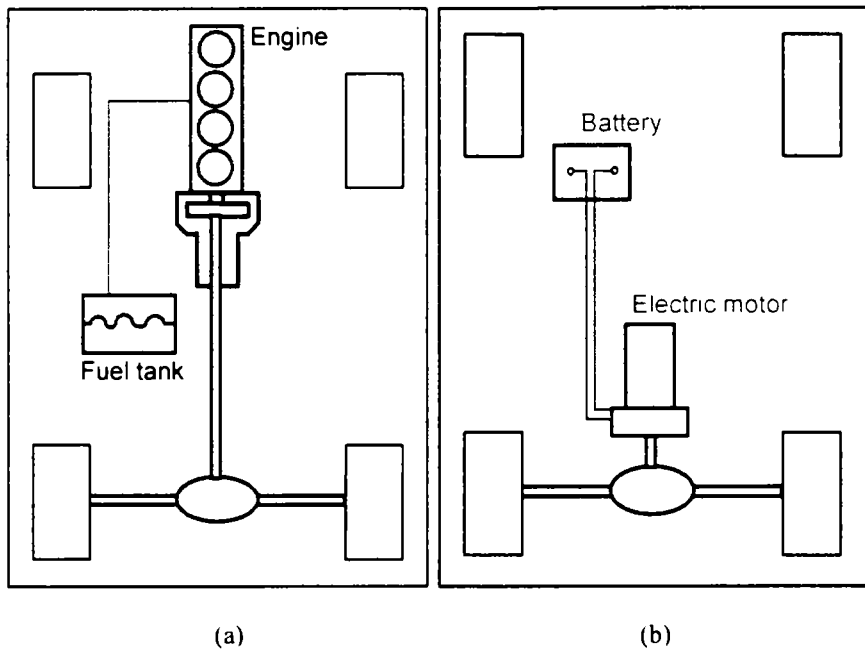


Figure 1.1. Classical configuration of a vehicle
(a) Internal combustion engine vehicle (ICE); (b) Electric vehicle (EV)

1.2.1 Series hybrid configuration

An HEV with a series configuration (Figure 1.2.a) uses the heat engine or fuel cell with a generator to produce electricity for the battery pack and electric motor [21]. Series HEVs have no mechanical connection between the hybrid power unit and the wheels; this means that all motive power is transferred from chemical energy to mechanical energy, to electrical energy, and back to mechanical energy to drive the wheels. Here are some benefits of a series configuration:

- The engine never idles, which reduces vehicle emissions.
- The engine drives a generator to run at optimum performance.
- The design allows for a variety of options when mounting the engine and vehicle components.
- Some series hybrids do not need a transmission.

The downside is that series HEVs require larger, and therefore, heavier battery packs than parallel vehicles. In addition, the engine works hard to maintain battery charge because the system is not operating in parallel.

Battery charging can be done off-board by external DC power link from the electric-grid. Due to the decoupling between the ICE and the wheels, the ICE can be operated in its efficient operating region, while maximizing efficiency for generating electricity. So, in the series hybrid vehicle all the propulsion power comes from the

electric motor. While this configuration is simple, there are two issues that must be considered in this design, efficiency and cost.

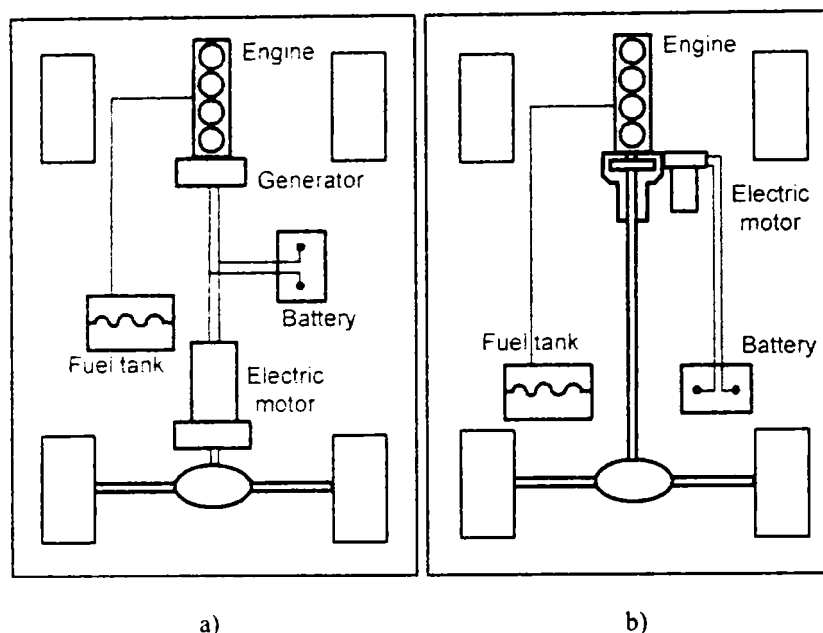


Figure 1.2. a) Series hybrid configuration, b) Parallel hybrid configuration.

1.2.2 Parallel hybrid configuration

An HEV with a parallel configuration (1.2.b) has a direct mechanical connection between the hybrid power unit and the wheels, as in a conventional vehicle, but also has an electric motor that drives the wheels [22]. For example, a parallel vehicle could use the power created from an internal combustion engine for highway driving and the power from the electric motor for accelerating. Some benefits of a parallel configuration are:

- The vehicle has more power because both the engine and the motor supply power simultaneously.
- Most parallel vehicles do not need a separate generator because the motor regenerates the batteries.
- Because the power is directly coupled to the road, it can be more efficient.

A combination alternator/starter/"flywheel" is being considered for parallel HEVs. This is essentially an electric machine that can electronically balance the engine, start the engine, and take power from the engine and turn it into electricity. It could also provide extra power to the driveline when power assist is needed for hill climbing or quick acceleration.

A hybrid's efficiency and emissions depend on the particular combination of subsystems, how these subsystems are integrated into a complete system, and the control strategy that integrates the subsystems. A hydrogen fuel cell hybrid, for example, would produce only water as a by-product and run at greater overall efficiency than a battery-electric vehicle that uses wall-plug electricity.

In contrast to series configuration, battery size is more decreased due to a lower energy storage device. Battery voltage varies between 42 V for mild hybrid up to 300 V for full hybrid vehicle. The minimum requirement for the storage energy system is to ensure 6 kW, for 15s at -25°C , power necessary for cold cranking situation. For this situation, electric motor works as an auxiliary for the engine, so they are demanded to be smaller in size, lighter in weight and higher in efficiency in order to improve fuel consumption and to ensure low emissions of exhaust gas.

In all hybrids and electric vehicle the air conditioning and some auxiliaries should remain on duty during idle stop. Idle stop means stopping the engine and (or) electric driving during halts in traffic jams or in traffic stop lights.

The main advantage of the parallel hybrid over the series hybrid are in energy conversion efficiency due to the mechanical connection between the ICE and the wheels, reducing the amount of energy of power conversion from energy sources and the downsize engine and electric motor due to its co-assisted capability in terms of propulsion power generation, resulting in enhanced fuel economy and reduced pollutant emissions.

1.2.3 Series – parallel hybrid configuration

In the series-parallel hybrid (Figure 1.3), the configuration incorporates the features of both the series and parallel HEVs, but involves an additional mechanical link compared with the series hybrid and also generator compared with the parallel hybrid. Although possessing the advantageous features of both the series and parallel HEVs, the series and parallel HEV is relatively more complicated and costly. Nevertheless, with the advances in control and manufacturing technologies, some modern HEVs prefer to adopt this system. [23, 24]

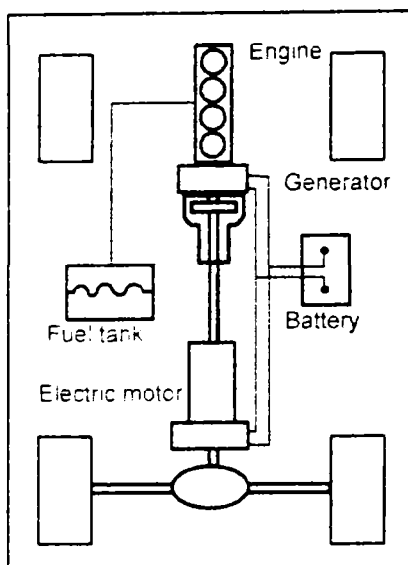


Figure 1.3. Series-parallel hybrid configuration

1.3 Hybrids on the market: Brief state of the art in HEV

1.3.1 Toyota Hybrids

A. THS – Toyota Hybrid System - Prius

One of the main goals of the Toyota Prius (Figure 1.4) is to improve emissions in urban driving. To accomplish this, Toyota has designed a parallel hybrid powertrain, called the Toyota Hybrid System (THS), which adds some of the benefits of a series hybrid. [24-27]

Unlike Honda, Toyota has focused primarily on the powertrain to achieve its emissions and mileage goals. The Prius weighs 2,765 pounds (1,255 kg) and has as much interior space and trunk space as a Toyota Corolla.

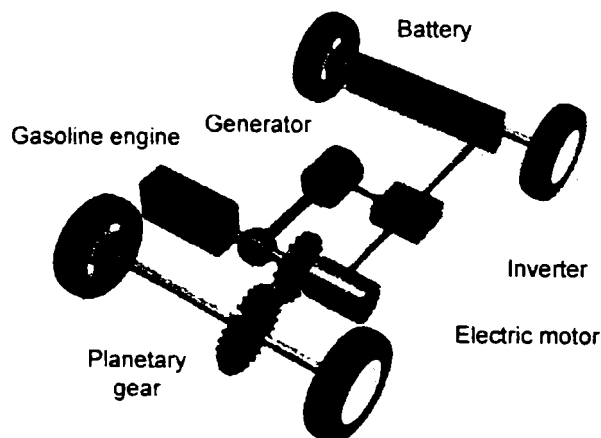


Figure 1.4. THS (Toyota Hybrid System) – Toyota Prius

Efficiency and Reduced Emissions

The Prius mainly relies on two features to optimize efficiency and reduce emissions:

Its engine only runs at an efficient speed and load - In order to reduce emissions, the Prius can accelerate to a speed of about 15 mph (24 kph) before switching on the gasoline engine. The engine only starts once the vehicle has passed a certain speed. And once the engine starts, it operates in a narrow speed band.

It uses a unique power split device (Figure 1.5) - Gasoline engines can be tuned to run most efficiently in certain speed and load ranges. The power split device on the Prius, which we'll talk about in a minute, allows the engine to stay in its most efficient load and speed range most of the time.

Toyota designed the 1.5-liter engine in the Prius to run at a maximum speed of only 4,500 rpm, where it makes 70 horsepower. Keeping the maximum speed of the engine low allows for the use of lighter components that improve efficiency.

Table 1. Toyota Prius characteristics

THS – Toyota Hybrid System - Prius	
Gasoline Engine	
Power output	76 hp @ 5,000 rpm (57 kW @ 5,000 rpm)
Torque	82 lb.-ft. @ 4,200 rpm (111 N-m @ 4,200 rpm)
Emission ratings	Advanced Technology Partial Zero Emission Vehicle (AT-PZEV)
Electric Motor	
Motor type	Permanent magnet AC synchronous motor
Power output	67 hp @ 1,200-1,540 rpm (50 kW @ 1,200-1,540 rpm)
Torque	295 lb.-ft. @ 0-1,200 rpm (400 N-m @ 0-1,200 rpm)
Voltage	500V maximum
Traction Battery	
Type	Sealed Nickel-Metal Hydride (Ni-MH)
Power output	28 hp (21 kW)
Voltage	201.6V
Hybrid System Net Power	110 hp (82 kW)

The electric motor on the Prius is rated at 44 horsepower from 1,040-5,600 rpm. It produces 258 pound-feet of torque from 0 to 400 rpm, which is more than enough to get the car going without the aid of the gasoline engine.

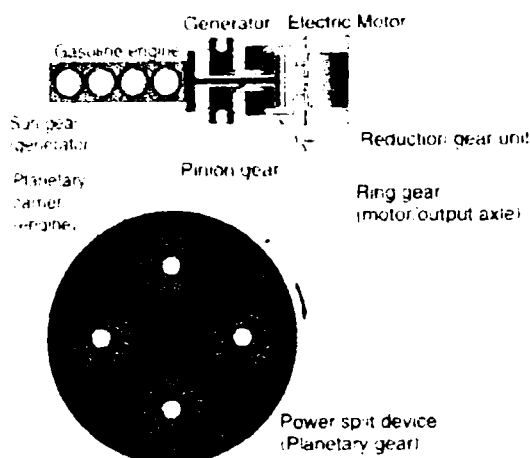


Figure 1.5. Toyota Prius's power split device

Driving the Prius

When you accelerate, initially the electric motor and batteries provide all of the power. The ring gear of the power split device is connected to the electric motor, so it starts to spin with the motor. The planet carrier, which is connected to the engine, is stationary because the engine is not running. Since the ring gear is spinning, the planets have to spin, which causes the sun gear and generator to spin. As the car accelerates, the generator spins at whatever speed it needs to in order for the engine to remain off. Once you reach about 24 kph (15 mph), the gasoline engine will turn on. The generator suddenly changes speed, causing the planet carrier to turn and start the engine. Once the engine is running, it settles into a constant speed while the generator varies its speed to match the output speed with the electric motor. If you are really accelerating hard, the motor will draw extra power from the batteries. Once you are up to freeway speed, the car will move under a combination of gas and electric power, with all of the electricity coming from the generator.

B. THS-C – Toyota Hybrid System-CVT (4-Wheel Drive) – Toyota Estima

THS-C (Figure 1.6) features a gasoline engine, electric motor and CVT (Continuously Variable Transmission) for front-wheel power, and is designed for larger cars and minivans. The most distinctive features of the Estima Hybrid related to Prius are the addition of an F-Four or rear-mounted, rear-wheel-propelling electric motor, which regulates itself and also coordinates electric power distribution to all four wheels, providing added kick during hard acceleration, and electronic 4-wheel drive for improved traction on slippery surfaces.

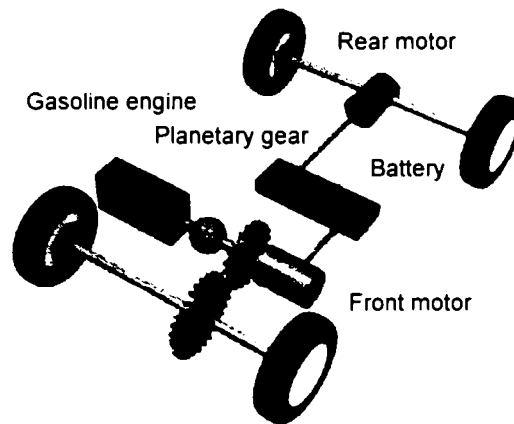


Figure 1.6. THS-C – 4 Wheel drive

C. THS-M – Toyota Mild Hybrid System – Toyota Crown

The THS-M (Figure 1.7) is a simpler and less expensive alternative. A motor / generator is connected to the engine's drive shaft via a belt and an electromagnetic clutch. While stationary, the engine shuts off and the electric motor runs the air conditioner and other accessories. It also powers the vehicle during startup. The engine propels the vehicle under normal driving conditions, while the motor generates electricity to top off its battery. It also utilizes the vehicle's kinetic energy to charge the battery during decelerations and braking. [28]

The motor/generator uses a 36 V battery for driving and generating. The battery is a Valve regulated lead-acid battery, which uses less battery fluid and makes stratification more difficult than a conventional "flooded battery". This type of battery produces a stable open circuit voltage and for this reason the battery state of charge (SOC) can be detected with higher accuracy. The battery weights only 27 kg and has a capacity of 20 Ah, with a starting performance of 6.1 kW for 1 sec.

The motor/generator used is an AC synchronous motor with a maximum torque of 56 Nm (0-300 rpm) and a rated output of 3 kW (motoring) and 3.5 kW (generating).

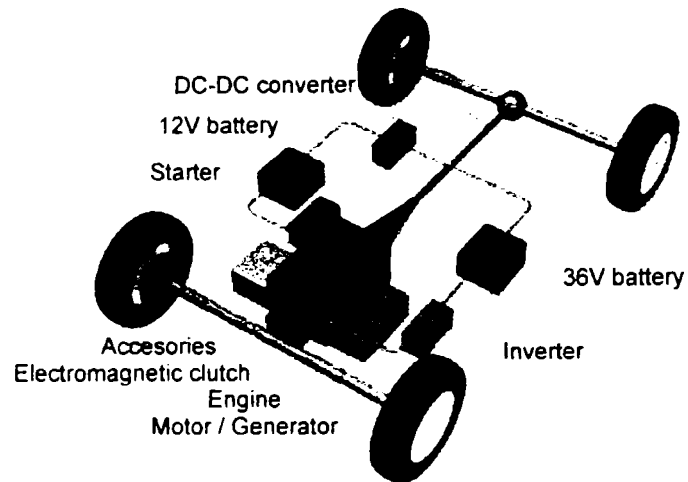


Figure 1.7. THS-M

This system is used not only for starting and stopping of the engine, but also for regenerative generation, auxiliary operations when the engine is stopped and supplementary operations on engine started.

For the same vehicle with the same engine, the system proved a 15 % fuel saving.

D. FCHV-4 – Fuel Cell Hybrid Vehicle

The FCHV-4 (Figure 1.8) incorporates a fuel cell and a battery to ensure a constant supply of electrical power.

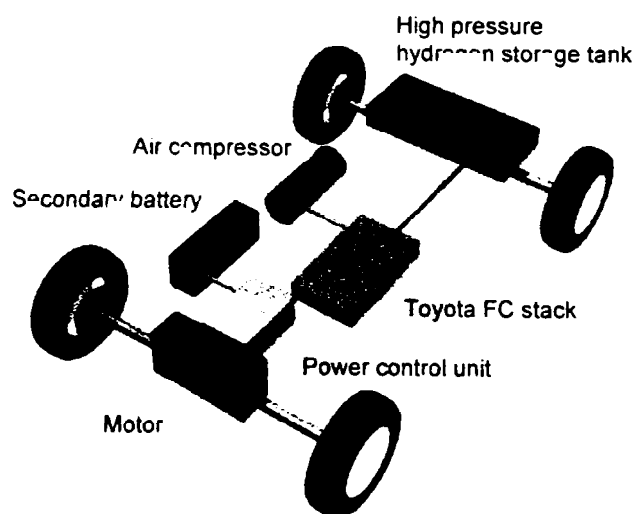


Figure 1.8. The FCHV System – main components

1.3.2 Honda Hybrid - Honda Insight

Honda Insight is a simplified parallel hybrid. It has an electric motor coupled to the engine at the spot where the flywheel usually goes. Honda calls this system "Integrated Motor Assist". The Insight also has a conventional five-speed manual transmission. For those of you that have trouble changing gears, or prefer an automatic transmission, the Insight CVT is now available.

The electric motor (Figure 1.9) on the Insight helps in several ways. It can:

- Assist the gasoline engine, providing extra power while the car is accelerating or climbing a hill
- Provide some regenerative braking to capture energy during braking
- Start the engine, eliminating the need for a starter

However, the motor cannot power the car by itself; the gas engine must be running for the car to move.

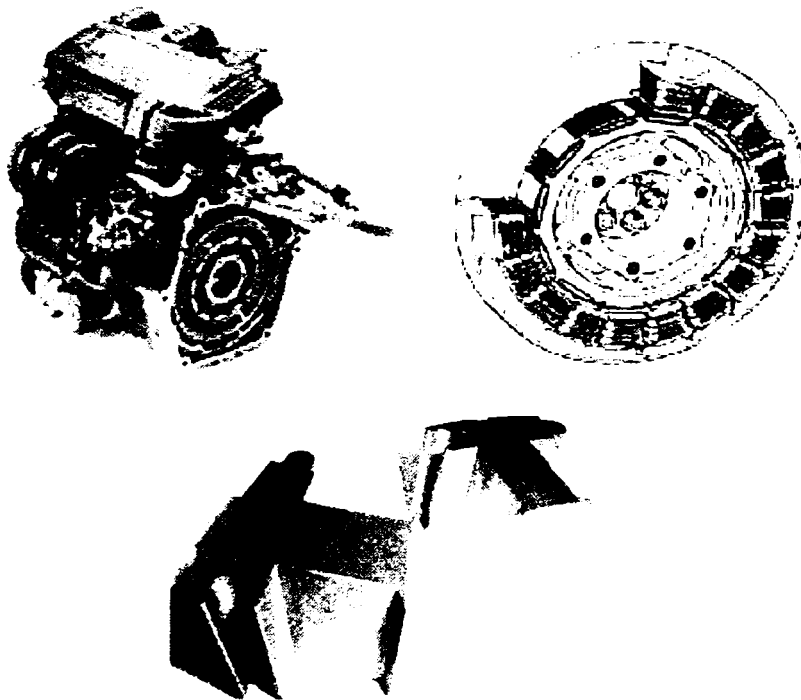


Figure 1.9. The engine and the electric motor of Honda Insight: engine, electric motor and the stator core of the electric motor

Honda Insight Fuel Efficiency

Because the Insight was designed to get the best mileage possible, Honda used all of the tricks discussed in the previous section. But the Insight relies mainly on three areas:

- ***It reduces the weight*** - Already a small car, the Insight uses a lightweight aluminum body and structure to further reduce weight. By making the car lightweight, Honda was able to use a smaller, lighter engine that could still maintain the performance level we have come to expect from our cars. The Insight weighs less than 1,900 pounds (862 kg), which is 500 pounds (227 kg) less than the lightest Honda Civic.

- ***It uses a small, efficient engine*** - The engine in the Insight, weighs only 56 kg and produces 67 horsepower at 5,700 rpm. It incorporates Honda's VTEC system and uses lean burn technology to maximize efficiency. The Insight achieves an EPA mileage rating of 61 mpg/city and 70 mpg/highway. Also, with the additional power provided by the small electric motor, this system is able to accelerate the Insight from 0 to 60 mph in about 11 seconds.

With the electric motor running, the Insight produces 73 horsepower at 5,700 rpm. If you compare that to the engine horsepower alone, it looks like the electric motor only adds 6 horsepower. But the real effectiveness of the electric motor occurs at ***lower engine speeds***. The electric motor on the Insight is rated at 10 kilowatts (about 13 horsepower) at 3,000 rpm.

- It's the peak torque numbers that really tell the story. Without the electric motor, the Insight makes its peak torque of 66 pound-feet at 4,800 rpm. With the electric motor, it makes 91 pound-feet at 2,000 rpm. So the motor adds a lot of torque to the low end of the speed range, where the engine is weaker. This is a nice compromise that allows Honda to give a very small engine the feel of a much larger one.

- ***It uses advanced aerodynamics*** - The Honda Insight is designed using the classical teardrop shape: The back of the car is narrower than the front. The rear wheels are partially covered by bodywork to provide a smoother shape, and some parts of the underside of the car are enclosed with plastic panels. These tricks result in

a drag coefficient of 0.25, which makes it one of the most aerodynamic cars on the market.

The IMA electric motor

The ultra-thin DC brushless motor of 10 kW output sandwiched between the engine and transmission is highly efficient, light and compact. The central rotor is manufactured using the lost wax method to give a precise shape and high strength, which achieves a 20 percent weight reduction. For the rotor magnet, improvements to the neodymium sintered magnet used in the Honda EV Plus means an improvement in the magnetic flux density or torque ratio by 8 percent, while improved heat resistance has made a cooling system unnecessary. In order to create a thin motor, a split stator with compact salient-pole field winding and centralized bus ring forms a very simple structure allowing a width of 60 mm, 40 percent thinner than if conventional technologies were used.

Table 2. The honda insight hybrid system characteristics

Permanent Magnet Motor	
Power output	10 kW @ 3000 rpm
Motor Width (mm)	60
Nickel Metal Hydride (Ni-MH) Battery	
Output	144 V (120 cells @ 1.2 V)
Rated capacity	6.5 Ah

1.3.3 Daimler Chrysler hybrids

A. SMART hyper HEV

The SMART HEV (Figure 1.10) is a parallel prototype version of the SMART two seater mass-production vehicle.

The SMART HEV uses a 25 kW permanent-magnet motor with a 1.8 kWh NiMH battery to provide capability for pure EV running, stop-start, power-boost, smooth shifting, and regenerative braking. The drivetrain design and conversion was made by Zytec EV Ltd.

Table 3. Smart HEV motor specifications

Motor type	Permanent Magnet, DC Brushless
Max. torque	55 Nm
Max. power	25 kW (36 BHP)
Max. speed	14500rpm
Coolant	Water-jacket using engine coolant
Dimensions	285 x 150 x 160 mm
Weight	19.1 kg

Table 4. Smart HEV inverter (hybrid-controller) specifications:

Type	IGBT 3-phase bridge
Processor	Infineon c167CR
Supply voltage (nominal)	274 V
Max. motor current	400 A
BMS & vehicle comm's	Dual – CAN
Coolant	Forced air-cooling
Weight	23.5 kg

Table 5. Energy storage specification

Manufacturer	Panasonic EV Energy Co.
Type	38 off EV-MH6R5
Chemistry	Nickel-Metal Hybrid
Energy	1.8 kW/h
Coolant	Forced air-cooled
Weight	48.6 kg

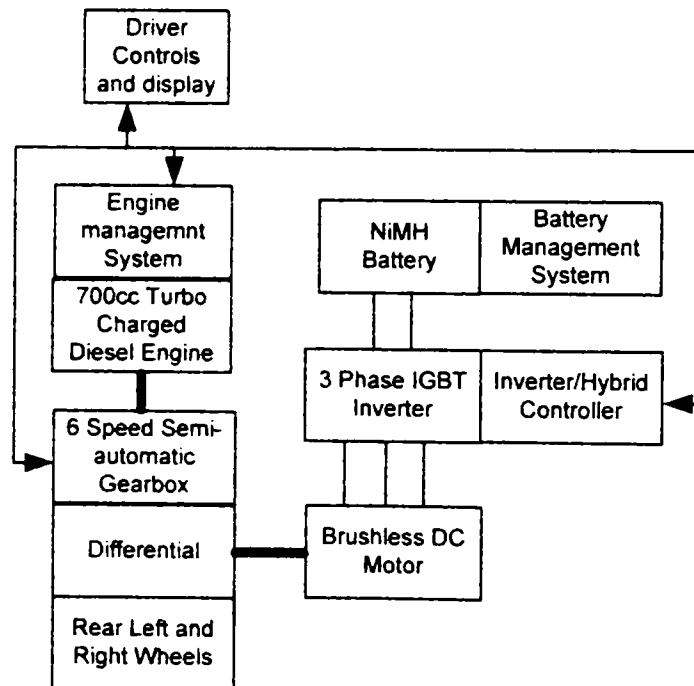


Figure 1.10. Block diagram of SMART Hybrid Drivetrain

B. M-Class HEV

DaimlerChrysler Research has introduced the M-Class HYPER — a new hybrid vehicle that consumes up to 20 percent less fuel than a comparable production model. The powertrain of this sporty four-wheel drive vehicle is equipped with a special clutch and an electric motor that eliminate the need for a generator or starter. The result is not only a reduction in vehicle weight, but also reduced costs.

If you took a peek under the hood of one of the latest hybrid vehicles developed by DaimlerChrysler Research — the M-Class HYPER — you would hardly believe that this sport-utility vehicle is a hybrid. Although the standard 2.7-liter CDI diesel engine would be impossible to overlook, you would notice that the M-Class HYPER doesn't appear to be equipped with a conventional electric motor and the associated battery.

The electric motor is being ever-more tightly integrated into the powertrain and now takes up almost no additional space. It is positioned directly on the clutch shaft, between the clutch and the transmission, with which it forms a connected unit.

With an output of 45 kW, the high-torque disc motor has the advantage that it can be easily incorporated into existing drive trains. And its sophisticated electronic control system and state-of-the-art clutch offer even more benefits:

- The disc motor serves as both a starter and a generator, eliminating the need for these components. In addition to reducing vehicle weight, this also simplifies the entire powertrain and the wiring.
- There also is no need for the second electric motor found in the majority of hybrid vehicles already on the market. Such second motors increase the weight and costs of a vehicle, and they also take up a lot of space.
- And in contrast to hybrid concepts realized to date, the regenerative power — the electrical energy recovered from the vehicle's kinetic energy per time unit — is twice as much as achieved by previous hybrid concepts. One result of this is that the M-Class HYPER consumes up to 20 percent less fuel than the comparable Mercedes-Benz ML 270 CDI production vehicle, according to the New European Driving Cycle.

When starting up, driving at low speeds in city traffic or when stuck in a traffic jam, the diesel engine is switched off altogether; only the electric motor propels the vehicle. Depending on driving conditions, the clutch ensures that the combustion engine is push-started once the vehicle reaches approximately 25 km/h. In normal driving mode, the combustion engine powers the car. Here, the electric motor is only used to synchronize the transmission during gear shifts. During the acceleration process — while overtaking, for example — the electric motor is automatically activated, so that the torques of the motor and the engine are combined. This is what engineers call the “booster function.” During extended application of the vehicle's brakes, the diesel engine switches off and the electric motor is used for regeneration.

The motor is powered by the wheels via the transmission and functions as a generator, converting kinetic energy into electrical energy. This energy is then fed into the car's battery. The battery is also charged when the vehicle is being driven at a constant highway cruising speed, and the combustion engine is not required to operate at its maximum output. In this mode it is the engine, not the transmission, that turns the motor so that it functions as a generator and charges the battery.

The battery used in the hybrid vehicle is a water-cooled, nickel metal-hydride battery with an output of 50 kW. It is installed together with the electronic battery control in the spare wheel well at the rear of the vehicle. And in addition to being a space-saver, this arrangement also solves the mystery of that missing second energy-storage device.

C. Mercedes S-Class Hybrids

An early Mercedes hybrid, the first RWD hybrid, was shown in 1999 at the IAA show in Frankfurt. It was a S-Class (Figure 1.11) with parallel hybrid drive utilizing two electric motors and gasoline V6 engine. Later on it was presented at the North American International Auto Show 2004 in Detroit, again with hybrid drive with V6 gasoline engine and two electric motors in an S-Class test vehicle.

Table 6. Mercedes S-Class characteristics

electric hybrid drive system		
Output	V6 engine Elec. motors (EM)	180 kW/245 hp EM 1: 30 kW; EM 2: 25 kW
Max. torque	V6 engine Elec. motors (EM)	350 Nm EM 1: 150 Nm; EM 2: 300 Nm

1.3.4 FORD ESCAPE HYBRID

The Escape Hybrid was the first Ford vehicle to combine SUV capability with the outstanding fuel economy and low environmental impact of a full hybrid.

The Ford Escape Hybrid is a full hybrid with a no compromise approach to hybridization that minimizes exhaust emissions and maximizes fuel efficiency. There are six major components in the Powertrain that contribute to the Escape Hybrid's efficient operation. [29]

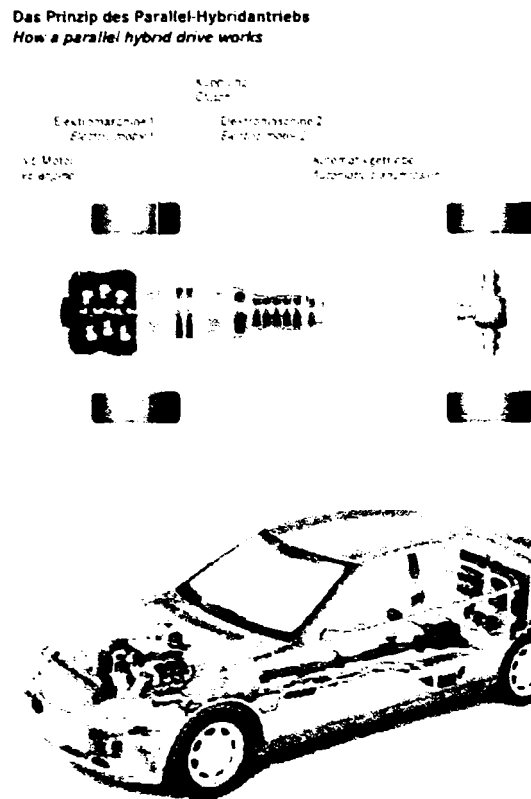


Figure 1.11. Mercedes S-Class Hybrid

The Escape Hybrid's electric motor is a compact design that operates on power drawn both from the battery pack and from a very intelligent generator motor. Its peak power is 70 kWatts (equivalent to an extra 93 horsepower). When required, the generator motor restarts the gas engine (remember, the gas engine shuts down automatically for stoplights and when coasting). And when the gas engine is running, it helps recharge the battery pack.

This powerful, compact electric motor is capable of powering the full hybrid Escape up to 25 mph.

That means in city or stops and go driving, you could spend a lot drive time without using fuel. The ingenious generator motor provides power boosts during heavy load situations, helping Escape Hybrid accelerate briskly to speed. When required, the generator motor restarts the gas engine (remember, the gas engine shuts down automatically for stoplights and when coasting). And when the gas engine is running, it helps recharge the battery pack. Aside from the fact that electric motors use no fuel, they also deliver maximum torque at low rpm so they are an ideal compliment to gasoline engines, which generate best torque at higher rpm.

In a conventional vehicle when you brake, the energy is lost as heat. During braking in the Escape Hybrid, the electric motor captures this energy that is normally lost and sends it back to the battery pack to be stored for later use.

Whenever you apply the brakes, you are, in effect, recharging the battery pack. Engineers call this regenerative braking and it represents a major part of the Escape Hybrid's fuel efficiency advantage over conventional vehicles. Although Escape Hybrid will never make stop and go driving any more enjoyable, that is actually when it is at its fuel saving best.

The Escape Hybrid is expected to be certified for sale as an Advanced Technology Partial Zero Emissions Vehicle (AT-PZEV), the strictest of emissions certifications. By itself, the Escape Hybrid's 2.3L engine is very fuel-efficient. However, an innovative stop/start function makes it even more so. The stop/start function automatically shuts the engine down when it isn't needed such as at stop lights, low speeds or when coasting. This puts the Escape Hybrid at its fuel saving best in stop and goes driving. The stop/start cycling is completely automatic and seamless requiring no driver input.

The sealed nickel-metal hydride (NiMH) battery pack in the Escape Hybrid is rated at 330 volts. Its function is to store electrical energy for starting the gasoline engine and for added boosts in acceleration performance. Nickel-Metal Hydride batteries have been used with excellent success for years. The Escape Hybrid battery pack will also come with a limited warranty of at least 8 years/100,000 miles.

When called upon, Escape Hybrid's battery pack also helps provide fun to drive V-6-like acceleration or cruising at high speeds. Much like a conventional vehicle, when you press hard on the accelerator pedal of the Escape Hybrid, the VSC (Vehicle System Controller) signals all the contributing components to pitch in with their extra power. The Electric motor, generator motor and battery pack all kick in to contribute and combine their extra power with that of the gasoline engine.

Seven different microprocessor-based control modules manage the Escape Hybrid's powertrain-related functions. The master device is the VSC built into the Escape's Powertrain Control Module.

The VSC helps to manage charging, drive assist, and engine starting functions. It shuts the engine down during coasting and at stoplights to save fuel. It also converts the traction motor into a generator during braking to help recharge the batteries.

The electronically controlled, continuously variable transmission (eCVT) is integral with the generator motor. It harnesses internal combustion and electric power sources to drive the wheels.

You're left with a seamless acceleration from a standing start to cruising speed. The Escape Hybrid's eCVT works to blend together contributions from the engine and electric motor. At low speeds and light loads, it tells the gas engine to take a break and propulsion is handled solely by the electric motor.

The 2005 Ford Escape Hybrid is expected to be rated at between 35-40 mpg on the EPA city cycle – an improvement of at least 75 percent over the EPA city fuel economy rating of 20 mpg for the conventional V-6-powered Ford Escape, the best-selling small SUV in America. Escape Hybrid's fuel-efficient four-cylinder engine combines with an electric drive system to deliver acceleration performance similar to that of the V-6 Escape.

Escape Hybrid is an extremely clean vehicle to operate, producing 97 percent less hydrocarbon and oxides of nitrogen emissions than vehicles that meet today's nationwide Tier I emissions standard. That's clean enough to qualify the 2005 Escape Hybrid for the stringent Advanced Technology Partial Zero Emissions Vehicle (AT-PZEV) standards.

Escape Hybrid achieves the AT-PZEV standards by combining an efficient powertrain with an exhaust catalyst system that is very effective at lowering smog-forming emissions.

Ford Motor Company and other automakers are working on long-term research projects to someday make practical hydrogen-powered vehicles that will not produce any greenhouse emissions. In addition to the Escape Hybrid, PZEV Focus and Focus Diesel being produced today, Ford has developed a Focus hydrogen internal combustion engine, a hydrogen hybrid research vehicle and a Focus Fuel Cell Vehicle (FCV) that is operating in demonstration fleets in the U.S. and Canada.

Ecostar - Ballard - Xcellsys

Ecostar Electric Powertrain and Power Conversion Systems, and XCELLSIS, The Fuel Cell Engine company were formatted by the alliance of DaimlerChrysler, Ford Motor Company and Ballard Power Systems. Together, they create the complete fuel cell engine solution, offering original equipment manufacturers (OEMs) complete fuel cell systems or components to create their own electrically-powered vehicles.

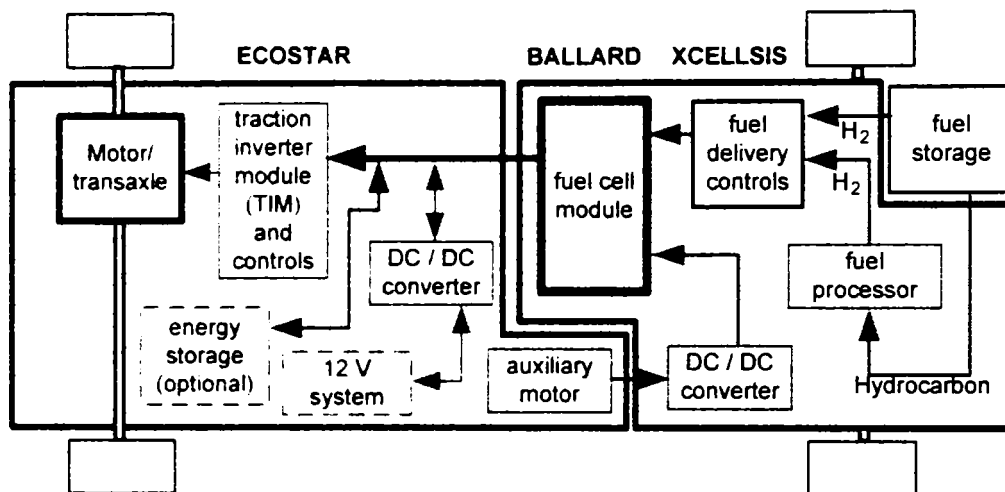


Figure 1.12. Ecostar-Ballard-Xcellsys Bus System

1.3.5 Hybrid Mileage Tips

You can get the best mileage from a hybrid car by using the same kind of driving habits that give you better mileage in your gasoline-engine car:

Drive slower - The aerodynamic drag on the car increases dramatically the faster you drive. For example, the drag force at 70 mph (113 kph) is about double that at 50 mph (81 kph). So, keeping your speed down can increase your mileage significantly.

Maintain a constant speed - Each time you speed up the car you use energy, some of which is wasted when you slow the car down again. By maintaining a constant speed, you will make the most efficient use of your fuel.

Avoid abrupt stops - When you stop your car, the electric motor in the hybrid acts like a generator and takes some of the energy out of the car while slowing it down. If you give the electric motor more time to slow the vehicle, it can recover

more of the energy. If you stop quickly, the brakes on the car will do most of the work of slowing the car down, and that energy will be wasted.

1.3.6 What's Next for HEVs?

HEVs are now at the forefront of transportation technology development. Hybrids have the potential to allow continued growth in the automotive sector, while also reducing critical resource consumption, dependence on foreign oil, air pollution, and traffic congestion.

Hybrids are a hot subject today and they are beginning to show up across the United States. Their widespread penetration into the automotive market hinges mainly on the economics of producing a complex hybrid power system, rather than the inherent capabilities of the technology itself. The hybrid's complexity, and the fact that some of the best storage and conversion systems have yet to be fully developed, is responsible for varied opinions on hybrids' ultimate impact in the marketplace. As with any new technology, there may be obstructions to its ready acceptance by consumers. But time will soon tell.

1.4 Characterization of electrical systems in Hybrid Vehicles

Starter-alternators systems on board of electric and (or) hybrid electric vehicle (HEV) constitute an aggressive novel technology aimed at improving comfort, gas – mileage and environmental performance of road vehicles. The degree of electrification in a vehicle may be defined by the electric fraction [1] %E:

$$\%E = \frac{\text{peak electric power} \times 100}{\text{peak electric power} + \text{peak ICE power}} = \frac{P_{(el)} \times 100}{P_{(el)} + P_{(ICE)}}$$

For a standard ICE (internal combustion engine) vehicle whose starter and alternator functions, only, are integrated %E < (5-10%). For a mild hybrid electric car %E goes to 10-15% at 42 Vdc. It may reach 60-70% for a full (strong) hybrid electric vehicle and it is 100% for a fully electric car. So there are basically 4 HEVs:

- ICE vehicle with ISA (integrated starter alternator)
- Mild HEV (with ISA)
- Strong (full) HEV (with ISA)
- Electric vehicle (with ISA)

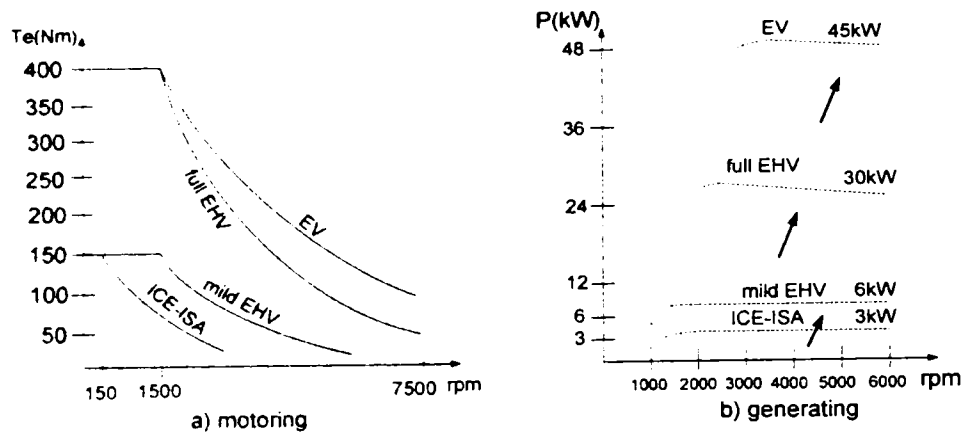


Figure 1.13. Typical electric torque at engine crankshaft speed (for motoring) and electric power/speed envelope for small-medium size cars with various degrees of electrification

1.4.1 42 V PowerNet in HEVs

Performance and handling improvements under the hood, such as dynamic stability controls, electronic suspensions, and precision-controlled fuel injection, also need power from the 14 – V system feature in today's car. To handle the situation, automotive manufacturers and suppliers are embracing a 42 – V standard for system voltage as they design new products.

The challenge for designers, however, is that the cost of the new electronics cannot prohibit the economic production of automobiles. This hurdle must be cleared before cars with 42 – V systems will become available to consumers.

The jump from 14 V to 42 V for system voltage may seem arbitrary, but it is the result of careful thought and years of work initiated by the MIT Consortium on Advanced Automotive Electrical/Electronic Systems and Components. The group eventually settled on 42 V as the optimum system voltage after considering safety constraints posed by global standards setting bodies, specifically a maximum voltage, including transient overvoltage of 60 V dc. [30-34]

The consortium was set up in 1994 as a working group organized by the Massachusetts Institute of Technology, in Cambridge, at the behest of Mercedes-Benz AG, Stuttgart. The German automaker was taking a fresh look at the power-supply options available after realizing the features planned for its 2005 – 15 luxury models would be restricted by an inadequate power supply.

Consider that the 12 V lead-acid batteries now in automobiles produce a system voltage of 14 V dc. That is, when the engine is running, it is effectively

charging all six 2 V cells that make up the battery. As each cell charges, its voltage rises to about 2.3 V, resulting in a higher voltage being measured across the terminals of the battery than is measured when the engine is off. This engine-on or system voltage of 14 V is what designers had to work with.

The upshot was a set of recommendations, chiefly the proposal for the 42 V PowerNet. According to the group, much attention was paid to whether it should propose a standard focused a 36 V lead-acid battery (equivalent to 42 V). Ultimately, the group decided on a standard for system voltage because selection of the battery standard would preclude taking advantage of any alternatives to lead-acid technology that might come along – including those capable of producing a 42 V system voltage from something other than a 36 V battery. [30-34]

Cost is one of the big factors in decisions made by automakers and consumers alike. Just recently, though, have manufacturers begun to appreciate the relationship between the rising electrical content of a car and the vehicle's cost. Electronic controls are proving to be more reliable and safer alternatives to mechanical actuators in cars, but the drawback is that the typical cost of a mid-sized sedan's electrical system is more than that of the engine and transmission.

Beyond the need for inexpensive, plentiful power in cars lies one key driving force for electrification of mechanical functions: packaging flexibility. Under the hood of any car, there is a limited amount of space in which to fit the engine, battery, air-conditioning compressor, electronics, and so forth. In most cars, the front-end accessory drive (FEAD) - or fan belt, as it is more commonly known – drives such devices as the water pump and air conditioning mechanically. That stipulation presents a jigsaw puzzle of sorts to designers as they try to fit everything in its place.

Further complicating the FEAD's ability to meet peak power loads are rising power requirements presented by the increasing number of devices it drives. If the fan belts were to be eliminated and the devices it runs switched to electronic actuators, car designers would gain significant styling flexibility under the hood. Devices dependent on proximity to the FEAD would be freed of that restriction.

As a result, automakers are spurring engineers, both in-house and at suppliers, to develop electrical alternatives to mechanical actuators. The goals are to improve

electrical system efficiency, to examine alternatives to the current 14 – V system, and to boost safety and comfort with new functions that are best controlled electronically.

While the proposed 42 V system seems to meet the increased power requirements presented by the plethora of in-development electronic controls, it is not yet an official standard of the International Organization for Standardization (ISO) or Society of Automotive Engineers (SAE). On the other hand, it is becoming something of a “de facto” standard since it is supported by the 44 current consortium members, including all the leading car manufacturers and component suppliers worldwide. [30-34]

Proposals are being prepared for both the SAE and the ISO, but standards development takes years. By reaching an industry-wide consensus now, consortium members can take advantage of the 42 V system right away rather than start from scratch whenever the standard is set officially.

Although 42 V is set as the system voltage, the structure of the 42 V electrical system is still fluid, and there is no guarantee that an industry standard will be chosen. The problem is not a disagreement between industry groups or individual companies, but rather the existence of two approaches to supplying 42 V system voltage – with or without today’s 12 V battery. Automakers are likely to make a choice based on their own criteria, just as they would decide, for example, on whether a car should have two or four doors, or a trunk or a hatchback.

The two practical alternatives being considered are the single and dual battery options (Figure 1.14). In a dual battery system, using today’s battery technologies, a 36 acid battery producing a 42 V system voltage into an existing 12 V battery supplying a 14 V system voltage. In a single battery system, the 36 V system rides alone. [30-34]

Both the single and dual-battery approaches to a 42 V system place the 42 V power source (a 36 V lead-acid battery today) between the starter motor and alternator. The dual battery version puts a 14 V source (a 12 V lead-acid battery in today’s car) between the converter and 14 V load. Both schemes use a dc-dc converter for the 14 V and 42 V loads. Distribution boxes handle switching and fuse functions between load demand points and power supplies.

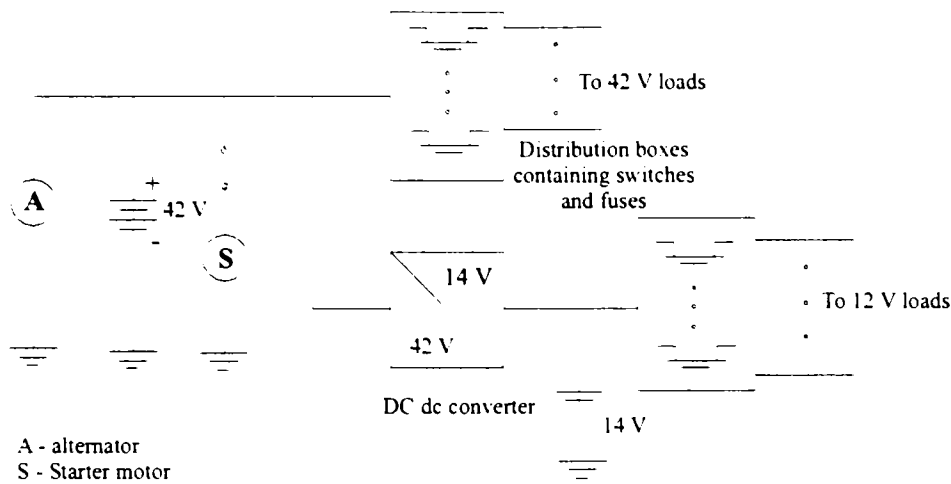


Figure 1.14. The dual battery system

The introduction of a 42V PowerNet enables new powertrain features in future vehicles. An Integrated Starter Generator (ISG) can combine several features in one component: fast engine start-up and shutdown, electric power generation with high efficiency, brake energy recuperation and launch assist. [30-34]

However, most of these features are restricted by the on-board energy storage capability.

Based on real world driving experience with a technology demonstrator vehicle, equipped with an ISG system and dual voltage PowerNet, the energy throughput of the high power 36V Lead Acid battery is analyzed in these papers. Of particular interest is the energy used for torque addition during launch assist phases. It is shown that in order to reduce battery service intervals, either the launch assist function must be restricted, or a different advanced storage system needs to be employed.

The European Automobile Manufacturers, assembled in the ACEA association, signed an agreement to achieve an average CO₂ emission figure of 140 g/km for all new cars sold in the European Union, measured in the European test procedure in the year 2008. Since CO₂ emission is directly coupled to fuel consumption, new vehicle and powertrain technologies are evaluated that can help to meet with the agreed objective. [30-34]

Apart from the use of lightweight materials and reduction of aerodynamic and rolling friction losses, improved powertrain efficiency is a major goal. The powertrain of European high volume passenger cars typically consists of an Internal Combustion

Engine and a manual or automated transmission. The powertrain efficiency under drive cycle and real world circumstances can be improved both on a component level and on a system level. Nowadays, the latter approach gains increasing attention, since the integration of intelligent engine and transmission control allows optimizing the powertrain operating efficiency and hence improving vehicle fuel economy.

The electrification of auxiliaries demonstrates the system approach. A typical example is the electric water pump: although driving the pump electrically is inefficient from a component point of view since the mechanical power fed to the pump shaft has experienced conversion losses via the generator and motor of the pump, the cooling system can be controlled on thermal demand, thus improving powertrain system efficiency.

Eliminating engine friction losses during idling by engine shutdown at vehicle standstill is nowadays seen as another approach to improve powertrain efficiency in both the NEDC and in real world driving. Since the successful exploitation of this feature is closely directed by customer acceptance of the resulting stop-start behavior, new electric machine technologies have been proposed to improve Noise, Vibration and Harshness (NVH) of the powertrain during the transient periods of engine start-up and shutdown.

In parallel to the required improvement of vehicle fuel economy, future comfort levels will force the vehicle electric PowerNet to deliver higher peak and average loads. In combination with the aforementioned ongoing electrification of powertrain auxiliaries, this trend of increasing on-board electric energy use demands a radical improvement of PowerNet efficiency. One step to this efficiency improvement is the introduction of the 42V PowerNet.

A so-called Integrated Starter Generator (ISG) system, that combines several powertrain functions when mounted directly on the engine crankshaft, can be seen as a logical step in the powertrain efficiency optimization on a system level. A technology demonstrator vehicle based on a Ford Focus is presented that combines various new powertrain technologies including an ISG system to improve vehicle fuel economy.

An important aspect of this vehicle is the integration of a 14 V / 42 V dual voltage PowerNet. With increased PowerNet loading, the used electric components

like ISG and storage system need careful evaluation in terms of functionality, dimensioning and efficiency. [30-34]

Although its prime reason may be the efficient generation of electric power, the installation of an ISG system allows the electric machine to be motored for torque supplements to the engine crankshaft.

Regardless of its power level, this functionality hybridizes vehicle propulsion.

Soft hybrids are marked as conventional vehicles with limited electrification of propulsion, typically in the range of 5 to 12 kW and storage capacity of less than 1 kWh. Full hybrids have higher electric power ratings and storage capacity, typically > 20 kW and > 1 kWh.

In order to achieve acceptable component costs and overall efficiency, the voltage range for soft hybrid vehicles is standardized to 42 V nominal by the 42 V PowerNet (Forum Bordnetz / MIT) consortiums. Since this 42 V standardization is generally accepted by the automotive industry, the content of this paper focuses on 42V ISG applications and the energy storage requirements involved with adding new ISG related features in future soft hybrid vehicles. [30-34]

1.4.2 Storage systems in HEV

Presently, possible energy source in HEVs are as it follows:

- **Battery**, has been the most popular choice of energy source for EVs since the beginning of research and development programs in these vehicles.
- **Fuel cells** are electrochemical devices that produce electricity by means of a chemical reaction, much like a battery. The major difference between batteries and fuel cells is that the latter can produce electricity as long as fuel is supplied, while the batteries produce electricity from stored chemical energy and hence, require frequent recharging.
- **Flywheels**, store kinetic energy within a rotating wheel-like rotor or disk-made of composite materials. However, the amount of energy storage required in the flywheels of ICE is small and it is limited by the need of the vehicle to accelerate rapidly. Modern flywheels are made of composite materials, such as

carbon fiber, instead of steel, with a view to increase the energy density, which can be up to 200 Wh/kg .

- **Ultracapacitors**, are derivative of conventional capacitors, where energy density has been increased at the expense of power density to make the devices function more like a battery. Power density and energy density of ultracapacitors are of order of 10^6 W/m³ and 10^4 Wh/m³ .

Batteries for hybrid cars

Batteries are an essential component of the HEVs currently under development. Although a few production HEVs with advanced batteries have been introduced in the market, no current battery technology has demonstrated an economical, acceptable combination of power, energy efficiency, and life cycle for high-volume production vehicles. The Partnership for a New Generation of Vehicles program has established technical targets for the program's hybrid battery development efforts for power-assist and dual-mode HEVs. [35-48]

Desirable attributes of high-power batteries for HEV applications are high-peak and pulse-specific power, high specific energy at pulse power, a high charge acceptance to maximize regenerative braking utilization, and long calendar and cycle life. Developing methods/designs to balance the packs electrically and thermally, developing accurate techniques to determine a battery's state of charge, developing abuse-tolerant batteries, and recycleability are additional technical challenges.

Voltage for PowerNet must be in the range of 21 to 50 V. In a vehicle equipped with a 42 V battery and all of the associated safety items required for commercial application, great care should be taken to minimize the resistance between the battery terminals and the ISG terminals, as well as the internal resistance of the battery itself. In fact, it has been accepted as an international standard that the DC bus voltage should not fall below 21V. The battery voltage versus dc current is presented in Figure 1.15. [34]

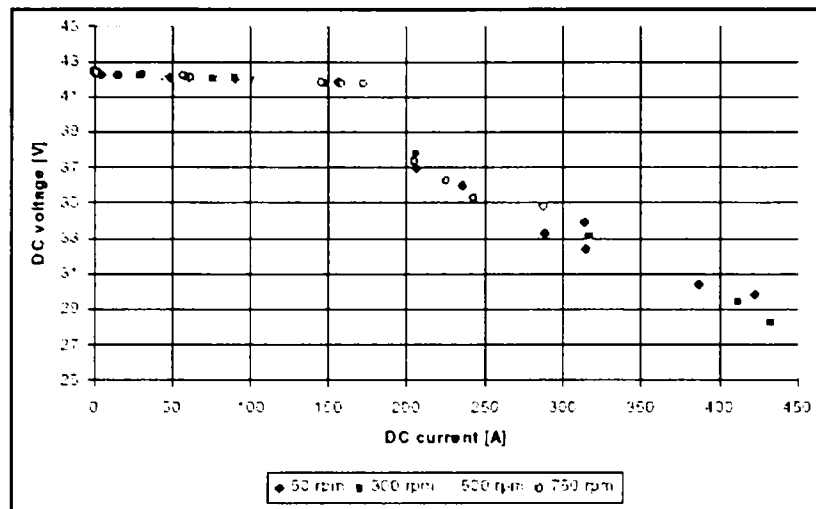


Figure 1.15. Battery voltage versus DC current in discharging process

Lead acid batteries, used currently in many electric vehicles, are potentially usable in hybrid applications. Lead acid batteries can be designed to be high power and are inexpensive, safe, and reliable. A recycling infrastructure is in place for them. But low specific energy, poor cold temperature performance, and short calendar and cycle life are still impediments to their use. Advanced high-power lead acid batteries are being developed for HEV applications.

Although **nickel-cadmium batteries**, used in many electronic consumer products, have higher specific energy and better life cycle than lead acid batteries, they do not deliver sufficient power and are not considered for HEV applications.

Nickel-metal hydride batteries used routinely in computer and medical equipment, offer reasonable specific energy and specific power capabilities. Their components are recyclable, but a recycling structure is not yet in place. Nickel-metal hydride batteries have a much longer life cycle than lead acid batteries and are safe and abuse-tolerant. These batteries have been used successfully in production EVs and recently in low-volume production HEVs. The main challenges with nickel-metal hydride batteries are their high cost, high self-discharge and heat generation at high temperatures, the need to control losses of hydrogen, and their low cell efficiency.

The **lithium ion batteries** are rapidly penetrating into laptop and cell-phone markets because of their high specific energy. They also have high specific power, high energy efficiency, good high-temperature performance, and low self-discharge. Components of lithium ion batteries could also be recycled. These characteristics make lithium ion batteries suitable for HEV applications in size up to 100 Ah.

Technically, Li-ion is probably a stronger candidate for use in 36/42 V systems. The power balance is comparable with that for Ni-Mh, but absolute values are even greater (60-100 Wh/kg specific energy, 700-1600 W/kg specific power) and they are operative over a wider SOC range (10-90%) [48]

Lithium polymer batteries with high specific energy, initially developed for EV applications, also have the potential to provide high specific power for HEV applications. The other key characteristics of the lithium polymer are safety and good cycle and calendar life. The battery could be commercially viable if the cost is lowered and higher specific power batteries are developed.

Table 7. provides a performance comparison between different battery couples.

Table 7. Battery Comparison

Battery Type	Specific Energy W-h/kg	Specific Power W/kg	Energy Efficiency %
Lead Acid	40	130	65
Aluminum Air	200	150	35
Lithium Iron-Disulfide	>130	>120	----
Lithium Polymer	100	100	----
Nickel/Cadmium	56	200	65
Nickel/Iron	55	130	60
Nickel Metal Hydride	80	200	65
Nickel/Zinc	80	150	65
Sodium Sulfur	100	120	85
Zinc/Air	120	120	60
Zinc/Bromine	70	100	65

Fuel cells for hybrid vehicles

Fuel cells (Figure 1.16) work on the principle of reverse electrolysis. Just as you can apply an electric current to water and split it into hydrogen and oxygen, you can also reverse this process to make electricity. Recent technological developments have shrunk fuel cells down small enough to fit under a car's back seat. An example uses stacks of proton exchange membranes, each one only a few tenths of a millimeter thick, that allows only the proton of the hydrogen molecule to pass through. This creates the voltage differential that powers the car. [49-52]

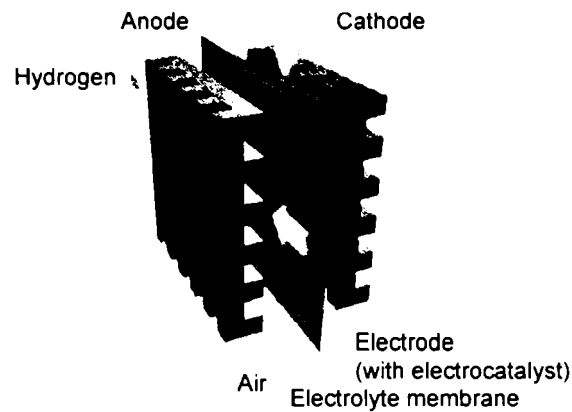


Figure 1.16. How a fuel cell works

Flywheels for hybrid vehicle

Although flywheels are being used in some bus applications today, more work needs to be done to make flywheels safe and effective for HEV automotive applications. Current flywheels are still very complex, heavy, and large for personal vehicles. In addition, there are some concerns regarding the safety of a device that spins mass at high speeds. [54-56]

Flywheels store kinetic energy within a rapidly spinning wheel-like rotor or disk. Ultimately, flywheels could store amounts of energy comparable to batteries. They contain no acids or other potentially hazardous materials. Flywheels are not affected by temperature extremes, as most batteries are.

The flywheel design objective is to maximize energy density. The energy U stored in the flywheel is given by

$$U = \frac{1}{2} \cdot J \cdot \Omega^2$$

where J is the polar moment of inertia and Ω is the angular velocity. Energy storage is increased by spinning at higher velocities without increasing the inertia, which is directly proportional to mass. Increasing angular velocity - Ω , in turn, increases centrifugal stress, which must not exceed failure stress with a given factor of safety. The material used in a flywheel must be lightweight with high tensile strength - condition satisfied by composite materials

Flywheels have been used in various forms for centuries, and have a long history of use in automotive applications. Early cars used a hand crank connected to a

flywheel to start the engine, and all of today's internal combustion engines use flywheels to store energy and deliver a smooth flow of power from the abrupt power pulses of the engine.

Modern flywheels employ a high-strength composite rotor, which rotates in a vacuum chamber to minimize aerodynamic losses. A motor/generator is mounted on the rotor's shaft both to spin the rotor up to speed (charging) and to convert the rotor's kinetic energy to electrical energy (discharging). A high-strength containment structure houses the rotating elements and low-energy-loss bearings stabilize the shaft. Interface electronics are needed to convert the alternating current to direct current, condition the power, and monitor and control the flywheel.

Flywheels could be used in HEVs in several ways, and all of them exploit the ability to deliver very high power pulses. One concept combines a flywheel with a standard engine, providing a power assist. Another concept employs a flywheel to load-level chemical batteries. Still another uses a large or multiple flywheels to replace chemical batteries entirely (in some uses, a flywheel is referred to as an "electromechanical battery"). For flywheels to have success in HEVs, however, they would need to provide higher energy densities than what is now available.

Ultracapacitors

Ultracapacitors are higher specific energy and power versions of electrolytic capacitors—devices that store energy as an electrostatic charge. They are electrochemical systems that store energy in a polarized liquid layer at the interface between an ionically conducting electrolyte and a conducting electrode. Energy storage capacity increases by increasing the surface area of the interface. Ultracapacitors are being developed as primary energy devices for power assist during acceleration and hill climbing, as well as recovery of braking energy. They are also potentially useful as secondary energy storage devices in HEVs, providing load-leveling power to chemical batteries. Current research and development aims to create ultracapacitors with capabilities of Wh/kg and 1,000 W/kg. Additional electronics are required to maintain a constant voltage, because voltage drops as energy is discharged. [53, 57, 58]

In terms of energy and power density, ultracapacitors are positioned between battery technology and electrolytic capacitor technology. Moreover, because they are capable of cycling millions of times, they are virtually maintenance free over the life of any product in which they are used.

1.4.3 Integrated starter/generator

The basic functions of the ISG system in the Focus demonstrator vehicle are introduced. A nonextensive list of five possible functions and their effect on fuel economy is shown in Table 8. [34]

Depending on the ISG system function employed, power density and accumulated energy throughput requirements of the storage system can vary significantly. [60-92]

Table 8. The ISG system functions

ISG system functions	Influence on fuel economy	Storage system requirements high (+); low (-)	
		Power density	Energy throughput
Controlled engine start-up and shutdown	+	++	-
Electric power generation with high efficiency	+	O	O
Energy recuperation during braking or coasting	+	+	+
Torque addition (Launch Assist)	-	+	++
Driveline oscillation damping	-	+	+

Controlled engine start-up and shutdown

Eliminating engine friction losses during idling at vehicle standstill is nowadays seen as a prime feature to improve fuel economy in both the NEDC drive cycle of the European test procedure and in real world driving. The fuel economy advantages of the resulting stop/start operation are reported in literature to vary between 3 and 10 %, depending on vehicle, powertrain and driving trip statistics.

The main advantage of an ISG system over a conventional starter motor can be found in the enhanced customer acceptance of fast engine stop/start behavior, especially in the case of a crankshaft mounted system. An ISG system has the potential of reduced Noise, Vibration and Harshness (NVH) during actively controlled engine start-up and shutdown procedures. Controlled start-up and shutdown can

enhance emissions as well. Apart from the ISG and storage system power dimensioning, correct integration of engine, ISG and transmission control plays a decisive role in this respect.

Normally, an ISG system is dimensioned sufficiently large to perform engine starts at extremely low temperatures, e.g. at $-30\text{ }^{\circ}\text{C}$. The cold start cranking torque depends on the sum of engine friction, compression, auxiliary and acceleration torque. In order to overcome the first compression stroke during start-up, the required maximum machine power at low speed can play a more dominant role in machine design criteria than the breakaway friction torque.

The storage system in the 42 V PowerNet must be able to provide a large number of warm restarts with high starting currents that are typically in the same order of magnitude as standard 12 V SLI Lead-Acid batteries. The higher voltage level provides higher starting power and therefore increased starting speed and comfort. The actual stress on the storage system depends on the type of electric machine technology. In general, permanent magnet machines tend to have higher motor efficiency at low speeds than asynchronous machines, and therefore require less starting power from the storage system.

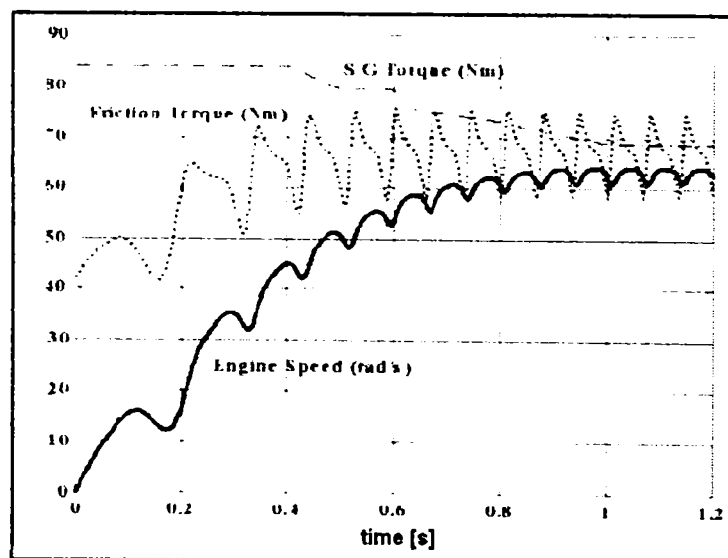


Figure 1.17. Cranking operations vs. time [17]

Since the internal resistance increases with decreasing electrolyte temperature for all battery technologies, the storage system often becomes the limiting factor for cold start cranking. This is especially the case for other than lead-acid based batteries.

The main advantage of an ISG system over a conventional starter motor can be found in the enhanced customer acceptance of fast engine stop/start behavior, especially in the case of a crankshaft mounted system.

Electric power generation with high efficiency

In order to enable all electric and electronic components to perform their function, the required electric energy must be provided by the PowerNet and hence generated on average by the ISG in generator mode. Typical figures that describe the linearised cost of electric power in terms of fuel consumption are in the order of magnitude of 1.2 to 1.5 l / 100 km per generated kW for a high-volume mid-class vehicle with gasoline heat engine while driving the European NEDC cycle. Taking into account the future increase of electric power consumption, optimising the electric PowerNet will play an important role in the quest for improved vehicle fuel economy, both in test procedures as in real world driving.

The use of an ISG system with modern power electronics ensures that the generation of electric energy takes place at high efficiency. Although maximum efficiencies exceeding 0.90 are claimed by ISG manufacturers, typically, the average system efficiency of a 42 V ISG system in drive cycle and real world operation can be expected in the order of magnitude of 0.70. This is still a significant improvement over the cost-optimised conventional 14 V alternator of the claw pole type, where average operating efficiencies of lower than 0.50 are known.

Energy recuperation during braking or coasting

Energy recuperation refers to the control of the ISG in generator mode in coast down situations or while applying the service brakes. It differs from normal generator mode in that the summed fuel cut-off ICE and generator efficiency is infinitely high

under these circumstances. Hence, an optimal energy management strategy will control the ISG to generate maximum power during decelerations, restricted only by momentary storage capacity, drive feel and dynamic vehicle stability functions. The fuel economy gains of regenerative braking depend on the total PowerNet loading, since it only improves the average efficiency of electric energy generation.

The charge acceptance of the storage system limits the high power, high-energy regenerative ISG braking function. Batteries tend to discharge more easily than accept high currents. If the battery capacity is mainly dimensioned to provide high starting currents, regenerative braking can normally not be exploited to its full extend.

Torque addition (Launch Assist)

Although for 42 V ISG systems, the power limitation restricts significant improvements of vehicle acceleration, correct control of torque addition from the ISG machine to the crankshaft during vehicle launch can improve longitudinal vehicle comfort, driveability, performance feel and even emissions.

During launch assist, the storage system must deliver high power to the ISG system. This operation mode typically has duration of several seconds, and consequently a launch assist action requires high-energy throughput from the storage system. Thus, when a launch assist function is included, the storage system's energy throughput capacity must be chosen sufficiently high to guarantee long durability and service intervals. This is especially the case when the vehicle control strategy does not restrict the launch assist function to operate only in first gear drive-away mode.

In principle, the generation, storage and re-use of electric energy come with storage and conversion losses. The influence of a launch assist function on fuel economy therefore depends on the average ISG and storage system efficiency over a trip.

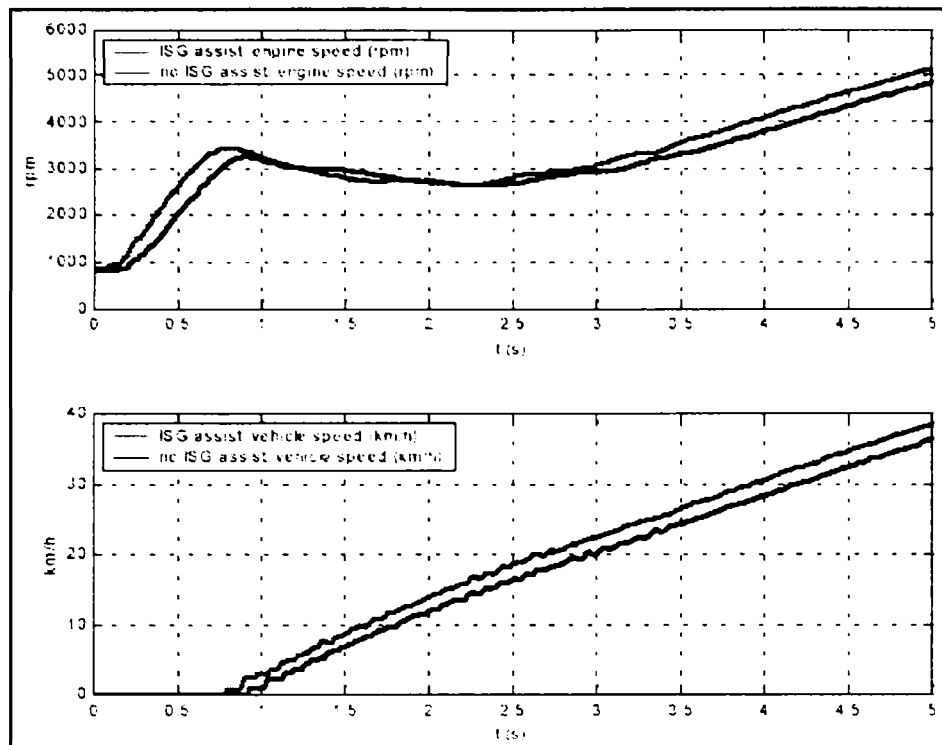


Figure 1.18. Comparison of a vehicle launch with and without launch assist by the ISG in first gear

As it can be seen in Figure 1.18, the launch assist has two effects on vehicle launch. Firstly, the engine response to a accelerator pedal step input is much faster, and secondly, the vehicle acceleration with ISG is higher. The conditions for activation of the launch assist functionality are as it follows: transmission: first gear only; battery: state of charge sufficient; accelerator pedal: applied.

Driveline oscillation damping

The use of an ISG system for torsional vibration damping of the heat engine and driveline is often mentioned. At low engine speed, a high frequency damping function similar of that of a dual mass flywheel can be obtained with a large electric machine and appropriate machine control. Internal capacitors of the power electronics can then partially replace the mechanical energy storage. However, the high power rates involved with anti jerk control of the driveline limit the practical use of electrochemical storage in batteries. In addition, conversion losses in the oversized electric machine and power electronics present a fuel economy penalty that restrict vehicle introduction of this ISG function.

1.5 Choosing an electric machine for traction application

Specifications and typical performance / costs for ISA systems

The following are considered as essential specifications for ISA:

- torque-speed envelope for motoring
- mechanical transmission ratio $K_t \geq 1$ between ISA and ICE speed
- power-speed envelope for generating
- battery voltage (minimum, maximum, rated)
- ISA & PWM inverter rated voltage (a voltage boost/buck dc.-dc. converter may be included between the battery and the PWM inverter to reduce the total power silicon costs and losses)
- Maximum ISA phase RSM current (for peak stall motoring torque)

There are also quite a few constraints on ISA system in terms of the shape of volume, over temperatures in critical points and system costs. In the design of ISA systems the ISA and the PWM converter (with and without d.c.-d.c. converter) the total losses per standard town driving cycle, for given specifications, should be constraint together with volume constraints, while the total system costs should be the main objective function. A comparison between various ISA system at 6 kW peak generating power at 42 Vdc, shown in Figure 1.19 , indicates that at low voltage (42 Vdc) the converter cost is much larger then the ISA cost and thus only system optimization design is meaningful.

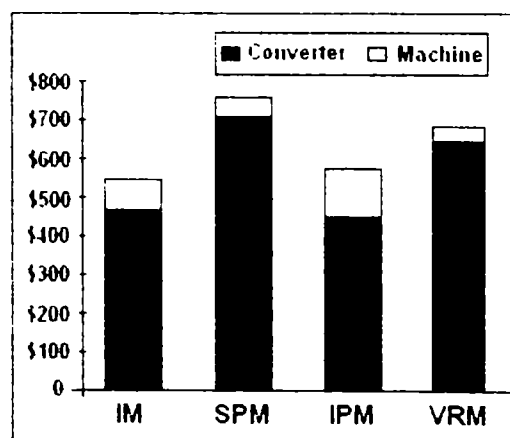


Figure 1.19. ISA systems costs at 6 kW peak generating power [7]

Comparison of four types of motors for EV and HEV

The comparison is for four different types of ac machines, which share the same stator and differ in the rotor structures. These machines are:

- The SMPM (surface mounted permanent magnet) synchronous motor, “brushless motor”.
- The induction motor.
- The synchronous reluctance motor, with traverse laminated rotor.
- The “mixed” motor. This can be considered a brushless motor with anisotropic rotor, or a synchronous motor assisted by permanent magnet (PM RSM).

The identical stator structure of the four machines considered leads to simple and well-balanced hypotheses of comparison. [60-92]

The simple classical traction scheme will be considered, with one only drive, a differential gear and a fixed speed ratio between wheels and motor shaft.

The choice of fixed gear between motor and wheels makes of crucial importance the value of constant – power speed range r , as defined in (1). The large torque at low speed is required to drive up – hill or simply to go out of a garage (and for accelerating), while the torque at maximum speed is mainly due to aerodynamic load, at least for a flat drive.

$$r = \frac{\omega_{m.max}}{\omega_{m.base}} = \frac{T_{basespeed}}{T_{maxspeed}} \cong \frac{m \cdot g \cdot \sin \epsilon}{F_{maxspeed}} \quad (1)$$

From (1) it is evident that different choices of the gradability angle ϵ and the vehicle max speed lead to different requirements for the value of r . However, the situation is even more complicated, since electric motors accept overload and this feature is welcome, in general. Driving out an underground garage can mean slopes up to 30 % or more, clearly representing a short time overload situation. In addition, some motor overload must be accepted also at maximum speed, at least if this one is wanted to be independent of an independent of an even light slope of the road.

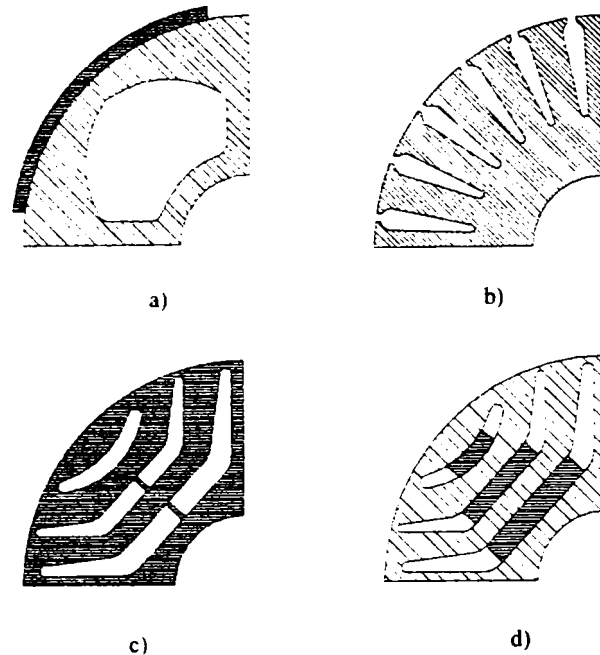


Figure 1.20. Considered types of rotor

The degree of motor overload is another variable to be discussed, since it directly affects the converter design. The battery pack is not affected so far, since the battery weight is mainly due to the wanted autonomy. This is still true for modern NiMH batteries, which show a quite good specific power ($\sim 200 \text{ W / kg}$) but still low specific energy ($\sim 70 \text{ Wh / kg}$).

ACEA EUROVED represents a well-known specification for a small vehicle. It requires $15 / 30 \text{ kW}$ for a range $r = 4$, from 2200 rpm to 9000 rpm . The range of the battery voltage was quite large ($130 \text{ V} \div 290 \text{ V}$). For $\sim 250 \text{ kg}$ of NiMH batteries, the range would go from 125 V to 225 V .

The specification from ACEA EUROVED can be considered those from Figure 1.21. [93, 94, 95]

We can observe that the constant power (30 kW) hypothesis from 2200 rpm to 9000 rpm is not strictly a constraint, since the essential limitation regards the converter, acting differently for the different motors. The overload power can not be so far from the specified battery maximum power: consequently the constant power specification becomes at least opportune, to save autonomy and battery life.

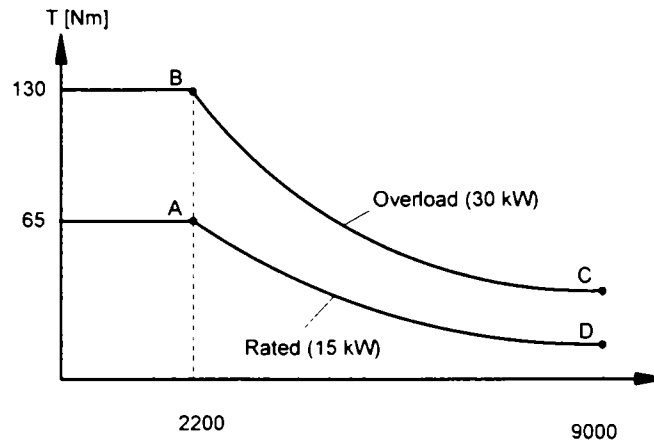


Figure 1.21. Specified torque and speed characteristics

Motor comparison

The rated (continuous) torque given by a motor basically depends on heat dissipation, which in turn is related to the adopted cooling means. In general, liquid cooling is adopted, for this kind of application. [93-95, 97]

For simplicity, the motors have the same outer diameter, and the heat – dissipation capability can be proportional to the active length (a good hypothesis for not too long motors).

a) Comparison at fixed W / m

In this case (with outer diameter fixed), the motor, which is characterized by an inherent lower dissipation, will be both shorter and more efficient, while the winding temperature will be roughly equivalent for all motors.

b) Comparison at fixed length (volume)

If the same length is supposed for each motor (the volumes are the same), we can consider roughly that the weights are nearly equal. The winding temperatures will be different: the more efficient motor will not be fully exploited in this case.

All machines are four poles, except brushless which is six - pole (trade off between iron loss, overload capability and amount of rare material NdFeB - 1 T remanence).

The inner diameter has been chosen identical (200 mm – outer diameter and 120 mm inner diameter).

The heat dissipation capability has been fixed to 10.5 kW / m² (6.6 kW / m), a good value for a liquid cooled machine, trading – off specific torque and efficiency.

The cross – saturation has been disregarded together with additional losses produced by the inverter switching frequencies.

Flux weakening capability and control laws

A quite large constant power speed range is requested. In general the torque can be written as:

$$T = \frac{3}{2} p \bar{\lambda} \bar{i} \quad (2)$$

If the resistive drops and slip speed are disregarded, as a first approximation, we can write:

$$v \cong p \omega_m \lambda \quad (3)$$

Once the maximum motor voltage is given (p C in Figure 1.21), pλ is obtained, giving the minimum flux value (vs. speed).

The parameter kVA_{ref} represents a good indication of the needed inverter size to give a set active power (kW) on a predetermined speed range r.

$$\text{kVA}_{\text{ref}} = \frac{\sqrt{3}}{2} I_{\text{max}} V_{\text{max}} \quad (4)$$

The ratio kVA_{ref} / kW is an important quality factor of the motor, since it heavily affects cost and losses of the associated inverter. Once I_{max} and V_{max} are given, that is the inverter size, the shape of allowed power vs speed is calculated, for a given motor.

The larger the range r is, the lower kW are, at predetermined V_{max}, I_{max}.

Compared motor performances

All motors have been wound for 131 V, corresponding to the lowest considered battery voltage (125 V × 1.05). When the boost converter is used, the motor are wound for 420 V. [93-95, 97]

Table 9 (fixed W / m)

	Brushless	Mixed	Reluctance	Induction
l (mm)	121	138	158	195
kVA _{ref}	112.0	50.0	79.1	56.5
V _{max}	131	131	131	131
I _{max}	985	440	696	497

Point A (2200 rpm, 15kW)

η	0.950	0.943	0.935	0.921
Cos φ	0.96	0.96	0.82	0.86
W _{tot}	790	907	1037	1286
P _{fe}	97	162	188	222
W / l	6530	6570	6520	6594

Point B (2200 rpm, 30 kW)

η	0.912	0.909	0.904	0.881
Cos φ	0.86	0.92	0.79	0.84
W _{tot}	2881	3019	3190	4056
P _{fe}	128	185	242	281
W / l	23813	21880	20061	20801

Point C (9000 rpm, 30 kW)

η	0.973	0.958	0.953	0.912
Cos φ	0.92	1.00	0.67	0.71
W _{tot}	864	1309	1485	2903
P _{fe}	601	192	453	287
W / l	6991	9488	9342	14889

Table 10 (fixed volume, length)

	Brush less	Mixed	Reluctance	Induction
l (mm)	195	195	195	195
kVA _{ref}	99.5	50.8	80.8	56.5
V _{max}	131	131	131	131
I _{max}	875	447	711	497

Point A (2200 rpm 15 kW)

η	0.971	0.963	0.952	0.921
Cos φ	1.00	0.97	0.82	0.86
W _{tot}	448	582	761	1286
P _{fe}	178	206	211	222
W / l	2299	2985	3904	6594

Point B (2200 rpm, 30 kW)

η	0.960	0.949	0.934	0.881
$\cos \varphi$	0.95	0.94	0.80	0.84
W_{tot}	1256	1596	2107	4056
P_{fe}	202	244	269	281
W/I	6443	8184	10803	20801

Point C (9000 rpm, 30 kW)

η	0.959	0.974	0.967	0.912
$\cos \varphi$	0.58	0.98	0.77	0.71
W_{tot}	1269	807	1029	2903
P_{fe}	957	289	565	287
W/I	6507	4140	5279	14889

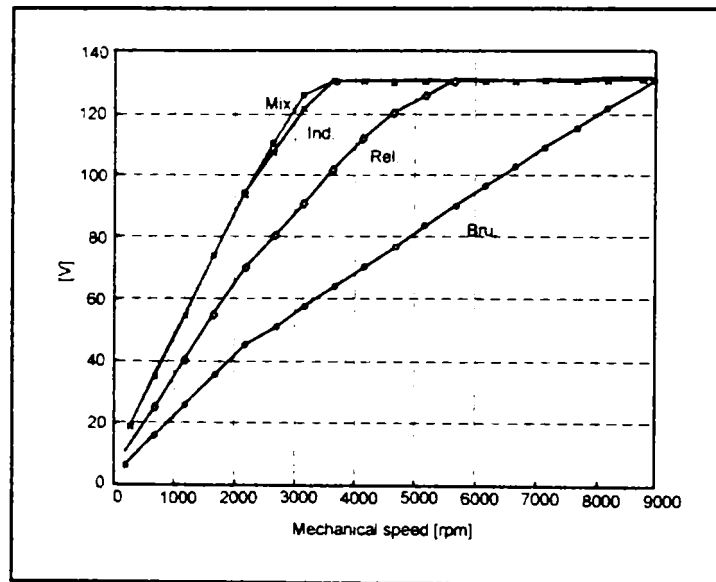


Figure 1.22. Motor voltages vs. speed, at 30 kW max delivered power, motor design of Table 3

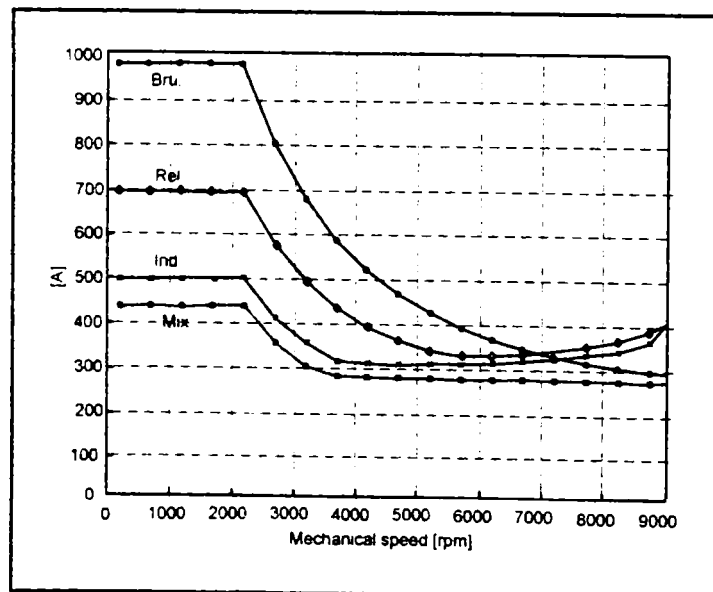


Figure 1.23. Motor currents vs. speed, at 30 kW max delivered power, motor design of Table 3

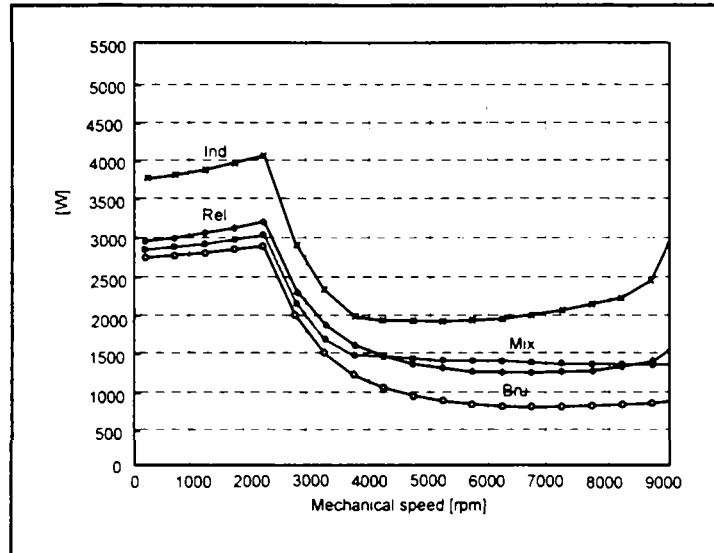


Figure 1.24. Power loss in the motors at a 30 kW max delivered power, motor design of Table 9

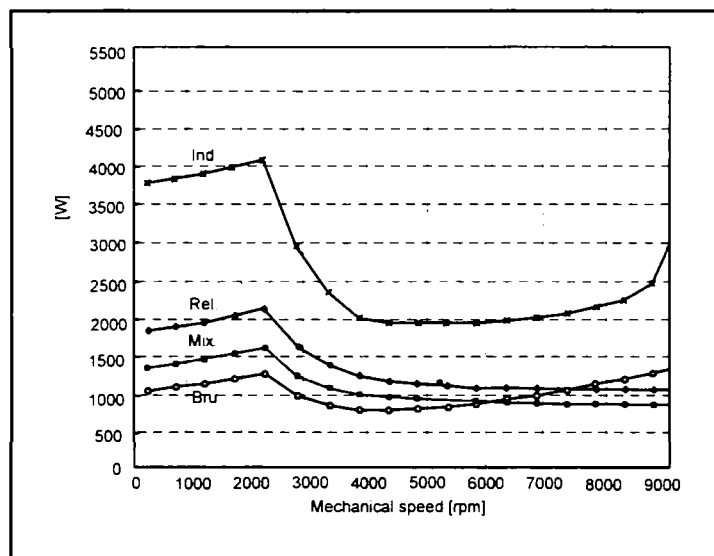


Figure 1.25. Power loss in the motors at a 30 kW max delivered power, motor design of Table 10

It is apparent that the brushless motor gives the best torque density, while needing the largest kVA_{ref} value (this is due to the poor flux – weakening feature of this motor). On the opposite side, the IM show a low kVA_{ref} value, associated to a low torque density. The reluctance motor performance is intermediate. The mixed motor represents a singularity with good value for both torque density and kVA_{ref} . At rated (point A in Figure 1.21), the W / l value is the same. At overload, the W / l value is different, with a visible best-combined performance for the mixed motor.

Regarding Table 10, the hypothesis of equal length lowers the power dissipation of all the synchronous motors, related to IM. [93-95, 97]

Table 10 show the relevant effect of over-sizing on the comparison. The brushless motor is far from practical, because in a real design different magnetic materials should be used. The other two motors show a much lower power loss than the IM, without affecting the kVA_{ref} ratings.

Regarding efficiency, the power loss is shown for the motors from Table 9 in Figure 1.24 and for motors in Table 4 in Figure 1.25. From Figure 1.24, the best efficiency is given by the brushless motor, and the IM is the worst case. In Figure 1.25 where the oversizing of synchronous machines creates a larger gap between these ones and the induction counterpart. [93-95, 97]

Electronic power converter and related losses

A three phase bridge inverter is needed; its size will depend on the type of motor, as above introduced, though the parameter kVA_{ref} . In addition, a dc – dc converter can be used, in between battery and inverter, to adapt and stabilize the inverter supply voltage V_c .

The inverter size is conventionally given by :

$$A_{inv} = 6V_{dim} I_{dim} \quad (5)$$

where V_{dim} is the rated voltage of the device and I_{dim} is the design current (supposed equal to the maximum current I_{max}). The maximum voltage V_{max} (point C Figure 1.21) is different from V_{dim} (lower) and depending on the inclusion of a dc – dc converter. When a dc – dc converter is included, a safe value would be:

- $V'_{max} = V_{Cmax} = 400V$ - for 600 V IGBTs
- $V''_{max} = V_{bmin} = 125V$ - if the inverter is directly coupled to the battery.

This effect is pointed – out in (6), with the influence of the motor type (kVA_{ref} / P_m). P_m is the output overload mechanical power.

$$\frac{A_{inv}}{P_m} = 4\sqrt{3} \frac{V_{dim}}{V_{max}} \cdot \frac{kVA_{ref}}{P_m} \quad (6)$$

The size of the dc – dc converter is given by (6). Introducing the total efficiency η_{tot} between battery and motor shaft, we can write:

$$\frac{A_{boost}}{P_m} = \frac{2}{\eta_{tot}} \cdot \frac{V_{dim}}{V_{bmin}} \quad (7)$$

The adoption of a dc – dc boost converter reduces the size and the cost of the power electronic. The reference type of boost converter is shown in Figure 1.27.

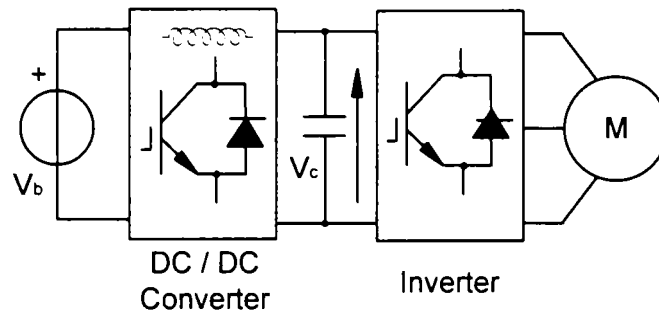


Figure 1.26. Power conversion scheme including a dc – dc converter

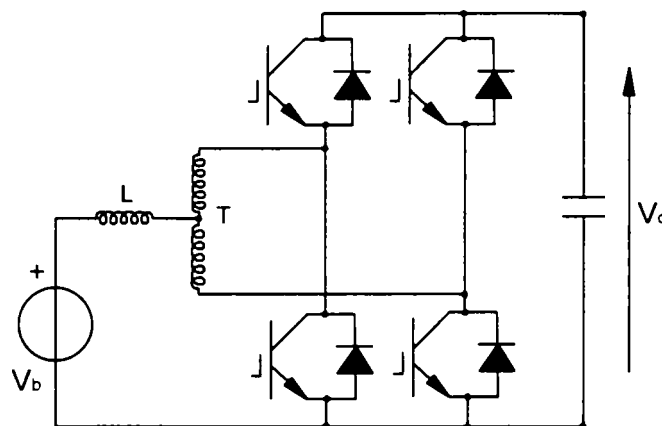


Figure 1.27. H – Bridge boost converter with Transformer + Inductance (T + L) coupling scheme

Regarding power loss in IGBTs, a distinction can be done between conduction losses and switching losses. Thanks to the practical equivalence of transistor / diode voltage drops, we can write:

$$P_{cond.leg} = V_I |I|_{avg} + \frac{\Delta V_R}{I_{rated}} (I)_{rms}^2 \quad (8)$$

$$P_{sw.leg} = \beta_{sw} V_C |I|_{avg} \quad (9)$$

β_{sw} is considered constant for a first approximation. The current I is the load current of the leg. For simplicity, the IGBT rating is posed equal to the peak value of the maximum motor current, assumed sinusoidal (the superimposed ripple is disregarded). The hypothesis is made that the inverter is over – modulated on the limit hexagon (when possible) and the voltage is regulated by the dc – dc converter. In this case, the switching losses are reduced, depending on the power factor $\cos \varphi$.

$$P_{sw.HEX} = \frac{\sin|\varphi|}{2} P_{sw.PWM}; |\varphi| > \frac{\pi}{6} \quad (10)$$

$$P_{sw.HEX} = \frac{(2 - \sqrt{3} \cos \varphi)}{2} P_{sw.PWM}; |\varphi| \leq \frac{\pi}{6} \quad (11)$$

The losses can be calculated and compared for each type of motor, with or without the dc–dc converter. The adopted parameters for this comparison are:

$$V_l = 0.9 \text{ V}, \Delta V_R = 1.1 \text{ V}, \beta_{sw} = 0.0042$$

For the induction motor, in Figure 1.28. The IGBT losses are shown versus battery voltage at overload power (30 kW, shaft), for base (2200 rpm) and maximum speed, with or without the boost converter.

As can be seen, the power loss reduction due to the boost converter is consistent for all working points. So, the five-leg scheme (with the boost converter) works better than the battery – coupled three-leg inverter.

In Figures 1.29 and 1.30 the total power losses of the drives are presented. Figure 1.29 refers to Table 9 and Figure 1.30 refers to Table 10. [93-95, 97]

Regarding the considered drive scheme, the boost converter is included and the battery voltage is set to the rated value (180 V). The maximum delivered power is 30 kW (shaft).

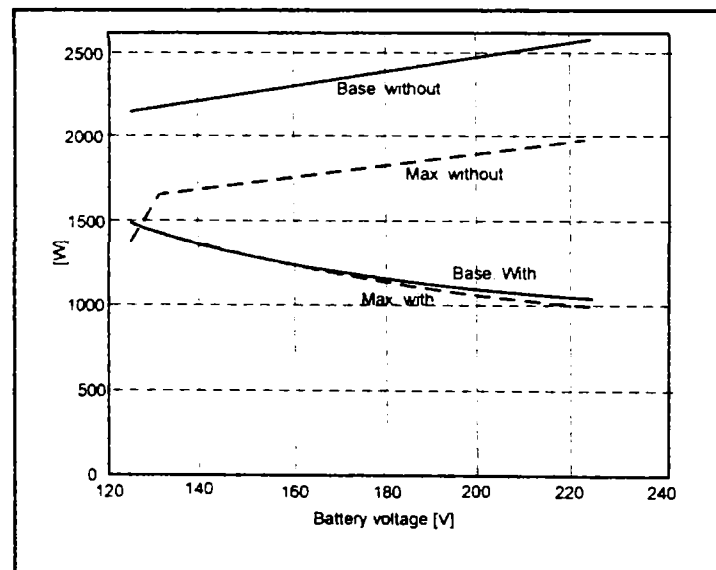


Figure 1.28. IGBT losses for the induction motor drive

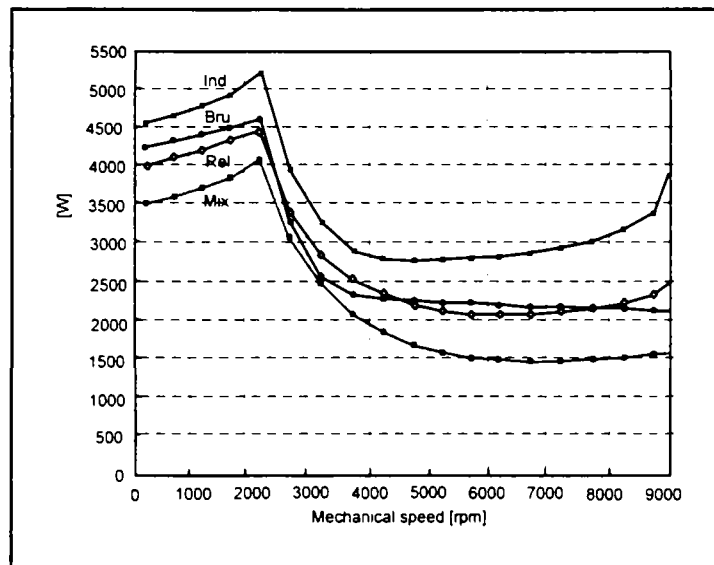


Figure 1.29. Total power loss at a 30 kW max delivered power; motor design of Table 3, with boost converter, $V_b = 180$ V.

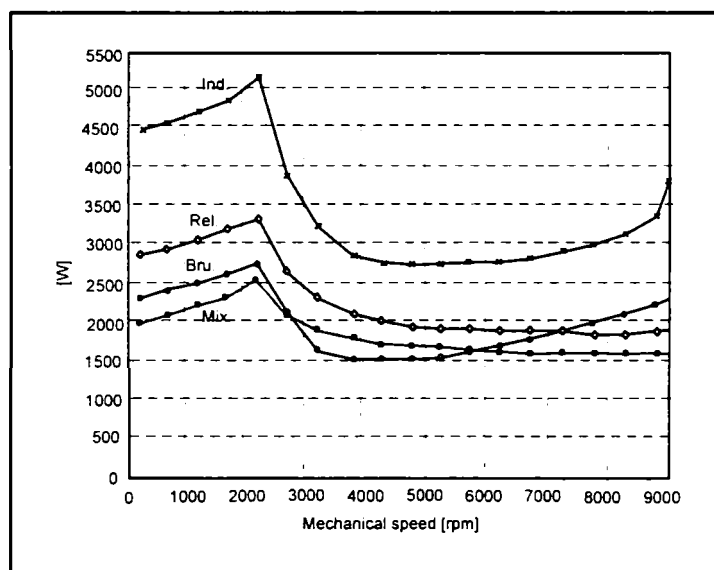


Figure 1.30. Total power loss at a 30 kW max delivered power; motor design of Table 4, with boost converter, $V_b = 180$ V.

As we can see, the synchronous motor drives are the most efficient. The difference between the IM and synchronous motors becomes evident concerning motors of equal volume.

The best performance is given by the mixed-motor (PM RSM) based drives (almost a half of the induction motor-drive). The reluctance-motor-drive give a slightly worst performance, but better than the induction-motor-drive. The performance of the brushless drive points out as usual the penalty of the too large iron loss. [98-106]

For larger powers, 75 kW, and lower speed vehicles (hybrid electric town buses) and rather large mechanical transmission ratio K_r ($K_r > 4$) the excited synchronous motor/generator and the transverse flux PM synchronous machine (TF-PMSM) have been found very competitive in [93-95, 97]. (Table 11).

Table 11. Motors comparison

Feature / Machine	IM	SRM	HPSM	RSM	PMSM	TFM
Volume (10^{-3} m)	53.2	44.0	37.6	35.0	38.9	22.3
Active Mass (kg)	272	147	106	79	71	73
Magnet Mass (kg)	-	-	2.7	4.7	7.0	11.5
Efficiency	0.900	0.930	0.932	0.941	0.949	0.976
Inverter Power (kVA)	396	984	254	361	385	455

Though Ref. 7,8,9 indicate as clear winners the IPMSM for wide constant power speed range (>4) (Fig.4) and TF-PMSM, for moderate constant power speed range ($\omega_{max} / \omega_b < 4$), in terms of losses and total system costs, the induction type ISA and the switched reluctance-ISA due to their robustness, for ($\omega_{max} / \omega_b < 4$), should not be ruled out. [98-106]

1.6 Conclusion

In spite of many problems to be solved, the practical use of electrical vehicle is very close in the future because of the increasingly environmental concerns. There are various topologies of hybrid vehicles on the market, while the electric vehicle will follow, depending on the technical problems. The key problem of electrical vehicle still regards the weight of the battery pack.

A first conclusion is drawn that the inclusion in the power converter structure of a boost section is generally advantageous, from both cost and loss points of view. The larger the motor kVA_{ref} , the larger the advantage is.

In an efficiency-based competition the induction motor-based drive typically takes the last position. The mixed (PM assisted rel. synchronous motor) gives the best average performance, because of its high efficiency and low kVA_{ref} value. The costs of the PM are reasonable.

The inexpensive synchronous reluctance motor requires more kVAs, while the brushless penalties are kVAs and motor cost. If a lower constant power speed range

would be considered, these motors could improve their position, in particular the former.

Anyway, it is really difficult to explain (technically) why the induction motor actually represents the first choice in this application.

Consequently, because of its good results, we will study the **Permanent Magnet assisted Reluctance Synchronous Motor (PM - RSM)**.

1.7 References

- [1] The Union of Concerned Scientists. "A New Road: The Technology and Potential of Hybrid Vehicles". www.ucsusa.org
- [2] V. Wouk. "Hybrids: then and now", IEEE Spectrum, Vol. 32, No. 7, pp. 16-21, July 1995
- [3] Riezenman, michael J. Jones, Willie D, "EV watch", IEEE Spectrum, Vol 35, No 12, p 16. Dec. 1998
- [4] Hermance, David, Sasaki, Schoichi, "Hybrid electric vehicles take to the streets.", IEEE Spectrum, Vol 35, No. 11, pp 48-52, Nov. 1998.
- [5] O. Bitsche, J. Friedrich, K.E. Noreikat – "Electric Drives for Hybrid, Fuel Cell and Battery Powered Vehicles", ICEM 2000, 28 – 30 August, Espoo Finland.
- [6] John G. Kassian, John M. Miller, Norman Traub – "Automotive electronics power up". IEEE Spectrum, May 2000.
- [7] John Kassakian, Hans Chistoph Wolf, John Miller, Charles Hurton – "Automotive electrical systems circa 2005", IEEE, Spectrum 1996.
- [8] Avernethy Francisco, Andrew Frank, Fidelis Eke – "Plug-In Hybrid Electric Vehicles With Full Performance From Sports Cars to Full Sized Trucks" EVS 18, Berlin 2001.
- [9] Piotr Drozd, Richard Siegenthaler – "Hybrid Powertrain Architecture for Medium Duty Commercial Vehicles", EVS 18, Berlin 2001.
- [10] Volker Pickert – "Bora Electric: A Concept Car to test Components for Power Drive Trains", EVS 18, Berlin, 2001
- [11] Fred Flett – "The Electrification of the Automobile", Power conversion, June 1999, Proceedings 133
- [12] Fred Flett – "Automotive Electronics with Particular Reference by Power Steering", Intelligent Motion, June 1999, Proceeding 65.
- [13] B. Asaei, "Electric Vehicle Design Based on Maximum Efficiency and Minimum Cost", EVS 18, Berlin, 2001
- [14] J.M. Miller, V.R. Stefanovic, D. Kak, D. Pelergus, "Progress for starter alternator systems in automotive applications", Record of EPE - PEMC – 2002, Dubrovnik & Cartat, Croatia.
- [15] Electric Vehicle Forum Committee, "SAE J1711, Hybrid Electric Vehicle Emissions and Energy Consumption Test Procedure".
- [16] K. L. Butler, K. M. Stevens, M. Ehsani, "A versatile computer simulation tool for design and analysis of electric and hybrid drive trains", SAE 970199.
- [17] J.M. Miller, V.R. Stefanovic, D. Kak, D. Pelergus, "Progresses For Starter – Alternator Systems In Automotive Applications", Record of EPE – PEMC – 2002, Dubrovnik & Cavtat, Croatia .

- [18] Z.V. Lakaparampil, K.A. Fathima, Gautam Poddar, B. Sreekumari, Renji V. Chacko, V.K. Neelakandhan, *Simulation of HEV with Typical Driving Cycle for a crowded city application*, EPE 2001 – Graz
- [19] M. Ehsani, K. M. Rahman, H. A. Toliyat, “*Propulsion system design of electric and hybrid vehicles*”, IEEE Trans. On Ind. Electronics, vol. 44, no. 1, pp. 19-27, Feb 1997.
- [20] I. Husain, “*Electric And Hybrid Vehicles*”, book, CRC Press, Florida, 2003
- [21] E.C. Losic, T.M. Lindback, W.M. Arshad, P. Telin, E. Nordlund, “*Application of Free – Piston Generator In A Series Hybrid Vehicle*”, Record of LDIA – 2003, Birmingham, UK, pp. 541 – 544.
- [22] Z. Rahman, K. L. Butler, M. Ehsani, “A comparison study between two parallel hybrid control concepts”, SAE 2000-01-0994.
- [23] Takashi Yanase, Nobuaki Takeda, Yuta Susuki, Sadao Imai – “*Evaluation of Energy Efficiency in Series-Parallel Hybrid Vehicle*” EVS 18, Berlin 2001.
- [24] J. Voelker, “*Top 10 Tech Cars : Here Come The Hybrids*”, IEEE Spectrum, March 2004, pp. 20 – 27.
- [25] Sasaki, S.; Toyota's newly developed hybrid powertrain, Power Semiconductor Devices and ICs, 1998. ISPSD 98. Proceedings of the 10th International Symposium on, 3-6 June 1998 Page(s):17 – 22
- [26] Kelly, K.J.; Mihalic, M.; Zolot, M.; Battery usage and thermal performance of the Toyota Prius and Honda Insight during chassis dynamometer testing, Battery Conference on Applications and Advances, 2002. The Seventeenth Annual, 15-18 Jan. 2002 Page(s):247 – 252
- [27] Jinming Liu; Huei Peng; Filipi, Z.; Modeling and Control Analysis of Toyota Hybrid System, Advanced Intelligent Mechatronics. Proceedings, 2005 IEEE/ASME International Conference on, July 24-28, 2005 Page(s):134 – 139
- [28] T. Teratani et al. “*Development Of Toyota Mild Hybrid System (THM - M) With 42 V Power Net*”, Record of IEEE – IEMDC – 2003, Vol 1, pp. 3 – 9.
- [29] W. Buschhaus, L. R. Brandenburg, R. M. Stuntz, “*Hybrid electric vehicle development at Ford*” Proc. of 15th Elect. Veh. Symp. 1998.
- [30] Daniel Kok, Engbert Spijker, Achim Seibertz, Stephan Buller – “*42V Energy Storage Systems for Stop-Start Application in Hybrid Vehicles*”, EVS 18, Berlin 2001.
- [31] R. Blumel – “*Asymmetrical Three level Converter Feeding a 42 / 14 V Automobile Network*”, Intelligent Motion, June 1997, Proceeding 223.
- [32] Engbert Spijker, Achim Seibertz, Rainer Busch, Daniel Kok, Dirk Pelagrus – “*An ISG with Dual Voltage Power Net Stretching the technology Boundary for higher Fuel Economy*”, EVS 18, Berlin 2001.
- [33] Françoise VAREILHIAS, MOTOROLA Semiconductors, *SMARTMOSTM in 42V Automotive System*, EPE 2001 – Graz
- [34] D. Kok, E. Spijker, A. Seibertz, S. Buller, “*42 V Energy Storage Systems for Stop – Start Applications in Hybrid Vehicles*”, EVS 18, Berlin 2001.
- [35] D.H. Davis, L.W. Turner – “*Battery Pack System for General Motor’s Partnership for a New Generation Vehicle (PNGV) – Percept Vehicle*”, EVS 18, Berlin, 2001.
- [36] H.R. van Niekerk – “*Drive system design philosophy for mass minimization of battery – powered vehicles*”, IEE Proceedings, vol. 133, no. 2, March 1986
- [37] DH Davis, LW Turner, Battery pack system for general motor's partnership for a new generation vehicle (PNGV)-percept vehicle, EVS 18, Berlin, 2001

- [38] Stefano Barsali, Massimo Ceraolo, *Dynamic models of lead-acid batteries: implementation issues* IEEE Transaction on Energy Conversion, vol. 17, no. 1, March 2002.
- [39] YH Kim, HD Ha, *Design of interface circuits with electrical battery models*, IEEE Transaction on Industrial Electronics, vol. 44, no. 1, february1997, EVS 18, Berlin, 2001.
- [40] Otmar Bitche, G. Gutmann, A. Schmolz, L. d'Ussel, *Daimler Chrysler EPIC Minivan powered by Lithium Ion Bateries*, IEE Proceedings, vol. 133, Pt. B, No. 2, march 1986.
- [41] HR van Nieker, *Drive system design philosophy for mass minimisation of battery powered vehicles*, IEE Proceedings, vol. 133, Pt. B, No. 2, march 1986
- [42] Bosia, Genova, Mazzucchelli, etc, *Battery management and energy supervision for hybrid vehicles in urban transport: application cases in Italy*, EPE 2001 – Graz
- [43] Carnevali, Genova, Mazzucchelli, Sasso, *State of the art technology and perspectives in battery management for electric vehicles in urban public transport*, EPE 2001 – Graz
- [44] W. Lee, M. Sunwoo, “*Vehicle Electric Power Simulator for Optimizing the Electric Charging System*”, International Journal of Automotive Engineering, Vol. 2, no 4, 2001, pp. 157-164
- [45] Cristina Carnevali, Riccardo Genova, Maurizio Mazzucchelli, Alessandro Sasso, *State-of-the art technology and perspectives in battery management for electric vehicles in urban public transport*, EPE 2001 – Graz
- [46] D.A.J Rand, R.Woods and R.M Dell, “*Batteries for Electric Vehicles*” . SAE International
- [47] Hirai, J., Kim, T. W. and Kawamura, “*Study on intelligent battery charging using inductive transmission of power and information*”, IEEE Trans. Power Electron., Vol. 15, March 2000, pp 335-345.
- [48] R. F. Nelson, “*High Power Batteries for the New 36/42 V Automotive System*”, Journal of Power Sources, 2002, pp.226-239.
- [49] Jiang, Z.; Dougal, R.A.: *Control design and testing of a novel fuel-cell-powered battery-charging station*, Applied Power Electronics Conference and Exposition, 2003. APEC '03. Eighteenth Annual IEEE, Volume 2, 9-13 Feb. 2003 Page(s):1127 - 1133 vol.2
- [50] Adams, W.A.; Blair, J.D.; Bullock, K.R.; Gardner, C.L.; Laishui Li; *Cost/benefit analyses of a new battery pack management technique for telecommunication applications: future directions with fuel cell/battery systems*, Telecommunications Energy Conference, 2004. INTELEC 2004. 26th Annual International, 19-23 Sept. 2004 Page(s):73 – 82
- [51] Cook, B.; *Introduction to fuel cells and hydrogen technology*, Engineering Science and Education Journal, Volume 11, Issue 6, Dec. 2002 Page(s):205 – 216
- [52] Emadi, A.; Williamson, S.S.; *Fuel cell vehicles: opportunities and challenges*, Power Engineering Society General Meeting, 2004. IEEE, 6-10 June 2004 Page(s):1640 - 1645 Vol.2
- [53] Thounthong, P.; Rael, S.; Davat, B.; *Utilizing fuel cell and supercapacitors for automotive hybrid electrical system*, Applied Power Electronics Conference and Exposition, 2005. APEC 2005. Twentieth Annual IEEE, Volume 1, 6-10 March 2005 Page(s):90 - 96 Vol. 1
- [54] PP Acarnley, JS Burdess, BC Mecrow, JN Fawcett, JG Kelly, PG Dickinson – “*Flywheel Energy Storage in Road Vehicles*”, EPE, Sevilla 1995.
- [55] J. Wang, R. Perryman, *Modelling and Control of a Flywheel Powered Ultra Light Rail Bus*, EPE 2001 – Graz
- [56] Hardan, F, Bleijs, J., Jones, R., Bromley, P. and Ruddlell, A. J., "Application of a power controlled flywheel drive for wind power conditioning in a wind/diesel power system", Proceeding of EMD'99, pp 65~70.

- [57] M. Schmidt, A. Egger. Double-Layer Capacitor Short-Time Storage Device in a Hybrid Vehicle, EPE '99, Lausanne
- [58] R.D.King, P.E. J.Schwartz; M.Cardinal; L.Salasoo and Garrigan. Development and System Test of a High Efficiency Ultracapacitor/Battery Electronic Interface, General Electric Research and Development, Schenectady - New York
- [59] Klaus Bolentz – “*Design Modifications of the Electrical System to use Intermittent Engine Operation*”, The Institution of Electrical Engineering, IEE, Savoy Place, London WC2R, UK, 1996.
- [60] Z. Rahman, K. L. Butler, M. Ehsani, “Effect of extended speed, constant-power operation of electric drives on the design and performance of EV-HEV propulsion system”, SAE 2000-01-1557.
- [61] C. Hochgraf, M. Ryan and H. Weigman, “Engine control strategy for a series hybrid electric vehicle incorporating load-leveling and computer controlled management”, SAE 960230.
- [62] E.C. Lovelace, T.M. Jahns, J.L. Kirtley, J.H. Lang, “*An Interior PM Starter Alternator For Automotive Applications*”, Record of ICEM – 1998, Instambul, Vol. 3, pp. 1802 – 1808.
- [63] S. Chen, B. Lequensne, R.R. Henry, Y. Xuo, J. Ronning, “Design And Testing Of Belt – Driven Induction Starter - Generator”, IEEE Trans., Vol. IA – 38, no. 6, 2002, pp. 1525 – 1532.
- [64] A. V. Radun, C. A. Ferreira, E. Richter, “*Two Channel Switched Reluctance Starter-Generator Results*”. IEEE Trans. Vol. IA-34, no 5, 1998, pp. 1026-1034
- [65] L. Ferraris, F. Profumo, A. Tenconi, Realization and tests of EV drives with driving comfort optimization. EPE 2001 – Graz
- [66] Ion Boldea – “*Automotive electric generator systems. A review*”, Electromotion 1999, Patras, Greece.
- [67] Feng Liang, John Miller, Xingyi Xu – “A Vehicle Electric Power Generation System with Improved Output Power and Efficiency”, Electromotion 98 – 11.
- [68] *Machines and Drives for Electric and Hybrid Vehicles* (Digest No: 1996/152), IEE Colloquium on 1996, Page(s): 4/1 -4/6.
- [69] I. Boldea, L. Tutelea, C. I. Pitic, “Characterization Of PM Assisted Reluctance Synchronous Motor/Generator (PM-RSM) For a Mild Hybrid Vehicle”, IEEE Trans. Vol. IA-40, no2, 2004, pp. 492 – 498.
- [70] T. Jahns, “Component Requirement for Wide Constant Power Operation of IPMSM Drives”, Record of IEEE-IAS, 2000, Rome
- [71] KM Rahman, Mehrdad Ehsani – “*Design consideration for EV and HEV motor drives*”, ICEM – 1998, vol. 3.
- [72] RD Schultz – “Performance Model of an Automotive Starter - Generator”, 2000.
- [73] EC Lovelace, TM Jahns, JL Kirtley Jr., JH Lang - “*An Interior PM Starter / Alternator for Automotive Applications*”, Record of ICEM – 1998, Istambul Turkey.
- [74] G Altenbernd, H Schafer, L Wahner - “*Vector - Controlled Crankshaft Starter – Generator for Motor Vehicle*”, ICEM 2000, 28 – 30 August 2000, Espoo Finland.
- [75] H Schaefer – “*Starter generator system for cars based on an induction machine*”, Intelligent Motion, June 1999, Proceedings 75.
- [76] WL Soong, N Ertgrul, EC Lovelace, TM Jahns – “Investigation of Permanent Magnet Offset – Coupled Automotive Integrated Starter / Alternator”, 2001

- [77] CA Ferreira, Eike Richter, “*Detailed Design of a 250 kW Switched Reluctance Starter/Generator for an Aircraft Engine*”, SAE Aerospace Atlantic Conference & Exposition, Dayton, Ohio, April, 1993.
- [78] Baham Amin - “*High Density Torque Motor Structures*”, ICEM, ESPOO Finland, august 2000.
- [79] Thomas M Jahns - “*Uncontrolled Generator Operation of Interior PM Synchronous Machines following High – Speed Inverter Shutdown*”, Electromotion, 1998.
- [80] EC Lovelace, TM Jahns, JH Lang – “*Impact of Saturation and Inverter Cost on Interior PM Synchronous Machine Drive Optimization*”, IEEE Transactions on Industry Applications, vol. 36, No. 3, May – June 2000.
- [81] A. Vagati, M Pastorelli, F Scapino, G Franceschini – “*Cross – Saturation in Synchronous Reluctance Motors of Traverse – Laminated Type*”, IEEE 1998
- [82] I. Boldea “*Reluctance synchronous machine and drives*” Book OUP 1996
- [83] N. Schofield, M. K. Jenkins, “*High performance brushless permanent magnet traction drives for hybrid electric vehicles*”.
- [84] T. J. E. Miller, “*Switched Reluctance Motors and Their Control*”, Magna Physics publishing division, Jan. 1993. Page: 145.
- [85] K.M. Rahman, B. Fahimi, G. Suresh, A. V. Rajarathnam, M. Ehsani, “*Advantages of switched reluctance motor applications to EV and HEV: design and control issues*”, IEEE Trans. on Ind. Application, vol. 36, Issue 1, pp. 111 –121, Jan/Feb 2000.
- [86] Mihai Comanescu, Ali Keyhani, and Min Dai, “*Design and Analysis of 42-V Permanent-Magnet Generator for Automotive*, IEEE Transactions on Energy Conversion, vol. 18, no. 1, march 2003
- [87] W. Cawthorne, P. Famouri, N. Clark, “*Integrated Design Of Linear Alternator/Engine System For HEV Auxiliary Unit*”, Record of IEEE – IEMDC – 2001.
- [88] S. Scridon, I. Boldea, I. Tutelea, F. Blaabjerg, “*BEGA – Biaxial Excitation Generator For Automobiles. Full Characterization And Testing*”, Record of IEEE – IAS – 2004 Meeting.
- [89] J. Luo, S. Huang, S. Chen, T. A. Lipo, “*Design and Experiments of a Novel Axial Circumferential Current PM (AFCC0) Machine with Radial Airgap*”, Record of IEEE IAS-2001 Annual Meeting
- [90] A. Njeh, A. Masmoudi, A. El-Antably, “*3D-FEM based Investigation of Cogging Torque of a Transverse Flux PM Machine*”, Record of IEEE-IEMDC-2003, Vol.1, pp. 319-324
- [91] H. Weh, M. May, “*Achievable Force Densities With PM Excited Machines In New Configurations*”, Record of ICEM-1986, Munchen, Vol 3, pp. 1107-1011
- [92] K. M. Rahman, S. E. Schultz, “*High Performance Fully Digital Switched Reluctance Motor Controller For Vehicle Propulsion*”, IEEE Trans. Vol. IA-38, no 4, 2002, pp. 1062-1071
- [93] A Lange, WR Candors, F Laube, H Mosebach- “*Comparison of different drive systems for a 75 kW electrical vehicle drive*”, ICEM 2000, 28 – 30 August 2000, Espoo Finland.
- [94] A. Vagati, A Fratta, P. Guglielmi, G. Franchi, F. Villata, “*Comparison of AC motor based drives for electric vehicle application*” Record of PCIM – Intelligent motion, Issue 1999, pp.173 – 181
- [95] A. Vaggati, A. Fratta, P. Gagliehni, G. Franchi, F. Villata, “*Comparison Of A.C. Motor Based Drives For Electric Vehicle Application*”, Record of PCIM – 1999, Europe, Vol. IE, pp. 173 – 180.
- [96] H. Baush, A. Grief, K. Kanelis, A. Milke, “*Torque Control Of Battery Supplied Switched Reluctance Drives For Electric Vehicle*”, Record of ICEM-1998, Istambul, Vol 1, pp.229-234
- [97] A. Vagati, A. Fratta, G. Franceschini, R.M. Roso: “*AC motors for high-performance drives: a design-based comparison*”, IEEE IAS Annual Meeting Record, Vol. 1, 1995, pp. 725-733

- [98] D.M. Ionel, J.F. Eastham, T.J. Miller, E. Demeter “*Design consideration for permanent magnet synchronous motors for flux weakening applications*” Proc. IEEE vol. EPA – 145, No.5, 1998 pp.435 – 440
- [99] W.L. Srong, T.J. Miller “*Field weakening performance of 5 classes of brushless synchronous AC motor drives*” Proc. IEEE vol EPA – 141, No.6, 1999 pp.331 – 340
- [100] W. L. Soong, M. Ertrugrul. “*Field Weakening Performance of IPMSM*”, Record of IEEE-IAS-2000, Rome.
- [101] I. Boldea, S.A. Nasar, “*Induction Machine Handbook*”, book, CRC Press, Florida, 2001, pp.130
- [102] I. Boldea, S.A. Nasar, “*Electric Drives*”, book, CRC Press, 1999.
- [103] I. Boldea, “*Reluctance Synchronous Machine And Drives*”, book, Oxford University Press, 1996
- [104] G. Hennenberger, I. A. Viorel, “*Variable Reluctance Electrical Machines*”, book, Shaker Verlag, Aachen, 2001, chapter 6
- [105] T. J. E. Miller, “*Optimal Design Of Switched Reluctance Motors*”, IEEE Trans. Vol. IE-49, no 1, 2002, pp.15-27
- [106] R. B. Inderka, M., R. De. Doncker, “*Control Of Switched Reluctance Drives For Electric Vehicle Applications*”, IEEE Trans. Vol. IE-49, no 1, 2002, pp. 48-53

Chapter II

PM assisted starter/generator – conceptual design and FEM analysis

Abstract

In this chapter, a specified design program - after the specifications are determined, assisted by finite element method (FEM) is presented. Then, the results obtain by FEM are shown – with the torque capability validation. At the end, a sample design for PM-RSM is revealed.

2.1.Introduction: considered specifications & constraints

This chapter introduces the conceptual design and FEM (finite elements method) analysis of PM – assisted reluctance synchronous motor / generator (PM - RSM) for mild hybrid vehicles where a large constant power speed range (6:1) is required and machine volume and converter peak KVA, batteries size are main constraints.

Careful flux – barrier and PM sizing, high magnetic saturation and current density are main requirements for maximum torque production with constraint volume.

The mild hybrid vehicle block diagram is presented in Figure 2.1. This topology contains the combustion engine, the electric motor (integrated starter – generator: ISG), the 42 V battery pack and the power electronic system. The traction system contains also the gearbox. The main advantage of an ISG system over a conventional starter motor can be found in the fast engine stop / start behavior and the potential of reduced Noise, Vibration and Harshness during actively controlled engine start-up and shutdown procedures. During launch assist, the storage system must deliver high power to the ISG system. In the last few years the need for more power introduced the

new 42 V systems instead of the actual 14 V. A mild hybrid vehicle should use this 42 V dc power bus (3 standard 14 V dc batteries in series) only, for ISG.

Typical specifications for a hybrid (or electric) vehicle application are related to:

- peak torque versus speed envelope;
- continuous constant power speed range;
- maximum current for given d.c. link voltage and Vdc given maximum emf at maximum speed E_0 (in the d.c. link);
- maximum current density j (A / mm²);
- losses versus speed for given torque – speed envelope;
- peak torque / kg of active materials;

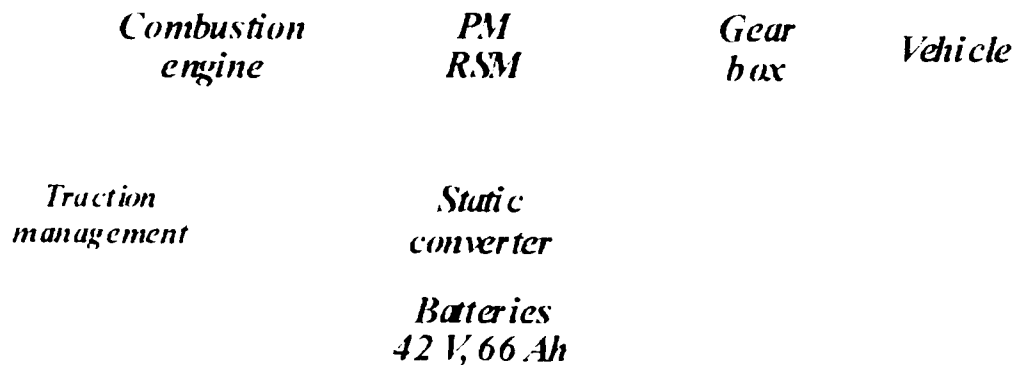


Figure 2.1. Mild hybrid vehicle diagram block

The following are considered specifications & constraints for the PM – RSM design [1-15]:

- Peak torque at stall: $T_{\max} = 140$ Nm;
- Base speed: $n_b = 750$ rpm;
- Speed range: from 750 rpm to 6000 rpm;
- Inverter d.c. bus voltage: $V_{dc} = 48$ V – for mild hybrid vehicle a pack of three 14 V batteries are considered;
- Maximum current: $I_{\max} = 150$ A;
- The peak torque/speed characteristic is presented on Figure 2.2.

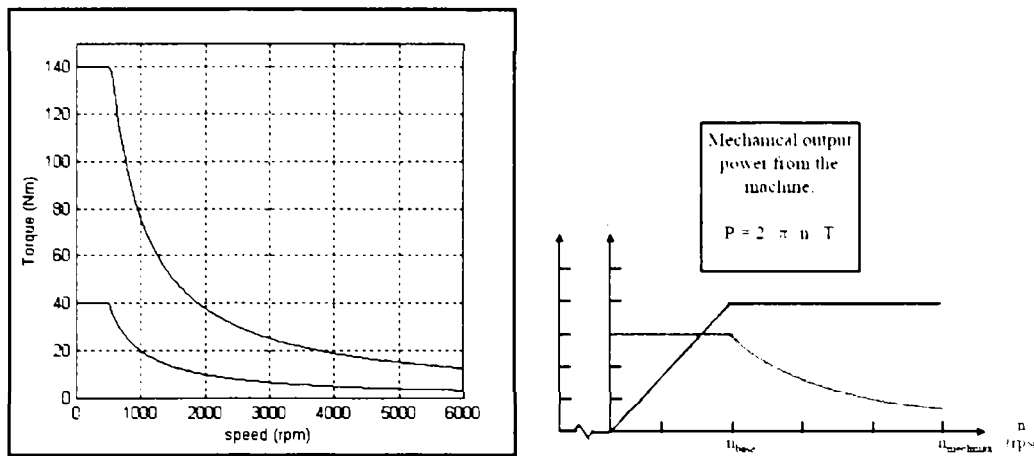


Figure 2.2. Torque and power versus speed

A typical wide power speed range for continuous 2.5 KW from 1000 rpm (idle engine speed) to 6000 rpm (direct on the crankshaft drive) is shown on Figure 2.2.

The unusually large constant power speed range is typical for crankshaft motor / generator. The elimination of any additional transmission is thus paid for.

The solution is volume (weight) constraint also and, consequently, for the maximum torque (developed below base speed) a torque density in range of 15 – 20 Nm / kg of active materials (stator and rotor) is required.

On top of that the maximum phase current (RMS) for maximum torque has to be limited to cut the costs of the converter. Also the machine has to be able to deliver constant power over a 6:1 speed range.

To meet these contradictory specifications a bit of machine oversizing is required, in spite of heavy electrical and magnetic design loadings, together with some inverter oversizing as the voltage required at base speed is notably lower than maximum voltage available. While a rather complete mathematical approach of these aspects is in principle possible, we will adopt here an engineering, more practical approach starting with a practical PM – RSM configuration and conceptual design for heavy electrical and magnetic loadings. [16-33]

2.2. The practical configuration and conceptual design aspect

Once the motor type has been chosen, PM assisted Reluctance Synchronous, we can proceed with the selection of the motor configuration.

2.2.1. Selecting a suitable PM-SM configuration

Present-day power electronics make it possible to select the nominal frequency of a low speed, high torque machine without limitations. In many applications the nominal frequency 50 Hz appears to be invalid. Since the PMSM is usually not designed for network use at all, it is a task of designing to select the frequency and other parameters of the PMSM during the process of designing. [34]

Because of the numerous different variables and parameters varying over wide ranges, the design of the motor is a demanding and complicated task. Considering this, the design also depends on the purpose of the motor, on the goal and on the design constraints.

The design constraints are e.g. temperature limits in the magnets and windings, maximum current densities, maximum magnet flux densities in the stator teeth and yoke, minimum power factor and maximum efficiency, maximum cost of the magnets etc. Consequently, as different objects and constraints of design are concerned, calculations will bring as a result the designing of different motor constructions.

In design calculations the pole pair number is given values between 2 and 14. A smaller pole pair number requires more magnetic material to achieve the demanded torque and a larger pole pair number causes an exceeding of e.g. the mechanical constraints. While depending on the chosen frame size and pole pair numbers the stator slot per pole and phase number varies from 1 to 5. A low slot per pole and phase number brings a heavily distorted MMF wave-form of the stator, which may cause a torque ripple. Therefore, a higher slot per pole and phase number should be preferred to the lower ones. However, with a greater pole pair number, the value $q = 1$ is the only possible integer, because with a higher slot per pole and phase numbers the teeth and slot widths become too thin and fragile. It should be mentioned that fractional numbers for q may be used but such windings are left out of this study for reasons of simplicity.

The initial value for the width of the teeth and yoke is defined by the maximum flux densities in the teeth and yoke. The maximum flux densities are chosen quite large since in low frequency machines the iron losses are typically lower than the

copper losses and it may be obtained slightly better values for the efficiency by making the slots larger.

There are a few challenging performance specifications which are crucial for selecting the rotor configuration once the number of poles is found to be $2p_l=8$, to limit the frequency to 500 Hz.

- The unusually large constant power speed range $n_b = 750$ rpm, $n_{max} = 6000$ rpm;
- The large torque density;
- The very large constant power speed range (6:1) can not be met with an SPM rotor because the q axis reactance would remain high: $X_q = X_d \approx (0.5-0.8)$. This would require a large inverter peak KVA. On top of that the demagnetization current i_d above the base speed would be large and produce unnecessary additional winding losses.

The standard IPM rotor, even with a flux barrier along axis q to reduce the q axis reactance, is also ruled out because the e.m.f. is still high and $x_d = e$ for wide constant power – wide speed range.

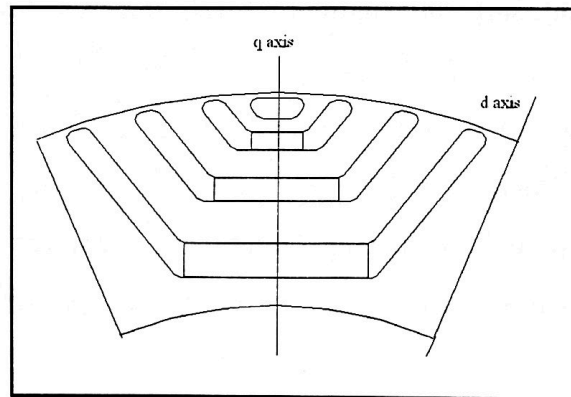


Figure 2.3. PM – RSM rotor

On the other hand high saliency $L_d/L_q \gg 2$ reluctance synchronous motor with PMs in q axis have been shown to be able to handle very wide field weakening ranges. This is due to the fact that the PMs q axis field tends to reduce the influence of X_q voltage drop while flux weakening is produced by reducing i_d (Figure. 2.3).

The higher the saliency – the better.

While the axially laminated anisotropic (ALA) rotor produces highest saliency it is not mechanically rigid enough for rotor peripheral speeds above 50 m/s.

On the other hand the multiple flux barriers rotor is superior to ALA rotor in terms of mechanical ruggedness though it shows lower magnetic saliency.

Inverting axis d with q we might consider this rotor similar to the IPM.

The two components of flux linkage λ_d and λ_q are:

$$\begin{aligned}\lambda_d &= (L_{s\sigma} + L_{dm}) \cdot i_d \\ \lambda_q &= (L_{s\sigma} + L_{qm}) \cdot i_q - \lambda_{qPM}\end{aligned}\quad (1)$$

Apparently the maximum value of i_q corresponds to zero q axis flux linkage λ_q , to avoid PM demagnetization.

However as the leakage flux $L_{s\sigma}i_q$ does not cross the PMs in the rotor a new limit occurs:

$$L_{qm}i_{q\max} \leq \lambda_{qPM}\quad (2)$$

Even this limit is somewhat conservative when the PMs are located as on Figure 2.3 in the middle of flux barriers.

Only FEA would tell the realistic maximum I_q current which does not demagnetize the PMs.

Usually ferrite PMs are recommended for the PM – RSM but in this case strong PMs are necessary (SmCo_5).

It is to be seen if the flux barriers thickness is enough to protect them from demagnetization at maximum torque at start with full d axis flux.

The torque is:

$$T_e = 3p_1(\hat{\lambda}_d i_q - \lambda_q i_d) = 3p_1[\lambda_{qPM} i_d + (L_d - L_q) \cdot i_q i_d]\quad (3)$$

As expected, with $L_d > L_q$, to allow for both torque components to be positive i_q is always positive:

$$i_q > 0\quad (4)$$

i_d, i_q (RMS) are phase quantities.

This is so both for motoring and generating.

To switch from motoring to generating the sign of i_d is changed:

$$i_d > 0 \text{ for motoring}\quad (5)$$

$i_d < 0$ for generating

The mechanism of flux weakening in PM – RSM is quite special: as i_d is decreased λ_d decreases but with i_q simultaneous increasing the torque may be maintained at reasonable values while axis q flux λ_q decreases. So the total flux λ_s decreases while the torque will not decrease to the same extent:

$$\lambda_s = \sqrt{\lambda_d^2 + \lambda_q^2} \quad (6)$$

$$\lambda_s \approx \frac{K_{IR} V_s}{\omega_r}; K_{IR} = 0.95 - 0.97 \quad (7)$$

K_{IR} accounts for stator resistance voltage drop.

So, as the flux decreases notably, ω_r may increase for given maximum voltage V_s produced by the inverter.

Let us remember that for a good design the inverter cost, given by peak inverter KVA, should be kept low:

$$peakKVA = \frac{\sqrt{3}}{2} I_{maxl} V_{maxl} \quad (8)$$

I_{max} – peak line current in the motor

V_{max} – peak line voltage in the motor

For given d.c. link (battery) voltage V_{dc} :

$$(V_{maxl})_{peak} = K_{max} V_{dc} \frac{2\sqrt{3}}{\pi}; K_{max} \approx 0.95 - 0.96 \quad (9)$$

$K_{max} \leq 1$ accounts for the PWM limitations.

For $V_{dc} = 48$ V (rated battery voltage), $K_{max} = 0.95$.

$$(V_{maxl})_{peak} = 0.95 \cdot 48 \frac{2\sqrt{3}}{\pi} = 50.2V \quad (10)$$

I_{maxl} and V_{maxl} do not occur simultaneously.

I_{maxl} occurs at stall for peak torque conditions while V_{maxl} occurs above base speed and up to maximum speed.

The smaller the speed for which V_{max} is used, the smaller I_{max} needed at stall for peak torque, so the smaller peak KVA and inverter ratings (costs). In the same time, the larger the flux weakening zone, the larger and more costly the motor and the inverter are.

In our case the motor size restraints are very severe.

Because of this precondition the voltage at base speed is chosen:

$$V_b = (V_{\max l})_{\text{peak}} K_V b \quad (11)$$

with $K_V \approx 0.4 \div 0.8$ variable as a parameter.

Lower values of K_V would mean large peak KVA and inverter costs.

The voltage would vary with speed as on Figure 2.4.

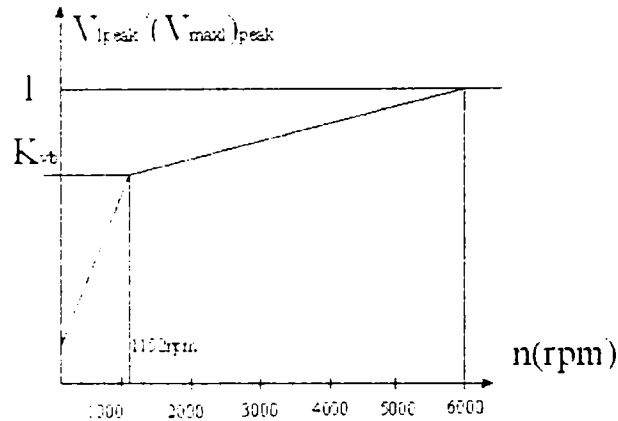


Figure 2.4. Peak line voltage (P.U.) versus speed

According to (10), the max. phase voltage fundamental (RMS value)–star connection–is:

$$(V_{\max ph})_{RMS} = \frac{(V_{\max l})_{\text{peak}}}{\sqrt{6}} = \frac{50.2}{\sqrt{6}} = 20.5V \quad (12)$$

As in our case, the inverter's characteristics are given (considering the battery voltage and current) and so is the peak current / phase (line) envelope, the design philosophy will be to use the peak current, speed envelope as a constraint and attempt the motor efficiency maximum (minimum losses) value. The given geometry data are to be used in the design directly.

The variables are:

- airgap flux density $B_g (T)$ at peak torque up to base speed;
- stator tooth flux density, B_{ts} ;
- stator yoke flux density at base speed, B_{csmax} ;
- rotor iron flux density, B_{crmax} ;

The decision to choose variables related to the peak (continuous) torque at base speed is determined by the value of the torque (40 Nm) in comparison with peak torque at stall (140 Nm) – Figure. 2.2.

2.2.2. Rotor design with FEA assistance

Once the rotor configuration has been chosen, with $2p_1 = 8$, the first variable here would be the rotor outer diameter ODR, besides the ratio between the total thickness of flux barriers and the iron bridges between them:

$$K_{iFe} = \frac{b_{sr1} + b_{sr2} + b_{sr3} + \dots + b_{srn}}{b_{Fer1} + b_{Fer2} + b_{Fer3} + \dots + b_{Fern}} \quad (13)$$

where n is the number of the flux barriers (dummy slots) per half a pole.

To set the number of the flux barriers per pole $2n$ is necessary to compromise two tendencies: it is good to have a large $2n$ to increase the magnetic saliency L_{dm}/L_{qm} .

On the other hand, due to technological limitations and mechanical resiliency, the number of stator slots N_s is further constraint to avoid unnecessary synchronous parasitic torques.

With $q = 2$ slots / pole / phase in the stator and $2p_1 = 8$ poles the number of stator slots N_s will be:

$$N_s = 2pqm = 8 \cdot 2 \cdot 3 = 48 \text{ slots}$$

$$2n \cdot 2p_1 = 2p_1qm \pm 2p_1 \quad (14)$$

$$7 \times 8 = 56 \quad 48+8=56$$

So, we choose $2n = 8$ flux barriers per pole.

Such a situation is good for increasing the saliency but the mechanical ruggedness of the rotor is weakened a little. Considering that the PMs will be only on the bottom of the barriers, the air / iron K_{iFe} in the rotor multiple flux barrier structure may vary in the interval:

$$\frac{1}{2} < K_{iFe} < 1 \quad (15)$$

Smaller values will decrease the saliency though only mildly because the rotor iron is less saturated. However the PMs may be demagnetized for high i_q currents required at stall for the peak torque.

At the other hand $K_{iFe} = 1$ would mean heavy saturation at full flux (in d axis) and peak torque and thus somewhat reduced magnetic saliency due to L_{dm} reduction, though L_{qm} is also reduced.

Heavy saturation tends also to increase torque pulsations.

Further on, the external rotor diameter can be calculated as:

$$\frac{ODR}{2} \approx \frac{IDR}{2} + \frac{B_{g \max}}{B_{Fer \max}} \cdot \frac{ODR}{2p_1} (1 + K_{iFe}) \quad (16)$$

With $B_{g \max} = 0.8$ T, $B_{Fer \max} = 1.9$ T, $K_{iFe} = 0.66$:

$$ODR = \frac{IDR}{1 - 2 \frac{B_{g \max}}{B_{Fer \max}} \cdot \frac{(1 + K_{iFe})}{2p_1}} = \frac{113}{1 - \frac{2 \cdot 1 \cdot (1 + 0.66)}{1.2 \cdot 8}} \approx 174.2 \text{ mm} \quad (17)$$

IDR = 113mm results from the shaft specifications.

We choose $ODR = 174.2$ mm, by allowing 0.6 mm iron bridges in the rotor flux barriers.

This would mean that in fact:

$$\frac{(ODR - IDR)}{2} = \frac{(174.2 - 113)}{2} \approx 30.6 \text{ mm} \quad (18)$$

Now we may calculate the pole pitch at the stator interior diameter:

$$\tau = \frac{\pi \cdot IDS}{2p_1} = \frac{\pi \cdot 113}{8} = 44.37 \text{ mm} \quad (19)$$

For $B_{g \max} = 0.8$ T the average rotor iron flux density:

$$B_{Fer \max} = B_{g \max} \cdot \frac{2\tau(1 + K_{iFe})}{\pi(ODR - IDR)} = 1 \cdot \frac{44.37(1 + 0.66)}{\pi \cdot 30.6} = 0.76 \text{ T} \quad (20)$$

This flux density might seem small. However the contribution of the current in axis q combined with the PM is not yet considered. Also there are mechanical limitations in the thickness of iron between flux barriers.

The airgap is to be small, but it is mechanically limited.

Due to the flux barrier rotor structure, it is believed that an airgap $g = 0.4 - 0.6$ mm has to be adopted. Let us choose $g = 0.4$ mm.

Again the interior stator diameter IDS is:

$$IDS = ODR + 2g = 174.2 + 2 \cdot 0.4 = 175 \text{ mm} \quad (21)$$

The stator outer diameter $ODS = 245.2$ mm (to take into account the integration of the motor)

Consequently the stator slot height h_s plus the stator yoke height h_{cs} is:

$$h_s + h_{cs} = \frac{(ODS - IDS)}{2} = \frac{(245.2 - 175)}{2} = 35.1 \text{ mm} \quad (22)$$

The peak core flux density in the B_{csmax} is a variable in the interval (1.0 – 1.6) T.

For $B_{csmax} = 1.2$ T, the stator yoke height h_{cs} is:

$$h_{cs} = \frac{B_{g \max}}{B_{cs \max}} \cdot \frac{\tau}{\pi} = \frac{0.8}{1.2} \cdot \frac{44.37}{\pi} \approx 13.55 \text{ mm} \quad (23)$$

This would leave for the total slot height:

$$h_s = 35.1 - 13.55 = 21.55 \text{ mm} \quad (24)$$

A smaller value for B_{csmax} would mean less space for the slots. Consequently the current density increases and so does the winding loss. A higher value of B_{csmax} would mean higher core loss and lower saliency but also more room for slots and thus mildly lower winding losses.

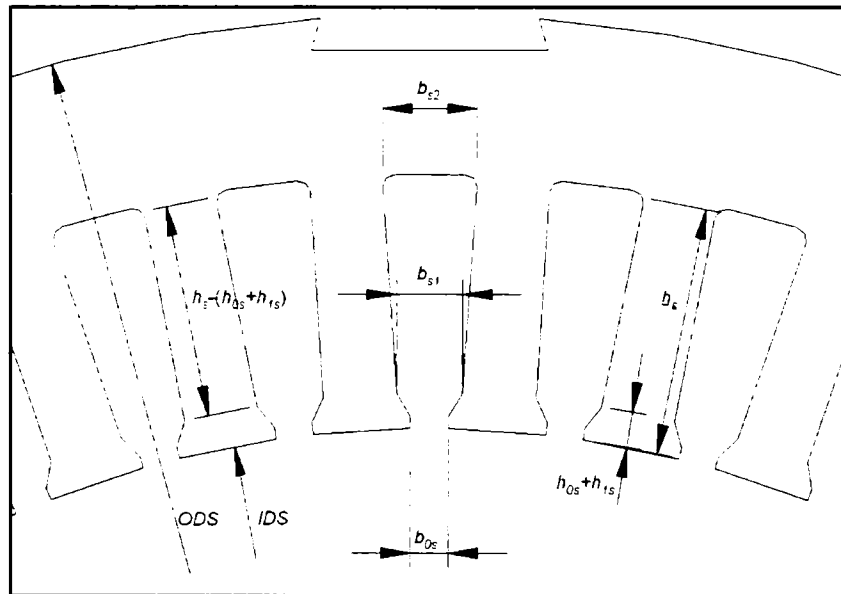


Figure 2.5. Stator slot geometry

With stator tooth flux density $B_{tmax} = 1.03$ T the stator tooth thickness b_{ts} (fig.1.6) is:

$$b_{ts} \approx \frac{B_{g \max} \tau}{B_{ts \max} \cdot 3q \cdot K_l}; K_l = 1.03 - 1.05 \quad (25)$$

K_l accounts for useful flux, which takes the slot path to reach the airgap – due to stator tooth saturation:

$$b_{1s} = \frac{0.8 \times 44.37}{1.03 \times 3 \times 3 \times 1.01} \approx 6.13 \text{mm} \quad (26)$$

The slot bottom width b_{s1} is:

$$b_{s1} = \frac{\pi(IDS + 2(h_{0s} + h_{1s}))}{N_s} - b_{1s} = \frac{\pi(175 + 2 \cdot 3)}{48} - 6.13 \approx 5.6 \text{mm} \quad (27)$$

The stator slot bottom width b_{s2} is:

$$b_{s2} = \frac{\pi(IDS + 2(h_{0s} + h_{1s} + h_{sr}))}{N_c} - b_{1s} = \frac{\pi(175 + 2 \cdot 21.55)}{48} - 6.13 = 8.14 \text{mm} \quad (28)$$

The slot active area A_{astot} is:

$$A_{astot} = \frac{b_{s1} + b_{s2}}{2} h_{s\sigma} = \frac{5.6 + 8.14}{2} \times 18.55 = 127.4385 \text{mm}^2 \quad (29)$$

Assuming $2a = 2p_l = 8$ current path in parallel round wire may be used.

Consequently the total bare wire area in the slot A_{cos} is:

$$A_{cos} = A_{astot} K_{fill} \quad (30)$$

$K_{fill} = 0.47$ is the total filling factor (bare copper / slot active area);

For a very careful introduction of coils in slots the slot filling factor may run as high as:

$$A_{cos} = 127.4385 \times 0.47 = 59.9 \text{mm}^2 \quad (31)$$

Random wound coils are used to ease the manufacturing and accommodate the trapezoidal slot to make full use of the available room.

2.2.3. Stator winding design

As already stated the machine will have $N_s = 48$ stator slots for $2p_l = 8$ poles.

The winding contains random wound coils with round wire turns. The coils are chorded to $y/\tau = 8 / 9$ to reduce somewhat the fifth and seventh m.m.f. harmonics. [35-37]

The winding factor is:

$$K_{w1} = K_{q1}K_{v1} = \frac{\sin \frac{\pi}{6}}{q \sin \frac{\pi}{6q}} \sin \frac{y \pi}{\tau 2} \quad (32)$$

To allow for round wires, the largest number of current paths possible should be used: $a = 2p_1 = 8$. So each pole containing 4 coils / phase in series represents one current path.

Still the number of turns per coil n_c , for a double layer winding, is to be determined.

For this, we need the PM – RSM parameter expressions.

2.2.4. Inductances, resistances and PM flux linkage

First, we should investigate the magnetization inductance [15-16]:

$$L_{dm} = K_{dm} \frac{L_m^i}{1 + K_{sd}}; L_m^i = 6\mu_0 \left(\frac{qn_c 2p}{a} \right)^2 \frac{l_{stack}}{\pi^2 g K_c p}; K_{dm} \approx 0.97 \quad (33)$$

L_{mi} is ideal magnetization inductance with a current path, for infinitely permeable iron;

K_{sd} is the magnetic saturation factor which accounts for the magnetic voltage drop in the iron in relative terms to airgap;

n_c – number of turns / coil

K_{sd} is to be calculated as is done traditionally in IMs, though some FEA values are given for crucial points (peak torque at stall etc.);

K_c is the Carter coefficient,

τ - pole pitch,

L_{stack} – stack length = 69 mm – as a specification, for the electric motor to fit between the combustion engine and the transmission.

The geometrical stack length L_{gstack} is:

$$L_{gstack} = \frac{L_{stack}}{K_{stack}} = \frac{69}{0.95} = 72.63 \text{ mm} \quad (34)$$

Stacking factor: $K_{stack} = 0.95$, 0.014 inch M19 laminations ($B_{sat}=2.0$ T, $H_{sat}=34000$ A/m).

For the q axis magnetization inductance we may adopt:

$$L_{qm} = \frac{L_{mi} \cdot K_{qm}}{(1 + K_{sq})} \quad (35)$$

$$L_{qm} \approx \frac{1}{1 + K_{sq}} \left(0.022 + 4.35 \frac{pK_c g}{IDS} \cdot \frac{1.5}{1 + K_{iFe}} \right) \quad (36)$$

$2n$ is the number of flux barrier per pole.

$$K_c = 1.31;$$

Now K_{sd} and K_{sq} need to be calculated.

With $B_g = 0.8$ T, $H_g = 0.6369 \times 10^6$ A/m and maximum torque conditions let us consider the worst situation when:

$$B_{ls} = B_{cs} = B_{cr} = B_{sat} = 2 \text{ T and } H_{ls} = H_{cs} = H_{cr} = H_{sat} = 34000 \text{ A/m}$$

$$K_{sd} = \frac{H_{ls} \cdot h_s + H_{cs} \cdot \pi(OD - h_{cs})/12/p + H_{cr} \pi(ODR + IDR)/24/p}{H_g \cdot g \cdot K_c} \quad (37)$$

The stator phase resistance is:

$$R_s = \rho_{Cu} \frac{(n_c q)}{2p} \cdot \frac{l_c}{\left(\frac{A_{cos}}{2n_c} \right)} \quad (38)$$

with $\rho_{Cu} = 1.7 \times 10^{-8} \times \left(1 + \frac{120 - 20}{273} \right) \approx 2.3227 \times 10^{-8} \Omega m$; $2p = a = 8$ current paths in

parallel, A_{cos} – slot bare copper area, l_c – coil length:

$$l_c = 2 \left(l_{gstack} + 2 \times 0.005 + \frac{\left(\frac{y}{\tau} \right) \cdot \tau}{\cos 40^\circ} \right) = 248.25 \text{ mm} \quad (39)$$

$$l_{end} = \frac{l_c}{2} - l_{gstack} = 51.5 \text{ mm}$$

$$R_{s100^\circ C} = \frac{2.3227 \times 10^{-8} \times 2n_c^2 \times 0.249}{16 \times 64.91 \times 10^{-6}} = 1.921 \times n_c^2 \times 10^{-4} \quad (40)$$

The stator leakage inductance $L_{s\sigma}$ is:

$$L_{s\sigma} = \mu_0 (2n_c)^2 \frac{q}{a} (\lambda_s + \lambda_{end} + \lambda_z) L_{stack} \quad (41)$$

where:

$$a = 2p_l;$$

λ_s – slot geometrical permeance;

λ_{end} – end connection permeance coefficient;

λ_z – zig zag permeance coefficient;

$$\lambda_s = \frac{2h_{s\sigma}}{3(b_{s1} + b_{s2})} + \frac{h_{os}}{b_{os}} + \frac{2h_{1s}}{b_{s1} + b_{os}} \quad (42)$$

$$\lambda_z = \frac{5g}{4g + 5b_{os}} \quad (43)$$

$$\lambda_f = 0.34 \frac{q}{L_{gstack}} \left(l_{end} - 0.64 \frac{y}{\tau} \right) \quad (44)$$

Finally from (41) we can calculate $L_{s\sigma}$ as function of n_c .

In a similar way the magnetization inductances L_{dm} and L_{qm} can be calculated from (32) - (36) for max. torque at stall.

The PM flux density in the airgap B_{gPM1} fundamental is obtained through FEA.

Alternatively an analytical method may be applied.

First let us consider that the PM flux will saturate the iron bridges in the rotor that hold the rotor together as one piece.

The rotor bridge flux linkage ψ_{bridge} is:

$$\left(\psi_{bridge} \right)_{peak} = \frac{4}{\sqrt{3}} L_{stack} \frac{q \cdot n_c \cdot 2p}{a} K_{w1} \cdot W_b \cdot B_{sat} \quad (45)$$

$$W_b = 0.6 \times 10^{-3} \text{ m (fig.1.3)}$$

$$B_{sat} = 2 \text{ T for M19 lamination stack.}$$

The airgap flux linkage of the PMs is:

$$\left(\psi_{PMq} \right)_{peak} = \left(\frac{2}{\pi} B_{gPM1} L_{stack} \tau \right) q n_c \frac{2p}{a} K_{w1} \quad (46)$$

To calculate analytically the PM airgap flux density let us consider a 6 bridge rotor poles (Figure 2.6.)

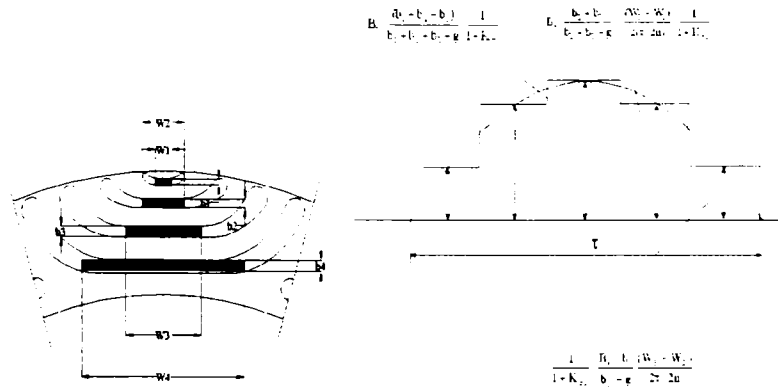


Figure 2.6. PM airgap field

To a good first approximation:

$$B_{gPM1} \approx \frac{W_1 + W_2 + W_3}{3\tau} B_r \frac{b_1 + b_2 + b_3}{b_1 + b_2 + b_3 + g} \cdot \frac{1}{1 + K_{\sigma A}} \quad (47)$$

From (50) - (52):

$$B_{gMP1} = B_{r120^\circ C} \frac{\left(\frac{h_i}{h_i + h_{Fe}} \cdot \frac{(ODR - IDR)}{2} \right)}{\frac{h_i}{h_i + h_{Fe}} \cdot \frac{(ODR - IDR)}{2} + g} \cdot \frac{1}{1 + K_{\sigma A}} \cdot \left[\frac{W_2}{2\tau} + \frac{W_3}{\tau} + \frac{W_4}{\tau} \right] \quad (48)$$

$$\frac{h_i}{h_i + h_{Fe}} = \frac{1}{3}; \quad \frac{(ODR - IDR)}{2} = 30.6 \text{ mm}; \quad K_{\sigma} = 0.4;$$

The value of for B_{gPM1} must be confirmed by FEM.

$$\left(\psi_{bridge} \right)_{peak} = \frac{4}{\sqrt{3}} L_{stack} \frac{q \cdot n_c \cdot 2p}{a} K_{wl} \cdot W_b \cdot B_{sat} = f(n_c) \quad (49)$$

$$\left(\psi_{PMq} \right)_{peak} = \left(\frac{2}{\pi} B_{gPM1} L_{stack} \tau \right) q n_c \frac{2p}{a} K_{wl} = f(n_c) \quad (50)$$

This is a conservative statement as in presence of stator current the rotor iron bridge are traveled by stator produced flux as well, which contributes to further saturation in the bridges.

Finally the flux in axis d is:

$$\psi_d = (L_{s\sigma} + L_{dm}) \cdot i_d \quad (51)$$

Similarly the flux linkage in axis q is:

$$\left(\psi_q \right)_{PM} = (L_{s\sigma} + L_{qm}) \cdot i_q + \psi_{bridge} - \psi_{PMq} \quad (52)$$

The only unknown left is the numbers of turns per coil n_c in the two layer winding of the stator.

2.2.5. Simplified core loss model

For M19, 0.35 mm thick laminations the core loss may be considered to be 17 W / Kg at 400 Hz and 1 T and dependent on flux density and frequency as:

$$p_{iron} = C_{iron} \cdot f^{1.7} \cdot B^2 \text{ (W / Kg)} \quad (53)$$

$$C_{iron} = 6.411 \times 10^{-4};$$

The stator tooth weight and yoke weight is:

$$G_{st} = h_s b_{ts} N_s L_{stack} \gamma_{lam} \quad (54)$$

$$G_{syoke} = \frac{\pi}{4} \left(ODS^2 - (ODS - 2h_{cs})^2 \right) \cdot L_{stack} \gamma_{lam} \quad (55)$$

The weights are small, so that even at peak speed (6000 rpm, $f_{max} = p_1 n = 400$ Hz) and 1.8 T (with full flux) the core losses would be:

$$P_{iron\ max} = (G_{st} + G_{syoke}) \cdot P_{iron} \times 1.5 \quad (56)$$

As it is a known fact that even during generating less than rated flux is allowed for at maximum speed to avoid a large over voltage in the battery terminals, the core losses are expected to be smaller.

The winding losses are expected to be notably higher in general as the slot area is small for the torque density required.

So the precision in estimating the core loss is not very important in this case.

The core loss will be included in the efficiency calculation, and in the input power but not when calculating the winding current.

2.2.6. Torque & turns / stator coil n_c

For peak torque at stall full flux in axis d is assumed. Also the maximum airgap flux density should not go above 0.8 – 0.85 T, if, possible, to avoid excessive saturation which would reduce torque capability as K_{sd} increases too much. [38-39]

Let us assume that for maximum torque conditions (140 Nm) the flux density fundamental component of i_d is limited to say $B_{gdmax} = 0.89$ T but the saturation coefficient corresponds to the find (through FEM) value of $n_c I_{dmax}$.

$$B_{gd1} = 3\sqrt{2} \frac{\mu_0 (2qn_c) \frac{i_{d\ max}}{a} K_{dm} K_{wl}}{\pi K_c (1 + K_{sd}) g} \quad (57)$$

From here we can calculate the phase d axis m.m.f. current $n_c i_{dmax}$ (total at terminals).

The stall peak torque $T_{esk} = 140$ Nm.

$$T_{esk} = 3p \left[(L_{dm} - L_{qm}) i_{q\ max} + \frac{\psi_{PM} - \psi_{bridge}}{\sqrt{2}} \right] \cdot i_{d\ max} \quad (58)$$

$$\frac{n_c I_{peak}}{a} = \sqrt{\left(\frac{n_c i_{d \max}}{a}\right)^2 + \left(\frac{n_c i_{q \max}}{a}\right)^2} \quad (59)$$

$$J_{peak} = \frac{n_c \frac{I_{peak}}{a}}{\frac{A_{cos}}{2}} \quad (60)$$

For the known peak current ($I_{peak} = 250$ A), we can calculate n_c :

$$n_c = \frac{n_c I_{peak}}{I_{peak}} \quad (61)$$

Copper conductor area

$$A_{cond} = \frac{I_{peak}}{a J_{co \max}} \quad (62)$$

$$d_{co} = \sqrt{\frac{4}{\pi} A_{cond}} \quad (63)$$

The maximum stator flux:

$$(\Psi_s)_{RMS} = \sqrt{\Psi_d^2 + \Psi_q^2}$$

$$\Psi_{d \max} = (L_{s\sigma} + L_{dm}) i_d$$

$$\Psi_{q \max} = (L_{s\sigma} + L_{qm}) \cdot i_q - (\Psi_{PM} - \Psi_{bridge}) \quad (64)$$

$$P_{mec} = T_e \frac{2\pi\Omega}{60} \quad (65)$$

The efficiency of the motor is:

$$\eta = \frac{P_{mec} - p_{mec}}{P_{mec} + 3R_s I_s^2 + p_{iron}} \quad (66)$$

$$p_{mec} = 1\% P_n \approx 1000W \quad (67)$$

At the end of this chapter a sample design program (MATLAB[®]) is presented (with the needed initial values, the calculation of the rotor magnetic circuit, stator winding design, the magnetic circuit design, the pm flux, the coil design, the starting characteristics, the motor characteristics, weights and losses).

2.3. Sample numerical analysis (FEM)

In Figure 2.7 the design configuration for the permanent magnets assisted reluctance synchronous machine is presented after calculations (prepared for FEA analysis)

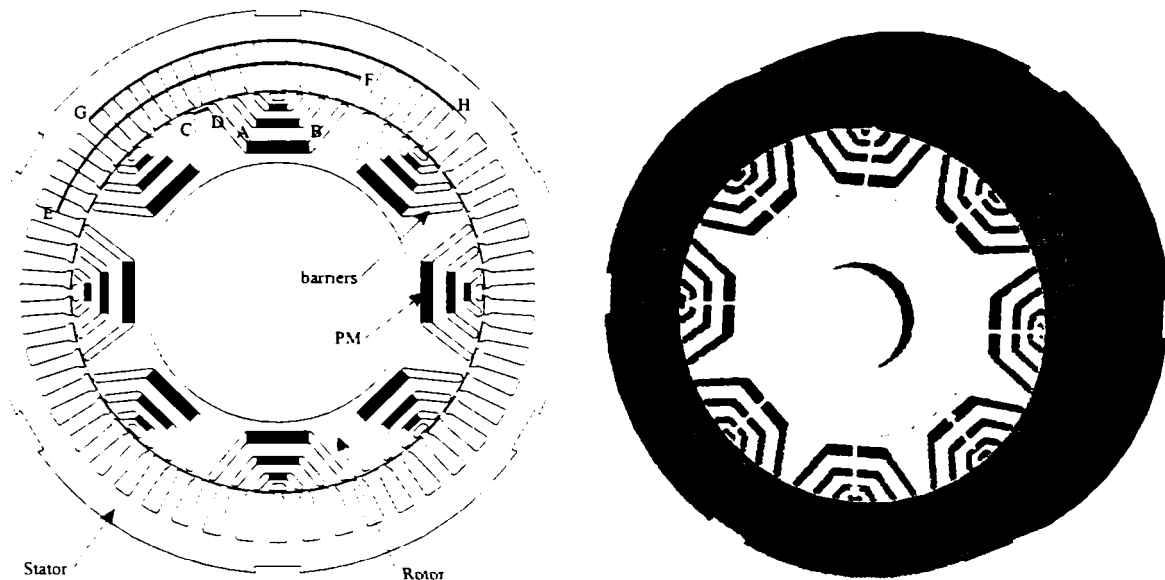


Figure 2.7. The PM – RSM machine

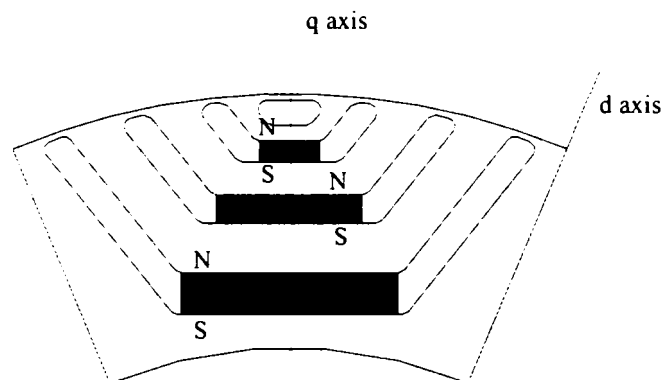


Figure 2.8. Rotor design and PM's polarity

Table 2.1. The geometric dimensions of the PM – RSM.

Geometric parameters		Value
Stator outer diameter	SOD	245.2 mm
Rotor outer diameter	ROD	174.2 mm
Rotor inner diameter	RID	113 mm
Airgap	g	0.4 mm
Stack length	l_{stack}	69 mm
PM parameters at 20 °C	B_r	0.87 T
	H_c	660000 A/m

The rotor topology and the polarization of the magnets are presented in Figure 2.8. The rotor design (the permanent magnet dimensions) was made with FEM assistance. [40-44]

The stator laminations were chosen from an existing motor in order to lower the costs of the prototype.

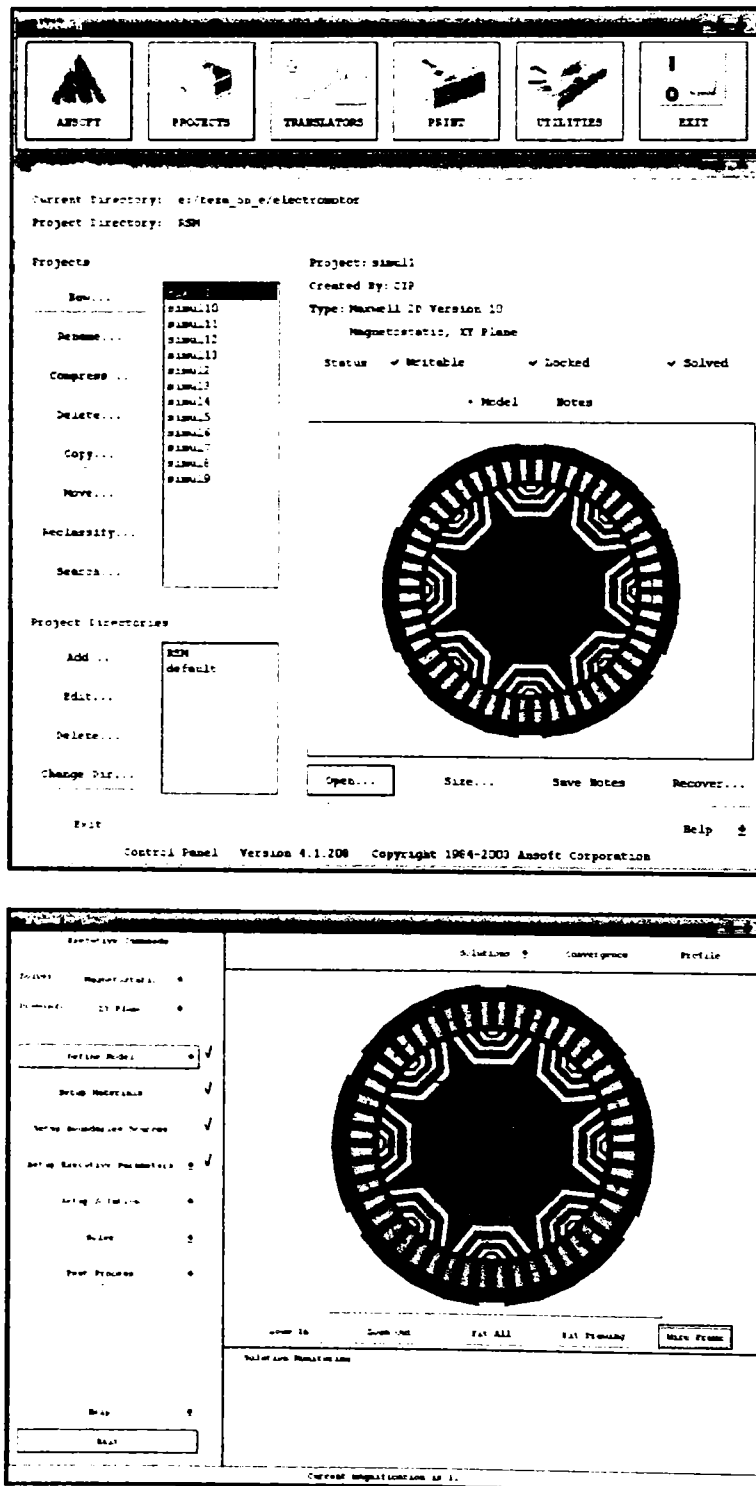


Figure 2.9. Ansoft Maxwell program used for FEM analysis.

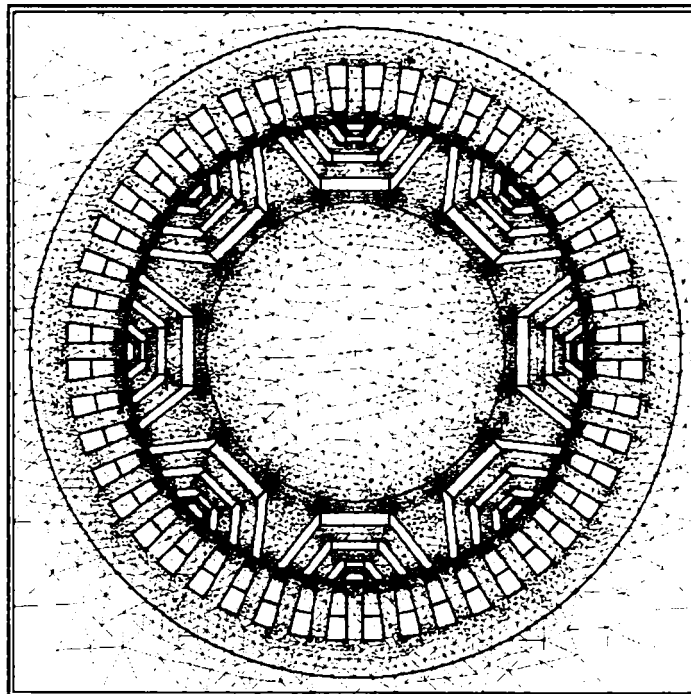
The software used for simulations is Ansoft Maxwell– Figure 2.9.

In Figure 2.10. the mesh made in Ansoft Maxwell for the permanent magnets reluctance synchronous machine simulation, with 3 layers in the airgap for a better precision of the flux distribution.

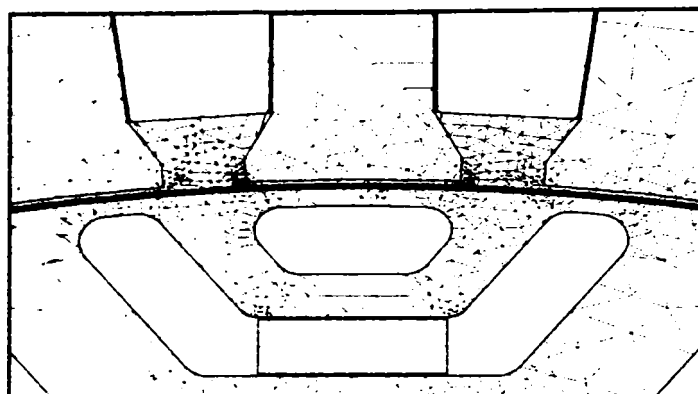
In Figure 2.11, with FEM support the torque values on different rotor positions are shown. As we can see the maximum torque is obtained at **11.5** mechanical degree (**140 Nm**).

In Figure 2.12. the permanent magnets flux lines are shown. Figures 7 and 8 present the PM airgap flux and flux density. The PM flux density in the airgap is approximately 0.3 T.

The flux distribution for the maximum obtained torque (140 Nm) is shown on Figure 2.15, and the Figure 2.16 and 2.17 represents the flux and flux density in the machine.



(a)



(b)

Figure 2.10. The mesh in the machine (a) full view; (b) zoom in (for the airgap view)

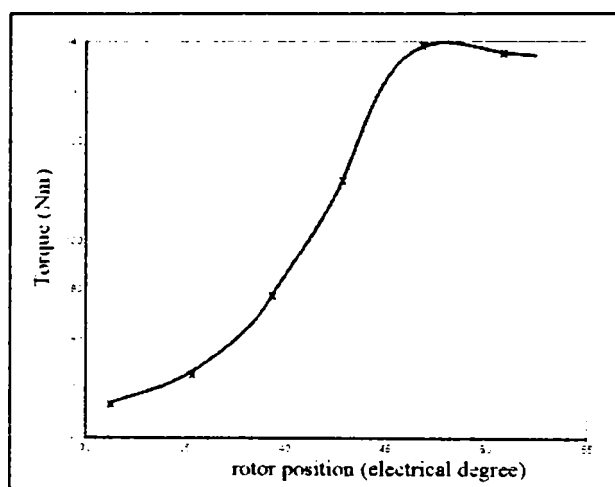


Figure 2.11. The FEM torque versus rotor position (max. current)



Figure 2.12. The PM flux lines in the machine.

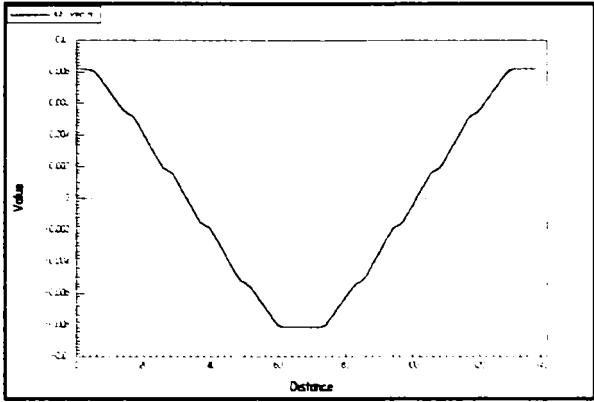


Figure 2.13. The PM airgap flux distribution

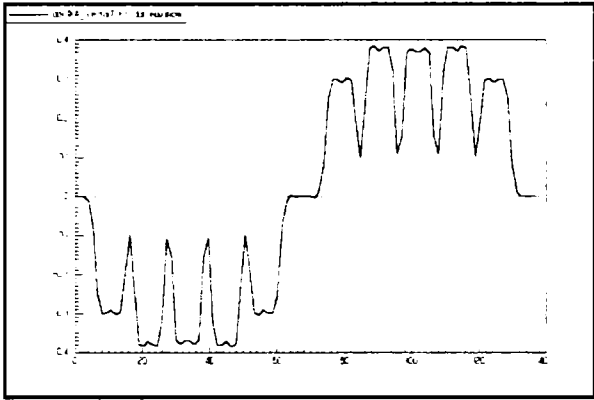


Figure 2.14. The PM airgap flux density

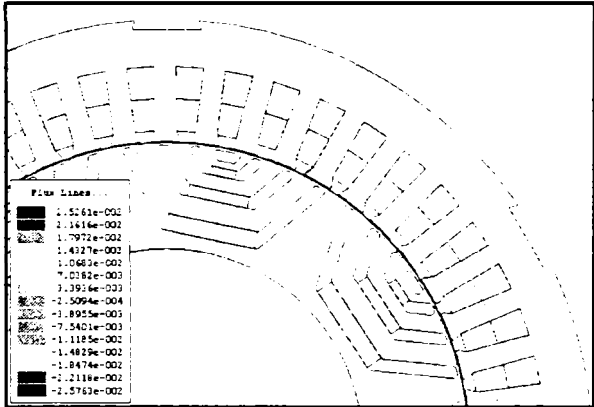


Figure 2.15. The flux lines for the maximum torque (140 Nm)

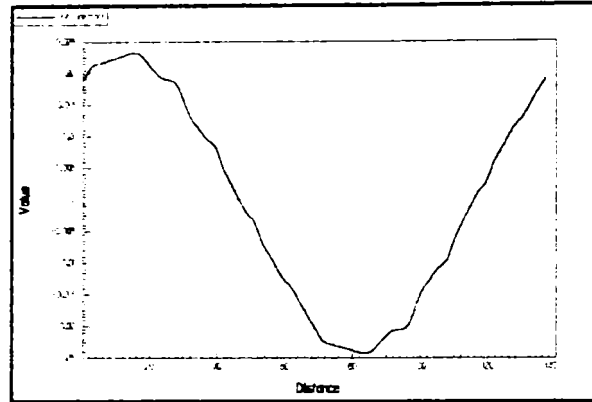


Figure 2.16. The airgap flux for the maximum torque (140 Nm)

With FEM corrections for torque, the above described design method, instrumented by the mentioned MATLAB[®] programme, which includes also the standard d-q voltage equations of the machine, was used to estimate the torque, phase voltage – RMS -, battery current (Figure 2.18) and efficiency (Figure 2.19) versus speed. [40-41]

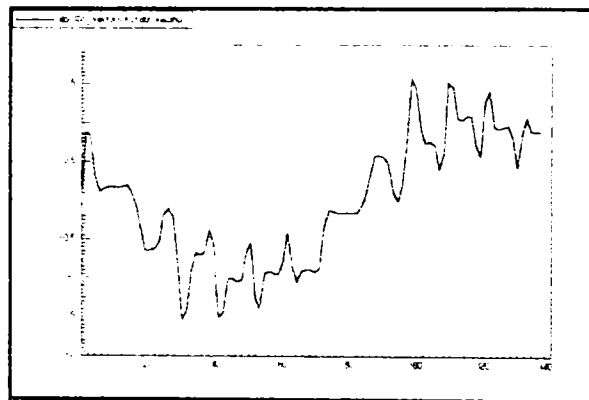


Figure 2.17. The airgap flux density for the maximum torque (140 Nm)

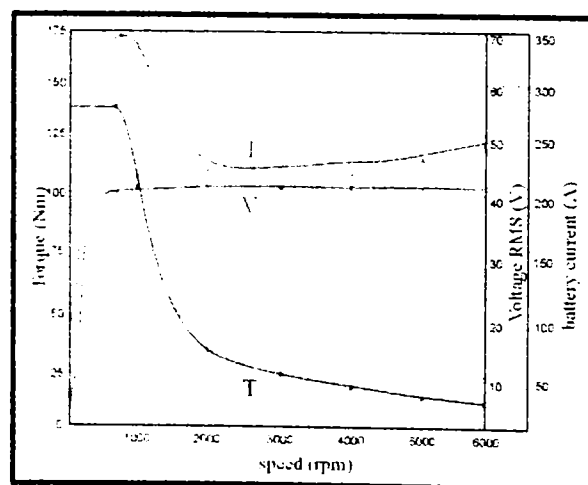


Figure 2.18. Peak torque and Voltage versus speed

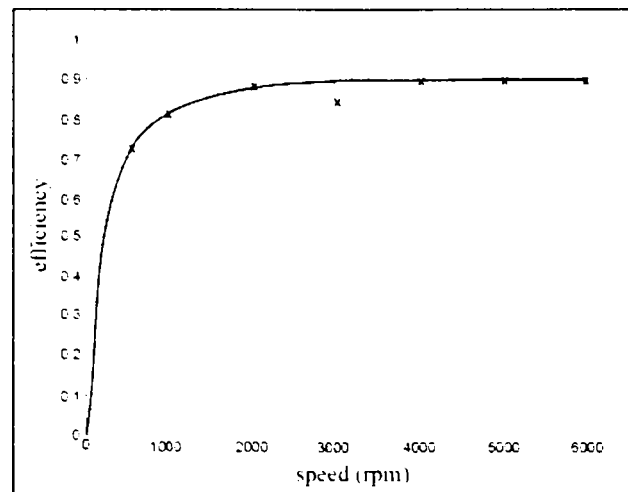


Figure 2.19. Efficiency versus speed at peak torque

The magnetic material load of is also checked using FEM simulations. Figure 2.20 shows the flux density distribution at peak torque on PM surface along contour (AB) marked on Figure 2.3. The flux density distribution at peak torque in Rotor inter – barriers, contour (CD) is shown in Figure 2.21. Stator tooth and slot flux density at peak torque is shown along middle of teeth, contour (EF), in figure 2.22 and along the bases of teeth, contour (GH), in figure 2.23.

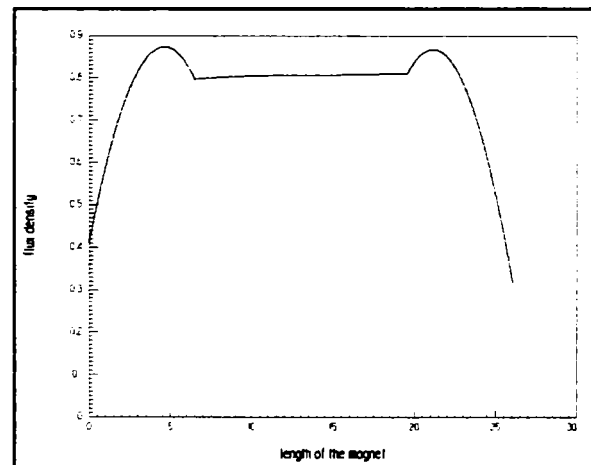


Figure 2.20. PM surface flux density distribution at peak torque along contour (AB)

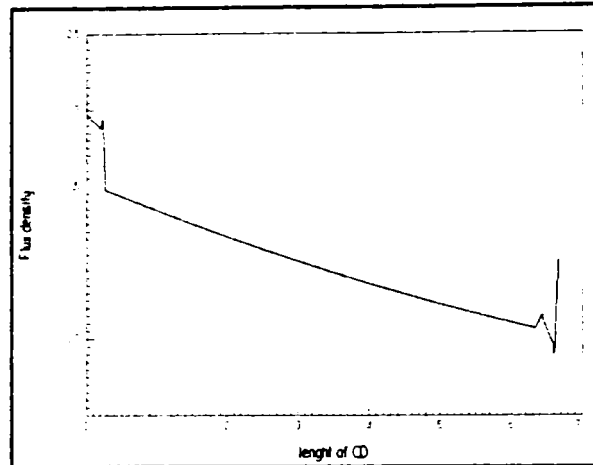


Figure 2.21. Rotor inter – barriers flux density distribution at peak torque along contour (CD)

The PM assisted reluctance synchronous motor gives good performance with good values for both torque density and kVA. [40-41]

In Figure 2.24 the cogging torque of the machine is presented for 22.5 mechanical degrees.

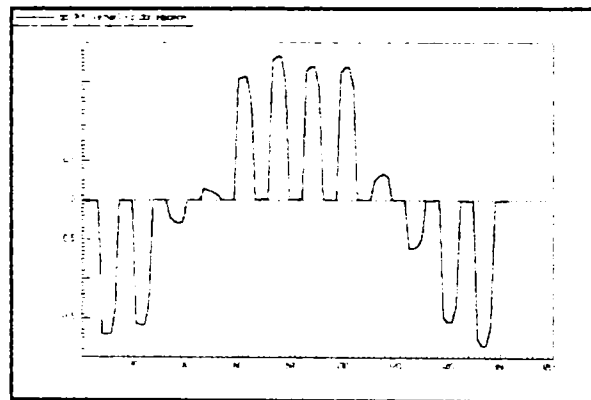


Figure 2.22. Stator tooth / slot flux density at peak torque along contour (EF)

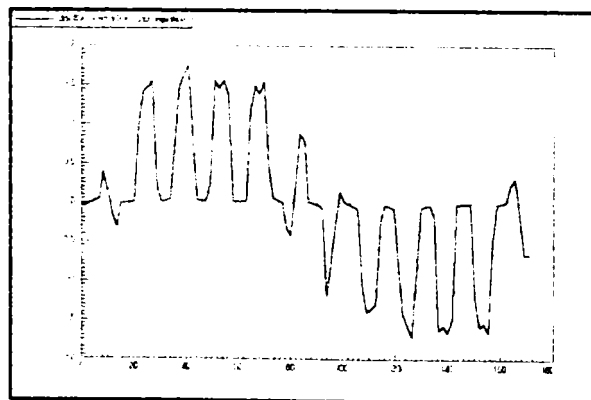


Figure 2.23. Stator tooth slot flux density distribution at peak torque along contour (GH)

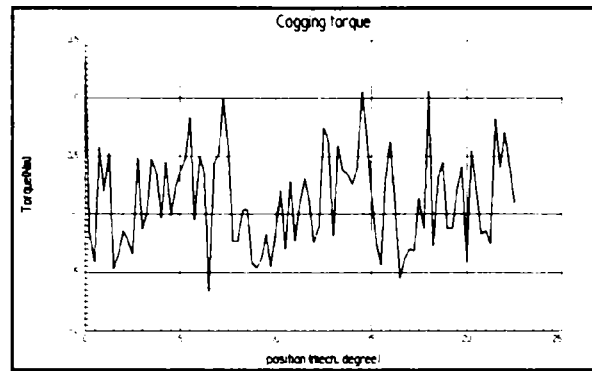


Figure 24. The cogging torque (zero current) for 22.5 mechanical degrees

Voltage management provides for the 6:1 constant speed power range. A peak torque density of 4.33 N / cm^2 is obtained. Rated (continuous) power-battery limited- is 2.5KW at 42Vdc, from 1000rpm to 6000 rpm. The peak torque of 140 Nm is obtained at 257 A (RMS / phase) and can be secured up to 500 rpm. Peak power is still 7.85 kW at 6000 rpm at 42 V dc with efficiency of 90 %. [40-41]

2.4.Sample design program for PM - RSM

The **initial values** for starting the general design are:

$$m = 3;$$

$$V_0 = 42 \text{ Volts (dc) - rated dc voltage;}$$

$$E_0 = 50 \text{ Volts (dc) - maximum e.m.f.;}$$

$$T_{sk} = 140 \text{ Nm - peak torque at stall;}$$

$$n_b = 750 \text{ rpm – base speed;}$$

$$n_{max} = 6000 \text{ rpm – maximum speed;}$$

$$P_{bc} = 6000 \text{ W - continuous power at base speed;}$$

$$P_{nmaxc} = 7850 \text{ W - peak power at maximum speed;}$$

$$p_1 = 4 \text{ - pole pairs;}$$

$$f_{tk} = 4.33 \text{ N/cm}^2 \text{ peak tangential specific force;}$$

$$l_{stack} = 69 \cdot 10^{-3} \text{ m - stack length (initial value);}$$

$$a = 8 \text{ - current path;}$$

$$j_{com} = 16 \text{ A/mm}^2 \text{ - peak current density;}$$

$$B_{tsmax} = 2 \text{ T - maximum stator teeth flux density;}$$

$B_{csmax} = 2 \text{ T}$ - maximum stator core flux density;
 $B_{crmax} = 2 \text{ T}$ - maximum rotor iron flux density;
 $B_{gmax} = 1.2 \text{ T}$ - maximum design airgap flux density;
 $B_{gmax1} = 1.1827 \text{ T}$ - to determine I_d , I_q , I_s , for the peak torque flux density in the airgap could be slightly lower than B_{gmax} ;
 $g = 0.4 \text{ mm}$ - the airgap;
 $q = 2$ - number of slot/pole/phase;
 $k_{sts} = 21.55 \text{ mm}$ - slot height/tooth width ($k_{sts} = h_s/b_t$);
 $k_{bos} = 6$ - slot opening ratio ($k_{bos} = b_{os}/g$) recommended 5...8;
 $h_{os} = 3 \text{ mm}$ - slot neck height - recommended (1...8) mm;
 $n = 4$ - flux barriers per pole ($2n$) recommended (4, 6, 8, 10, ...);
 $k_{iFe} = 0.66$ - flux barriers/iron thickness (k_{iFe}) recommended (0.5...1);
 $k_{max} = 0.95$ - Voltage utilisation (k_{max}) recommended (0.95...0.97);
 $k_{bridge} = 0.2$ - rotor core bridge PM flux linkage ratio (k_{bridge}) recommended 0.1...0.25;
 $B_{bridge} = 2 \text{ T}$, Rotor iron bridge saturation flux density recommended 2.0...2.3 T;
 $B_{gPM1} = 0.55 \text{ T}$, PM flux density fundamental recommended 0.3...0.65 T;
 $k_{fill} = 0.477$ - total slot fill factor recommended 0.4...0.5;
 $T_{Co} = 120$ - Copper temperature;
 $\gamma_{lam} = 7.6 \cdot 10^3 \text{ (kg/m}^3\text{)}$;
 $\gamma_{PM} = 7 \cdot 10^3 \text{ (kg/m}^3\text{)}$;
 $\gamma_{Co} = 8.9 \cdot 10^3 \text{ (kg/m}^3\text{)}$;
 $k_{PM} = 0.1$ - recommended ($k_{PM} < 0.1$);
 $R_{oCo20} = 1.7 \cdot 10^{-8}$ - copper resistivity ($\text{ohm} \cdot \text{m}$ at 20 C);
 $T = 120$ - allowed winding overtemperature [C];
 $k_{stack} = 0.95$ - Stack fill ratio;
 $\mu_{rel} = 10$ - Relative rotor bridge saturated permeability;
 $\mu_0 = 4 \cdot \pi \cdot 10^{-7}$ - air permeability;
 $C_{lam} = 2.5 \text{ \$/kg}$ - lamination costs;
 $C_{copper} = 6 \text{ \$/kg}$ - copper wire costs;
 $C_{PM} = 100 \text{ \$/kg}$ - PM costs;
 $P_{mec} = 100$ - mechanical losses (W) (variable with speed (frequency));

$I_s = 410 \text{ A}$ - peak current;

THE GENERAL DESIGN

THE MAGNETIC CIRCUIT DESIGN

Continuous torque at peak speed [Nm]:

$$T_{bc} = P_{bc}/(2\pi \cdot n_b);$$

$$T_{nmax} = T_{bc} \cdot n_b / n_{max};$$

The stator internal diameter 'SID' [m] is:

$$SID = \sqrt{2 \cdot T_{sk} / (\pi \cdot f_{tk} \cdot l_{stack})};$$

The pole pitch 'TAU' [m] is:

$$TAU = \pi \cdot SID / (2 \cdot p);$$

The stator core height 'hcs' [m] is:

$$hcs = B_{gmax} \cdot TAU / (B_{csmax} \cdot \pi);$$

The stator tooth width 'bts' [m] is:

$$bts = B_{gmax} \cdot TAU / (3 \cdot q \cdot B_{tsmax});$$

The stator slot height 'hs' [m] is:

$$hs = bts \cdot k_{sts};$$

The slot opening 'bos' [m] is:

$$bos = k_{bos} \cdot g;$$

External stator diameter 'SOD' [m] is:

$$SOD = SID + 2 \cdot (hos + hs + hcs);$$

ROTOR MAGNETIC CIRCUIT

The rotor will have $2n$ flux barriers per pole and to allow large flux densities their width per iron width ratio is $k_{iFe} = 0.5 \dots 1$.

The rotor external diameter 'ROD' [m] is:

$$ROD = SID - 2 \cdot g;$$

The rotor internal diameter 'RID' [m] is:

$$RID = ROD \cdot (1 - (2 \cdot B_{gmax} \cdot (1 + k_{iFe}) / (B_{crmax} \cdot 2 \cdot p)));$$

Carter coefficient is calculated neglecting the rotor iron saturated bridges.

$$\gamma_{a1} = k_{bos}^2 / (5 + k_{bos});$$

$$k_C = 1 / (1 - \gamma_{a1} \cdot g \cdot 3 \cdot q / TAU);$$

STATOR WINDING DESIGN

The number of stator slots 'Ns' is:

$$N_s = 2 \cdot p \cdot q \cdot m;$$

The coil span y_1 is:

$$y_1 = \tau \cdot (3 \cdot q - 1) / (3 \cdot q);$$

Each pole constitutes a current path a .

The winding factor 'kw1' is:

$$kw_1 = \sin(\pi/6) \cdot \sin((y_1/\tau) \cdot (\pi/2)) / (q \cdot \sin(\pi/(6 \cdot q)));$$

Mag inductance ratios (unsaturated),

$$k_{dm} = 0.97;$$

$$k_{qm} = 0.022 + 4.35 \cdot p \cdot k_C \cdot g \cdot 1.35 / (SID \cdot (1 + k_{iFe}));$$

THE PM FLUX

We first calculate the rated RMS phase voltage with V_0 (dc voltage), V_1 [V]:

$$V_1 = k_{max} \cdot V_0 \cdot \pi / (3 \cdot \sqrt{6});$$

The max allowable emf E_0 means, E_1 [V]:

$$E_1 = V_1 \cdot E_0 / V_0;$$

This value is obtained at max speed.

The RSM flux linkage per pole in the airgap produced by the PM should be,

$$\psi_{PMRSM} = E_1 / (2 \cdot \pi \cdot n_{max} \cdot p);$$

The iron bridges in the rotor should not consume more than $k_{bridge} = 0.2$ of PM flux to saturate heavily. Consequently the PM airgap flux density could be:

$$n_c B_{gPM1} = \psi_{PMRSM} \cdot (1.414) / ((kw_1 \cdot 2 \cdot p \cdot q \cdot \tau \cdot l_{stack} \cdot 2 \cdot (1 - k_{bridge})) / (a \cdot \pi));$$

This is the max product of n_c (turns/coil) and B_{gPM1} ,

$$n_c = \text{round}(n_c B_{gPM1} / B_{gPM1});$$

THE VALUE OF B_{gPM1} IS REALIZED BY CHANGING THE LENGTH OF VARIOUS PMs IN THE FLUX BARRIERS WITH FEM CHECK.

THE COIL DESIGN

The slot active area A_{slot} is,

$$\text{Aslota} = \text{hs}/2 * \text{kfill} * ((\text{SID} + 2 * \text{hos}) * \pi / \text{Ns} - \text{bts} + (\text{SOD} - 2 * \text{hcs}) * \pi / \text{Ns} - \text{bts});$$

Rotor iron bridge thickness w_b is:

$$w_b = \text{kbridge} * \text{psiPMRSM} * \text{sqrt}(6) / (4 * \text{lstack} * \text{Bbridge} * \text{q} * \text{nc} * 2 * \text{p} * \text{kw} / \text{a});$$

The magnetic saturation acts along both axes.

We suppose that the airgap flux density in fact counts and is a given value B_g .

Then we calculate the saturation factors k_{sd} and k_{sq} considering that the stator core saturation corresponds to the resultant airgap flux density.

Conductor diameter (wire gauge):

$$d_c = \text{sqrt}(2 * \text{Aslota} / (\pi * \text{nc}));$$

THE STARTING CHARACTERISTICS

$$B_{g1} = B_{g\max 1};$$

$$B_{ts} = B_{g1} * \text{TAU} / (3 * \text{q} * \text{bts});$$

$$B_{cs} = B_{g1} * \text{TAU} / (\text{hcs} * \pi);$$

$$B_{cr} = 2 * \text{ROD} * B_{g1} * (1 + k_{iFe}) / (2 * \text{p} * (\text{ROD} - \text{RID}));$$

Here we must read the magnetisation curve and interpolate it to find H_{ts} , H_{cs} , H_{cr} .

$$H_{ts} = \text{spline}(B, H, B_{ts});$$

$$H_{cs} = \text{spline}(B, H, B_{cs});$$

$$H_{cr} = \text{spline}(B, H, B_{cr});$$

$$F_{tg} = B_{g1} * (g * k_C / \mu_0);$$

$$F_{ts} = H_{ts} * (\text{hos} + \text{hs});$$

$$F_{cs} = H_{cs} * (\pi * (\text{SID} + 2 * (\text{hos} + \text{hs}) + \text{hcs}) / (4 * \text{p}));$$

$$F_{cr} = H_{cr} * (\text{sqrt}((0.95 * \text{TAU}^2 / 4) + (\text{ROD} - \text{RID})^2 / 16));$$

$$k_{sd} = (F_{ts} + F_{cs} + F_{cr}) / F_{tg};$$

The same calculation are done as before for $B_{cr} = B_g$,

$$F_{cr1} = B_{g1} * ((\text{ROD} - \text{RID}) * k_{iFe} / (\mu_0 * 2 * (1 + k_{iFe})));$$

$$k_{sq} = (F_{ts} + F_{cs}) / (F_{tg} + (0.2 * F_{cr1}));$$

$$i = 1;$$

vary k_{Bg} :

for $k_{Bg} = k_{Bg_min} : k_{Bg_stp} : k_{Bg_max}$

$$B_{gd1} = k_{Bg} * B_{g1};$$

$$I_{d1} = (a / \text{nc}) * B_{gd1} * \pi * k_C * (1 + k_{sd}) * g / (4.2426 * \mu_0 * 2 * \text{q} * \text{kdm} * \text{kw} / \text{a});$$

$$k_i = (-\sqrt{((B_{g1}/B_{gd1})^2 - 1) + (B_{gPM1}/B_{gd1})}) * (k_{dm} * (1 + k_{sq}) / (k_{qm} * (1 + k_{sd})));$$

$$I_{q1} = k_i * I_{d1};$$

$$I_{s1} = \sqrt{I_{d1}^2 + I_{q1}^2};$$

The d-q inductances for max saturation conditions may be calculated from the uniform airgap inductance:

$$L_m = 6 * \mu_0 * (q * n_c * 2 * p / a)^2 * \tau * l_{stack} / (\pi^2 * g * k_C * p);$$

$$L_{dm} = L_m * k_{dm} / (1 + k_{sd});$$

$$L_{qm} = L_m * k_{qm} / (1 + k_{sq});$$

$$T_{sk2} = 3 * p * I_{d1} * (\psi_{PMRSM} * (1 - k_{bridge}) + I_{q1} * (L_m * k_{dm} / (1 + k_{sd}) - L_m * k_{qm} / (1 + k_{sq})));$$

$$j_{Comax} = (2/a) * \sqrt{(n_c * I_{d1})^2 + (n_c * I_{q1})^2} / A_{slot};$$

WEIGHTS AND LOSSES

Copper resistivity at T,

$$R_{oCo} = R_{oCo20} * (1 + (T - 20) / 273);$$

The turn length l_c (m),

$$l_c = 2 * (l_{stack} / k_{stack} + 2 * 0.005 + y_1 / \cos(40 * \pi / 180));$$

stator teeth weight:

$$G_{st} = (h_s + h_{os}) * b_{ts} * N_s * l_{stack} * \gamma_{lam};$$

stator yoke,

$$G_{syoke} = \pi / 4 * (SOD^2 - (SOD - 2 * h_{cs})^2) * l_{stack} * \gamma_{lam};$$

The rotor core weight,

$$G_{gamcore} = 1 / (1 + k_{iFe}) * \pi * (ROD^2 - RID^2) * l_{stack} * \gamma_{lam};$$

PM weight:

$$G_{PM} = k_{PM} * k_{iFe} * G_{gamcore} * \gamma_{PM} / \gamma_{lam};$$

Copper weight:

$$G_{copper} = 3 * 2 * p * n_c * q * l_c * A_{slot} * \gamma_{Co} / (2 * n_c);$$

Materials weight:

$$G_{mat} = G_{st} + G_{syoke} + G_{gamcore} + G_{PM} + G_{copper};$$

Materials costs:

$$C_{mat} = (G_{st} + G_{syoke} + G_{gamcore}) * C_{lam} + G_{copper} * C_{copper} + G_{PM} * C_{PM};$$

End connection length l_{end} ,

$$l_{end} = l_c/2 - l_{stack}/k_{stack};$$

$$\Lambda_{das} = 2 \cdot h_s / (3 \cdot (2 \cdot b_{ts})) + h_{os} / b_{os};$$

$$\Lambda_{daz} = 5 \cdot g / (4 \cdot g + 5 \cdot b_{os});$$

$$\Lambda_{daf} = 0.34 \cdot q \cdot (l_{end} - 0.64 \cdot y_1) / l_{stack};$$

The stator resistance

Stator phase resistance

$$R_s = R_{oCo} \cdot 2 \cdot p \cdot n_c \cdot q \cdot l_c \cdot 2 \cdot n_c / (a^2 \cdot A_{slot});$$

Stator leakage inductance L_{σ} ,

$$L_{\sigma} = \mu_0 \cdot (2 \cdot n_c)^2 \cdot 2 \cdot p \cdot q \cdot l_{stack} \cdot (\Lambda_{das} + \Lambda_{daz} + \Lambda_{daf}) / a^2;$$

$$L_d = L_{dm} + L_{\sigma};$$

$$L_q = L_{qm} + L_{\sigma};$$

THE MOTOR CHARACTERISTICS

B_g for given voltage and speed:

$$\omega_{r} = 2 \cdot \pi \cdot p \cdot n_1 / 60;$$

$$W_{1a} = n_c \cdot 2 \cdot p \cdot q / a;$$

$$f_1 = \omega_{r} / (2 \cdot \pi);$$

$$E = 0.97 \cdot U_b;$$

$$f_{ipole} = E / (\pi \cdot 1.41 \cdot f_1 \cdot W_{1a} \cdot k_{w1});$$

$$B_g = f_{ipole} \cdot \pi / (2 \cdot \tau \cdot l_{stack});$$

$$B_{ts} = B_g \cdot \tau / (3 \cdot q \cdot b_{ts});$$

$$B_{cs} = B_g \cdot \tau / (h_{cs} \cdot \pi);$$

$$B_{cr} = 2 \cdot \tau \cdot B_g \cdot (1 + k_{iFe}) / (2 \cdot p \cdot (\tau - r_{ID}));$$

Here we must read the magnetisation curve

$$H_{ts} = \text{spline}(B, H, B_{ts});$$

$$H_{cs} = \text{spline}(B, H, B_{cs});$$

$$H_{cr} = \text{spline}(B, H, B_{cr});$$

$$F_{tg} = B_g \cdot (g \cdot k_C / \mu_0);$$

$$F_{ts} = H_{ts} \cdot (h_{os} + h_s);$$

$$F_{cs} = H_{cs} \cdot (\pi \cdot (r_{ID} + 2 \cdot (h_{os} + h_s) + h_{cs}) / (4 \cdot p));$$

$$F_{cr} = H_{cr} \cdot (\sqrt{(0.95 \cdot \tau^2 / 4) + (r_{ID} - r_{ID})^2 / 16});$$

$$k_{sd} = (F_{ts} + F_{cs} + F_{cr}) / F_{tg};$$

The same calculation are done as before for $B_{cr}=B_g$,

$$F_{cr1} = B_g \cdot ((ROD-RID) \cdot k_{iFe} / (\mu_0 \cdot 2 \cdot (1+k_{iFe})));$$

$$k_{sq} = (F_{ts} + F_{cs}) / (F_{tg} + (0.2 \cdot F_{cr1}));$$

$$i = 1;$$

$$\text{for } k_{Bg} = k_{Bg_min}:k_{Bg_stp}:k_{Bg_max}$$

$$B_{gd} = k_{Bg} \cdot B_g;$$

$$I_d = (a/nc) \cdot B_{gd} \cdot \pi \cdot k_C \cdot (1+k_{sd}) \cdot g / (4.2426 \cdot \mu_0 \cdot 2 \cdot q \cdot k_{dm} \cdot kw1);$$

$$k_i = (-\sqrt{((B_g/B_{gd})^2 - 1) + (B_g P_{M1}/B_{gd})} \cdot (k_{dm} \cdot (1+k_{sq}) / (k_{qm} \cdot (1+k_{sd}))));$$

$$I_q = k_i \cdot I_d;$$

$$\text{Gama} = \text{atan}(k_i);$$

$$I_s = \sqrt{I_d.^2 + I_q.^2};$$

The d-q inductances for max saturation conditions may be calculated from the uniform airgap inductance:

$$L_m = 6 \cdot \mu_0 \cdot (q \cdot nc \cdot 2 \cdot p/a)^2 \cdot \tau \cdot l_{stack} / (\pi^2 \cdot g \cdot k_C \cdot p);$$

$$L_{dm} = L_m \cdot k_{dm} / (1+k_{sd});$$

$$L_{qm} = L_m \cdot k_{qm} / (1+k_{sq});$$

$$T_{sk1} = 3 \cdot p \cdot I_d \cdot (\psi_{iPMRSM} \cdot (1-k_{bridge}) + I_q \cdot (L_m \cdot k_{dm} / (1+k_{sd}) - L_m \cdot k_{qm} / (1+k_{sq})));$$

% Though there is saturation along axis q we consider it small $k_{sq}=0.2$ to obtain conservative values for torque and flux.

The peak current density:

$$j_{Comax} = (2/a) \cdot \sqrt{(nc \cdot I_d).^2 + (nc \cdot I_q).^2} / A_{slot};$$

WEIGHTS AND LOSSES

Copper resistivity at T,

$$R_{oCo} = R_{oCo20} \cdot (1 + (T-20)/273);$$

The turn length l_c (m),

$$l_c = 2 \cdot (l_{stack}/k_{stack} + 2 \cdot 0.005 + y1/\cos(40 \cdot \pi/180));$$

stator teeth weight:

$$G_{st} = (h_s + h_{os}) \cdot b_{ts} \cdot N_s \cdot l_{stack} \cdot \gamma_{lam};$$

stator yoke,

$$G_{yoke} = \pi/4 \cdot (SOD^2 - (SOD - 2 \cdot h_{cs})^2) \cdot l_{stack} \cdot \gamma_{lam};$$

The rotor core weight,

$$G_{\text{gamcore}} = 1/(1+k_i\text{Fe}) \cdot \pi \cdot (\text{ROD}^2 - \text{RID}^2) \cdot l_{\text{stack}} \cdot \text{gamlam};$$

PM weight:

$$G_{\text{PM}} = k_{\text{PM}} \cdot k_i\text{Fe} \cdot G_{\text{gamcore}} \cdot \text{gamPM} / \text{gamlam};$$

Copper weight:

$$G_{\text{copper}} = 3 \cdot 2 \cdot p \cdot n_c \cdot q \cdot l_c \cdot A_{\text{slot}} \cdot \text{gamCo} / (2 \cdot n_c);$$

Materials weight:

$$G_{\text{mat}} = G_{\text{st}} + G_{\text{syoke}} + G_{\text{gamcore}} + G_{\text{PM}} + G_{\text{copper}};$$

Materials costs:

$$C_{\text{mat}} = (G_{\text{st}} + G_{\text{syoke}} + G_{\text{gamcore}}) \cdot C_{\text{lam}} + G_{\text{copper}} \cdot C_{\text{copper}} + G_{\text{PM}} \cdot C_{\text{PM}};$$

End connection length l_{end},

$$l_{\text{end}} = l_c / 2 - l_{\text{stack}} / k_{\text{stack}};$$

$$\text{Lambdas} = 2 \cdot h_s / (3 \cdot (2 \cdot b_{\text{ts}})) + h_{\text{os}} / b_{\text{os}};$$

$$\text{Lambdaz} = 5 \cdot g / (4 \cdot g + 5 \cdot b_{\text{os}});$$

$$\text{Lambdaf} = 0.34 \cdot q \cdot (l_{\text{end}} - 0.64 \cdot y_1) / l_{\text{stack}};$$

The stator resistance

Stator phase resistance

$$R_s = R_{\text{Co}} \cdot 2 \cdot p \cdot n_c \cdot q \cdot l_c \cdot 2 \cdot n_c / (a^2 \cdot A_{\text{slot}});$$

Stator leakage inductance L_{sigma},

$$L_{\text{sigma}} = \mu_0 \cdot (2 \cdot n_c)^2 \cdot 2 \cdot p \cdot q \cdot l_{\text{stack}} \cdot (\text{Lambdas} + \text{Lambdaz} + \text{Lambdaf}) / a^2;$$

$$L_d = L_{\text{dm}} + L_{\text{sigma}};$$

$$L_q = L_{\text{qm}} + L_{\text{sigma}};$$

$$V_d = I_d \cdot R_s - \omega \cdot (L_q \cdot I_q - \psi_{\text{PMRSM}} \cdot (1 - k_{\text{bridge}}));$$

$$V_q = I_q \cdot R_s + \omega \cdot L_d \cdot I_d;$$

$$V_s = \sqrt{V_d^2 + V_q^2};$$

$$P_m = 2 \cdot \pi \cdot n_1 \cdot T_{\text{sk}} / 60;$$

$$P_{\text{copper}} = 3 \cdot R_s \cdot I_s^2;$$

$$\psi_s = \sqrt{(L_d \cdot I_d)^2 + (L_q \cdot I_q - \psi_{\text{PMRSM}} \cdot (1 - k_{\text{bridge}}))^2};$$

$$P_{\text{iron}} = 81 \cdot (f_1 / 500)^{1.7} \cdot (\psi_s / 0.228)^2;$$

$$\text{EFF} = (P_m - P_{\text{mec}}) / (P_m + P_{\text{copper}} + P_{\text{iron}});$$

$$P_2 = P_{\text{copper}} + P_{\text{iron}} + P_{\text{mec}};$$

2.5. Conclusion

The sample numerical results obtained so far warrant conclusion such as: [40-41]

- The designed PM assisted RSM is able of high peak torque densities (4.33 N/cm² and 16 A/mm²).
- The magnetic saturation level in the machine is moderately large as documented with airgap, stator teeth, core and rotor iron flux densities values.
- At peak torque the PMs do not demagnetize as the flux density does not change sign along contour AB.
- The efficiency at maximum speed is 90 % while it is more than 73 % above 500 rpm.
- The peak kW / design (peak) kVA ratio, 0.568, is quite good for the application.

2.6. References

- [1] P.J. McCleer, I. Miller, A. R. Gale, M. W. Degner, F. Leonardi, „*Nonlinear model and momentary performance capability of a cage induction machine as an automotive starter - alternator*“, Record of IEEE – IAS – 1999 Annual Meeting.
- [2] G. Alenbernd, H. Schafer, L. Wahner, „*Vector controlled crankshaft starter generator for Motor vehicle*“, Record of ICEM 2000, 28 – 30 August, Espoo, Finland, vol. 3, pp. 1549 – 1553.
- [3] M. Paul, W. Hofmann, D. Bochinia, „*Design of permanent magnet motors for a hybrid electric vehicle*“, Record of ICEM – 2000, 28 - 30 August, Espoo, Finland, vol. 3, pp. 1535 – 1539.
- [4] H. Bausch, A. Graaf, A.B.A. Nickel, „*A switched reluctance and an induction machine in a drive train for an electrical vehicle under the conditions of car application*“, Record of ICEM – 2000, 28 - 30 August, Espoo, Finland, vol. 3, pp. 1313 – 1316.
- [5] M. Bebes, M. Gabbi, E. Hoang, M. Lecrivain, B. Grioni, C. Plasse, „*SRM design for Starter – Alternator system*“, IBID, vol. 3, pp. 1931 - 1935.
- [6] R. Blissenbach, G. Henneberger, U. Schafer, W. Hackmann, „*Developement of a transverse flux traction motor in a direct drive system*“, IBID, vol. 3, pp. 1457 – 1460.
- [7] R. Blumel, „*Asymmetrical three level converter feeding a 42 / 14 V automobile network*“, Intelligent motion, June 1997 Proceedings, pp. 233 - 242.
- [8] E.C. Lovelace, T.M. Jahns, I.L. Kirtley jr., I.M. Lang, „*An interior PM Starter/Alternator for automotive applications*“, Record of ICEM – 1998, Istanbul, Turkey, vol. 3, pp. 1801 – 1808.
- [9] A. Vagati, A. Fratta, P. Gaglielani, G. Franchi, F. Villata, „*Comparison of a.c. motor based drives for electric vehicle application*“, Record of PCIM – intelligent motion, June 1999, pp. 173 – 181.
- [10] A. Lange, W.R. Canders, F. Laube, H. Mosebach, „*Comparison of different drive systems for a 75 KW electrical vehicle drive*“, Record of ICEM 2000, 28 – 30 August, Espoo, Finland, vol. 3, pp. 1308 – 1312.
- [11] E.C. Lovelace, T.M. Jahns, J.H. Lang, „*A Saturating Lumped-Parameter Model for an Interior PM Synchronous Machine*“, IEEE Transactions on Industry Applications, vol. 38, no. 3, pp. 645-650, May/June 2002.
- [12] B.-H. Bae, S.-K. Sul, „*Practical Design Criteria of Permanent Magnet Synchronous Motor for 42V Integrated Starter-Generator*“, IEMDC 2003, pp. 656 - 662, vol.2, June 1-4, 2003, Madison, Wisconsin, USA.
- [13] J.G. Kassakian, J.M. Miller, and N. Traub, „*Automotive electronics power up*“, IEEE Spectrum, May 2000.

- [14] G. Kassakian, H.C. Wolf, J.M. Miller, and C.J. Hurton, "Automotive electrical systems circa 2005", IEEE Spectrum, August 1996.
- [15] I. Boldea, S.A. Nasar – "The Induction Machine Handbook", (book), CRC Press, 2002.
- [16] I. Boldea. "Reluctance synchronous machines and drives", (book), OUP 1996.
- [17] E. Schmidt, W. Brandl, *Comparative Finite Element Analysis of Synchronous Reluctance Machines with Internal Rotor Flux Barriers*
- [18] E.C. Lovelace, T.M. Jahns, T.A. Keim, J.H. Lang, *Mechanical Design Considerations for Conventionally Laminated, high speed, interior PM synchronous Machine Rotors*
- [19] Casasso P., Fratta A., Giraudo, Guglielmi, Pastorelli, Vagati, *High performance electric scooter,*
- [20] Kawase, Yamaguchi, Sano, Igata, Ida, *3D eddy current analysis in a silicon steel sheet of an IPM motor,* IEEE Transactions on Magnetics, vol. 39, no.3, May 2003
- [21] Ferreira, Richter, *Detailed design of a 250 kW switched reluctance starter/generator for an aircraft engine,* SAE technical paper series
- [22] Bahram Amin, *High density torque motor structures,* ICEM 2000 28-30 august 2000, Espoo, Finland
- [23] Fefermann, Randi, Astier, Roboam, *Synthesis models of PM brushless motors for the design of complex and heterogeneous system,* EPE 2001 Graz
- [24] M. Paul, W. Hofmann, D. Bochnia, *Design of permanent magnet motors for a hybrid electric vehicle,* ICEM 2000 28-30 august 2000, Espoo, Finland
- [25] P. Thelin, HP Nee, *Analytical calculation of the airgap flux density of PM SM with buried magnets including axial leakage, tooth and yoke saturations,* Power electronics and variable speed drives, 18-19 sept 2000, conf.publication no. 475 IEE2000
- [26] M. Comanescu, Ali Keyhani, Min Dai, *Design and analysis of 42 V PM generator for automotive applications,* IEEE Transactions on Energy Conversion, vol18, no.1, march 2003
- [27] Honda, Higaki, Morimoto, Takeda, *Rotor design optimisation of a multilayer interior PM SM,* IEE Proc - Electr Power appl vol 145, no 2, march 1998
- [28] WL Soong, N Ertugrul, EC Lovelace, TM Jahns, *Investigation of interior permanent magnet offset coupled automotive integrated starter/alternator*
- [29] Eckart Nipp. *Torque interrupt free winding reconfigurations - possibilities and difficulties,* ICEM 2000 28-30 august 2000, Espoo, Finland
- [30] Klaus Bolentz, *Design modifications of the Electrical System to use intermittent engine operation,* 1996 the institute of Electrical Engineers, IEE
- [31] DH Kim, IH Park, JH Lee, CE Kim, *Optimal shape design of iron core to reduce cogging torque of IPM motor,* IEEE Transactions on Magnetics, vol. 39, no.3, May 2003

- [32] EC Lovelace, TM Jahns, JH Lang, *Impact of saturation and inverter cost on IPM synchronous machine drive optimization*, IEEE Transactions on Industry applications, vol. 36, no.3, may/june 2000
- [33] SA Long, N Schofield, D Howe, M Piron, M McClelland, *Design of a switched Reluctance Machine for Extended Speed Operation*, IEMDC 2003
- [34] Bon-Ho Bae; Seung-Ki Sul; *Practical design criteria of interior permanent magnet synchronous motor for 42V integrated starter-generator*, Electric Machines and Drives Conference, 2003. IEMDC'03. IEEE International Volume 2, 1-4 June 2003 Page(s):656 - 662 vol.2
- [35] Ishibashi, K.; McInturff, A., *Winding design study of superconducting 10 T dipoles for a synchrotron*, Magnetics, IEEE Transactions on Volume 19, Issue 3, May 1983 Page(s):1364 – 1367
- [36] Dorrell, D.G.; Amemiya, J.; Chiba, A.; Takenaga, T., *Analytical modeling of a consequent-pole bearingless permanent magnet motor*, Power Electronics and Drive Systems, 2003. PEDS 2003. The Fifth International Conference on, Volume 1, 17-20 Nov. 2003 Page(s):247 - 252 Vol.1.
- [37] Odendaal. W.G.; Ferreira, J.A.; Cronje, W.A., *Combined numeric and analytic methods for foil winding design*, Power Electronics Specialists Conference, PESC '94 Record., 25th Annual IEEE, 20-25 June 1994 Page(s):843 - 849 vol.2
- [38] K. Yamazaki, *Torque and efficiency calculation of an interior PM motor considering harmonic iron losses of both the stator and rotor*, IEEE Transactions on Magnetics, vol. 39, no.3, May 2003
- [39] GH Kang, JP Hong, GT Kim, *Analysis of cogging torque in interior permanent magnet motor by analytical method*, Jurnal of KIEE, 11B, 1-8, 2001
- [40] Ion Boldea, Lucian Tutelea, Cristian Ilie Pitic, "*PM – assisted Reluctance Synchronous motor / generator (PM - RSM) for mild hybrid vehicles*", OPTIM 2002, Poiana Brasov, Romania.
- [41] Ion Boldea, Lucian Tutelea, Cristian Ilie Pitic, "*PM-Assisted Reluctance Synchronous Motor/Generator (PM-RSM) for Mild Hybrid Vehicles: Electromagnetic Design*", IEEE Transactions on Industry Applications, Vol. 40, No. 2, March/April 2004, pp. 492 – 498.
- [42] EC Lovelace, TM Jahns, J. Wai, etc, *Design and experimental verification of a direct drive interior PM synchronous machine using a saturable lumped-parameter model*, IAS 2002
- [43] J.H. Lee, J.C. Kim, D.S.Hyun, "*Effect Analysis of Magnet on L_d and L_q inductance of permanent magnet assisted synchronous reluctance motor using finite element method*", IEEE Transaction on Magnetics, vol. 35, no. 3, May 1999.

- [44] Mukherjee, S.; Adams, G.E.; Hoft, R.G.; *FEM analysis of inverter-induction motor rotor conduction losses*, Energy Conversion, IEEE Transactions on Volume 4, Issue 4, Dec. 1989
Page(s):671 – 680;

Chapter III

The PM –RSM: generator experimental characterization

Abstract

This chapter introduces a series of the tests for parameters and efficiency determination of a PM - assisted RSM in the generator mode. The testing methods consist in standstill tests (dc decay), generator no load testing with capacitor and on load ac and diode-rectifier dc tests.

3.1. Introduction

There is a continuous demand for better performance, lower emissions, and improved fuel economy in today's vehicles. Therefore, the manufacturers are investigating all kind of feature (electric power steering, electromechanical valves, etc) for the scope.

In order to meet this need for power a practical idea is considered – to be the replacing of the starter and the alternator in a vehicle with an electronically controlled very competitive electrical machine. Such a machine, mounted on the crankshaft, offers a very compact package and a very fast response in mater of transmitting the torque to the shaft.

Interior PM assisted Reluctance Synchronous Machine can be used for the scope. The need for a good efficiency in a very wide power-speed range of 6:1 in a hybrid electric vehicle can be accomplished by using this kind of machine when operates at high flux densities [1].

Because a very fast, robust and precise torque and power control is required, the parameters of the machine have to be known very well.

According to [2], the parameters cannot be determined by IEC Standard recommendations, therefore in this paper a combination of methods is presented.

3.2. PM-RSM prototype specifications

A photograph of the PM - RSM prototype is presented in Figure 3.1, and the configuration of the rotor lamination, with the marks for the PM's, appears in Figure 3.2. [1]

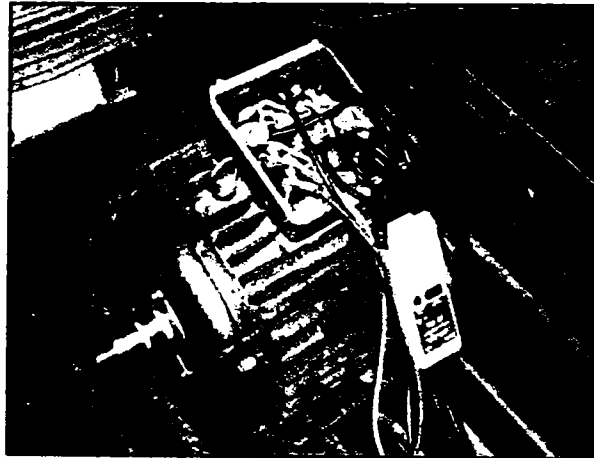


Figure 3.1. PM-RSM prototype

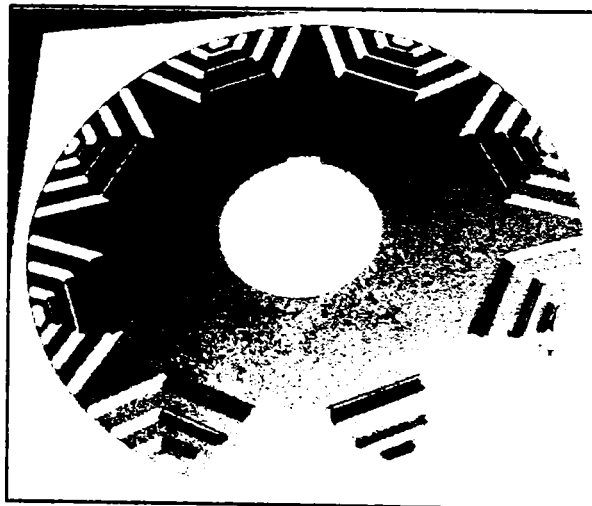


Figure 3.2. PM - RSM lamination

The prototype main dimensions are presented in Table 3.1. The experimental setup contains a belt transmission 10 / 13 kW (1500 / 3000 rpm) and an induction motor driven by an ACS 600 inverter (Figure 3.3).

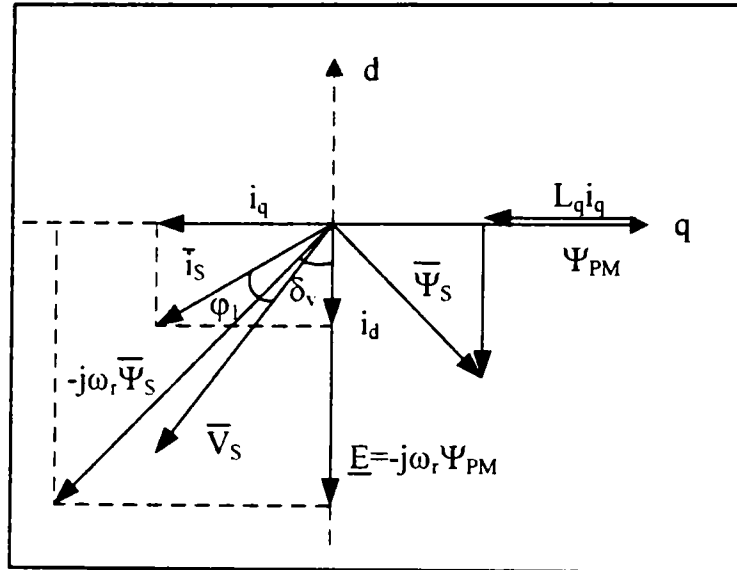


Figure 3.4. Vector diagram of PM – RSM for generating

$$\begin{aligned} I_q &= -I_s \cdot \sin(\delta_v + \varphi_l) \quad I_s = I_l \sqrt{2} \\ I_d &= -I_s \cdot \cos(\delta_v + \varphi_l) \quad V_s = V_l \sqrt{2} \end{aligned} \quad (3)$$

$$\begin{aligned} \psi_d &= \frac{-V_s \cos \delta_v - R_s I_s \cos(\delta_v + \varphi_l)}{\omega_r} \\ \psi_q &= \frac{V_s \cos \delta_v + R_s I_s \cos(\delta_v + \varphi_l)}{\omega_r} \end{aligned} \quad (4)$$

See Figure 3.4 for δ and φ_l visualization.

The torque can be estimated by:

$$T = \frac{3}{2} p_l (\psi_{PM} + (L_d - L_q) \cdot I_q) \cdot I_d \quad (5)$$

The copper and iron losses can be written:

$$\begin{aligned} P_{Cu} &= \frac{3}{2} R_s \cdot (I_d^2 + I_q^2) \\ P_{fe} &= \frac{3}{2} \frac{\omega_r^2}{R_{iron}} \left[(L_q I_q - \psi_{PM})^2 + (L_d I_d)^2 \right] \end{aligned} \quad (6)$$

3.2.2. Permanent magnets flux (Ψ_{PM}):

The PM's flux is considered to be constant and can be calculated from no load tests with [1]:

$$\Psi_{PM} = \frac{V_0 \cdot \sqrt{2}}{2 \cdot \pi \cdot p_l \cdot n} \quad (7)$$

3.2.3. Testing methods

The following testing methods [11-19] are considered in this chapter:

- Standstill tests for parameters - flux decay response;
- No load (with capacitors) and short circuit testing;
- On load ac and dc testing with capacitor excitation.

3.3. Standstill testing

The d – q inductances L_d and L_q are first measured in a standstill test. In this method the machine is set in d axis (by feeding it with 5V ac and moving the rotor until the current is minimum). With the experimental setup in Figure 3.5 we can determine $L_d = f(I_d)$. Then, changing the connections – in q axis – we repeat the measurements and obtain $L_q = f(I_q)$. [20-25]

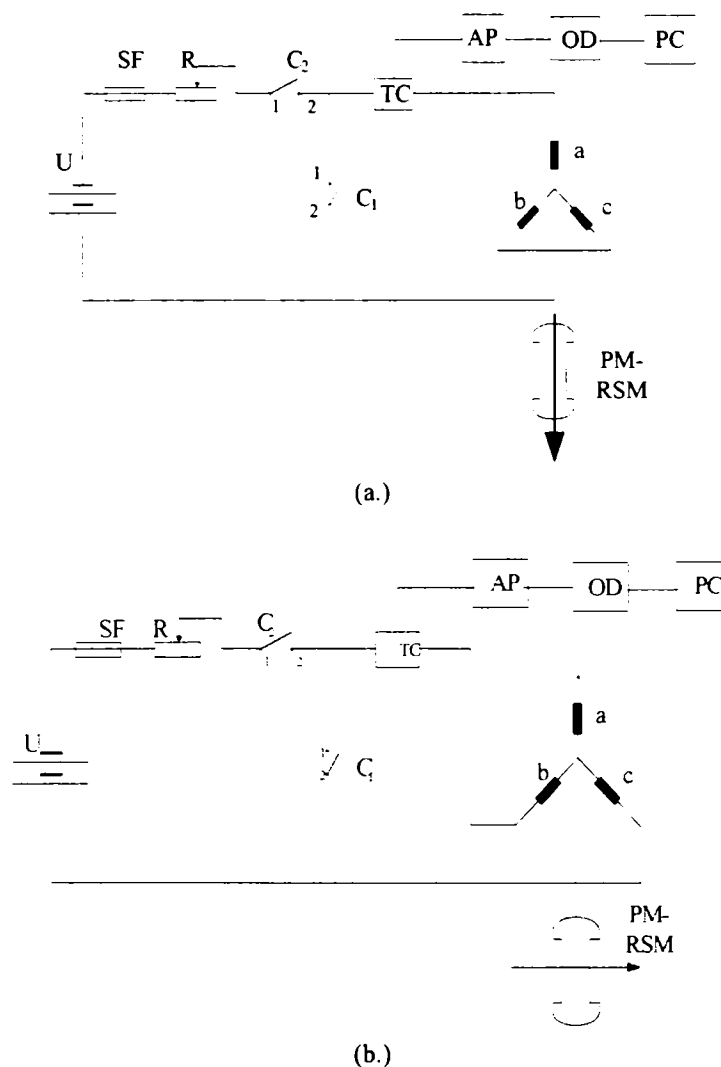


Figure 3.5. setup for dc decay tests:

(a.) - in d axis, (b.) – in q axis

Where:

- SF – fuse (63 A);
- R – variable resistor ($I = 7 \div 63$ A)
- U – battery;
- AP – adapter (for the visualisation of the current on oscilloscope);
- OD – Tektronics 4 channels oscilloscope.

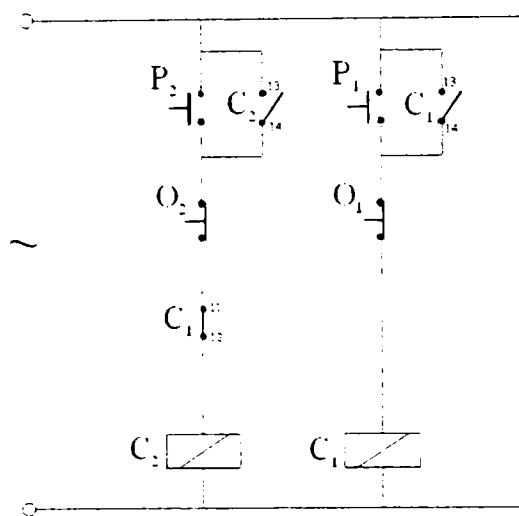


Figure 3.6. Command scheme for current decay tests

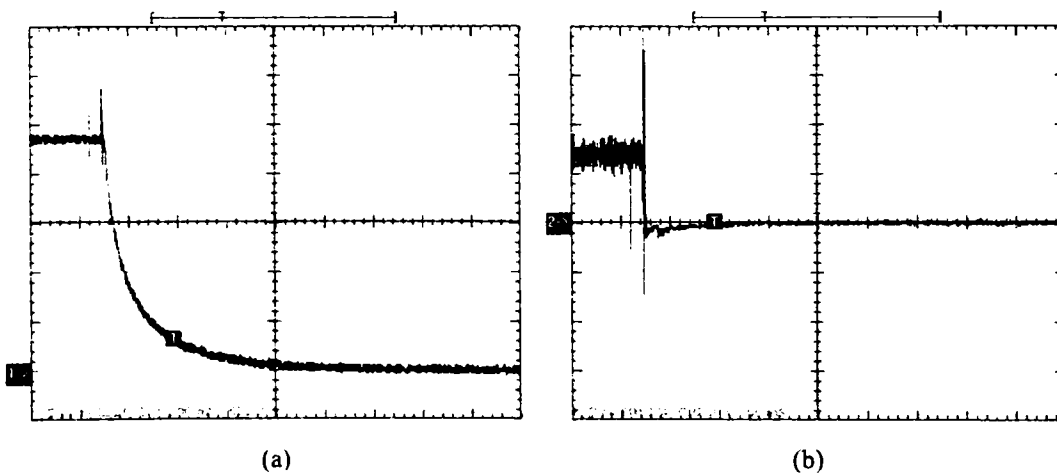


Figure 3.7. Sample experiments in d axis: a) current decay; b) d axis voltage

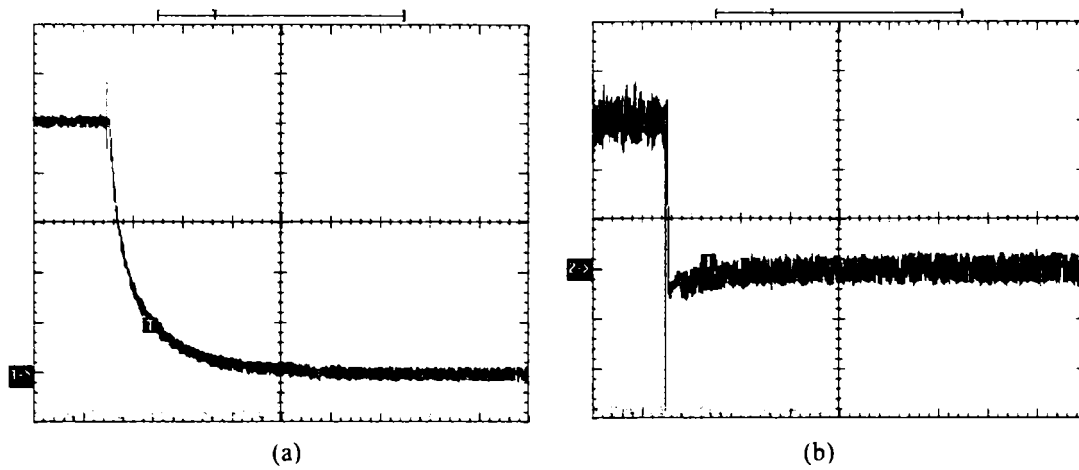


Figure 3.8. Sample experiments in q axis: a) current decay; b) q axis voltage

Table 3.2. d axis measurements

I[A]	V[V]	R[Ω]
6.53	0.46	0.07
11.9	0.86	0.07223
17.2	1.24	0.07207
26	1.78	0.06845
29.76	2	0.06719
33.28	2.21	0.06639
36.38	2.4	0.06595
38.98	2.57	0.06592
41.99	2.75	0.06548
49.66	3.22	0.06483
62.01	4.04	0.06514
68.4	4.35	0.06359

$$L_d = \frac{2}{3} \frac{R_{abc} \int_0^{\infty} i_a dt - \int_0^{\infty} v_{abc} dt}{I_0} ; \quad (8)$$

$$\Psi_d = \frac{2}{3} \left(R_{abc} \int_0^{\infty} i_a dt - \int_0^{\infty} v_{abc} dt \right) ; \quad (9)$$

With the measured value from Table 3.2 and the eqns (8) and (9), L_d and Ψ_d are:

Table 3.3. L_d and Ψ_d calculated values from Table 3.2.

I[A]	L[mH]	Ψ[Wb]
6.53	2.58	0.0168
11.9	2.69	0.0320
17.2	2.71	0.0466
26	2.7	0.0703
29.76	2.62	0.0782
33.28	2.52	0.0839
36.38	2.46	0.0896
38.98	2.36	0.0923
41.99	2.21	0.0929
49.66	2.06	0.1026
62.01	1.97	0.1226
68.4	1.79	0.1227

Table 3.4. d axis measurements

I[A]	V[V]	R[Ω]
6.54	0.59	0.0902
11.93	1.08	0.0905
16.93	1.54	0.0909
24.91	2.52	0.1051
30.55	2.92	0.0955
33.78	3.17	0.0938
36.11	3.41	0.0944
40.05	3.87	0.0966
46.43	4.46	0.0960
53.72	5.03	0.0936
58.87	5.47	0.0929
63.68	5.97	0.0937

$$L_d = \frac{1}{2} \frac{R_{abc} \int_0^{\infty} i_a dt - \int_0^{\infty} v_{abc} dt}{I_0} \quad (10)$$

$$\Psi_d = \frac{1}{2} \left(R_{abc} \int_0^{\infty} i_a dt - \int_0^{\infty} v_{abc} dt \right) \quad (11)$$

Table 3.5. L_q and Ψ_q calculated values from Table 3.4.

I[A]	L[mH]	Ψ [Wb]
6.53	0.73	0.00480
11.90	0.77	0.00923
17.20	0.80	0.01357
26.00	0.84	0.02101
29.76	0.74	0.02264
33.28	0.72	0.02458
36.38	0.73	0.02660
38.98	0.74	0.03004
41.99	0.74	0.03456
49.66	0.72	0.03909
62.01	0.73	0.04298
68.40	0.71	0.04543

Sample current decays acquired in d and q axes are shown in Figure 3.9. Stator resistance was calculated to be 0.039 Ω. [1]

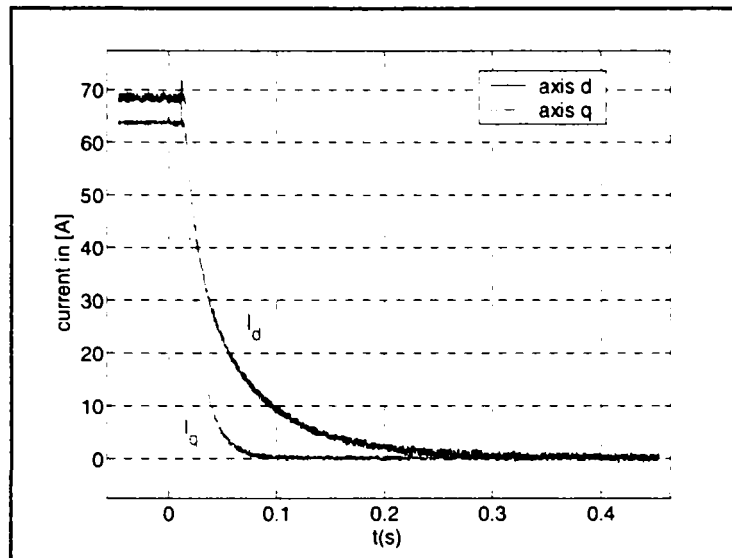


Figure 3.9. dc current decay at standstill in d and q axis

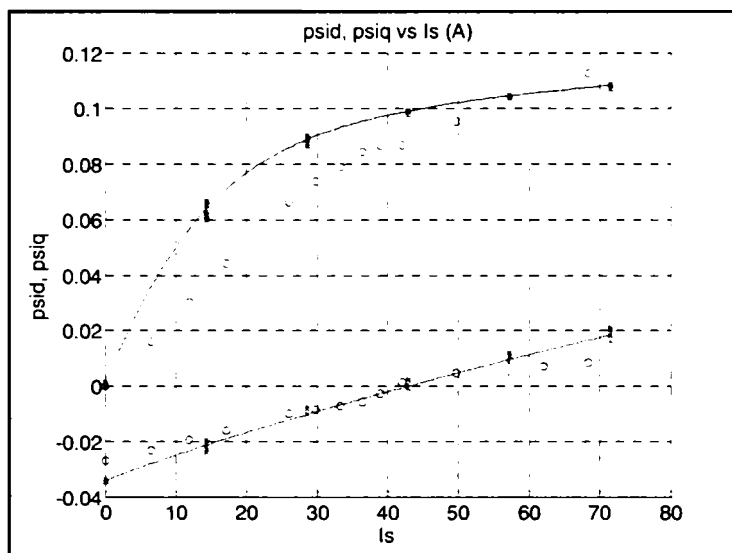


Figure 3.10. Magnetization curves Ψ_d, Ψ_q versus I_s , x – FEM [1]; o– dc decay tests.

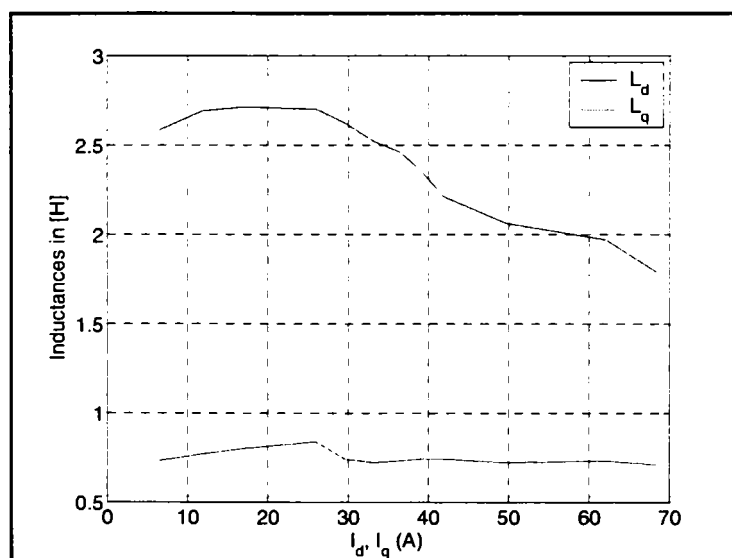


Figure 3.11. L_d, L_q vs I_d, I_q from dc decay tests

The results of the standstill tests in terms of magnetization curves are presented in Figure 3.10 together with theoretical ones (from [1]). The differences for the d axis (where the saturation is high) can be due to the manufacturing causes (the difference between the 0.4 mm theoretical airgap and $0.4^{+0.12}_{-0}$ mm of the prototype).

The d–q inductances extracted from the standstill tests are shown in Figure 3.11.

We should notice that the FEM curves in Figure 3.10 have been obtained for the machine in different positions with respect to axis d, and represented with respect to total (magnetization) current.

The rather unique magnetization curves with various (I_d , I_q) components in the FEM calculations, along d and q reflect a mild cross-coupling effect [1].

3.4. No load and shortcircuit testing

A sample of no load voltage [26-27] is shown in Figure 3.12 (with the spikes caused by the flux barriers) and the variation of no load voltage with frequency for the fundamental and harmonics appears in Figure 3.13.

The value of Ψ_{PMq} was calculated at 0.0474 Wb. [1]

The harmonics in the no load voltage are due to slotting for a small airgap and a full pitch double layer winding without skewing.

Further on the shortcircuit testing was performed at various speed.

The shortcircuit current shape and its peak value versus frequency are shown in Figures 3.14 and 3.15.

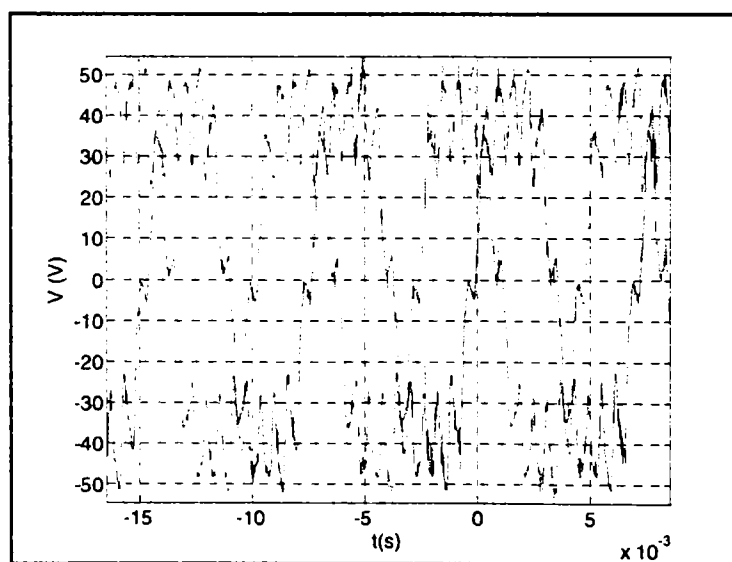


Figure 3.12. No load - phase voltage at 2000 rpm

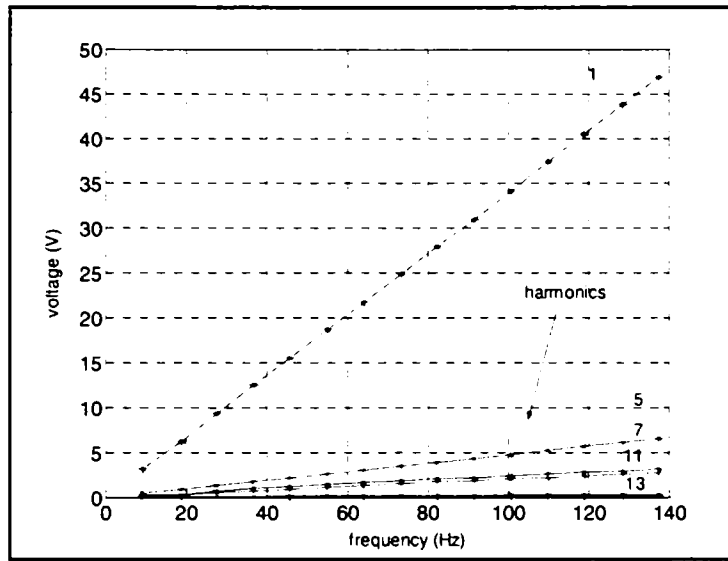


Figure 3.13. No load voltage fundamental and harmonics, versus frequency

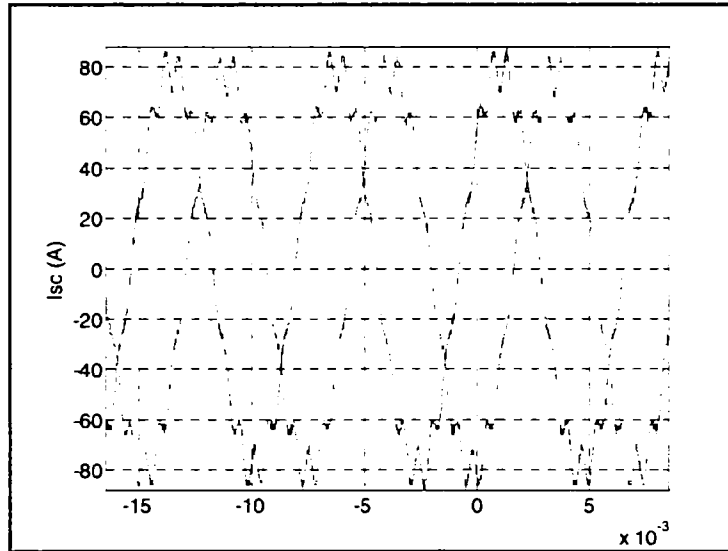


Figure 3.14. Short-circuit - phase currents at 2000 rpm

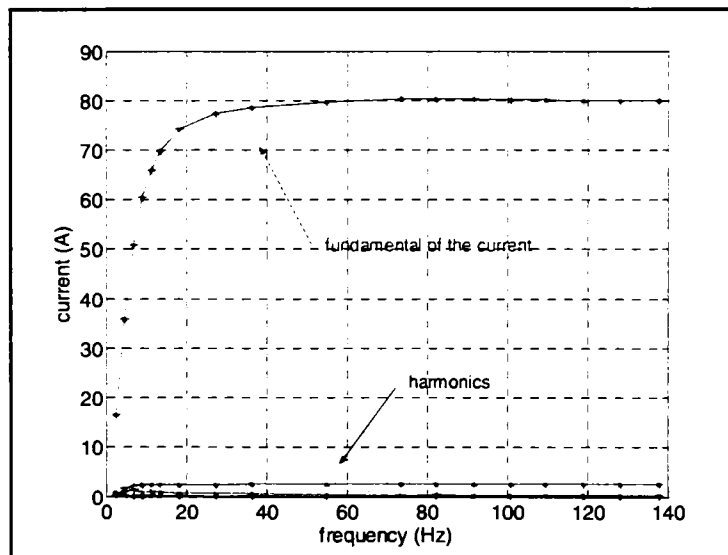


Figure 3.15. Short-circuit current versus frequency

From no load and shortcircuit tests the value of L_q inductance is obtained from:

$$Z_q = V_{no\ load} / I_{sc} \quad (12)$$

$$X_q = \sqrt{Z_q^2 - R_l^2} \quad (13)$$

$$L_q = \frac{X_q}{2 \cdot \pi \cdot f_l} \quad (14)$$

$$\Rightarrow L_q = 0.67655 \text{ mH}$$

The value of L_q was not dependent on the current (or speed) as a low level of magnetic saturation was present.

3.5. Capacitor – only load tests

In an effort to segregate mechanical and core losses capacitor only load testing was performed.

From load tests with capacitors the mechanical and iron losses were obtained (Figure 3.16) and with the stator resistance already found, the efficiency could be calculated from losses segregation and also from the drive data (by acquiring the torque and speed from the ACS 600 inverter).

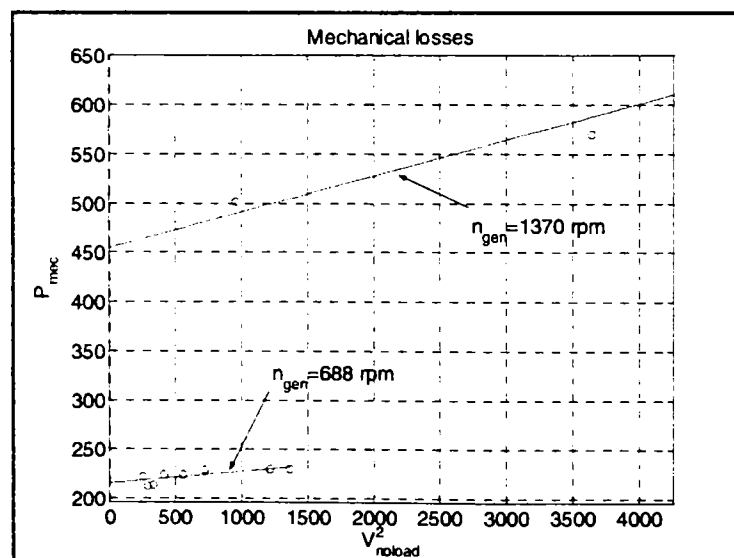


Figure 3.16. The mechanical losses versus squared voltage for two generator speed (1370 rpm and 688 rpm)

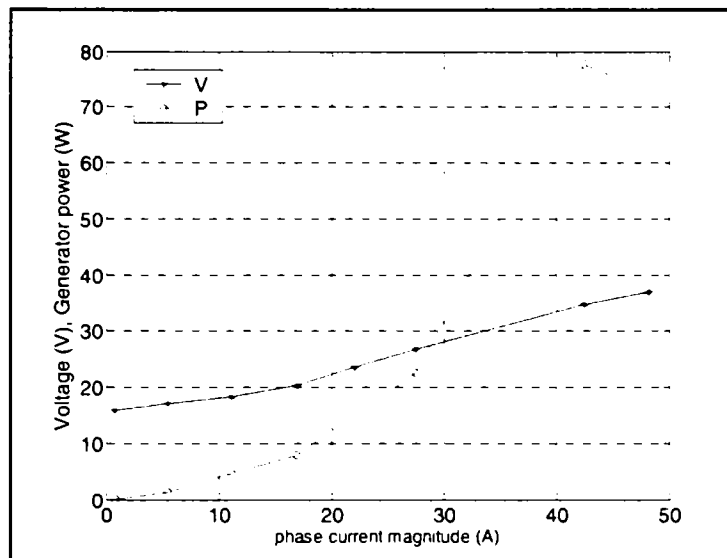


Figure 3.17. Voltage and generator (capacitor) power versus current with capacitor only load

The terminal voltage and the phase current (peak current) for capacitor only load are shown in Figure 3.17 versus the input (mechanical) power.

The core and mechanical losses are represented in Figure 3.16 as a function of terminal voltage squared for two speeds. The mechanical losses represent, in fact the PM-RSM plus the transmission and drive mechanical losses. The input power to the generator was calculated from the estimated value of torque and speed of the DTC induction motor drive.

3.6. On load a.c. testing with capacitor excitation

The load testing with resistive and with capacitive-resistive ac or dc (with a diode rectifier) load was used to validate the power capability and efficiency computed with the losses segregation. [28]

Sample generator phase current and voltage with resistive load and capacitor excitation appear in Figure 3.18, while load ac resistance test results with and without capacitor excitation are visible in Figures 3.19 and 3.20. The surplus in efficiency from segregated losses in Figure 3.20 is due to stray load losses.

By measuring V_1 , I_1 and $\cos\phi_1$ in the d–q flux equations, Ψ_d , Ψ_q and δ_v remain as unknowns.

$$P_1 = 3I_1V_1\cos\phi_1 \Rightarrow \cos\phi_1 \quad (15)$$

I_l – phase current (A);

V_l – voltage (V);

Because the magnetic saturation is small along q axis, we can consider L_q constant.

The value of L_q found from (12) - (14) is considered valid for the load tests as cross-coupling influence is small.

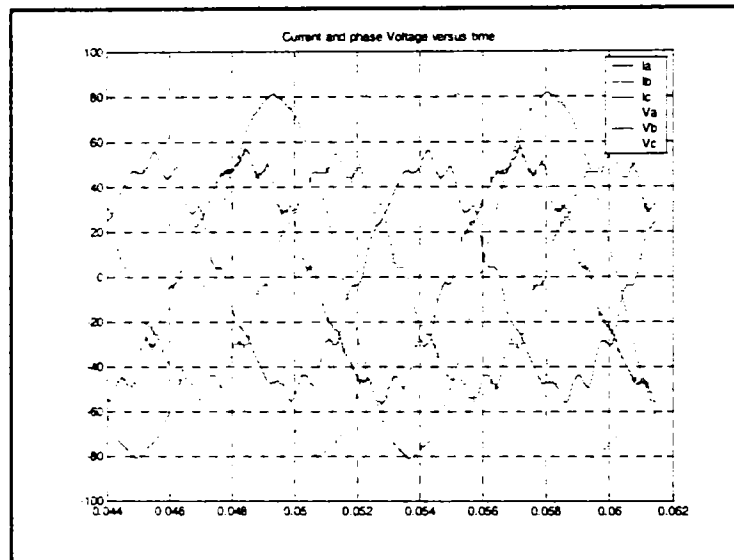


Figure 3.18. Current and voltage versus time at ac load (1370rpm)

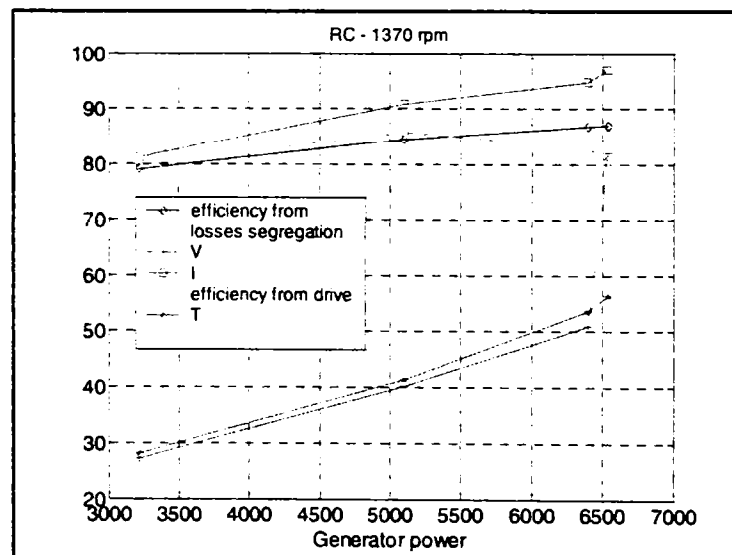


Figure 3.19. The characteristics for 1370 rpm with resistive load and capacitor excitation

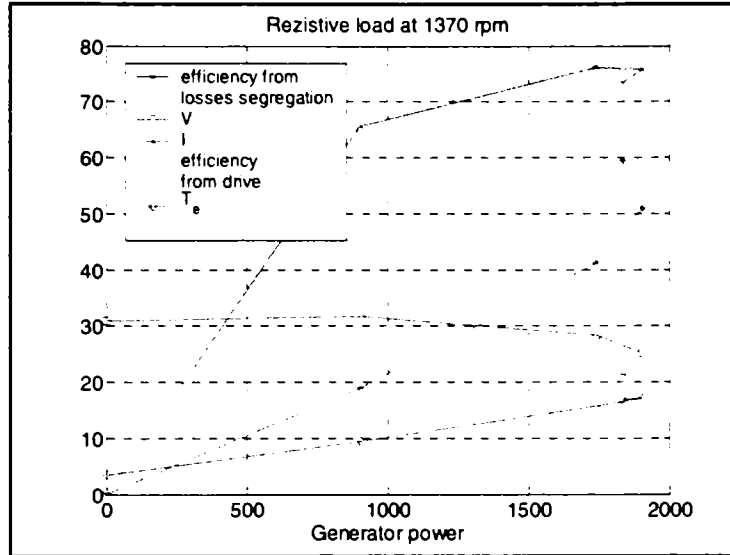


Figure 3.20. The characteristics for 1370 rpm with resistive load, without capacitor excitation

Many attempts to calculate the internal angle from on load tests have been made, with mathematical computation [3].

Based on the vector diagram for our case [3]:

$$\begin{aligned} -X_d \cdot I_d &= V_d \\ -V_{PM} + X_q \cdot I_q &= V_q \end{aligned} \quad (16)$$

$$\begin{aligned} V_d &= V_{e1} \cdot \cos \delta \\ V_q &= V_{e1} \cdot \sin \delta \\ I_d &= I_{s1} \cdot \sin(\delta + \varphi_1) \\ I_q &= I_{s1} \cdot \cos(\delta + \varphi_1) \end{aligned} \quad (17)$$

$$\begin{aligned} \underline{V}_{e1} &= \underline{V}_1 - R \cdot \underline{I}_{s1} \\ \varphi_1 &= \text{angle}(\underline{I}_{s1}, \underline{V}'_{e1}) \end{aligned} \quad (18)$$

$$-V_{PM} + X_q \cdot I_{s1} \cdot \cos(\delta + \varphi_1) = V_{e1} \cdot \sin \delta \quad (19)$$

The only unknown in eqn (15) is the power angle δ_v :

$$\delta_v = a_1 \tan 2(a_1, b_1) \pm a_1 \cos \frac{V_{PM}}{\sqrt{a_1^2 + b_1^2}} \quad (20)$$

With

$$\begin{aligned} a_1 &= -V_{e1} - X_q \cdot I_{s1} \cdot \sin \varphi_1 \\ b_1 &= X_q \cdot I_{s1} \cdot \cos \varphi_1 \end{aligned} \quad (21)$$

Consequently the power angle is directly computable.

In this equation the sign in (16) is chosen for L_d to be positive and greater than L_q .

$$L_d = -\frac{V_d}{\omega_1 \cdot I_d} \quad (22)$$

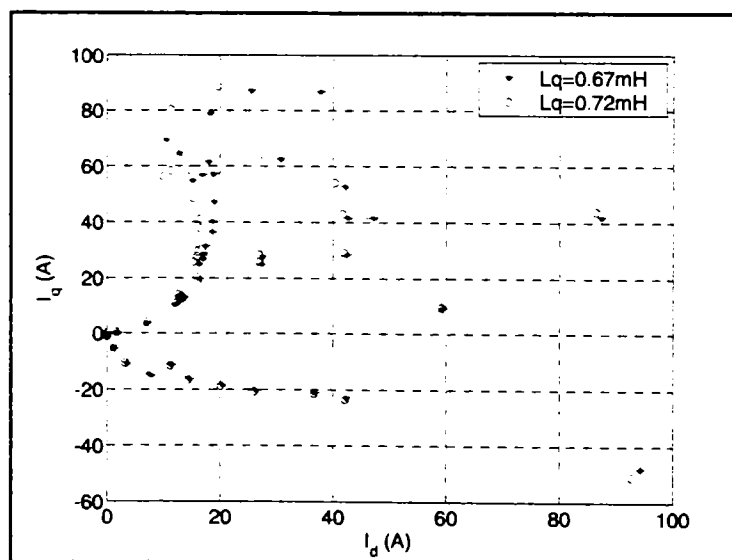
For 1370 rpm, with resistive load and capacitors excitation, a torque of 57 Nm has been obtained (Figure 3.19). The peak torque (for motoring) in the design was 140 Nm [1].

The I_q , L_d , δ , (I_d) curve obtained from load tests as indicated above is shown in Figure 18 (a, b, c). Comparing with results in Figure 8 we should notice differences up to 20 % which at this hour are thought to be due to heavy saturation in axis d and due to errors in the measurements. The various power angles and I_q values in Figure 18 suggest a wide range of load conditions.

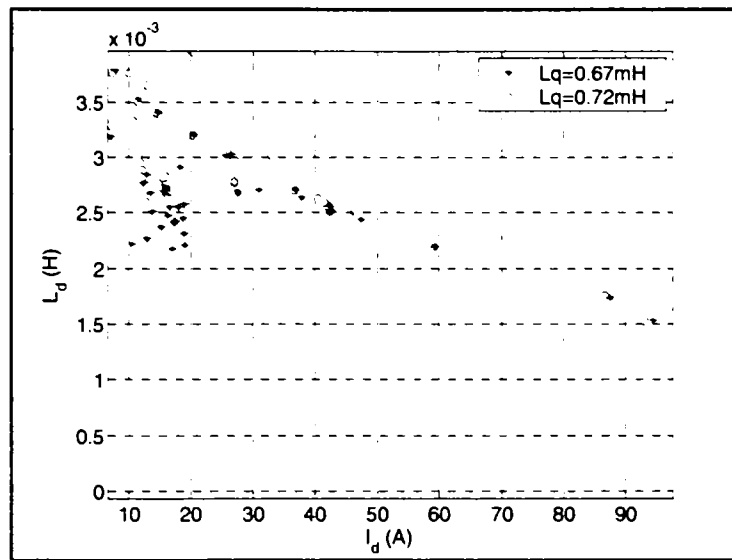
3.7. On load testing with diode rectifier

Some tests have been performed with a diode rectifier and resistive load. No capacitors have been present at generator terminals.

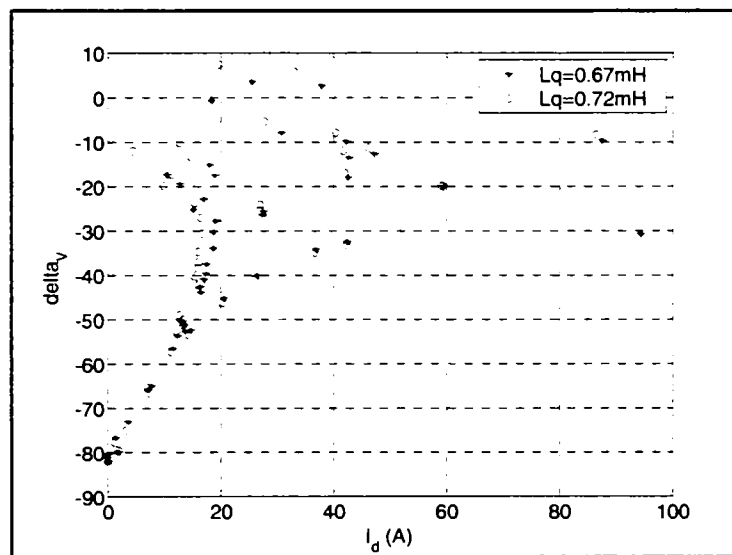
The low level of delivered power is explainable by the small contribution of PM to the machine torque (power) in Figure 3.21.



(a)



(b)



(c)

Figure 3.21. Determination of I_q (a), L_d (b) and δ_v (c) from on load ac tests – for both L_q calculated from standstill ($L_q = 0.72 \text{ mH}$) and from no load + shortcircuit ($L_q = 0.67 \text{ mH}$)

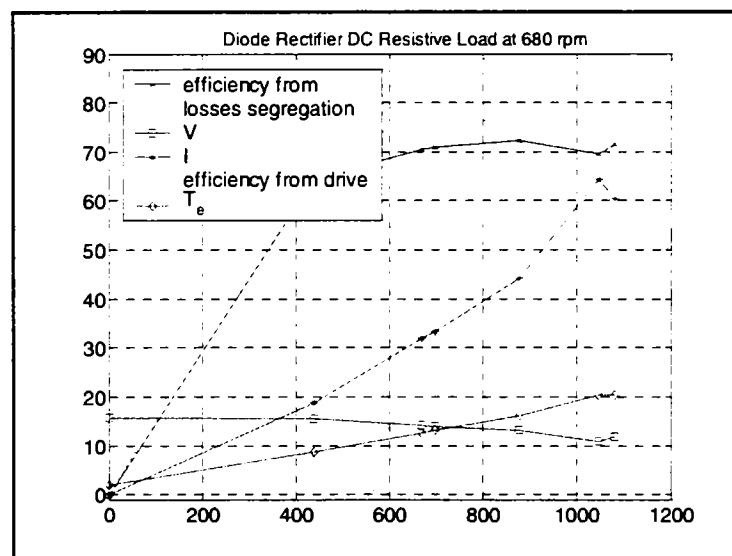


Figure 3.22. The characteristics for diode rectifier DC resistive loads at 680 rpm

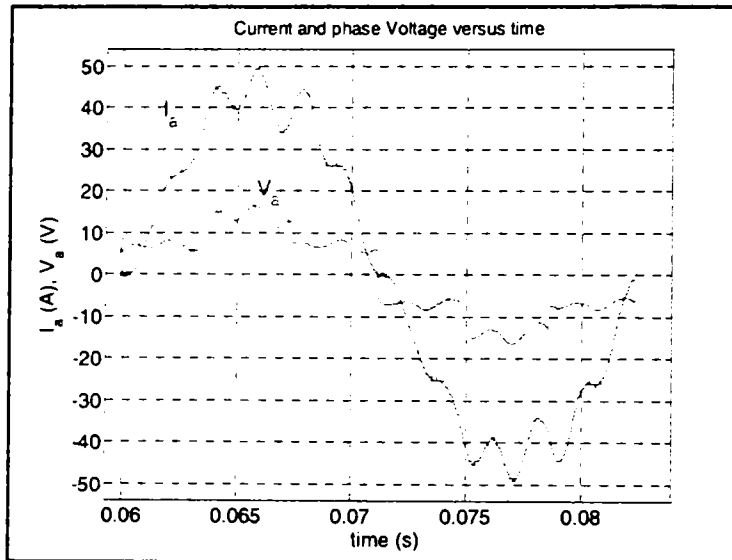


Figure 3.23. I_{phase} , V_{phase} with diode rectifier d.c. load at 680 rpm ($V_{dc} = 20,86$ V, $I_{dc} = 42$ A)

The typical phase voltage and rather sinusoidal phase current with diode rectifier dc load is clearly visible at 680 rpm (Figure 3.23).

3.8. Conclusion

- This chapter introduces a series of tests for the PM – assisted RSM in the generator regime to identify the parameters and energy conversion performance.
- The standstill dc decay tests have produced coherent unique magnetization curves along d axis (high permeance) and q axis (low permeance).
- The q axis inductance (along the PM axis) was proven rather constant also from no load and short-circuit tests.
- Capacitors were connected at machine terminals for generator loss segregation.
- With capacitors at terminals, resistive symmetric load was applied to load the generator and check the efficiency. Efficiency above 80 % was proven from 3 kW to 6.5 kW output at 1370 rpm.
- By segregation of losses higher efficiency was found. The stray load losses are the cause of this difference.
- We conclude by saying that the proposed generator series of tests proved rather successful in characterizing the machine.

3.9. References

- [1] Boldea, L.Tutelea, C.I. Pitic, "PM – assisted Reluctance Synchronous motor/generator (PM-RSM) for mild hybrid vehicle", OPTIM 2002, Brasov, Romania.
- [2] H.P. Nee, L. Lefevre, P. Thelin, J. Soulard, "Determination of d and q Reactances of Permanent-Magnet Synchronous Motor Without Measurement of the Rotor Position", IEEE Transactions on Industry Applications, vol. 36, no. 5, pp. 1330-1335, September-October 2000.
- [3] E.C. Lovelace et al., "Design and experimental verification of a direct-drive interior PM synchronous machine using a saturable lumped-parameter model", IAS 2002,
- [4] Boldea, "Reluctance synchronous machines and drives", (book), OUP 1996.
- [5] M.Comanescu, A. Keyhani, M. Dai, "Design and analysis of 42-V Permanent-Magnet Generator for Automotive Applications", IEEE Transactions on Energy Conversion, vol. 18, no.1, March 2003.
- [6] J.H. Lee, J.C. Kim, D.S.Hyun, "Effect Analysis of Magnet on Ld and Lq inductance of permanent magnet assisted synchronous reluctance motor using finite element method", IEEE Transaction on Magnetics, vol. 35, no. 3, May 1999.
- [7] S. Chen, B. Lequesne, R.R. Henry, Y. Xue, J.J. Ronning, "Design and testing of a belt-driven induction starter-generator", IEEE Transaction on Industry applications, vol. 38, no. , November - December 2002
- [8] J.R. Melgoza, G.T. Heydt, A. Keyhani, B.L. Agrawal, D. Selin, "Synchronous Machine parameter estimation using the Hartley series",IEEE Transaction on Energy Conversion, vol. 16, no. 1, March 2001.
- [9] K.Yamazaki,"Torque and efficiency calculation of an interior permanent magnet motor considering harmonic iron losses of both the stator and rotor"
- [10] E.C. Lovelace et al., "Design and experimental verification of a direct-drive interior PM synchronous machine using a saturable lumped-parameter model", IAS 2002
- [11] J.R. Melgoza, G.T. Heydt, A. Keyhani, B.L. Agrawal, D. Selin, "Synchronous Machine parameter estimation using the Hartley series",IEEE Transaction on Energy Conversion, vol. 16, no. 1, March 2001.
- [12] Merchant, R.W.; Gibbard, M.J.; Identification of synchronous machine parameters from standstill tests using recursive estimation with the bilinear operator, Generation, Transmission and Distribution, IEE Proceedings C, Volume 139, Issue 2, March 1992 Page(s):157 – 165
- [13] Boje, E.S.; Balda, J.C.; Harley, R.G.; Beck, R.C.; Time-domain identification of synchronous machine parameters from simple standstill tests, Energy Conversion, IEEE Transactions on, Volume 5, Issue 1, March 1990 Page(s):164 – 175

- [14] Castaldi, P.; Tilli, A.; Parameter estimation of induction motor at standstill with magnetic flux monitoring, *Control Systems Technology, IEEE Transactions on*, Volume 13, Issue 3, May 2005 Page(s):386 – 400
- [15] Asano, H.; Yamamoto, S.; Ara, T.; Oda, S.; Matsuse, K.; An estimation method of starting performance of squirrel-cage induction motor on DC decay testing method, *Industry Applications Conference. 1999. Thirty-Fourth IAS Annual Meeting. Conference Record of the 1999 IEEE. Volume 3*, 3-7 Oct. 1999 Page(s):1559 - 1564 vol.3
- [16] Cavagnino, A.; Lazzari, M.; Profumo, F.; Tenconi, A.; Axial flux interior PM synchronous motor: parameters identification and steady-state performance measurements, *Industry Applications. IEEE Transactions on*, Volume 36, Issue 6, Nov.-Dec. 2000 Page(s):1581 – 1588
- [17] Groza, V.; Biriescu, M.; Liuba, G.; Cretu, V.; Experimental determination of synchronous machines reactances from DC decay at standstill, *Instrumentation and Measurement Technology Conference. 2001. IMTC 2001. Proceedings of the 18th IEEE, Volume 3*, 21-23 May 2001 Page(s):1954 - 1957 vol.3
- [18] Tumageanian, A.; Keyhani, A.; Synchronous machine parameter estimation from standstill flux decay data, *Circuits and Systems, 1992.*, Proceedings of the 35th Midwest Symposium on, 9-12 Aug. 1992 Page(s):1288 - 1291 vol.2
- [19] Cavagnino, A.; Lazzari, M.; Profumo, F.; Tenconi, A.; Axial flux interior PM synchronous motor: parameters identification and steady-state performance measurements, *Industry Applications. IEEE Transactions on*, Volume 36, Issue 6, Nov.-Dec. 2000 Page(s):1581 – 1588
- [20] T. Senjyu, A. Omoda, T. Shingaki, K. Uezato, "Parameter measurement for synchronous reluctance motors considering stator iron loss in standstill condition"
- [21] Kiltbau, J.M. Pacas, "Measurement of the parameters of the synchronous reluctance machine including cross saturation", *EPE 2001, Graz*.
- [22] H.P. Nee, L. Lefevre, P. Thelin, J. Soulard, "Determination of d and q Reactances of Permanent-Magnet Synchronous Motor Without Measurement of the Rotor Position", *IEEE Transactions on Industry Applications*, vol. 36, no. 5, pp. 1330-1335, September-October 2000.
- [23] T Senjyu, A Omoda, T. Shingaki, K. Uezato, Parameter measurement for synchronous reluctance motors considering stator iron loss in standstill condition
- [24] T. Senjyu, A. Omoda, T. Shingaki, K. Uezato, "Parameter measurement for synchronous reluctance motors considering stator iron loss in standstill condition"
- [25] Yamamoto, S.; Ara, T.; Oda, S.; Matsuse, K.; Prediction of starting performance of PM motor by DC decay testing method, *Industry Applications Conference, 1999. Thirty-Fourth IAS Annual Meeting. Conference Record of the 1999 IEEE, Volume 4*, 3-7 Oct. 1999 Page(s):2574 - 2581 vol.4

- [26] F.F. Bernal, A.G. Cerrada, R. Faure, "Determination of Parameters in Interior Permanent – Magnet Synchronous Motors With Iron Losses Without, Torque Measurement", IEEE Transactions on Industry applications, vol. 37, no.5,pp. 1265-1272, September/October 2001.
- [27] F.F. Bernal, A.G. Cerrada, R. Faure, "Determination of Parameters in Interior Permanent – Magnet Synchronous Motors With Iron Losses Without, Torque Measurement", IEEE Transactions on Industry applications, vol. 37, no.5,pp. 1265-1272, September/October 2001
- [28] Boldea, I.; Chis, L.; Wallace, A.K.; Load testing of induction machines without torque measurements, Electric Machines and Drives, 1999. International Conference IEMD '99, 9-12 May 1999 Page(s):162 – 164

Chapter IV

Interior Permanent Magnet Synchronous Machine: Motion-Sensorless Direct Torque and Flux Control

Abstract

This chapter presents a comprehensive implementation of a wide speed motion-sensorless control of PMSM drives via direct torque and flux control (DTFC) with space vector modulation (SVM). Signal injection with a modified D-module filter and phase-locked loop (PLL) observer is used at low speeds to observe the rotor position and speed, to be used in the flux observer and, respectively, as speed feedback. A combined voltage-current model flux observer suits the whole speed range while the current model fades away as speed increases. PWM and inverter nonlinearities compensation provide for a smooth current waveform even at very low speeds.

4.1. Introduction

Motion control of PM synchronous machine requires accurate position and velocity signals to realize field orientation. In general, these feedback signals come from devices mechanically coupled to the rotor, electromagnetic resolvers, resolvers or optical encoders. However, this additional sensors, connectors and wiring increase the cost of the system and decrease the reliability. [1]

The reduction in mechanical robustness and cost of sensors makes elimination of these devices very desirable.

In the last several years, there have been numerous publications or methods to eliminate the position sensors on electrical machines. Most of these techniques are based on tracking back EMF, which limits the low speed operation of machine and his sensitive to the estimation of machine parameters, such as stator inductance and resistance.

It has been found that PMSM reacts in different ways to high frequency (400-1000Hz) phase voltage injection depending on its rotor speed and position. The

irregularities in the rotor structure generate amplitude oscillations in the current due to the high frequency carrier, which are proportional to the rotor position. At the same time the frequency of these amplitude modulations is proportional to machine speed. This is due to change in magnetic path when stator slots appear in different position respect to the rotor iron structure or to the PM position. A fast Fourier transform (FFT) analysis of the phase currents reveals spectral components at frequency related to both the rotor speed and the number of slots. The motor is therefore employed as a kind of resolver, due to change in magnetic reluctance that can be advantageously considered for the position estimate.

Two basic methods for initial position are to use pulse signal injection or sinusoidal carrier signal injection. The pulse signal injection methods are often based on estimating the minimum inductance location using a calculated di/dt obtained during some form of iterative square wave voltage injection to arbitrary axis such as that in [2-6] and can be applied to both surface [2, 3, 4, 6] and interior permanent synchronous machine [5-6].

Interior PM synchronous motor (IPMSM) drives are becoming more and more favored in wide speed range applications. Eliminating the shaft position sensor is welcome, based on cost and reliability constraints. Motion-sensorless control methods of PMSM fall into two main categories: 1) emf tracking based on the fundamental model, that fails at zero and very low speed, and 2) signal injection methods, which work from standstill but should be dropped at a certain low speed in favor of emf tracking methods.

The IPMSM is blessed with $d-q$ saliency, which is tracked for rotor position estimation. Persistent high-frequency carrier-voltage ($\omega_c = 300-1000$ Hz, $V_c = 1-10$ V) [1-6], or discrete voltage pulses [2] can be injected in machine for the rotor position tracking. The resulting carrier-current harmonics contains the rotor position information. While a low pass filter (LPF) separates the fundamental current, a band pass filter (BPF) in a specific reference selects the targeted carrier-current harmonic. The BPF is complemented by a phase-locked loop (PLL) tracking observer that extracts the rotor speed and position.

After reviewing saliency-tracking estimators [1-4, 6] and the mirror-phase estimator [5], a simplified estimator with only one D-module vector filter (compared with two in mirror-phase) is used to estimate the rotor position & speed.

A hybrid voltage-current model closed-loop flux observer takes the rotor position into its current model at low speed, and uses only the voltage model at medium-high speed.

In contrast to the vector control, the direct torque and flux control (DTFC), used in this paper, does not need the rotor position in decoupling networks, and thus the use of DTFC should be beneficially in motion-sensorless implementations.

However, to reduce torque pulsations, the space vector modulation (SVM) is applied. Finally, dead time and other nonlinearities in the PWM converter are compensated to further smooth up current waveform at very low speed.

A detailed presentation of the proposed drive with ample experimental results follows.

4.2. Implemented motion-sensorless DTFC-SVM system

The space vector IPMSM model includes: the voltage model in the general reference frame, rotating with ω speed (1); the current model in dq rotor reference (2); the electromagnetic torque T_e computed in $\alpha\beta$ stator reference (3). The magnetic saturation was considered rather constant and a small saliency rotor was used.

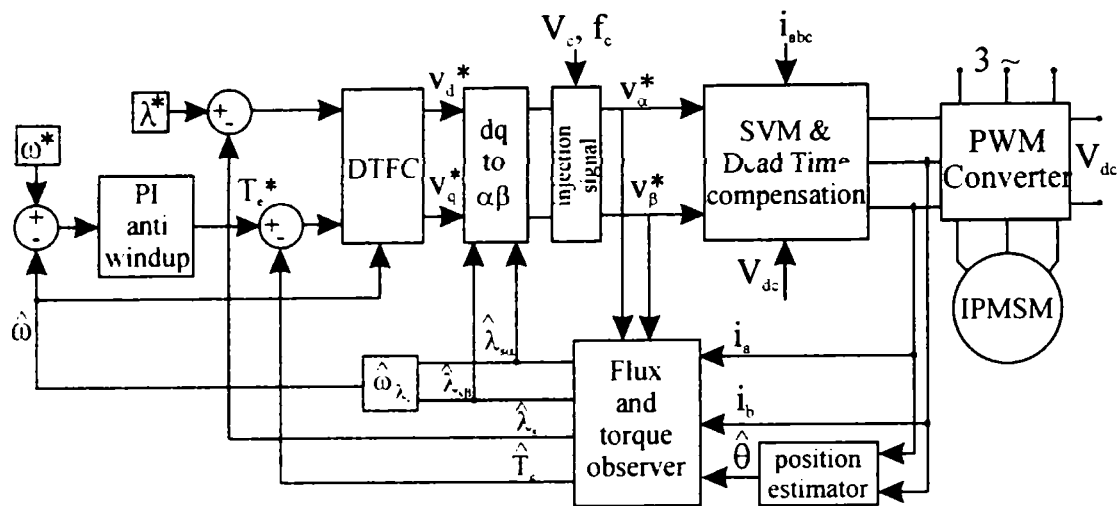
$$\underline{v} = R_s \underline{i} + d\underline{\lambda} / dt + j\omega \underline{\lambda} \quad (1)$$

$$\underline{\lambda} = (L_d i_d + \lambda_{PM}) + jL_q i_q \quad (2)$$

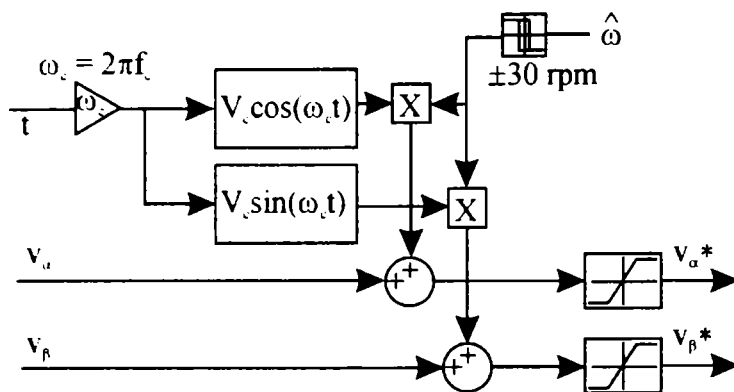
$$T_e = 1.5p(\lambda_\alpha i_\beta - \lambda_\beta i_\alpha) \quad (3)$$

where: \underline{v} , \underline{i} and $\underline{\lambda}$ are the stator voltage, current and flux vector, respectively; R_s is the stator phase resistance; L_d and L_q are the dq inductances; λ_{PM} is the PM flux; p is the pair pole number. Table I shows IPMSM specifications.

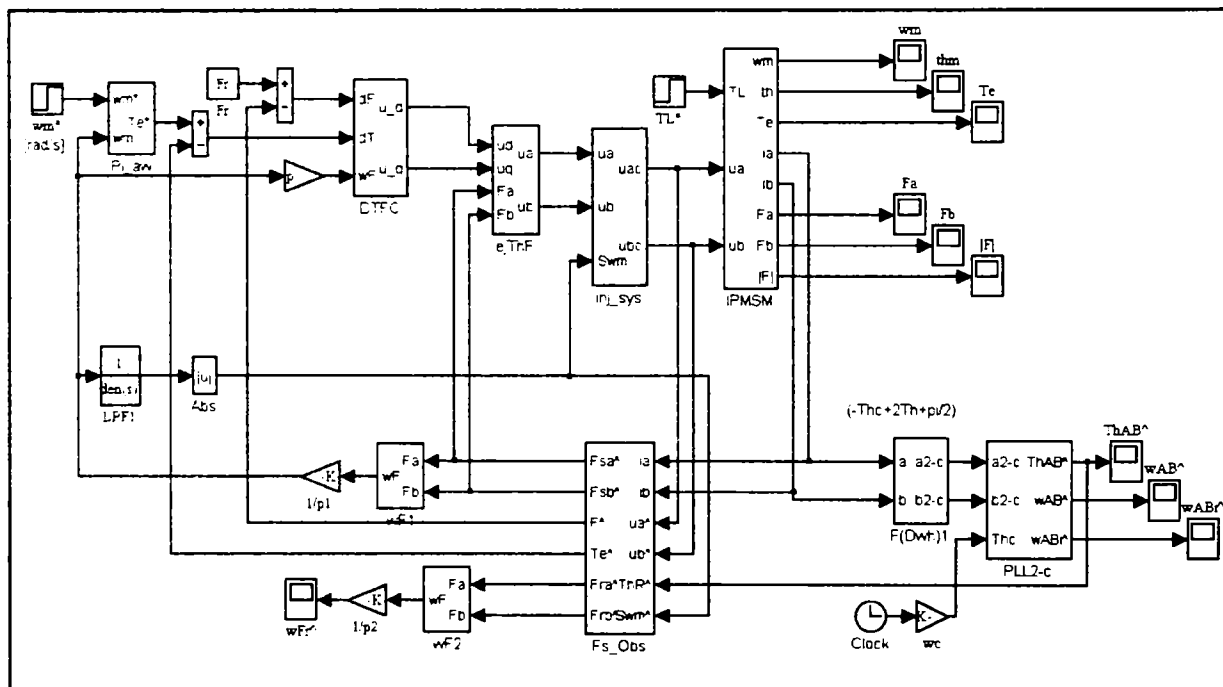
The proposed sensorless DTFC-SVM system for IPMSM is introduced in Fig. 1. It mainly contains: DTFC-SVM, flux and torque observer, position-speed estimator with signal injection, and a relay that inhibits the signal injection beyond ± 30 rpm.



(a)



(b)



(c)

Figure 4.1. a) The proposed sensorless DTFC-SVM for IPMSM, b) injection signal with $\omega_c = 2\pi 500$ rad/s for position estimation, c) MATLAB®/Simulink implementation.

The DTFC uses the voltage model (1) in stator flux reference with the flux position $\hat{\theta}_s$ in dq - $\alpha\beta$ transformation.

The hybrid voltage-current model structure of the flux observer is visible in Fig. 4.2. It is based on (1)-(3) with the voltage model in $\alpha\beta$ stator reference ($\omega = 0$). The PI compensator makes the current model prevail at low speed, and the voltage model at medium-high speed, with a smooth transition between them. The current model (Fig. 2a) output is inhibited by a relay above ± 30 rpm, where the position estimation is neither available nor necessary for DTFC. Only the speed feedback is required above ± 30 rpm. The speed of stator flux vector was finally used for speed feedback.

The realization example for a 3rd-order filtering with the inverse D-module $D^{-1}(s, \omega_c)$ [5, 7] is shown in Figure 4.3. This kind of vector filter discriminates for the phase-polarity and rejects the dc-offset originating in stator current acquisition process. If the scalar (single-input/output) filter $F(s)$ (as in Figure 4.4a) is designed as a low-pass filter (LPF) with the bandwidth B , then the associated vector (two-input/output) filter in D-module $F(D(s, -\omega_c))$ is a band-pass filter (BPF) with the central frequency ω_c and same bandwidth B [7].

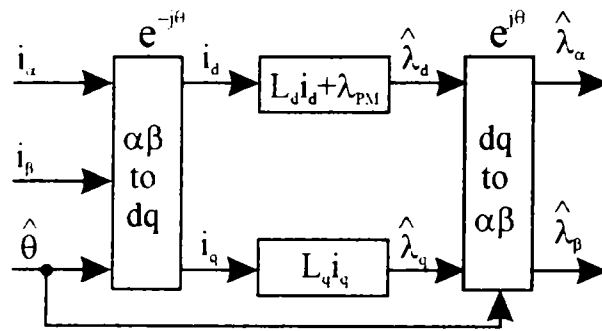
The position estimation with signal injection includes:

1) a BPF (Figure 4.6a) with only one vector filter using inverse D-module realization (Fig. 4.6b) to select the 1st carrier-current negative-sequence harmonic from the stator current

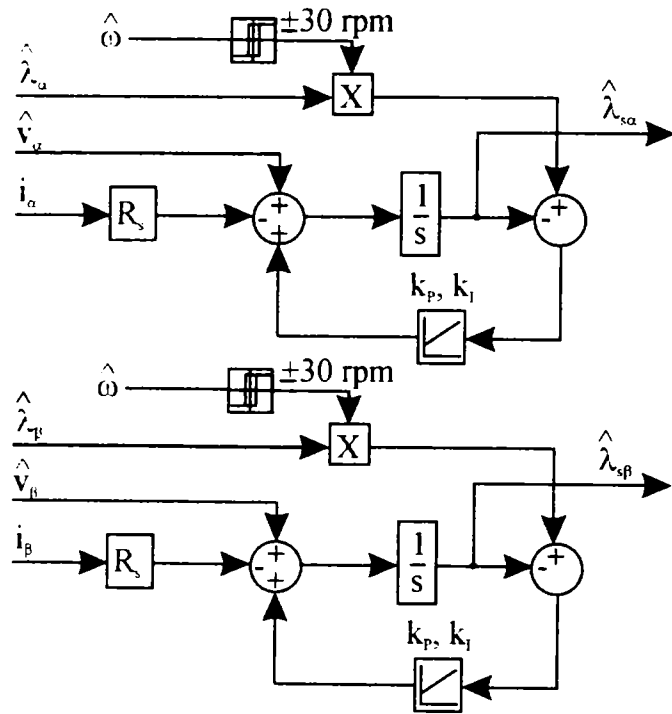
$$\underline{i}_c = I_c \exp\{j(-\theta_c + 2\theta + \pi/2)\}, I_c \approx V_c (L_d - L_q) / (2\omega_c L_d L_q) \quad (4)$$

with $\theta_c = \omega_c t$, that contains the rotor position θ , and

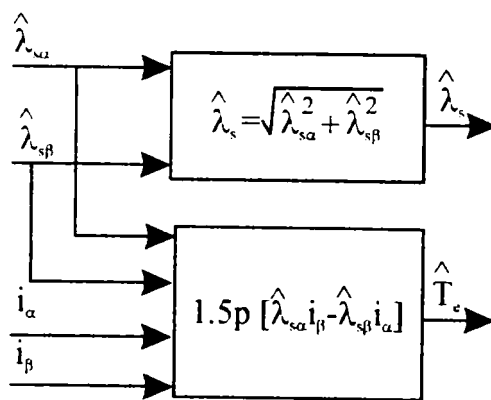
2) a PLL tracking observer to extract $\hat{\theta}$, $\hat{\omega}$ from the \underline{i}_c phase (Figure 4.4c).



(a)



(b)



(c)

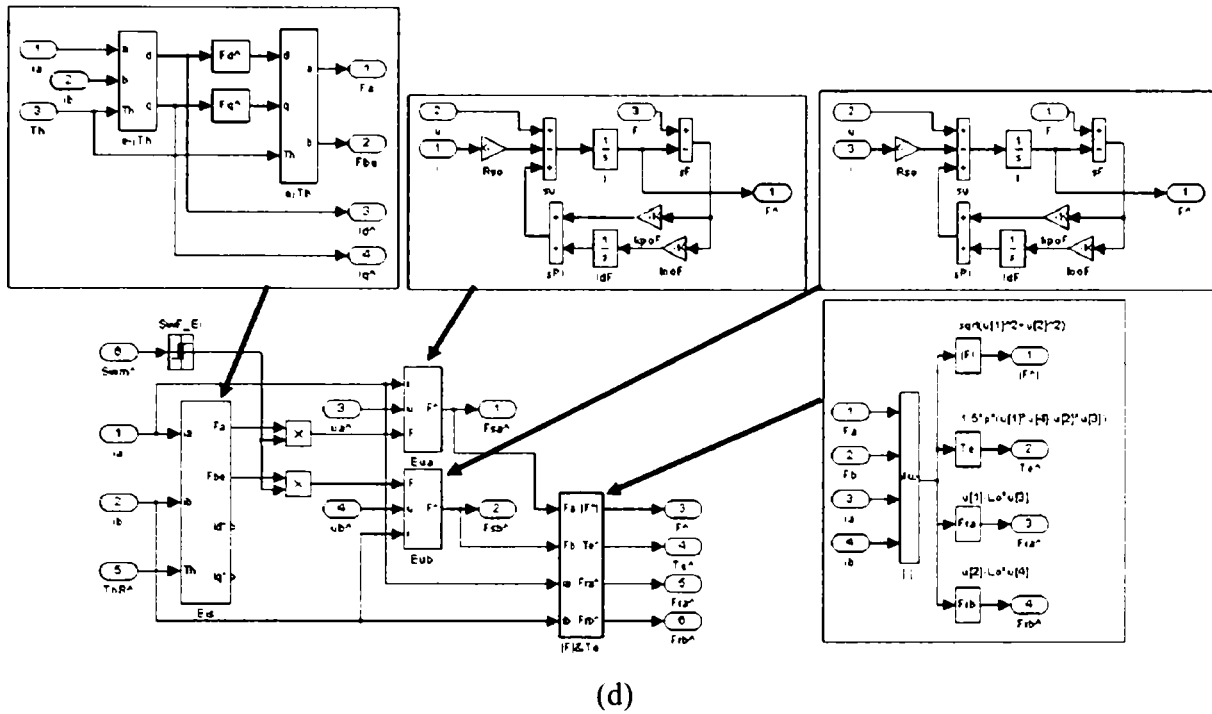


Figure 4.2. Flux and torque observer with combined voltage-current models

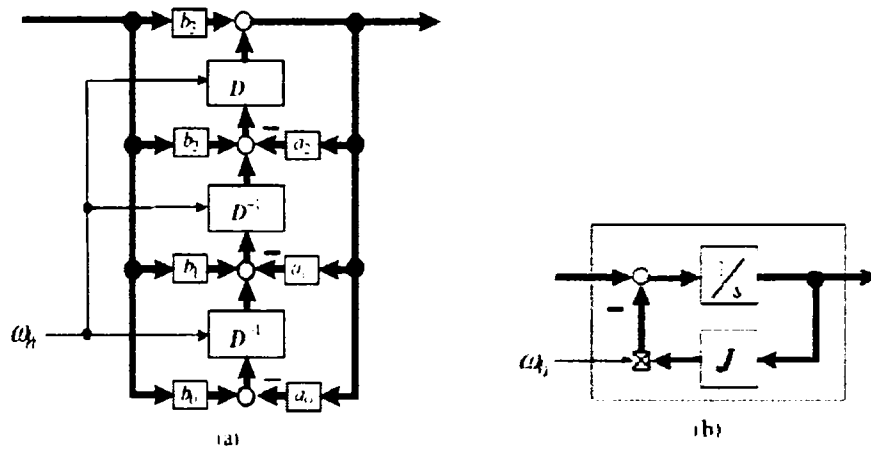
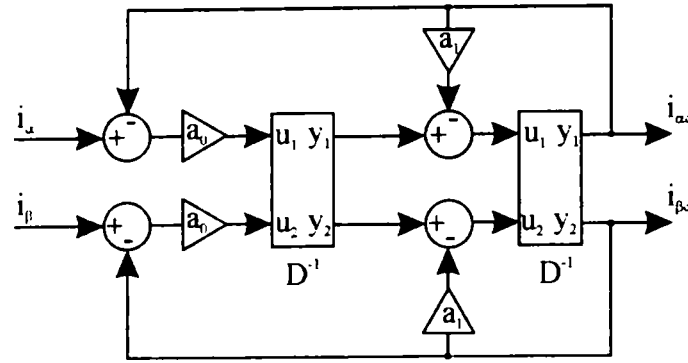


Figure 4.3. a) Realization example for 3rd-order filtering, b) inverse D-module

To improve dynamic estimations, an extended Luenberger observer with zero-phase lag [1] could be used in PLL.

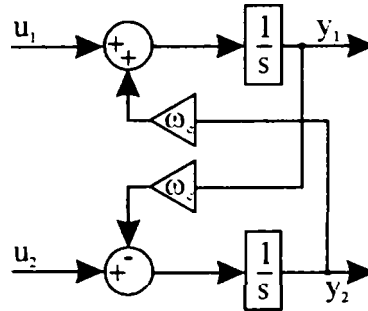
The initial rotor position is correctly estimated at standstill in $(-\pi/2, \pi/2)$ radians range. For the full angle range, an uncertainty of π radians appears that could be discriminated by the magnet polarity detection using other information as the 2nd-order carrier-current harmonics [4].

This rotor position / speed estimation with signal injection is very robust, independently of IPMSM parameters. The configuration in Figure 4.4 is believed to be less intensive in terms of online computation, in comparison with existing implementations of equivalent performance.

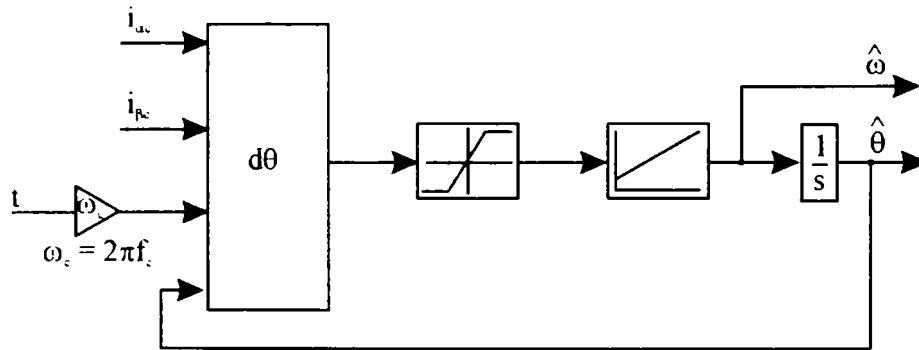


$$F(s) = \frac{a_0}{s^2 + a_1s + a_0}$$

(a)

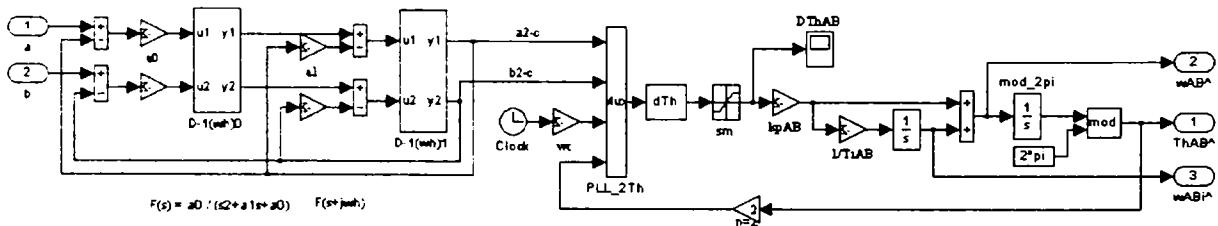


(b)



$$d\theta = \frac{i_{\beta c} \sin(\omega_c t - 2\hat{\theta}) - i_{\alpha c} \cos(\omega_c t - 2\hat{\theta})}{2I_c}$$

(c)



(d)

Figure 4.4. Position estimation: a) 2nd-order vector BPF with D-module, b) D⁻¹ realization, c) PLL for position estimation with dθ PLL error, d) MATLAB[®]/Simulink implementation

4.3. Digital simulation sample results

Digital simulations have been processed in MATLAB[®]/ Simulink package for an easy translation into the dSpace system for experiments.

Sample simulation results for the motor specified in Table 1, with speed reversal for full load (12 Nm) at ± 1 rpm and ± 5 rpm, are shown in Figures 4.5, 4.6 and 4.7.

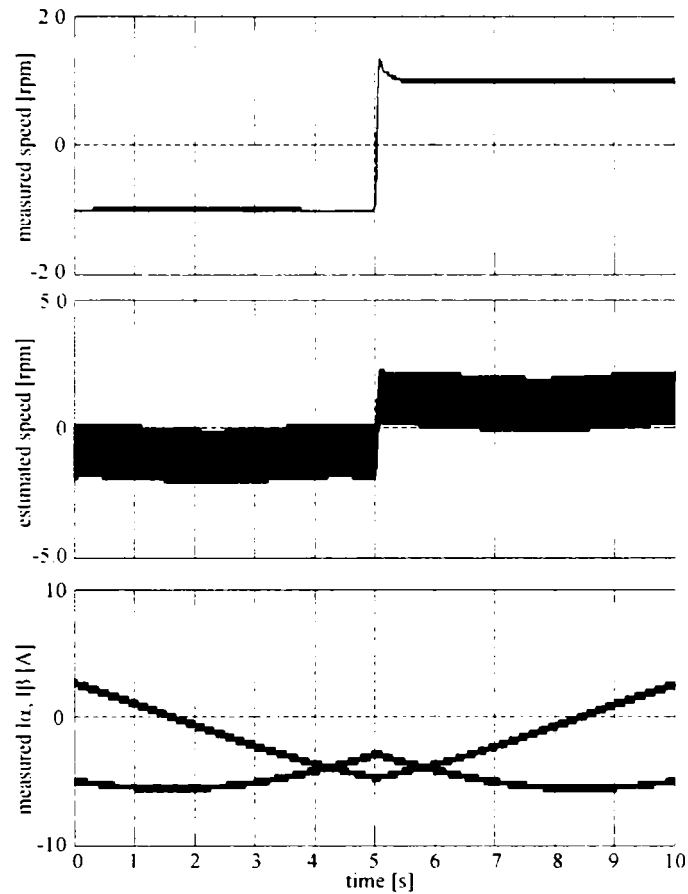


Figure 4.5. Simulation results at -1 to 1 rpm reversal speed for full load (12 Nm): measured speed, estimated speed and measured current i_α , i_β

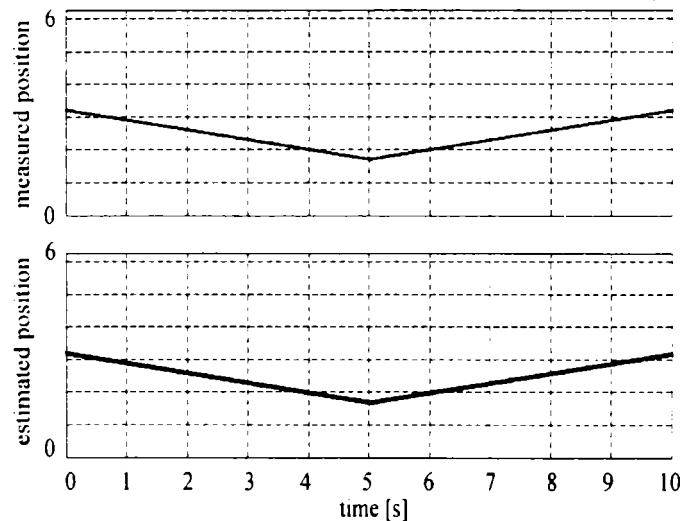


Figure 4.6. Simulation results at -1 to 1 rpm reversal speed for full load: measured and estimated position

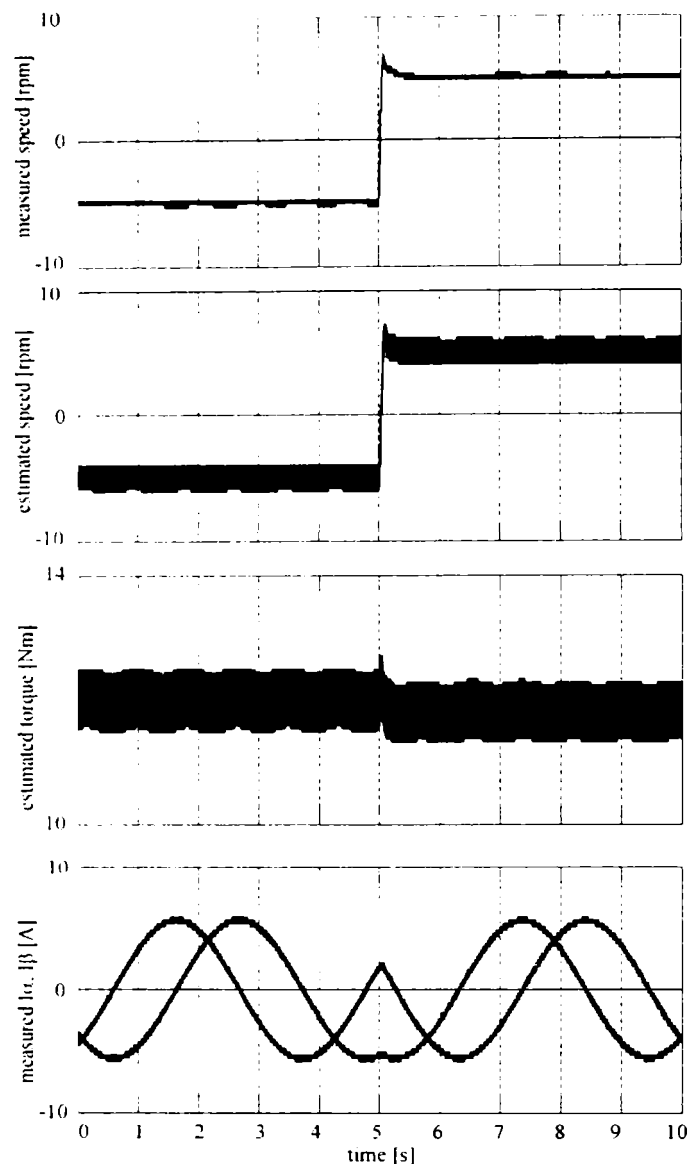


Figure 4.7. Simulation results at -5 to 5 rpm reversal speed for full load: measured speed, estimated speed, estimated torque and measured current components i_α i_β

The measured speed is also given for reference. About 1 rpm speed ripple is visible in the estimated speed. The position estimation during ± 1 rpm reversal speed transients is quite reliable and the SVM yields good current waveforms.

No-load startup transients from zero to 1750 rpm with full step load at 1.5 seconds (Figure 4.8), and on-load starting to 1750 rpm with generating (full load) at 2 seconds (Figure 4.9) show smooth performance with quick speed recovery.

Once, the digital simulations seem to give confidence into the proposed sensorless DTFC-SVM system for IPMSM drive, the experimental work was pursuit.

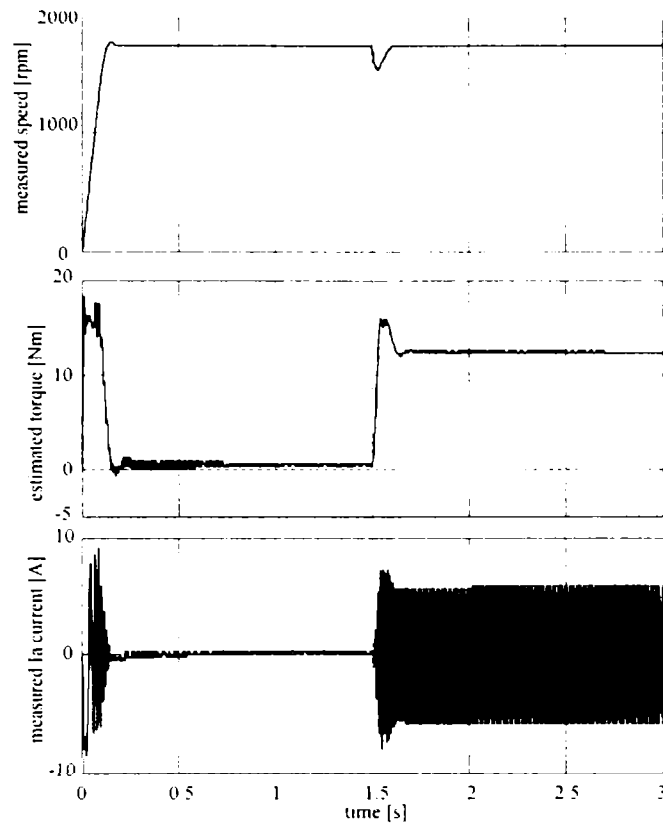


Figure 4.8. Start-up transients (0 to 1750 rpm) with full load applied at 1.5 s: measured speed, estimated torque and measured current - simulation results

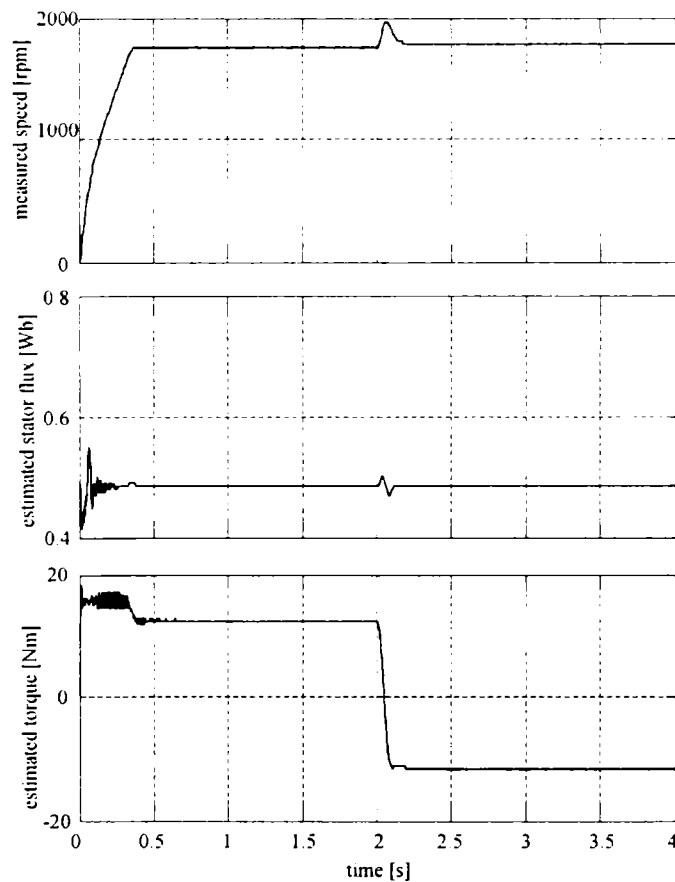


Figure 4.9. Start-up with full torque and motoring to generating crossing at 2 s: measured speed, estimated flux and estimated torque - simulation results

4.4. Experimental system

The testing setup consists in a IPMSM of 12 Nm rated torque driven by a Danfoss VLT 5005 and a Siemens SIMOVERT MASTERDRIVE as load (Figure 4.10).

The experiments were carried out on a dSpace DS 1103 system – with the model implemented in MATLAB[®]/Simulink – with the Control Desk real-time management of the running process (Figure 4.12).

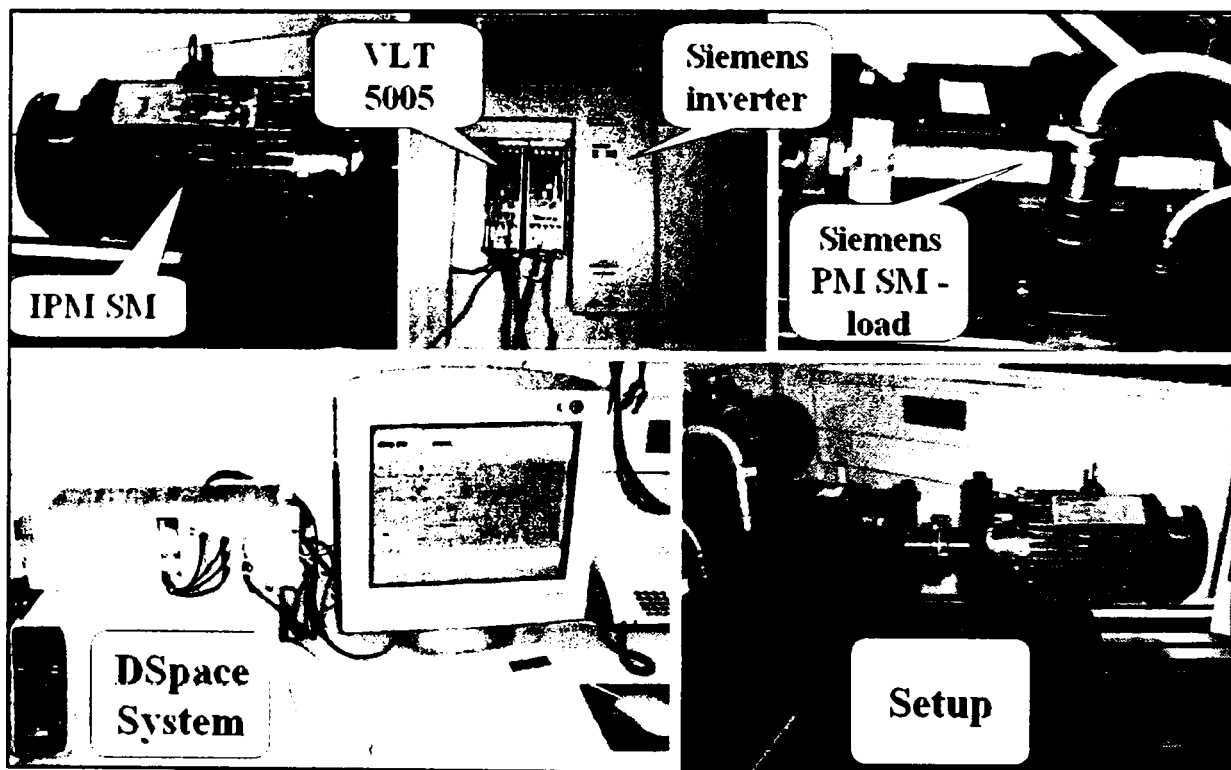


Figure 4.10. The testing setup

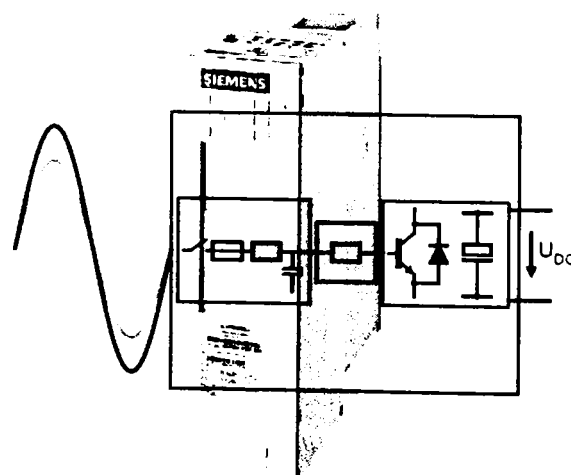


Figure 4.11. Simovert MasterDrive – Siemens

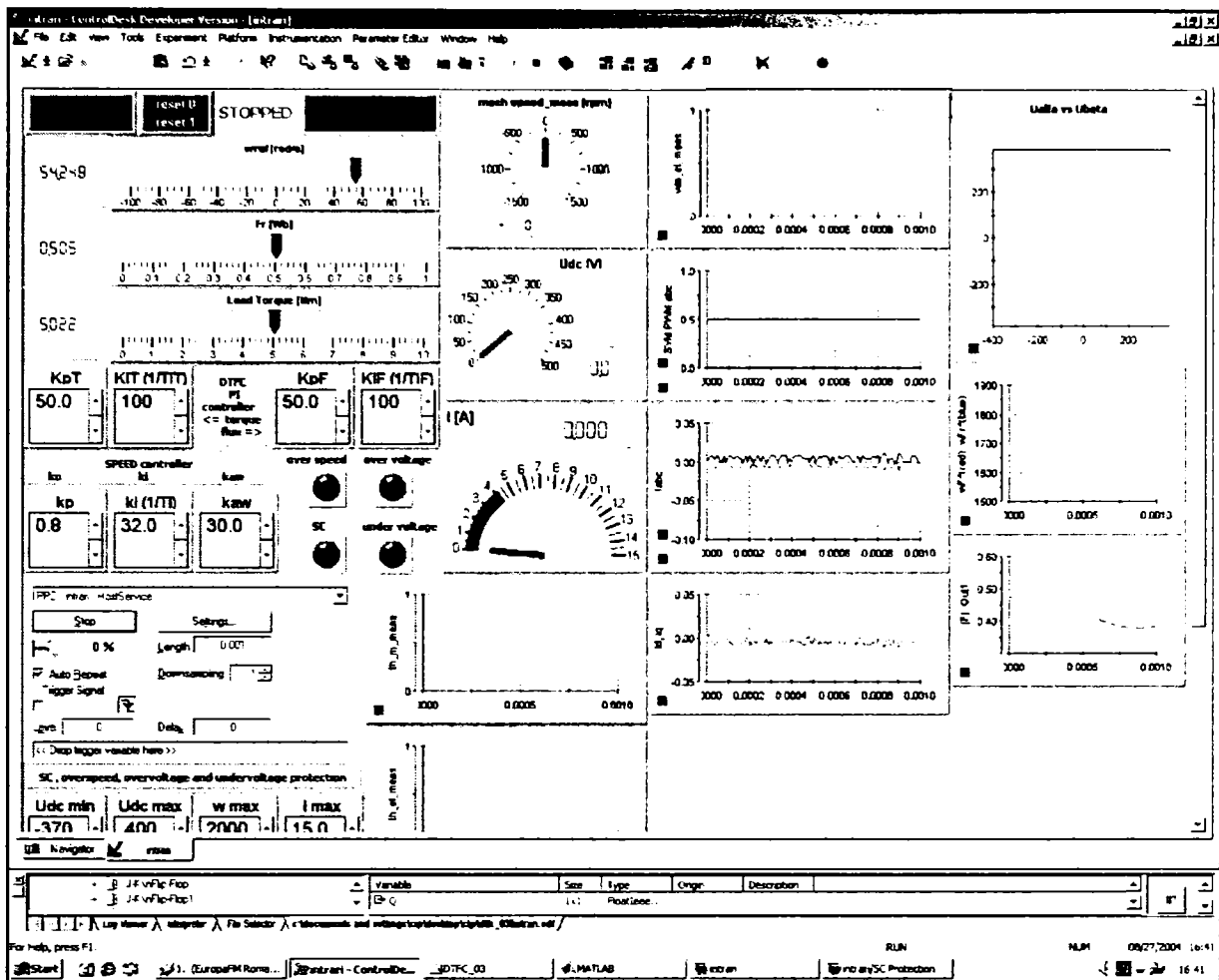


Figure 4.12. dSpace experimental layout (more detailed in Chapter 5)

The load control system: Simovert MasterDrive

The AFE (Active Front End) rectifier/regenerative feedback units belonging to the SIMOVERT MASTERDRIVES series are power electronics devices that are available as cabinet, chassis and as compact units.

The compact units described below are available only in the 400 V mains voltage range.

The units can be operated on a 3 - phase mains with or without an earthed neutral point.

400 V mains voltage range: 3AC 380 V (- 20 %) to 460 V (+ 5 %)

The core component of the AFE rectifier/regenerative feedback unit consists of a voltage source converter with the CUSA control unit and it generates a controlled DC voltage, the so-called DC link voltage, from a 3-phase mains.

This DC link voltage is kept constant almost independently of the mains voltage (also in the event of regenerative feedback). The prerequisite for this is that the DC voltage setpoint is within the operating range defined below.

DC link voltage operating range:

- Minimum: 1.5 times the rms value of the applied mains voltage.
Explanation: the DC link voltage of the AFE inverter must at least be greater than the peak rectified value of the applied mains voltage to ensure that the power system is no longer controlled via the freewheeling diodes of the IGBT switches.
- Maximum: for the 400 V mains voltage range: 740 V DC

Operating principle:

On the 3-phase end, a mains angle-oriented high-speed vector control is subordinate to the DC link voltage control and impresses an almost sinusoidal current on the network so as to minimize system perturbations with the aid of the subsequently connected Clean Power filter.

The vector control also enables setting of the power factor $\cos \phi$, and thus reactive power compensation, but the operating current requirement has priority.

The VSB module (Voltage Sensing Board), functions as the network angle sensor, similarly to the principle of an encoder.

For safety reasons, an AFE rectifier/regenerative feedback unit must be connected to the mains via a main contactor; see figure 2-1. For this reason, an external 24 V power supply is always needed to supply the VSB module and the AFE unit.

Configuration:

Both one and several inverters can be connected to the output. The maximum connected power of the inverters may amount to 4 times the rated power of the AFE inverter. The total active power drawn from the mains supply must not continuously exceed the rated power of the AFE; the plant must be configured to meet this requirement.

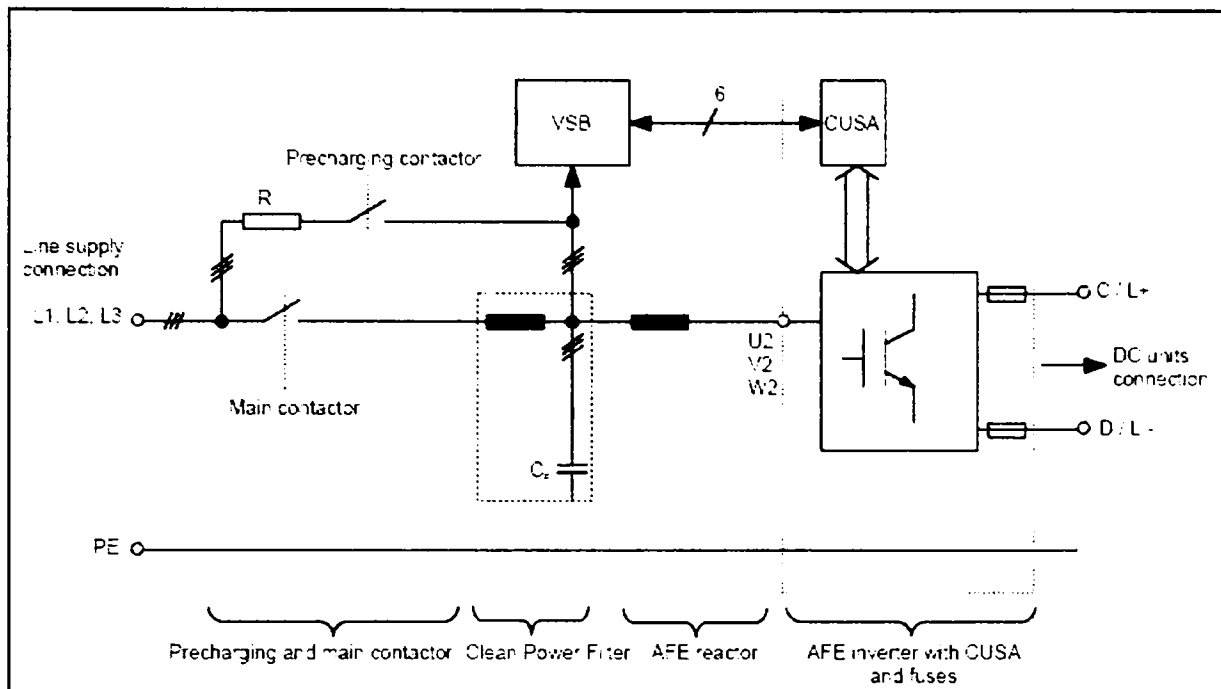


Figure 4.13. the basic circuit of Simovert MasterDrive

The AFE is suitable for coupling several inverters to a common DC busbar. This allows energy to be transferred between motoring and generating drives, thus providing a power-saving feature.

Line voltage dips can be bridged in voltage step-up operation without altering the DC link voltage value. This can be achieved up to 65 % of rated line voltage without additional components on condition that the power balance can be maintained.

To bridge line voltage dips below 65 % of rated line voltage, the auxiliary power supply must be supported by an external UPS or similar to prevent the contactors from dropping out.

Operation and control options:

The unit can be controlled and operated via

- the parameterization unit (PMU)
- an optional operator control panel (OP1S)
- the terminal strip
- a serial interface

In combination with automation systems, the AFE rectifier/regenerative feedback unit is controlled via optional interfaces (e.g. PROFIBUS) and technology boards (e.g. T100, T300).

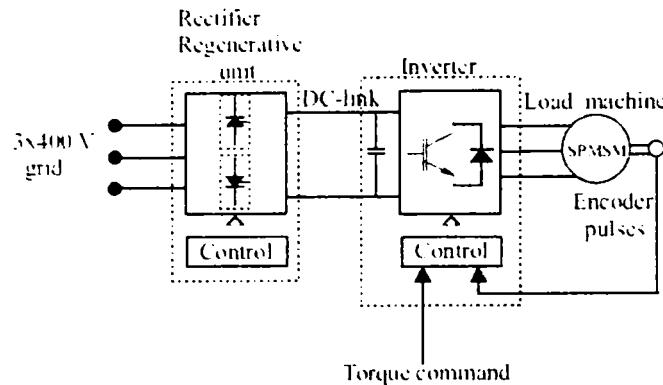


Figure 4.14. Block diagram illustrating sections of the load control system

The load machine is a SPMSM. It is also from Siemens and the type is ROTEC 1FT6. This machine is fitted with an encoder in order to provide position and velocity information of the rotor. The rated speed and the rated torque of this machine are 3000 rpm and 14.7 Nm respectively.

Control of the rectifier/regenerative unit and the inverter is provided by Siemens. In addition, those units are provided with software so that the user can programme them via parameters in order to adapt to a specific application. Key-pads with displays are also included so that the user can programme them easily. The torque command, which is needed to control the torque of the load machine, can be given to the inverter from the key-pad or using an analog voltage signal (0-10 V).

Danfoss VLT 5005:

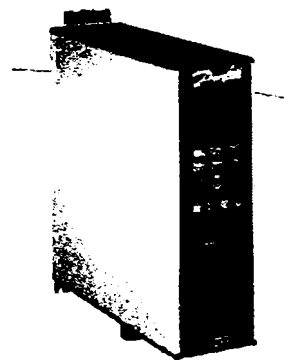


Figure 4.15. Danfoss VLT 5005

Control principle:

A frequency converter rectifies AC voltage from mains into DC voltage, after which this DC voltage is converted into a AC current with a variable amplitude and frequency.

The motor is thus supplied with variable voltage and frequency, which enables infinitely variable speed control of three-phased, standard AC motors.

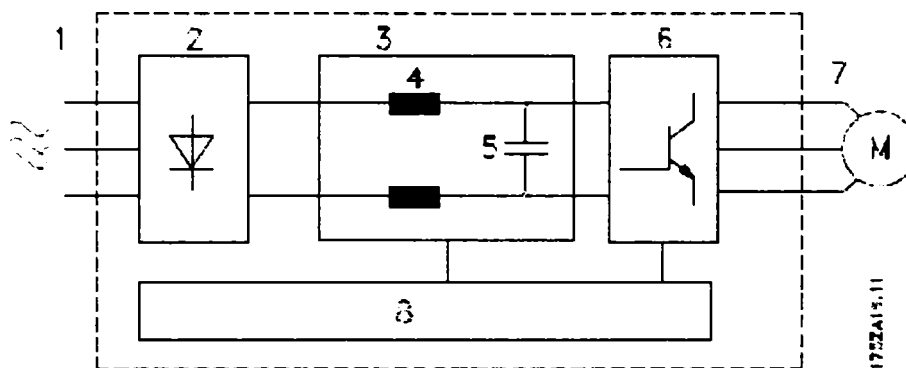


Figure 4.16 Danfoss principle

1. Mains voltage: 3 x 200 - 240 V AC, 50 / 60 Hz.
3 x 380 - 500 V AC, 50 / 60 Hz.
3 x 525 - 600 V AC, 50 / 60 Hz.
2. Rectifier: A three-phase rectifier bridge that rectifies AC current into DC current.
3. Intermediate circuit: DC voltage = 1.35 x mains voltage [V].
4. Intermediate circuit coils: Smooth the intermediate circuit current and limit the load on mains and components (mains transformer, wires, fuses and contactors).
5. Intermediate circuit capacitors: Smooth the intermediate circuit voltage.
6. Inverter: Converts DC voltage into variable AC voltage with a variable frequency.
7. Motor voltage: Variable AC voltage, 0-100% of mains supply voltage.
Variable frequency: 0.5-132/0.5-1000 Hz.

8. Control card: This is where to find the computer that controls the inverter which generates the pulse pattern by which the DC voltage is converted into variable AC voltage with a variable frequency.

The interior permanent magnets synchronous machine:

Type	ASKAWA SSR1-42P2AFNL
Number of poles pair	3
Rated power	2.2 kW
Rated speed	1750 rpm
Rated frequency	87.5 Hz
Rated torque	12 Nm
Rated phase to phase voltage	380 V (rms)
Rated phase current	4.1 A (rms)
Stator resistance per phase (R_s)	3.3
d-axis inductance (L_d)	41.59 mH
q-axis inductance (L_q)	57.06 mH
Rotor permanent-magnet flux (λ_{PM})	0.4832 Vs rad ⁻¹
Inertia of the rotating system (J)	10.07x10 ⁻³ kg m ²
Viscous friction coefficient (B)	20.44x10 ⁻⁴ Nm s rad ⁻¹

4.5. Sample results

After the setup and the implementation was done, a series of tests were set to validate the control system mostly for dynamic performance and very low speeds.

To check the lowest speed limit, operation at 120% load and 1 rpm has been tested with results in Figure 4.17. The torque pulsations are there but they are reasonable. The measured rotor position (Figure 4.17) is closed to the estimated one.

To see the current shape (if it goes perfectly sinusoidal), tests were done at 3 rpm (with lower load) => the shapes of the currents and fluxes looks much better than at 1 rpm. (Figure 4.18)

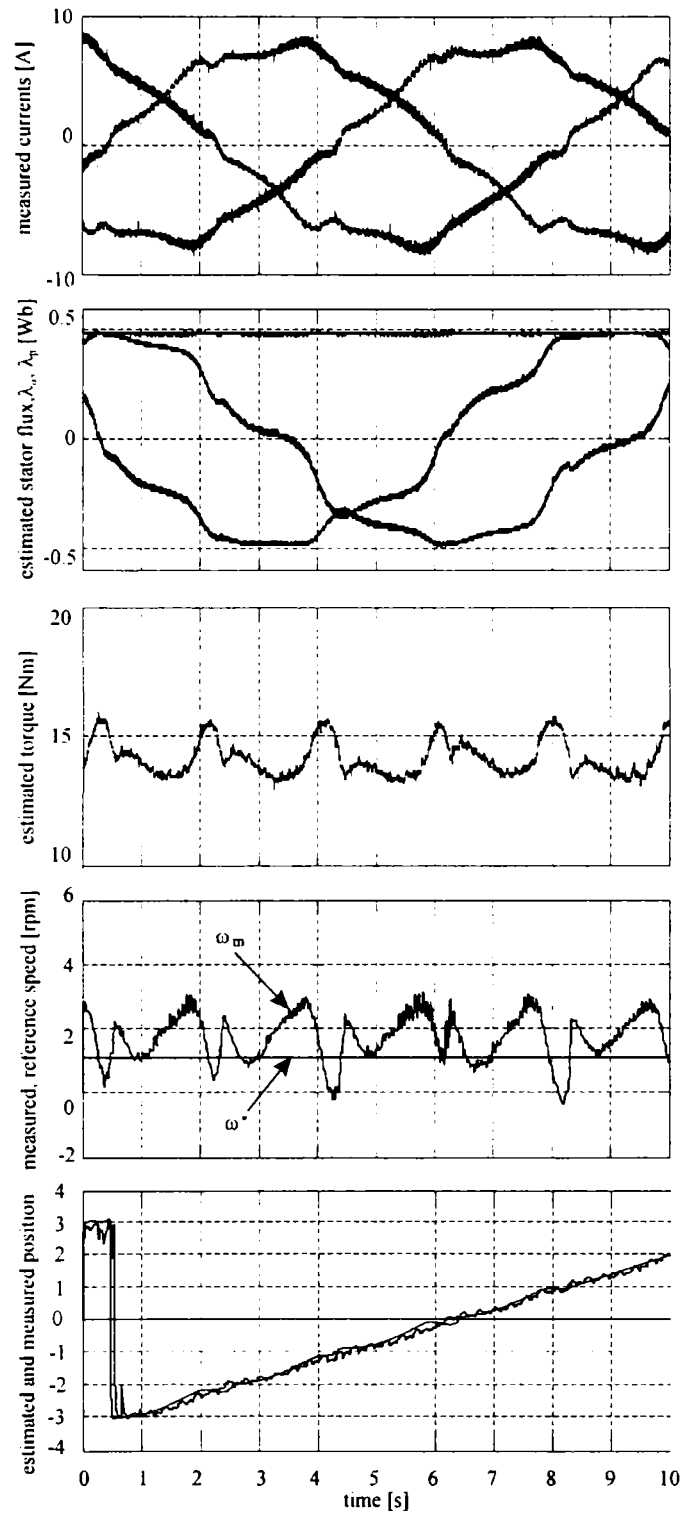


Figure 4.17. 1 rpm at 120 % of nominal torque: measured currents, estimated flux and its components (λ_s , λ_α , λ_β), estimated torque, measured and reference speed, estimated and measured position

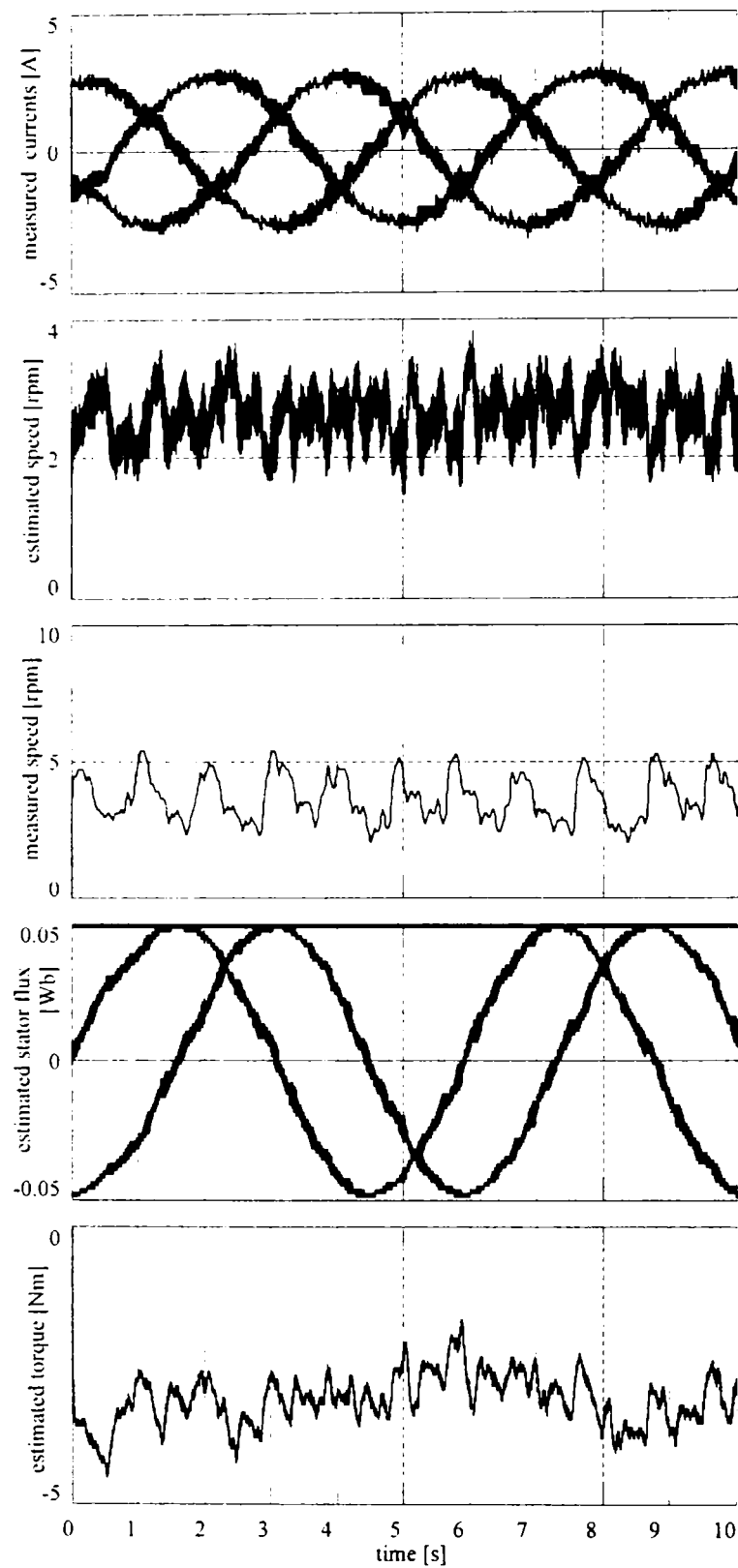


Figure 4.18. 3 rpm at no load: measured currents, reference and measured speed, estimated flux and its components (λ_s , λ_α , λ_β), estimated torque.

A speed reversal of ± 5 rpm on no-load was then investigated experimentally with quite good results (Figure 4.19). The estimated speed is smooth, but the measured one has notable pulsations as in Figure 4.19.

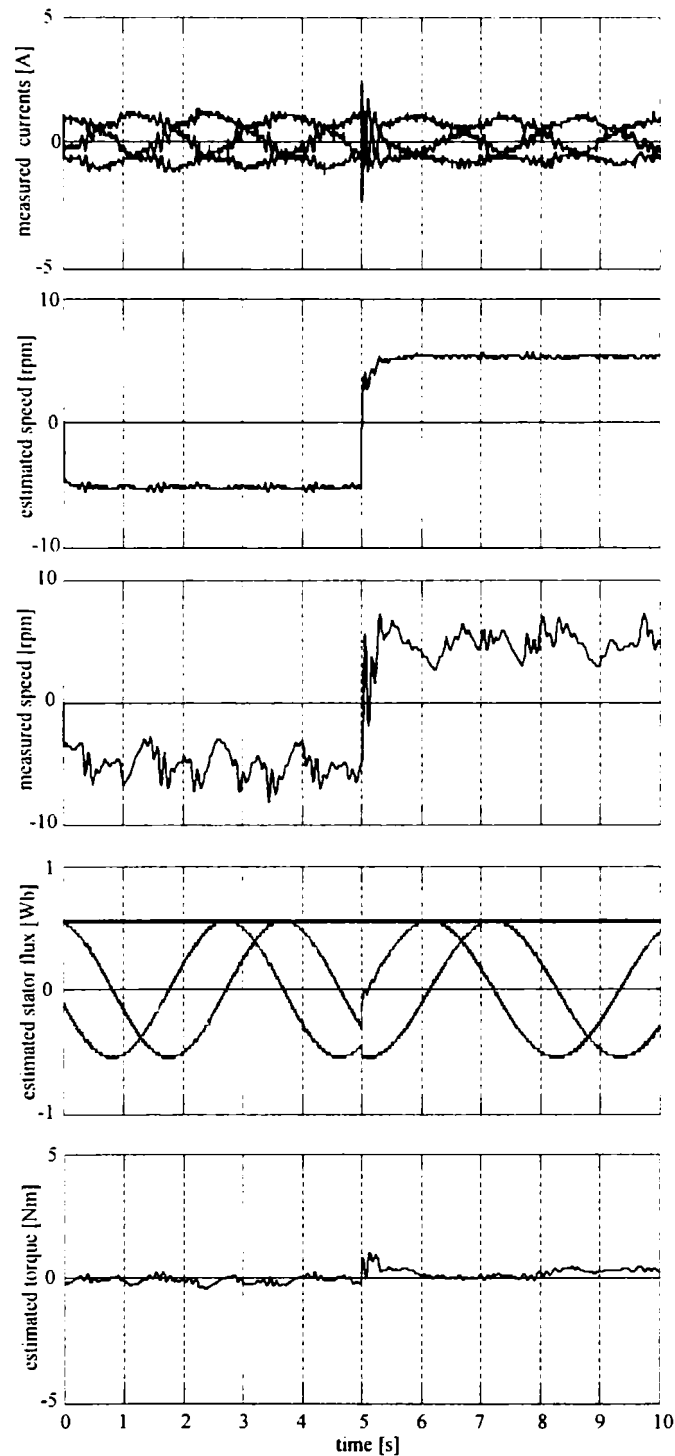


Figure 4.19. No-load speed reversal at ± 5 rpm: measured currents, estimated speed, measured speed, estimated stator flux and its components (λ_s , λ_α , λ_β), and estimated torque

Acceleration transients to 1750 rpm on no-load are shown in Figure 4.20. The torque goes back to almost zero, with reasonable ripple, while the estimated flux hodograph comes very close to a circle, as it should be (flux weakening has not been reached).

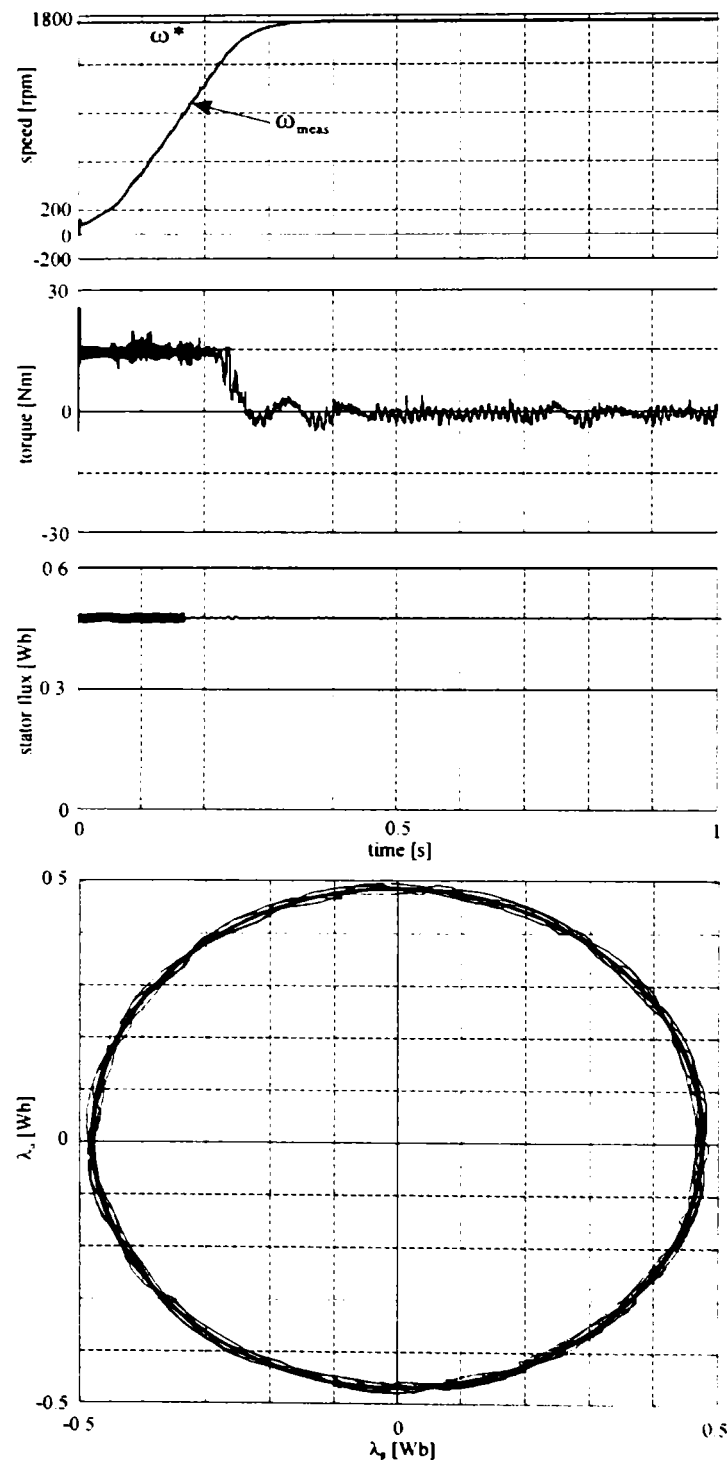


Figure 4.20. Start-up response from 0 to 1750 rpm: reference and measured speed, estimated torque, estimated stator flux, λ_α versus λ_β hodograph

Fast torque loading (from generating to motoring) at 1750 rpm is demonstrated in Figure 4.21, where swift speed recovery occurs, with small undershooting.

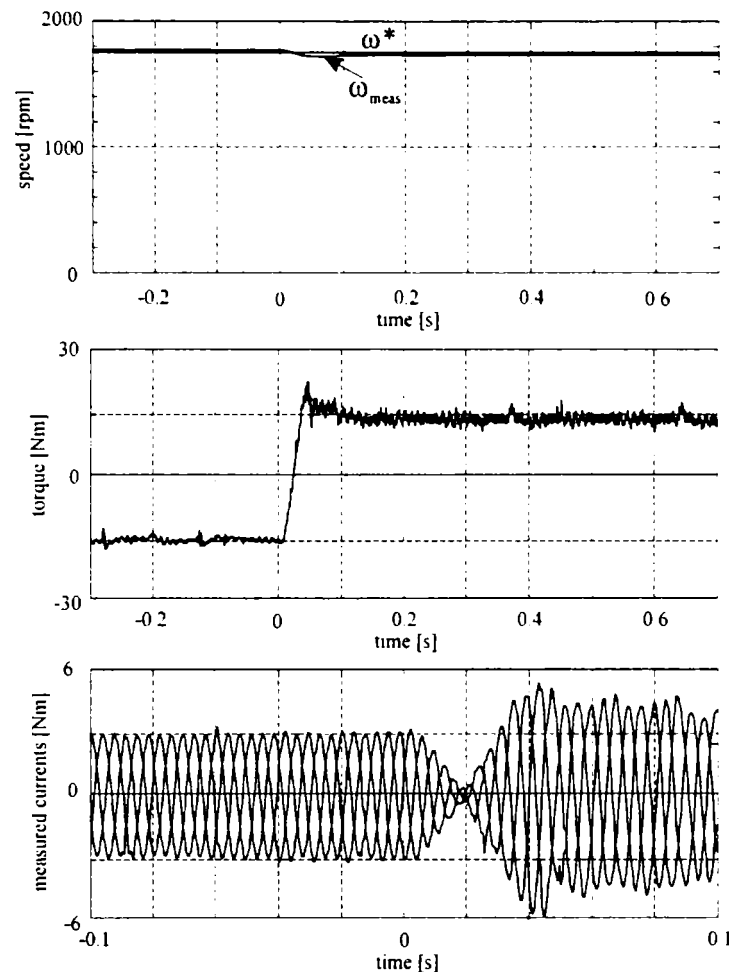


Figure 4.21. Torque transient response (from -15 to 15 Nm) at nominal speed: measured and reference speed, estimated torque and measured currents

4.6. Conclusion

The present chapter results warrant remarks such as:

- DTFC with SVM for IPMSM is shown capable of 1750 rpm to 1 rpm speed range full loaded in motion-sensorless implementation with signal injection used for rotor position estimation up to 30 rpm only.
- Fast torque response has been demonstrated both in motoring and generating mode.

- The compensation of SVM dead time and other inverter nonlinearities lead, also for DTFC (as they do for vector control) to smooth current ripple with reasonable torque ripple especially at very low speed.

4.7. References:

- [1] S.Bolognani, M.Ziglotto, M.Zordan, "Rotor position detection for sensorless pm synchronous motor drives"
- [2] P.B.Schmidt, M.L.Gaspary, G.Ray, and A.H.Wijenayake "Initial Rotor angle detection of a Non-salient Pole Permanent Magnet Synchronous Machine", Proc IEEE IAS Annual Meeting, Vol 1,1997 pp 459-463.
- [3] S.Nakashima, Y.Ianaki, I.Miki, "Sensorless initial rotor position estimation of surface permanent magnet synchronous motor ", IEEE Trans on Ind Appl. vol.36, no.6, Nov.2000, pp1598-1603.
- [4] K.Tanaka, T.Yuzawa, R.Moriyama, I.Miki, " Initial rotor position estimation for surface magnet synchronous motor", Proc. IEEE IAS Annual Meeting, Chicago, Illinois, Sept-Oct. 2001, pp. 2592-2597.
- [5] T.Takeshita, N.Matsui, "Sensorless control and initial position estimation of salient-pole brushless DC motor", Proc.Adv.Motion Control Workshop, 1996 ,pp 18-23.
- [6] M.Schroedl "Sensorless control of ac machine at low speed and standstill based on the "INFORM" method " Proc. IEEE IAS Annual Meeting, October 6-10 1996 Pp. 270-277.
- [7] Jung-Ik Ha, Kozo Ide, Toshihiro Sawa, and Seung-Ki Sul, "Sensorless Position Control and Initial Position Estimation of an Interior Permanent Magnet Motor",Proc. IEEE IAS 2001
- [8] Y.Jeong, R.D. Lorenz, T.M. Jahns, „Initial rotor position estimation of a Interior Permanent Magnet Synchronous Machine using Carrier-Frequency Injection Methods”
- [9] H.Kim, K-K.Huh, R.D.Lorenz, T.M.Jahns, „A novel Method of Initial Rotor Position Estimation for IPM Synchronous drives”
- [10] H.Kim, K-K.Huh, J.Wai, R.D.Lorenz, T.M.Jahns, „Initial Rotor Position Estimation for Integrated Starter Alternator IPM Synchronous Machine”

- [11] L.A.Ribeiro, M.W.Degner, F.Briz, R.D.Lorenz, „Using Carrier Frequency Current Injection for Estimation of Flux, Position and Velocity in AC drives”
- [12] F.Briz, M.W.Degner, J.M.Guerrero, A.Zamarron, R.D.Lorenz, „Implementation Issues Affecting the Performance of Carrier Signal Injection Based Sensorless Controlled AC drives”
- [13] L.Wang, R.D.Lorenz, „Rotor Estimation for PMSM using Saliency Tracking Self Sensing Method”
- [14] N.Patel, T.O'Meara, J.Nagashima, R.D.Lorenz, „Encoderless IPM Traction drive for EV/HEV's”
- [15] Shinji Shinaka, “ New “Mirror-Phase Vector Control” for Sensorless Drive of Permanent Magnet Synchronous Motor With Pole Saliency”. IEEE Trans on Industry Applications, Vol. 40, NO.2, March/April 2004.
- [16] Matthew J.Corley and Robert Lorenz “Rotor position and velocity estimation for a salient-pole permanent magnet synchronous machine at standstill and high speeds” IEEE IAS, Annual Meeting, San Diego, CA, October 6-10, 1996.
- [17] Ryoji Mizutani, Takaharu Takeshita, N.Matsui “Current model-based sensorless drives of salient-pole PMSM at low speed and standstill”, IEE IAS, vol .34, NO.4, July/August 1998.
- [18] Abdelkrim Benchaib, Jean-Claude Alacoque , Serge Poullain and Jean-Luc Thomas “Initial Rotor Position Detection of Permanent-Magnet Synchronous Motor”.
- [19] Fernando Briz, Michael W. Degner, Pablo Garcia, R.D. Lorenz, “Comparison of Saliency-Based Sensorless Control Techniques for AC Machines”,IEEE IAS Annual Meeting, Salt Lake City, October 13-17, 2003
- [20] Y. Jeong, R.D. Lorenz ,T.M. Jahns S. Sul,” Initial Rotor Position Estimation of an Interior Permanent Magnet Synchronous Machine Using Carrier-Frequency Injection Methods”,IEEE 2003
- [21] Hyunbae Kim, Kum-Kang Huh, Michael Harke,Jackson Wai, Robert D. Lorenz and Thomas M. Jahns, “Initial Rotor Position Estimation for an Integrated Starter Alternator IPM Synchronous Machine
- [22] H.Kim, K.K Huh, R.D. Lorenz, T.M Jahns, “A Novel Method for Initial Rotor Position Estimation for IPM Synchronous Machine Drives” ,Research –report 2003

- [23] N. Patel, T. O'Meara, J. Nagashima, R.D. Lorenz, " Encoderless IPM Traction Drive for EV/HEV's IEEE Industry Applications Society Annual Meeting, Chicago, September 30-October 4, 2001
- [24] Hyunbae Kim, M.C. Harke, and R.D. Lorenz," Sensorless Control of Interior Permanent Magnet Machine Drives with Zero-Phase-Lag Position Estimation", In Proc. of IEEE IAS Annual Meeting, Pittsburgh, Oct 11-19, 2002

DTFC – SVM motion – sensorless control of PM–RSM

5.1. Introduction

The integrated starter-alternators (ISA) topic represents a hot subject for internal combustion engines (ICE) and hybrid electric vehicles (HEV). Typical specifications for ISAs depend on the degree of vehicle electrification (% E) [1]:

$$\%E = \frac{\text{peak electric power} \times 100}{\text{peak electric power} + \text{peak ICE power}} \quad (1)$$

$\%E$ varies from less than 10% in conventional ICE vehicles to 10-25% in mild hybrid vehicles, 25-50% in full parallel hybrid vehicles, and 100% in series hybrid and fully electric vehicles. In all cases a wide constant power-speed range (from 4:1 to 12:1) is beneficial. From this point of view, corroborated with low inverter kVA and low total system losses, the permanent magnet reluctance synchronous motor (PM-RSM) seems to be one of the best [2], together with the electrically dc-excited claw-pole [3], or standard rotor synchronous machines [4]. Quite a few research teams have recently investigated in depth the design, performance [5-8] and vector-control [5] of PM-RSM.

Sensorless vector-control for internal permanent magnet synchronous motors (IPMSM) [9-11] close to PM-RSM [5] has been presented with rather comprehensive solutions containing initial position estimation for non-hesitant starting via signal injection methods. As the PM-RSM has notable saliency that is strongly influenced by magnetic saturation, the vector-control has to account for it explicitly both in the stator flux observers and in the control itself (in sensorless operation), especially as speed increases above the base speed and the stator flux is weakened due to battery dc voltage limitation.

Sensorless direct torque and flux control with space vector modulation (DTFC-SVM) for induction machines has been successfully proven, from very low speed with robust dynamics, in a sliding-mode approach [12]. It has been applied also to reluctance synchronous motors [13]. The direct torque control (DTC) for PMSM has been reported

recently [14], but not in the motion-sensorless SVM implementation, and not for ISA where the specifications are much tougher than for industrial drives.

The present paper develops a complete solution for sensorless DTFC-SVM of PM-RSM drive for integrated starter-alternator in mild hybrid electric vehicles, from zero speed to wide speed range for motor/ generator control. A stator flux reference with a quasi-optimal flux versus torque functional is proposed. Stator flux observers in wide speed range employing combined voltage-current models for low speed and only the voltage model for medium-high speed in PI closed loops, are developed. A novel rotor speed and position observer with fusion strategy employs signal injection and only one D-module vector filter in stator reference - for low speed, corroborated with a speed observer from the stator flux vector estimation - for medium-high speed. The effectiveness of this solution has been confirmed by extensive experimental test results in wide speed range including artificial loading.

5.2. Typical ISA (integrated starter – alternator) specifications

The ISA has to perform (at most):

1) Motoring: for vehicle self-starting (in torque control mode) and for auxiliaries driving during ICE shut-off (in speed control mode).

2) Generating: for vehicle regenerative braking and for battery recharge during exclusive ICE running. In essence, for both motoring and generating regime, the electromagnetic torque (T_e) versus speed (positive or negative) envelopes are given in Figure 5.1.

These envelopes have to be tempered further by the battery state of charge (accessibility) both in motoring and generating. The division of torque between ICE and PM-RSM may also be decided by the optimum gas-mileage or lowest pollution criteria for the ICE.

Further on, we will just retain the fact that: 1) the torque closed-loop control is mandatory, and 2) an external power control-loop may be required for generating. As the battery power flow can be easily measured ($V_{dc} I_{dc}$), this fact seems to be a good way to go.

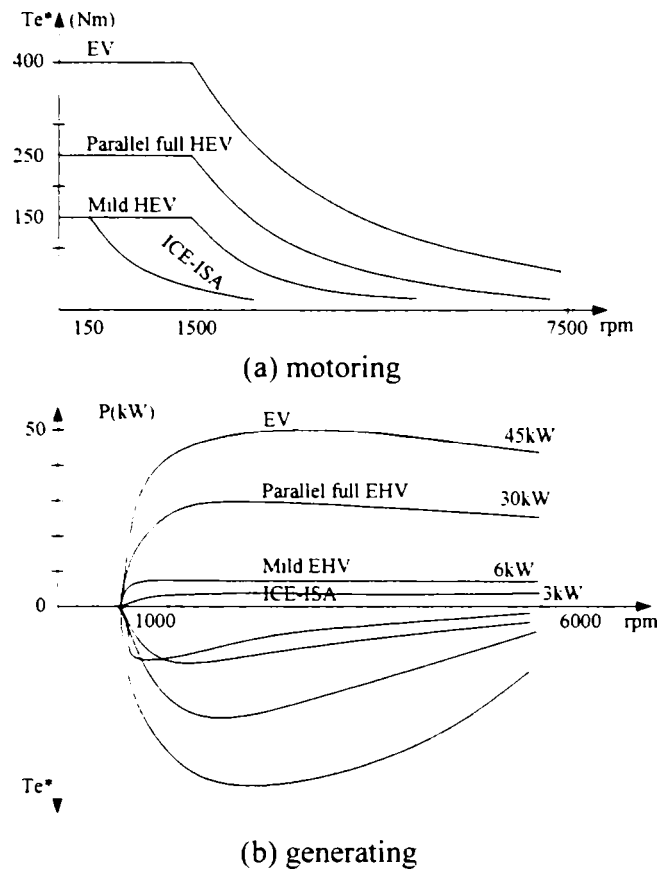


Figure 5.1. Typical integrated starter-alternator requirements: a) electric torque (T_e) versus speed at crankshaft for motoring, and b) electric power (P) versus speed for generating, with various degrees of vehicle electrification.

5.3. Flux reference

In what follows, the PM RSM is presented, with the novel stator flux referencer for the starter-alternator applications (for better performances in a high speed range).

A. PM-RSM Model

The PM-RSM is a rather good saliency interior PM rotor synchronous machine (Figure 5.2) [7]. The rotor contains a multiple flux barrier structure with PMs placed on the bottom of flux barriers. The PM flux (Ψ_{PMq}) produces a limited electromotive force (emf), of 150-200% at highest speed, to limit the inverter switches voltage rating (and costs). The PMs are placed in the q -axis, while the d -axis shows higher magnetic permeance ($L_d > L_q$).

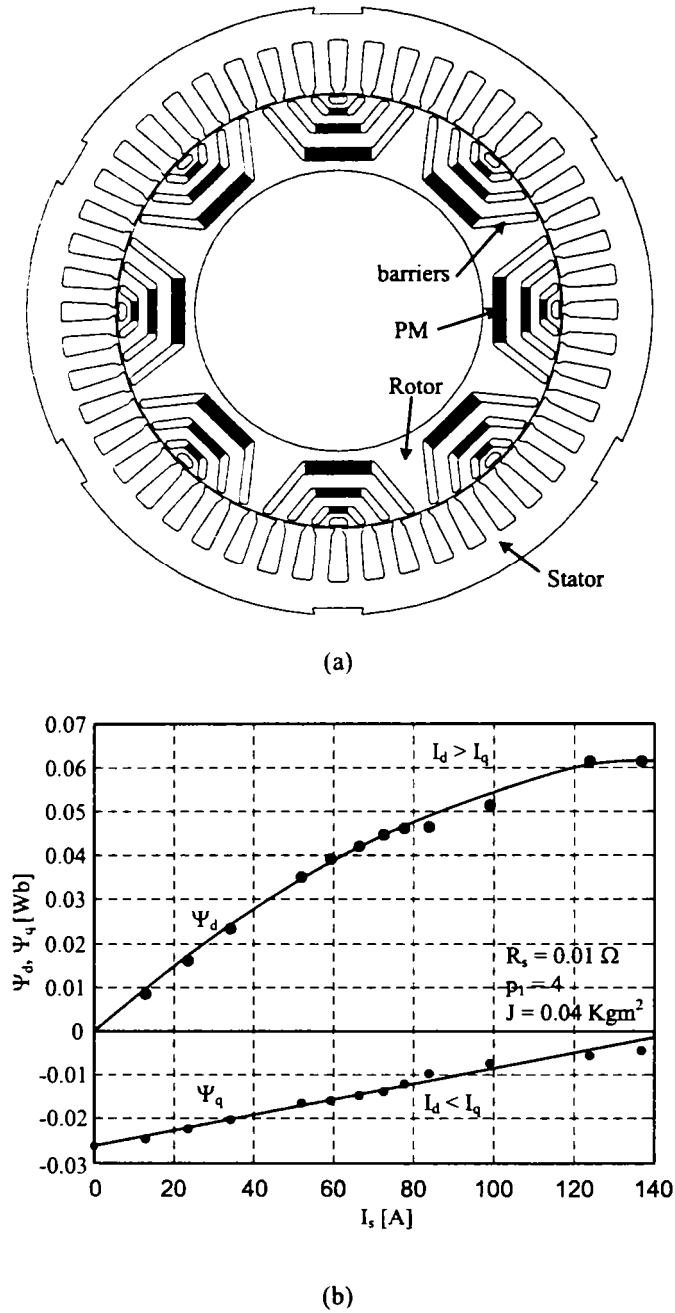


Figure 5.2. (a) Permanent magnet reluctance synchronous motor cross section; (b) Measured magnetization curves $\Psi_d(I_s)$, $\Psi_q(I_s)$ [Wb], I_s [A].

The PM-RSM model in dq -rotor reference, considering the emf and inductances that vary sinusoidally with the rotor position, is given by:

$$\begin{aligned} \frac{d\underline{\Psi}_s}{dt} &= -j\omega_r \underline{\Psi}_s - \underline{I}_s R_s + \underline{V}_s \\ \underline{\Psi}_s &= L_d \underline{I}_d + j(L_q \underline{I}_q - \Psi_{PMq}) \\ T_e &= 3/2 p_1 [\Psi_{PMq} + (L_d - L_q) \underline{I}_q] \underline{I}_d = 3/2 p_1 \text{Im}(\underline{\Psi}_s^\# \underline{I}_s) \end{aligned} \quad (2)$$

where: $\underline{\Psi}_s$, $\underline{I}_s(I_d, I_q)$ and \underline{V}_s are the stator flux, current and voltage vector, respectively; R_s is the stator resistance; ω_r is the electrical rotor speed; L_d, L_q are the d, q inductances; p_1 is the pole-pair number; and $\#$ means the conjugate vector operator. The magnetic saturation is considered only in the d -axis $L_d(I_d)$, with $L_q = \text{constant}$, and cross-coupling saturation effects are neglected.

B. Flux Reference

In DTFC, the stator flux reference (Ψ_s^*) is coordinated with the torque reference (T_e^*) to produce the required (below maximum) torque for a given speed. The problem is that for a given flux Ψ_s^* and torque T_e^* there are two current pairs (I_d, I_q) that can produce them:

$$\Psi_s = \sqrt{(L_d I_d)^2 + (L_q I_q - \Psi_{PMq})^2}. \quad (3)$$

The torque equation from (2) shows clearly that a specific torque T_e can be obtained with $I_{d1}, I_{d2} > 0$, when $\Psi_q = L_q I_q - \Psi_{PMq} \neq 0$, for a given stator flux Ψ_s . An example is shown in the vector diagram in Figure 5.3, based on the 2nd equation from (2).

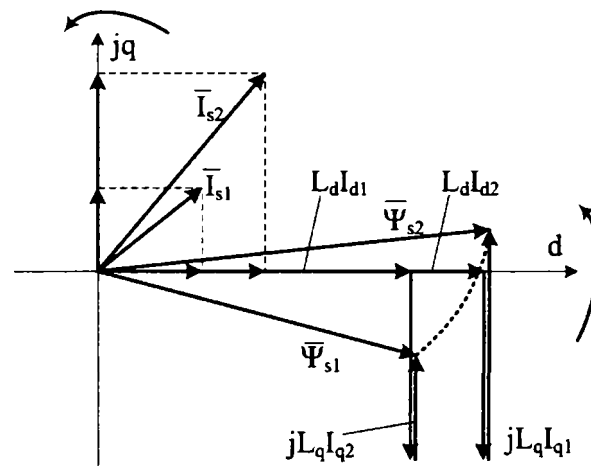


Figure 5.3. Two stator current pairs (I_d, I_q) for a given torque T_e^* and flux Ψ_s^* .

The $\underline{I}_{s1}, \underline{\Psi}_{s1}$ couple is better because the current amplitude is smaller, and also the PM is less stressed ($\Psi_q < 0$). Thus, the control should make sure that the flux vector $\underline{\Psi}_s$ is always in the 4th quadrant for positive torque, or in the 3rd quadrant for negative torque. One possibility to realize this fact in DTFC is to make the reference flux $\Psi_s^* =$

Ψ_{PMq} for zero torque (point 0' in Fig. 4), which guaranties zero stator current ($I_d = I_q = 0$) for zero torque, and then the control starts from there to travel the reference flux Ψ_s^* functional, depending on the reference torque T_e^* (Figure 5.4).

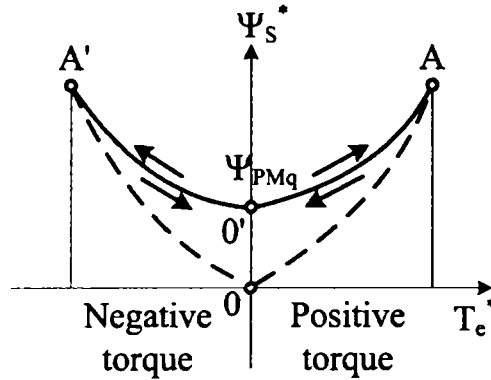


Figure 5.4. Flux-torque functional $\Psi_s^*(T_e^*)$ from zero to base speed for the PM-RSM.

On the other hand, for fast torque response in a machine which works mostly under heavy load and in flux weakening, the control goes to around zero stator flux at zero torque (point 0 in Figure 5.4), when:

$$I_{q\max} = \Psi_{PMq} / L_q. \quad (4)$$

When the maximum torque/ speed envelope is required, $I_{q\max}$ is applied and therefore:

$$T_{e\max}^* = 3/2 p_1 \Psi_d I_{q\max}, \quad \text{and thus } (\Psi_s^*)_{T_{e\max}} = \frac{2T_{e\max}^* L_q}{3 p_1 \Psi_{PMq}}. \quad (5)$$

Also:

$$\begin{aligned} (\Psi_s^*)_{T_{e\max}} &\approx K_{MG} \frac{V_{sb}}{\omega_b} = \Psi_{s0}; & \text{for } \omega_r < \omega_b \\ (\Psi_s^*)_{T_{e\max}} &\approx \Psi_{s0} \frac{\omega_r}{\omega_b}; & \text{for } \omega_r \geq \omega_b \end{aligned} \quad (6)$$

where: K_{MG} is a coefficient in the range of 0.95-0.97 for motoring, and 1.03-1.07 for generating; ω_b is the electrical rotor base speed; V_{sb} is the stator voltage at base speed. In this way, the functional (limiters) $\Psi_{s\max}^*(\omega_r)$ and $T_{e\max}^*(\omega_r)$ are provided for.

Whenever the required torque at a certain speed is smaller than the available (maximum) $T_{e\max}^*(\omega_r)$ value, the control may relax the I_q^* value by maintaining the latter positive:

$$I_q^* = \frac{\Psi_{PMq}^*}{L_q} \sqrt{\frac{|T_c^*|}{|T_{cmax}^*|}}; \quad \Psi_q^* = L_q I_q^* - \Psi_{PMq}^* \quad (7)$$

For a given reference torque T_e^* , the required d -axis flux Ψ_d^* is computed, and then I_d^* from $\Psi_d^*(I_d^*)$ curve. The novel on-line flux reference for the flux versus torque $\Psi_s^*(T_e^*)$ functional, valid for all situations, is introduced in Figure 5.5. This is a quasi-optimal choice.

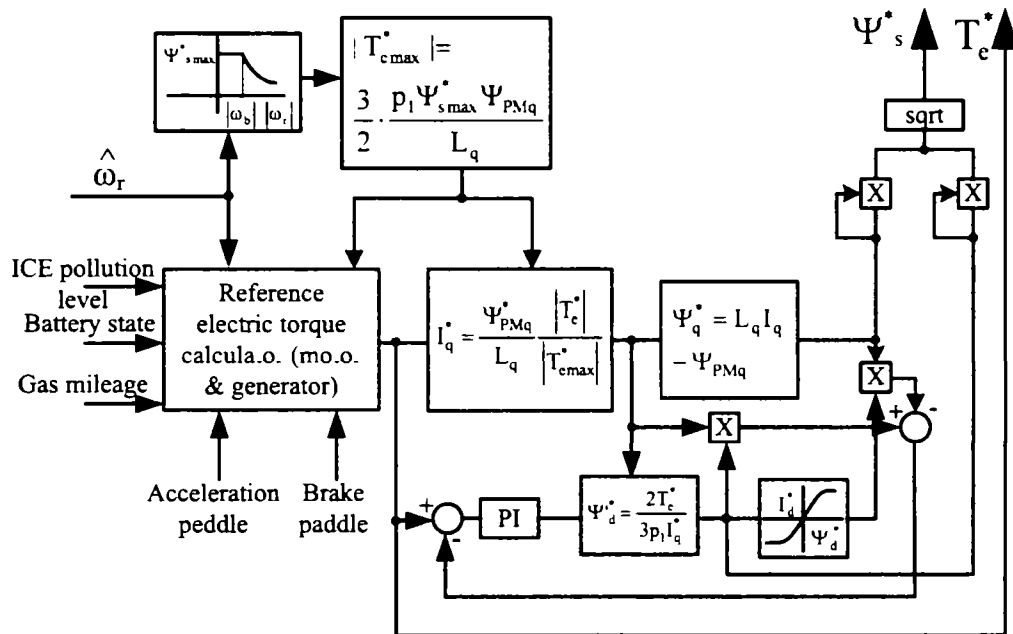


Figure 5.5. PM-RSM stator flux reference for the starter-alternator.

The q -axis inductance L_q does not vary notably with stator current, and therefore the d -axis magnetization curve $\Psi_d(I_d)$ is used, that is very robust. The PI controller introduced in the flux referencer (Figure 5.5) is a very fast one and allows for solving an otherwise involved nonlinear equation. The flux-weakening zone is implicitly covered by the proposed flux referencer.

The reference electric torque calculator from Figure 5.5 reflects the overall HEV control strategy and is not followed up here.

5.4. Sensorless dtfc-svm of pm-rsm: the observers

The comprehensive state observer includes the rotor speed and position observers and the stator flux observer.

A. Stator Flux Observers

For DTFC-SVM, the main estimations are for the stator flux vector $\hat{\underline{\Psi}}_s$ and for the electromagnetic torque \hat{T}_e . The stator flux observers combine voltage-current models (Figure 5.6): the current model, including magnetic saturation, prevails at low speed, while the voltage model prevails at medium-high speed with a smooth transition between them depending on speed. Two flux observers have been used for comparison.

The serial observer (Figure 5.6a) contains the voltage model in stator reference serially connected with the current model in the rotor reference frame, using a PI compensator driven by the current estimation error. Both models are enclosed within the correction loop. The parallel observer (Figure 5.6b) contains the same models but connected in parallel and using the flux estimation error. This time, the PI correction loop encloses only the voltage model, while the current model is open loop operated.

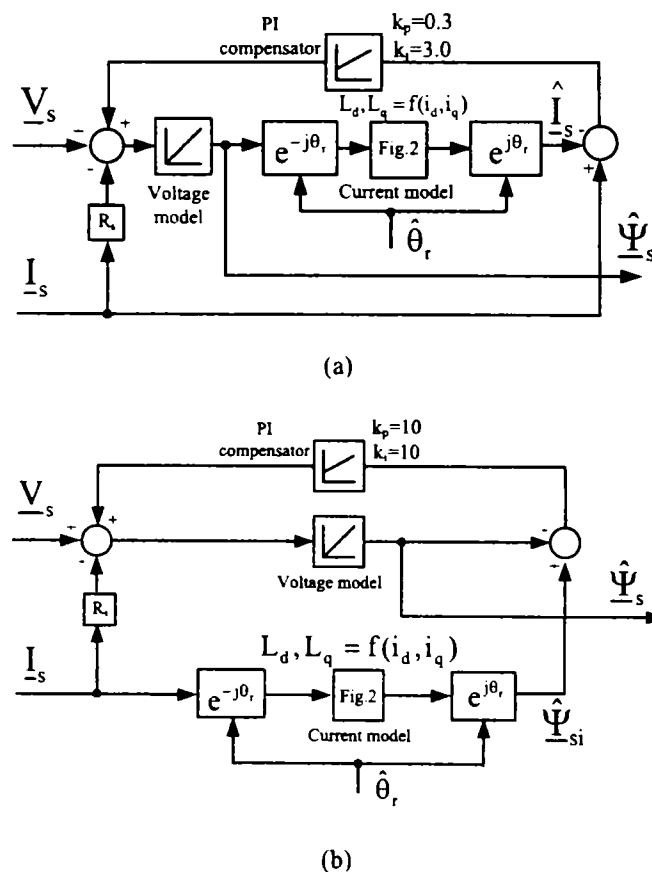


Figure 5.6. Stator flux observers with combined voltage-current models:
(a) serial observer; (b) parallel observer.

With accurate stator flux estimation and measured currents, the torque estimation is simply calculated in $\alpha\beta$ -stator reference as:

$$\hat{T}_c = 3/2 p_1 (\hat{\Psi}_\alpha I_\beta - \hat{\Psi}_\beta I_\alpha). \quad (8)$$

The rotor position estimation $\hat{\theta}_r$ is required in the current model within the flux observer – but only at low speed, below 50rpm, because at medium-high speed the voltage model becomes dominant and the signal injection (which gives $\hat{\theta}_r$) discontinuation does not produce a notable influence on the flux observer. The rotor speed estimation $\hat{\omega}_r$ in the whole speed range is required in the flux (and torque) referencer, and accurately – in the speed controller.

B. Speed and Position Observers with Signal Injection

For low speed operation a speed observer using signal injection has been implemented as shown in Figure 5.7. A rotating carrier-voltage $\underline{V}_c = V_c \exp(j\omega_c t)$ with $V_c = 1V$ and $\omega_c = 500$ Hz is injected in the stator superimposing on top of driving fundamental stator-voltage \underline{V}_s . The resulting stator current \underline{I}_s , modulated by the position dependent inductances with magnetic saliency, contains carrier-current harmonics with rotor position information θ_r . Usually, the negative 1st order sequence carrier harmonic $\underline{I}_{cn1} = I_{cn1} \exp\{j(-\theta_c + 2\theta_r + \pi/2)\}$ with $\theta_c = \omega_c t$ [9] is selected from the measured stator current.

Two schemes have been tested: 1) Observer with synchronous low-pass filter (LPF) in carrier reference (upper part of Figure 5.7a) [10]. 2) Novel observer with vector filter in D-module in stator reference as band-pass filter (BPF) with central frequency ω_c and phase-sign discrimination (lower part of Figure 5.7a). Both observers select the \underline{I}_{cn1} harmonic. A phase-locked loop (PLL) tracking observer shown in Fig. 7b extracts the estimation of rotor speed $\hat{\omega}_r$ and position $\hat{\theta}_r$ from the phase of \underline{I}_{cn1}^c harmonic in carrier reference, with PLL error $\sigma \sim 2I_{cn1}(\theta_r - \hat{\theta}_r)$. During the experiments it was noticed that both observers in Figure 5.7a have similar behavior, with very robust estimation, almost independent of machine parameters.

The initial rotor position $\hat{\theta}_{r0}$ is correctly identified at standstill by both observers in the range of $(-\pi/2, \pi/2)$ radians. For full angle range, an uncertainty of π radians appears, and this is discriminated by the magnet polarity detection using the 2nd order harmonics [9-10].

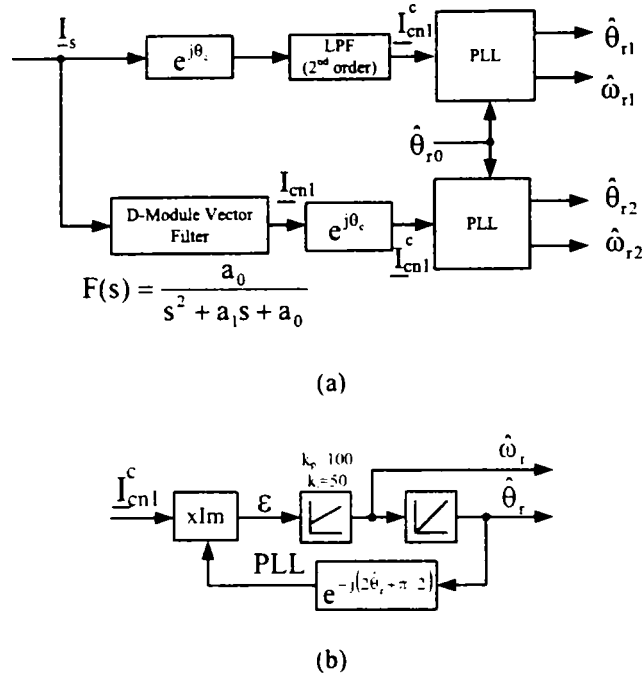


Figure 5.7. Speed and position observers with signal injection: (a) Observers with synchronous low-pass filter and with vector filter in D-module; (b) PLL used in (a).

C. Speed Estimation from Stator Flux

For medium-high speed operation, above 50 rpm, the signal injection is disabled to reduce losses, and thus the associated speed and position observer from Figure 5.7 is also inhibited. Now, additional speed estimation is required, with a smooth transition between the two of them. The proposed solution estimates the rotor speed $\hat{\omega}_r$ from the estimated stator flux vector $\hat{\underline{\psi}}_s$:

$$\hat{\omega}_r = \hat{\omega}_{\psi_s} + \frac{d\hat{\theta}_{\psi_{dq}}}{dt}; \quad \hat{\omega}_{\psi_s} = \frac{d\hat{\theta}_{\psi_s}}{dt} \quad (9)$$

where $\hat{\omega}_{\psi_s}$ and $\hat{\theta}_{\psi_s}$ are the estimated speed and position of $\hat{\underline{\psi}}_s$ in $\alpha\beta$ -stator reference, which is given by the stator flux observer in Figure 5.6; $\hat{\theta}_{\psi_{dq}}$ is the estimated position of $\hat{\underline{\psi}}_s$ in dq -rotor reference (Figure 5.3).

The 1st main component of the rotor speed in (9), i.e., $\hat{\omega}_{\psi_s}$ is extracted together with $\hat{\theta}_{\psi_s}$ from the $\hat{\underline{\psi}}_s$ phase by a PLL observer similarly as in Figure 5.7b. The 2nd component, living only in transient regimes, is obtained from the electric torque expression that can be derived as:

$$\hat{T}_e = \frac{3}{2} p_1 \frac{\hat{\Psi}_s \Psi_{PMq}}{L_q} \cos \hat{\theta}_{\psi,dq} + \frac{3}{2} p_1 \frac{\hat{\Psi}_s^2}{2} \left(\frac{1}{L_q} - \frac{1}{L_d} \right) \sin 2\hat{\theta}_{\psi,dq}. \quad (10)$$

The angle $\hat{\theta}_{\psi,dq}(\hat{T}_e, \hat{\Psi}_s)$ is extracted from a look-up table with linear interpolation based on (10) using \hat{T}_e (8) and $\hat{\Psi}_s$ from Fig. 6, with an average value for L_d , because magnetic saturation is not so important. Then $d\hat{\theta}_{\psi,dq}/dt$ is calculated to finally decide $\hat{\omega}_r$ in (9).

Note: As the torque and flux response of the machine is faster than the speed response in automotive applications, the angle $\hat{\theta}_{\psi,dq}$ may alternatively be calculated as:

$$\sin \hat{\theta}_{\psi,dq} = \hat{\Psi}_q^* / \hat{\Psi}_s^*; \quad \cos \hat{\theta}_{\psi,dq} = \hat{\Psi}_d^* / \hat{\Psi}_s^* \quad (11)$$

from the flux referencer in Figure 5.5, provided that the flux and torque references do not experience step variations, or some filtering is applied.

D. DTFC-SVM Motion-Sensorless Control System

Now that the proposed flux/torque referencers and the comprehensive state observers have been introduced, the proposed sensorless DTFC-SVM system for PM-RSM is illustrated in Figure 5.8 with the main components discussed above.

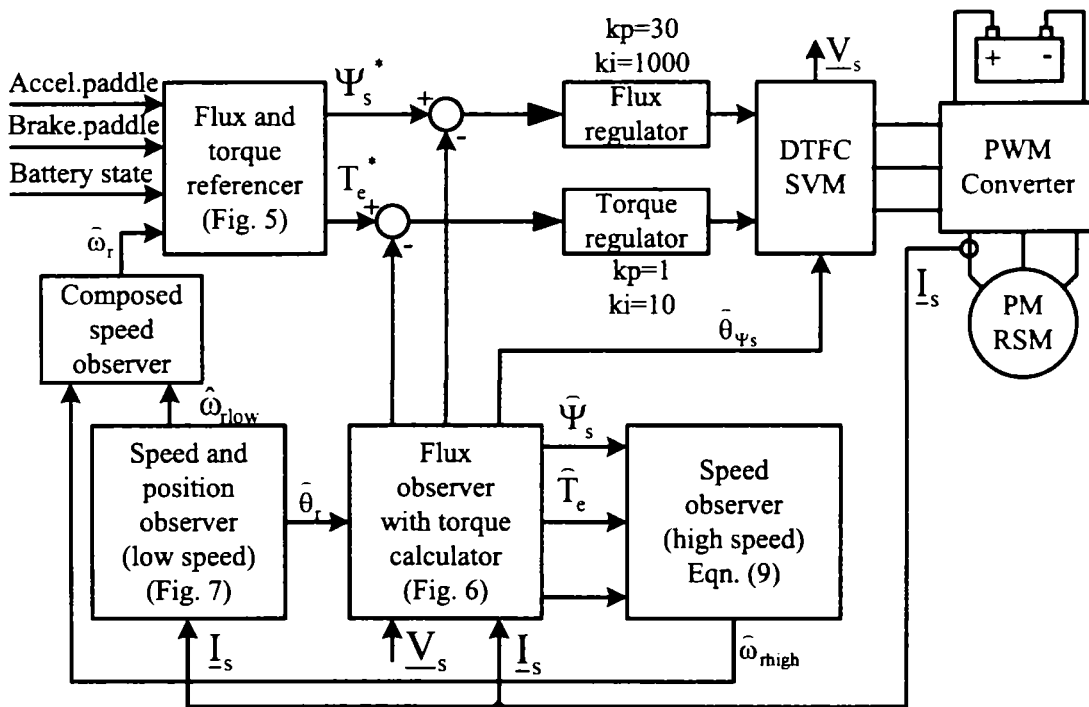
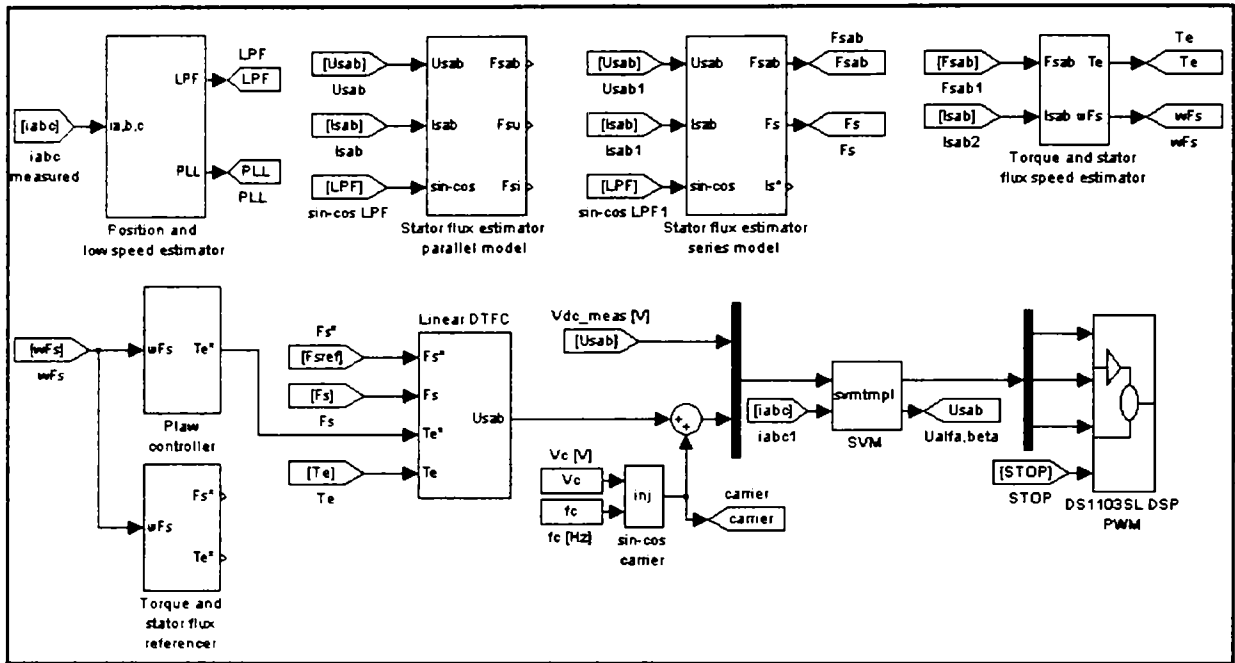
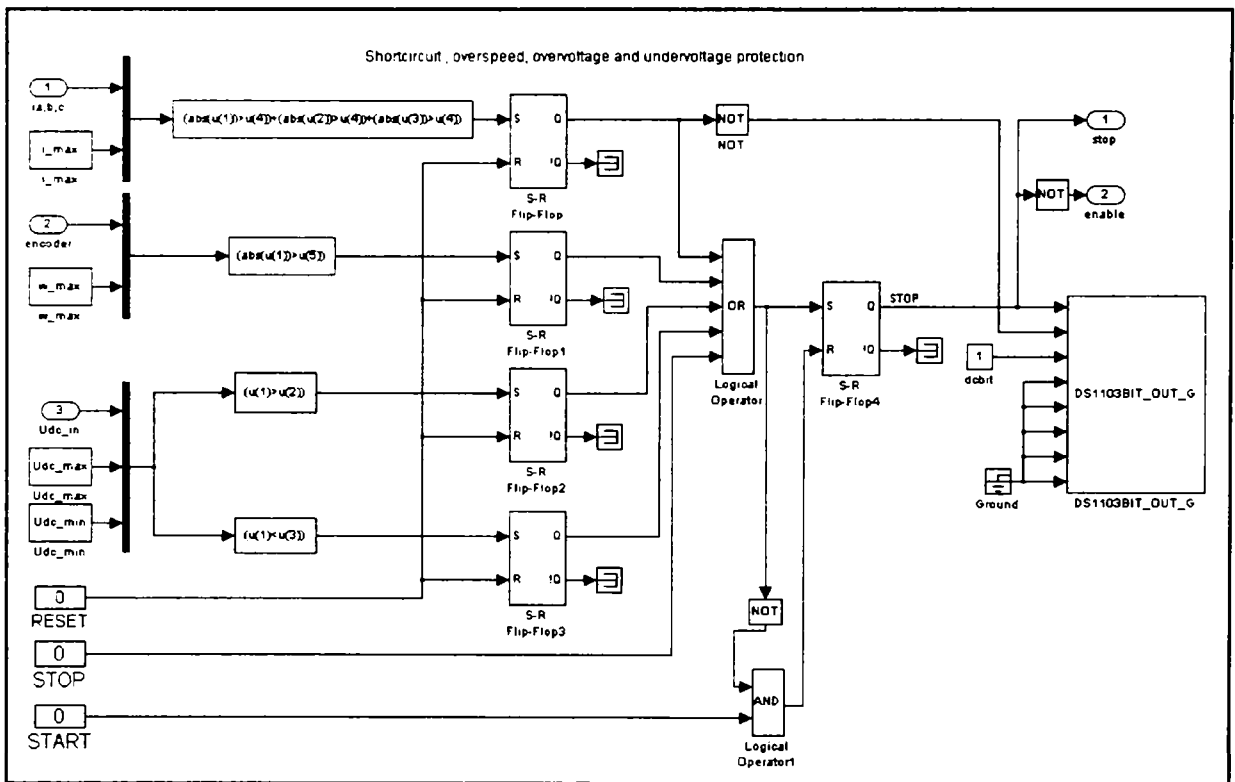


Figure 5.8. DTFC-SVM motion-sensorless control of PM-RSM.



(a)



(b)

Figure 5.9. a) DSpace implementation of the Simulink model, b) the shortcircuit, overspeed, overvoltage and undervoltage protection

Two solutions were tried (Figure 5.9): one with a PI anti-windup (Figure 5.10) controller as torque reference and the second one with the torque and flux referencer described above.

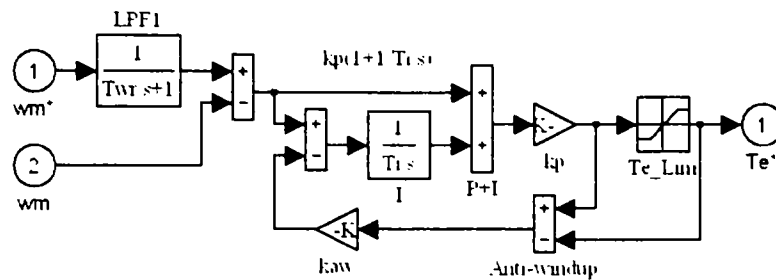


Figure 5.10. PI antiwindup controller

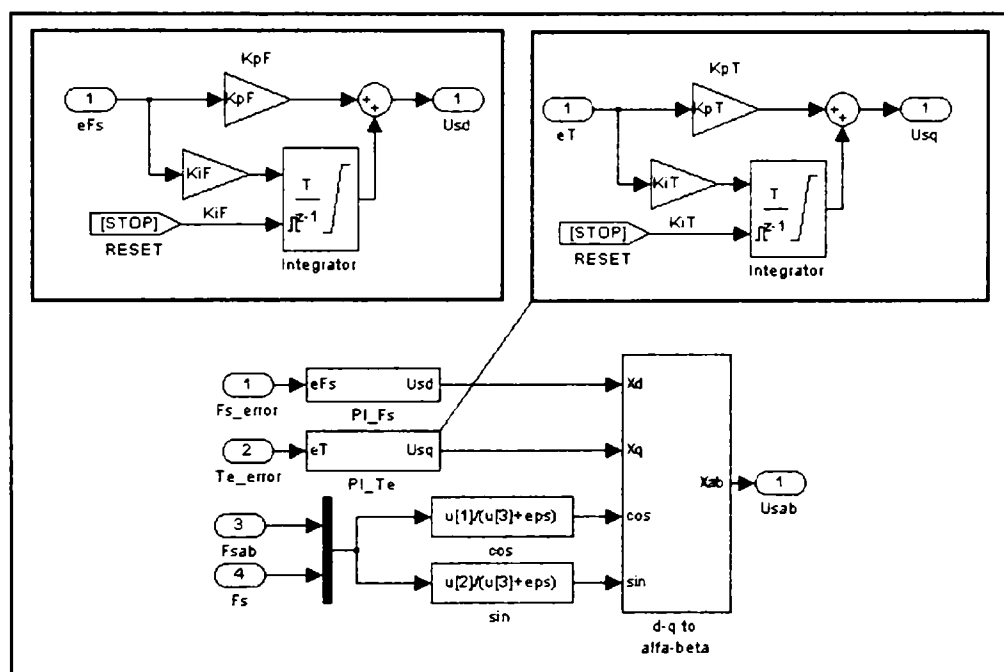


Figure 5.11. The PI flux and torque regulators for DTFC

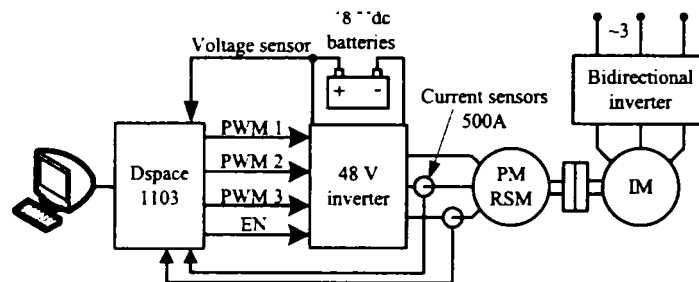
$$\begin{aligned} u_{sd}^* &= K_{pF} + K_{iF} \frac{1}{s} \\ u_{sq}^* &= K_{pT} + K_{iT} \frac{1}{s} \end{aligned} \quad (12)$$

Only the PI flux and torque regulators of DTFC-SVM have not been detailed so far. Their design is presented in Figure 5.11 and in (12), where K_{iF} , K_{iT} , K_{pF} , K_{pT} are the controllers gains [12].

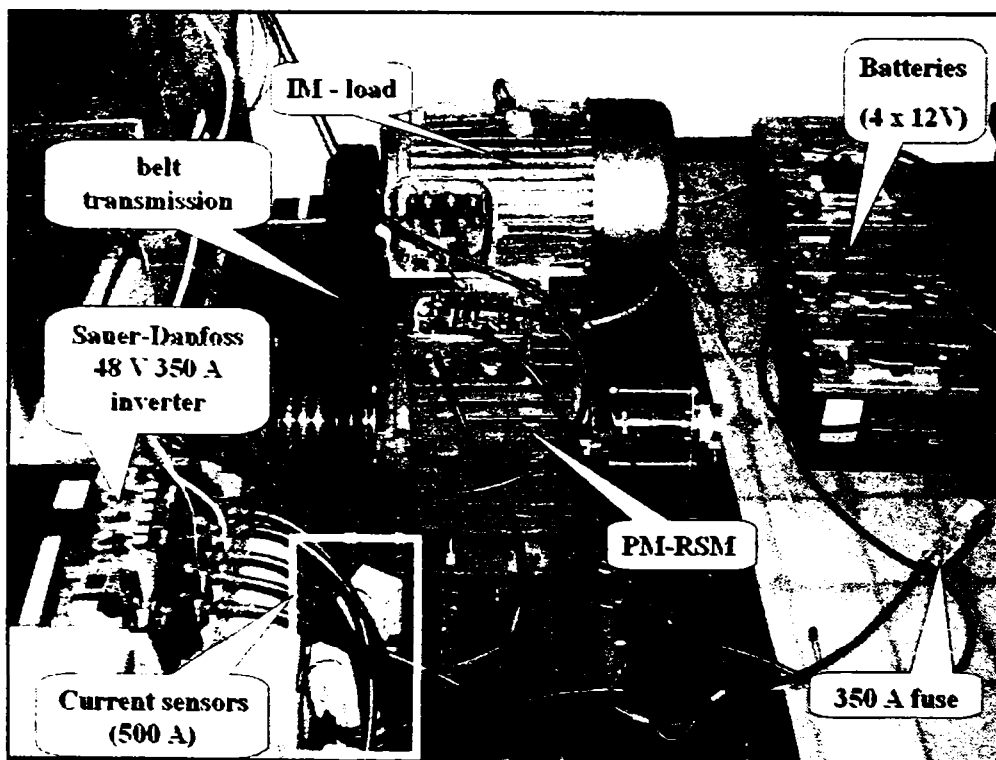
In what follows, the digital implementation and the experimental results with the proposed DTFC-SVM system will be tackled directly.

5.5. EXPERIMENTAL SETUP

The experimental setup for the sensorless DTFC-SVM of PM-RSM (Figure 5.12) contains a belt transmission 10/13 kW (1500/3000 rpm) with an induction motor driven by an ABB ACS600 bidirectional inverter. The 140 Nm peak torque PM-RSM is fed through a 48Vdc, 350A inverter from 48V, 55Ah battery pack. The simulations have been managed in MATLAB[®]/Simulink, and implemented on a dSpace DS 1103 control board (Figure 5.13).



(a)



(b)

Figure 5.12. Experimental setup for sensorless DTFC-SVM of PM-RSM:
a) the scheme; b) the real setup containing the PM-RSM, the load machine, the belt-transmission, the batteries and the Sauer-Danfoss inverter.

5.5.1. dSpace DS 1103

The DS1103 PPC is a very flexible and powerful system featuring both high computational capability and comprehensive I/O periphery. Additionally, it features a software SIMULINK interface that allows all applications to be developed in the MATLAB[®]/Simulink friendly environment. All compiling and downloading processes are carried out automatically in the background. An experimenting software called Control Desk, allows real-time management of the running process by providing a virtual control panel with instruments and scopes (Figure 5.13).

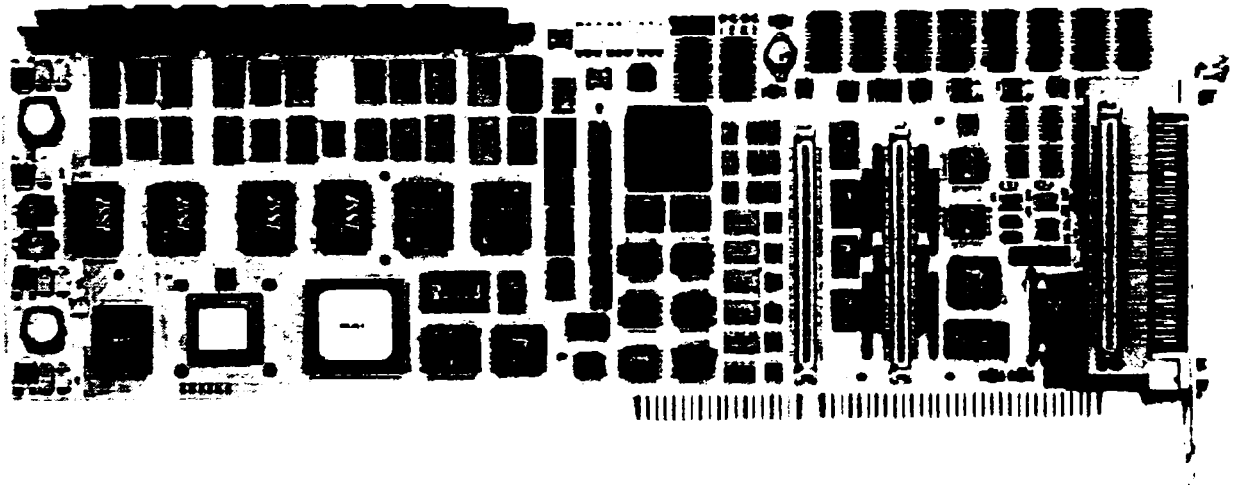


Figure 5.13. The single board control system dSpace DS 1103

The DS1103 is a single board system based on the Motorola PowerPC 604e/333MHz processor (PPC), which forms the main processing unit.

The DSP subsystem, based on the Texas Instruments TMS320F240 DSP fixed-point processor, is especially designed for the control of electric drives. Among other I/O capabilities, the DSP provides 3-phase PWM generation making the subsystem useful for drive applications.

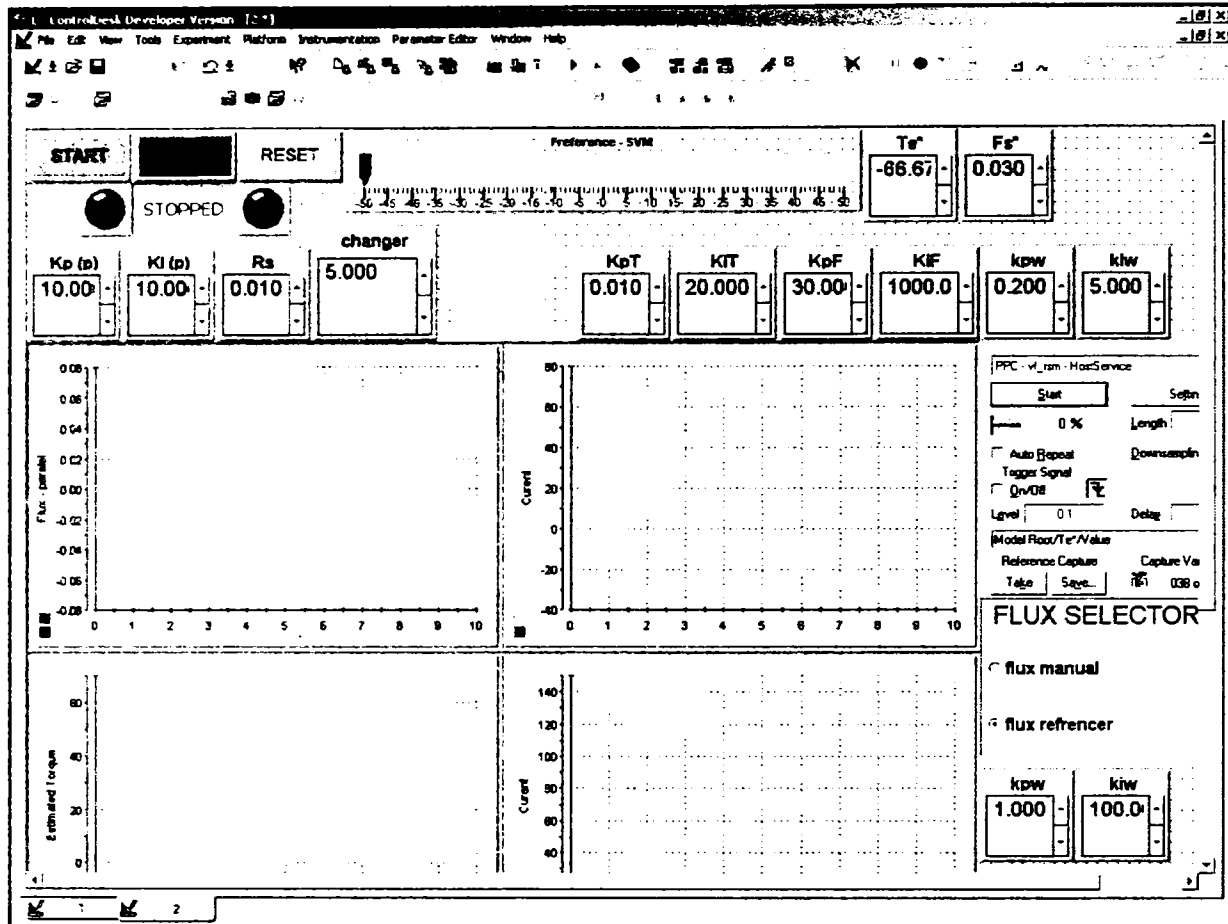


Figure 5.14. dSpace Control Desk environment

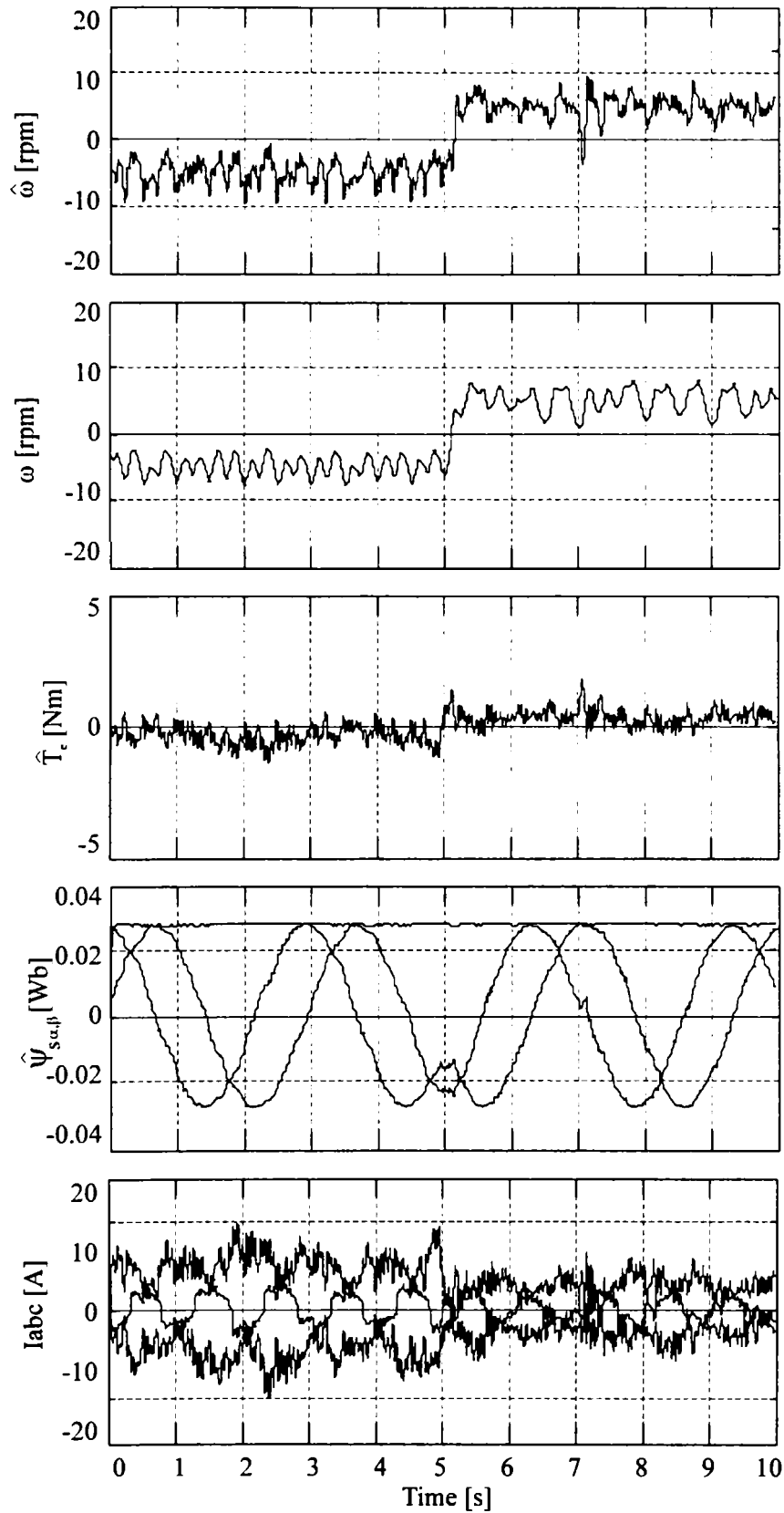
5.6. EXPERIMENTAL Results

A series of experiments have been processed to test the behavior of the proposed sensorless DTFC-SVM of PM-RSM. Two stator flux observers (Figure 5.6), and two rotor speed/position observers with signal injection (Figure 5.7) have been tested.

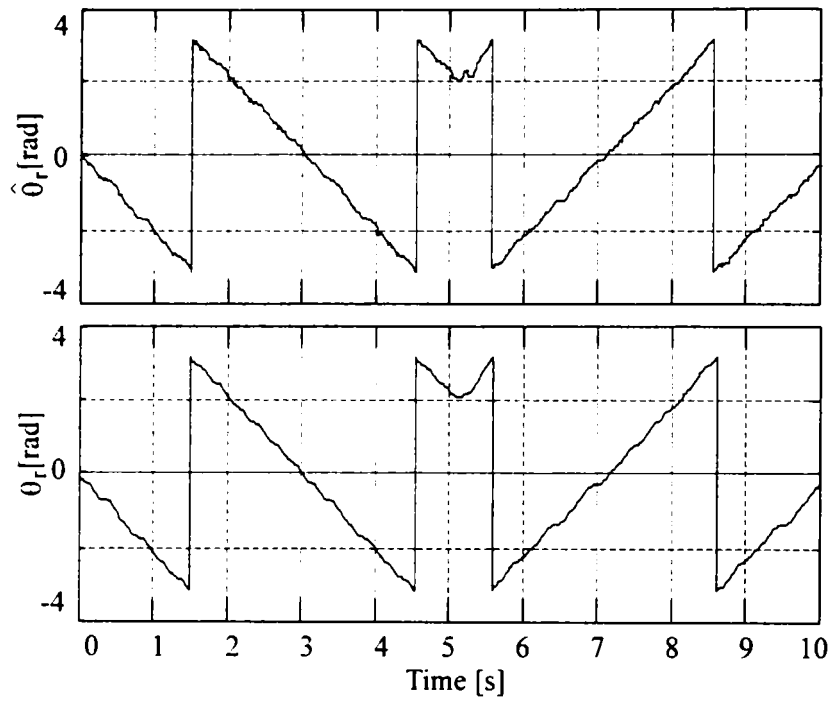
The experimental test results at low and high speeds are shown. A fusion strategy (Figure 5.8) is proposed using the speed/position observer with signal injection for low-speed, and the speed estimation from stator flux for medium-high speed.

Figure 5.15 shows the no-load speed reversal at very low speed: from -5 rpm to 5 rpm. The flux hodograph is almost circular (Figure 5.15c), the position estimation is very good (Figure 5.15b) and the speed estimation is acceptable. The use of SVM in DTFC has made a smooth operation possible at 5 rpm. Figure 5.16 shows the no-load start from zero to 10 rpm, again with good results. For a higher speed (from -15 rpm to 15 rpm) the reversal is shown in Figure 5.17.

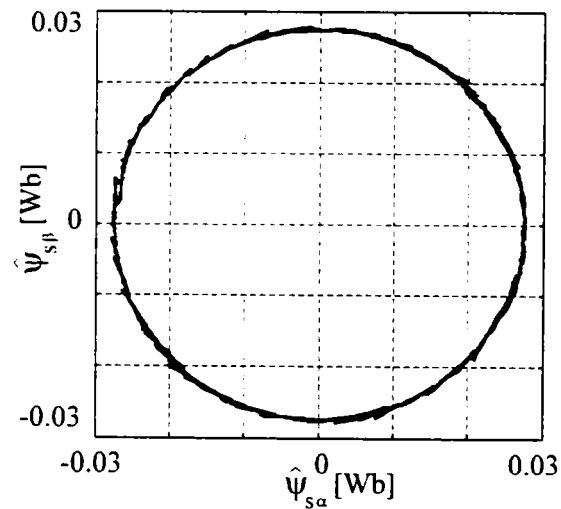
The speed reversal at high speed from -750 rpm to 750 rpm, which requires the transition of the speed observer from signal injection at low-speed to estimation from stator flux at high-speed, is illustrated in Figure 5.18 with good results.



(a)



(b)



(c)

Figure 5.15. Test results at ± 5 rpm speed reversal without load: (a) from top to bottom: estimated speed ($\hat{\omega}$), measured speed (ω), estimated torque (\hat{T}_e), estimated flux components ($\hat{\Psi}_s$), and measured currents (I_{abc}); (b) estimated and measured rotor position (θ_r); (c) estimated flux in $\alpha\beta$ -plane $\Psi_{s\alpha}^0$ ($\Psi_{s\beta}^0$) [Wb].

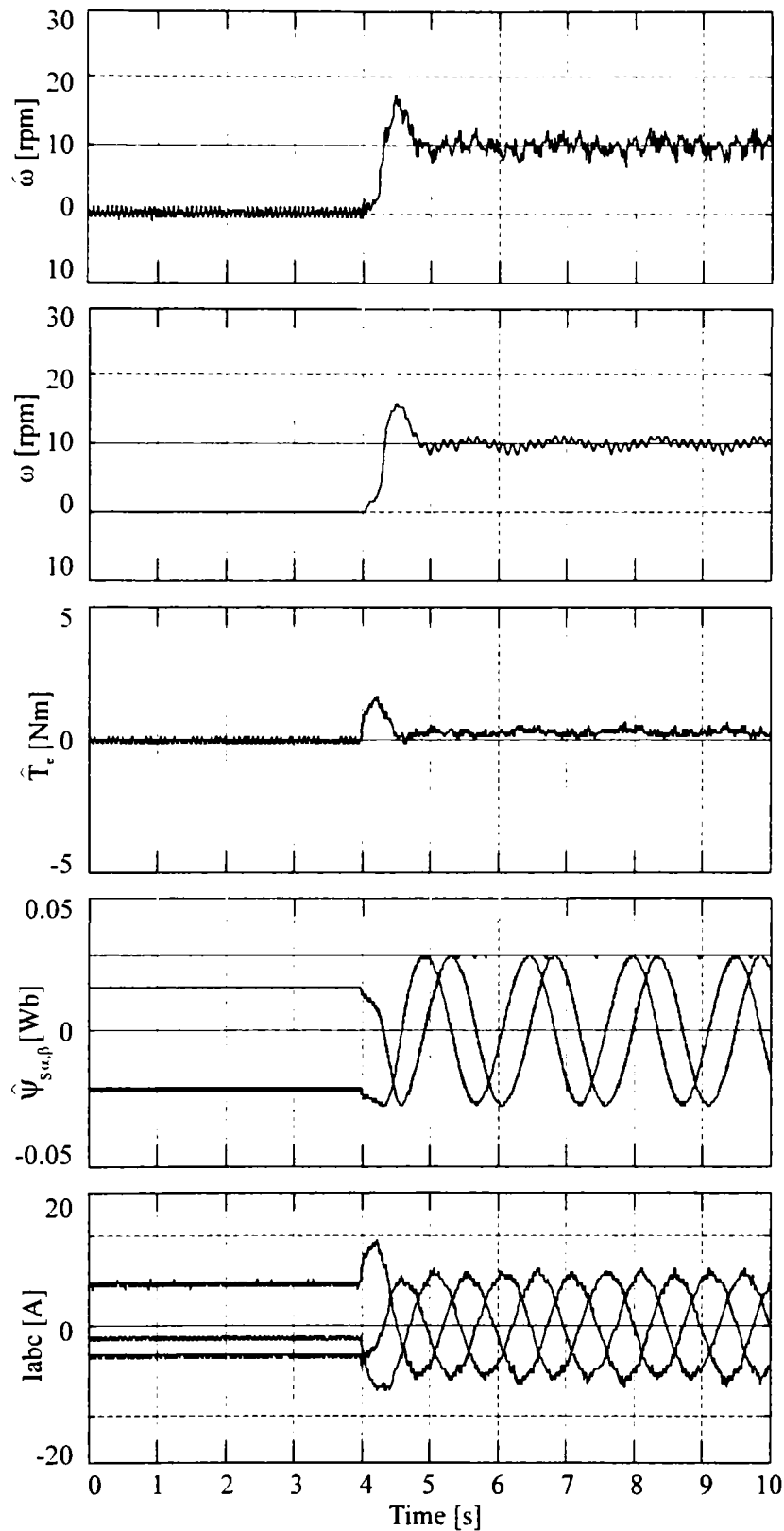


Figure 5.16. Test results at start-up to 10 rpm without load; from top to bottom: estimated speed ($\hat{\omega}$), measured speed (ω), estimated torque (\hat{T}_e), estimated flux components ($\hat{\Psi}_s$), and measured currents (I_{abc}).

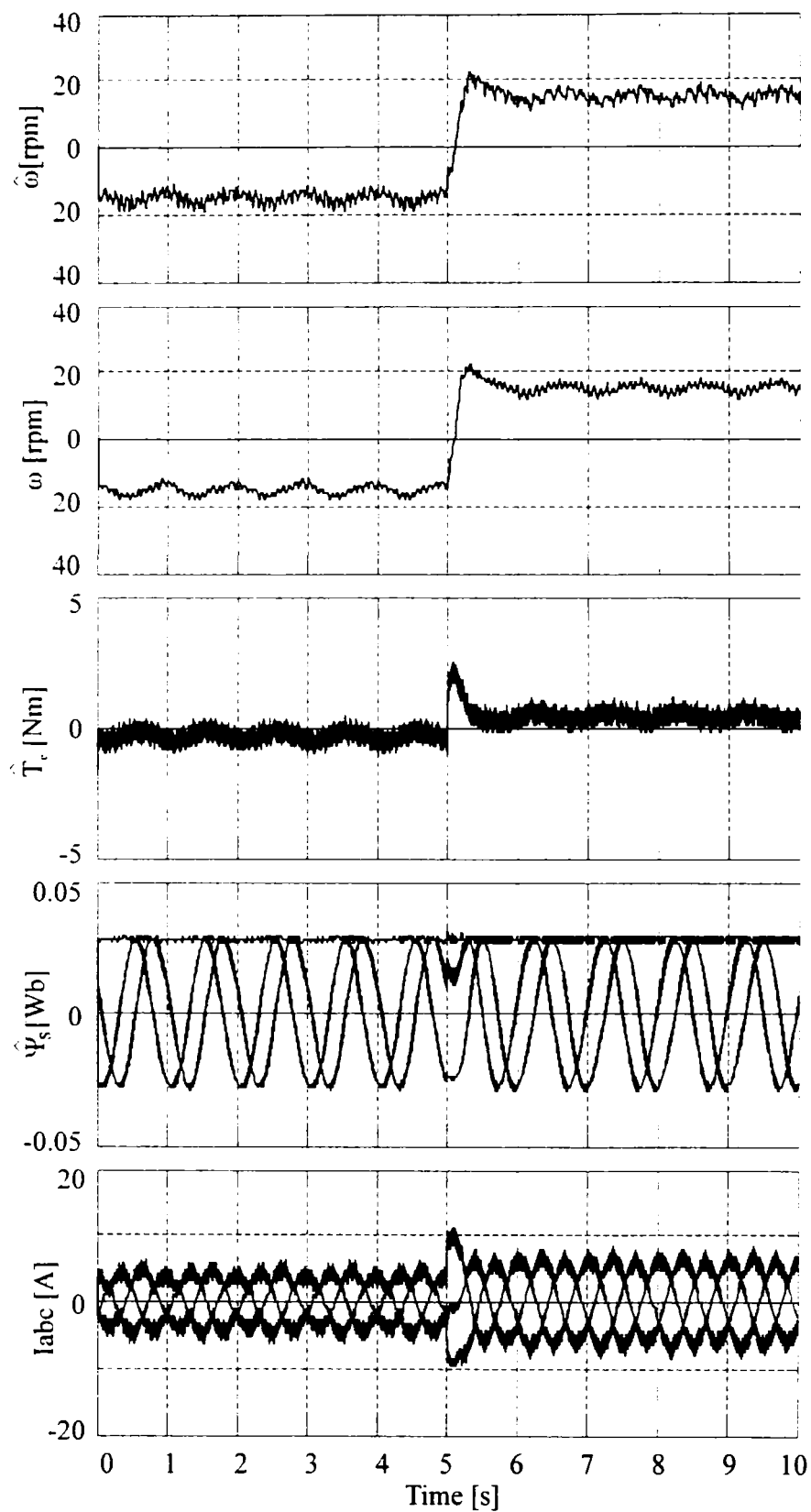


Figure 5.17. Test results at ± 15 rpm speed reversal without load: from top to bottom: estimated speed ($\hat{\omega}$), measured speed (ω), estimated torque (\hat{T}_c), estimated flux components ($\hat{\Psi}_s$), and measured currents (I_{abc}).

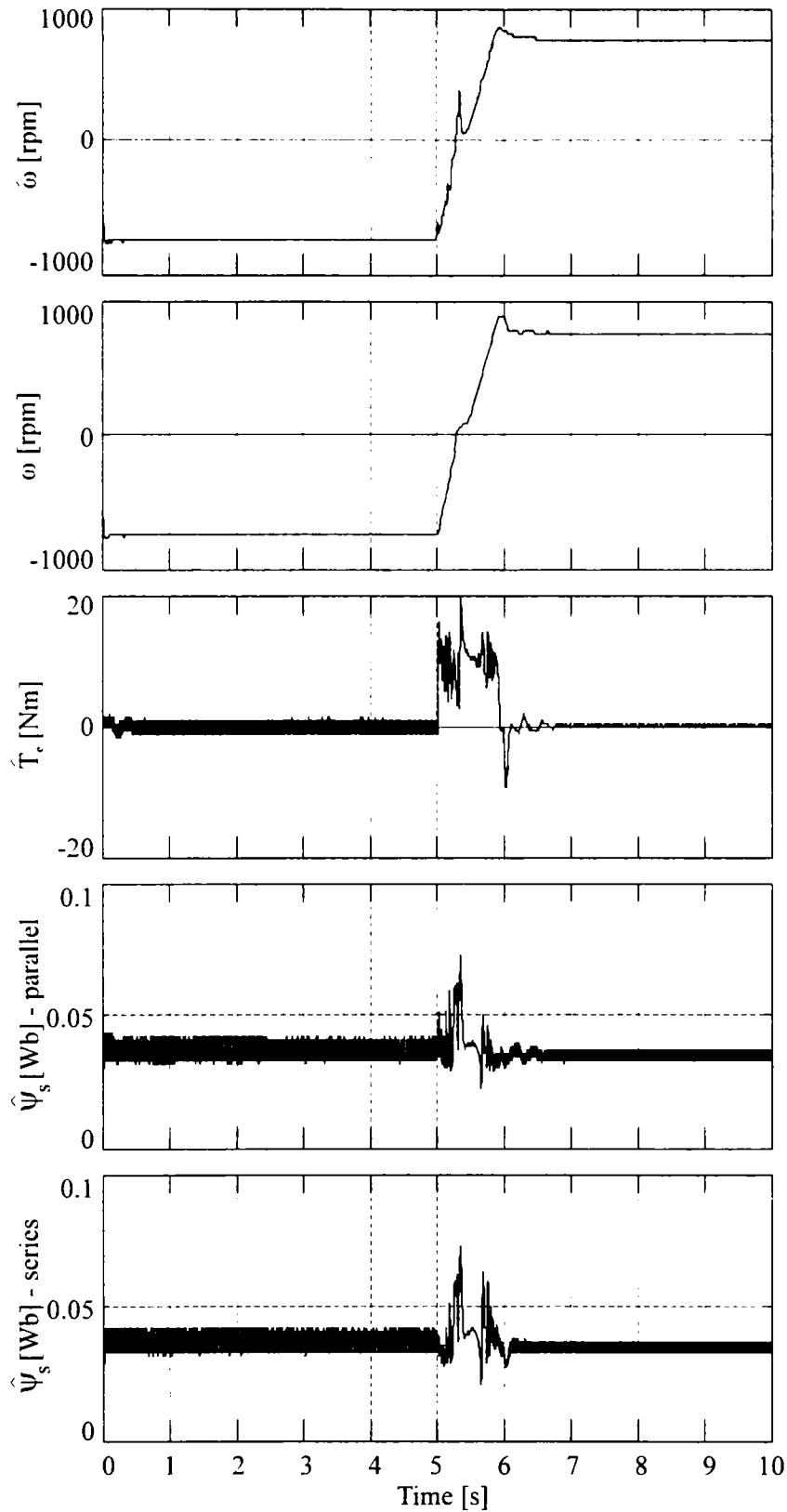


Figure 5.18. Test results at ± 750 rpm speed reversal without load; from top to bottom: estimated speed ($\hat{\omega}$) and measured speed (ω) (estimated from the stator flux and from signal injection at low speeds until 50 rpm), estimated torque (\hat{T}_e), estimated flux magnitude ($\hat{\Psi}_s$) - from serial and parallel observers.

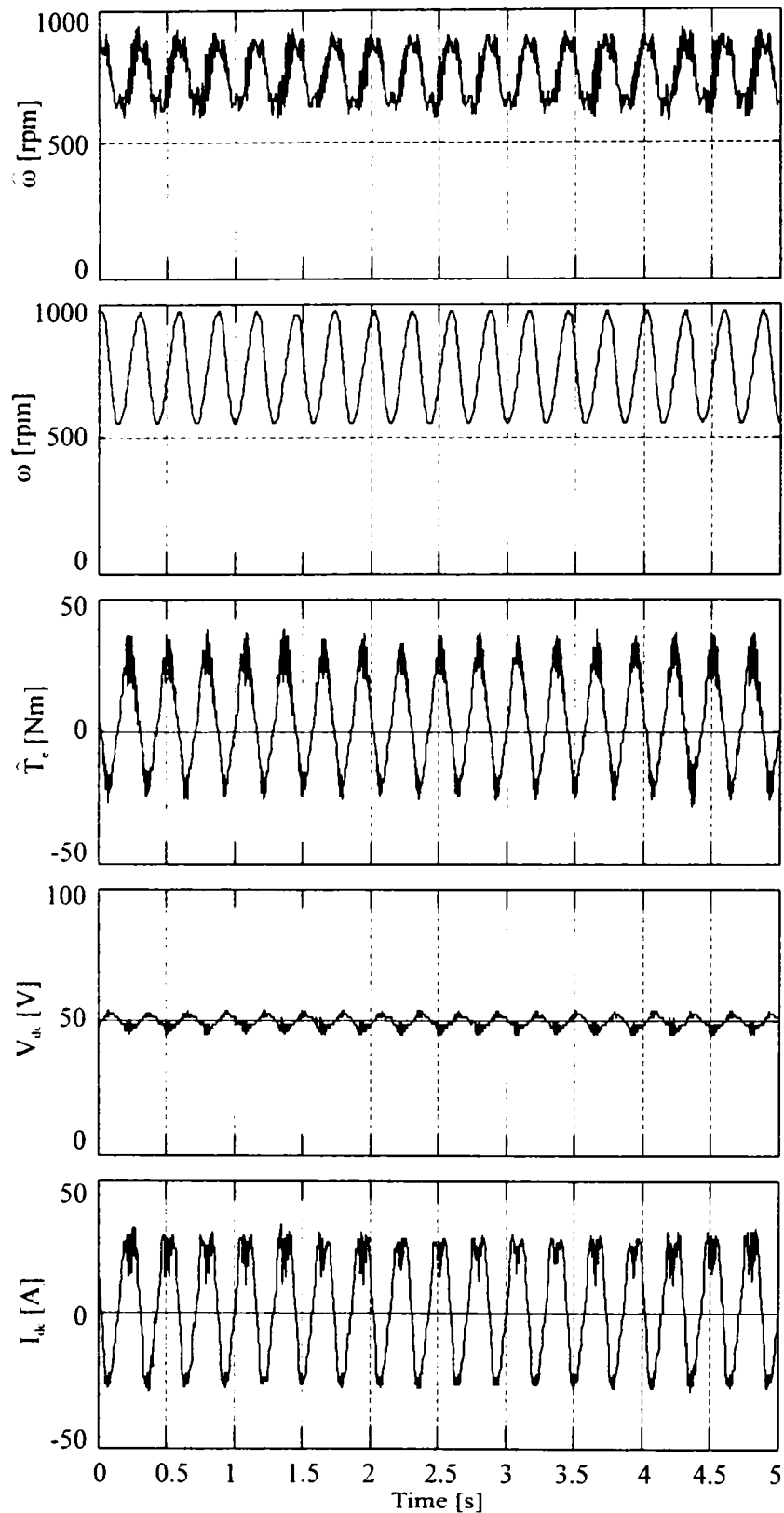


Figure 5.19. Artificial loading with fast switching from motoring to generating: estimated speed ($\hat{\omega}$), measured speed (ω), estimated torque (\hat{T}_e), measured battery voltage (V_{dc}), measured battery current (I_{dc}).

The switching from motoring to generating - as in artificial loading [15], by pulsating the speed reference, is shown in Figure 5.19, where the battery current

changes sign with fast response. This artificial loading has allowed for to reach 35 Nm peak torque with substantial battery charging (negative) current.

5.7. Conclusion

The proposed sensorless DTFC-SVM of PM-RSM includes the following contributions:

- A quasi-optimal flux referencer to optimize the energy consumption in wide speed range, with a flux versus torque functional leading to unique flux and torque reference values;
- A stator flux observer that uses a combined current-voltage models with PI compensator for low speed below 50 rpm, and only the voltage model in PI closed loop for medium-high speed.
- A speed and position observer with fusion strategy that employs signal injection and only one D-module vector filter in stator reference for low speed below 50 rpm, corroborated with a speed observer from stator flux vector estimation for medium-high speed.
- Extensive experimental test results on a laboratory prototype focused on very low speed to high speed sensorless operation for motoring and generating, including artificial loading, prove the effectiveness of the proposed solution.

Further investigations on on-line initial position estimation in full range, generator and motor heavy loading over the entire speed range are still to be added to take full advantage of the sensorless DTFC-SVM robust control capabilities.

5.8. References

- [1] J.M. Miller, V.R. Stefanovic, D. Kak, D. Pelergus, "Progress for starter alternator systems in automotive applications". Record of EPE - PEMC – 2002, Dubrovnik & Cartat, Croatia.
- [2] A.Vagati, A.Fratta, P. Guglielmi, G. Franchi, F. Villata, "Comparison of ac motor – based drives for electric vehicles", Record of PCIM – 1999 – Europe, vol.I, pp. 173 – 180.
- [3] T. Teratani et al, "Development of Toyota Mild Hybrid System (THM-M) with 42 V Power Net", Record of IEEE – IEMDC – 2003, vol. I, pp. 3 – 9.
- [4] A. Lange. W.R. Canders, F. Laube, N. Mosebach, "Comparisons different drive systems for a 75 kW electrical vehicle". Record of ICEM 2000, Espoo, Finland.
- [5] P. Guglielmi, M. Pastorelli, G. Pellegrino, A Vagati, "Position sensorless control of PM- assisted synchronous reluctance motor". IEEE Trans. Vol. IA – 40, no.2, 2004, pp. 615-622.
- [6] E.C. Lovelace, T.A. Jahns, F. Leonardi, JM Miller, P.J.McCleer, T.Keim, J.McLang, D.D. Wentzloff, "Design and Experimental Verification of a Direct Drive IPM synchronous machine using saturable lumped parameter model", Record of IEEE-IAS-2002.
- [7] I.Boldea, L.Tutelea, C.I.Pitic, "Characterization of PM – assisted reluctance synchronous motor/generator for a mild hybrid vehicle". IEEE Trans. Vol. IA – 40, no.2, 2004, pp. 492-498.
- [8] B.A. Welchko, T.M. Jahns, W.C. Soong, J.M. Nagashina, "IPM Synchronous machine drive response to symmetrical and asymmetrical short circuit faults", IEEE Trans. Vol. EC-18, no. 2, 2003, pp. 291-298.
- [9] H. Kim, K.K. Huh, R.D. Lorenz, T.M.Jahns, "A novel method for initial rotor position estimation for IPM synchronous machine drives", IEEE Trans, vol. IA-40, no. 5, 2004, pp. 1369-1378.
- [10] Y.Jeong, R.D. Lorenz, T.M. Jahns, S. Sul, "Initial rotor position estimation of an IPM motor", Record of IEEE-IEMDC-2003, pp. 1218-1223.
- [11] S. Shinnaka, "New mirror-phase vector control for sensorless drive of PMSM with pole saliency", IEEE Trans. Vol.IA-40,no.2, 2004, pp. 599-606.
- [12] C. Lascu, I. Boldea, F. Blaabjerg, "Direct Torque Control of Sensorless Induction Motor Drives- a sliding-mode approach", IEEE Trans. Vol. IA-40, no.2, 2004, pp. 582-590.
- [13] I. Boldea, L.Ianosi, F.Blaabjerg, "Modified direct torque control of reluctance synchronous motor sensorless drive", EMPS Journal, vol. 28, 2000, pp. 115-128.
- [14] M.F.Rahman, M.E. Hoque, L. Tang, R. Zhang, "Problems associated with direct torque control of IPM synchronous motor drive and their remedies", IEEE Trans, vol.IE-51, no.4,2004, pp. 799-809.

- [15] Lascu, C.; Boldea, I.; Blaabjerg, F.; Variable-structure direct torque control - a class of fast and robust controllers for induction machine drives, *Industrial Electronics, IEEE Transactions on*, Volume 51, Issue 4, Aug. 2004 Page(s):785 – 792
- [16] Lascu, C.; Trzynadlowski, A.M.; Combining the principles of sliding mode, direct torque control, and space-vector modulation in a high-performance sensorless AC drive, *Industry Applications, IEEE Transactions on*, Volume 40, Issue 1, Jan.-Feb. 2004 Page(s):170 – 177
- [17] Qiu, A.; Bin Wu; Kojori, H.; Sensorless control of permanent magnet synchronous motor using extended Kalman filter, *Electrical and Computer Engineering, 2004. Canadian Conference on*, Volume 3, 2-5 May 2004 Page(s):1557 - 1562 Vol.3
- [18] Capecchi, E.; Guglielmi, P.; Pastorelli, M.; Vagati, A.; Position-sensorless control of the transverse-laminated synchronous reluctance motor, *Industry Applications, IEEE Transactions on*, Volume 37, Issue 6, Nov.-Dec. 2001 Page(s):1768 – 1776
- [19] Kye-Lyong Kang; Jang-Mok Kim; Keun-Bae Hwang; Kyung-Hoon Kim; Sensorless control of PMSM in high speed range with iterative sliding mode observer, *Applied Power Electronics Conference and Exposition, 2004. APEC '04. Nineteenth Annual IEEE*, Volume 2, 2004 Page(s):1111 - 1116 vol.2
- [20] Shinnaka, S.; Takeuchi, S.; Kitajima, A.; Eguchi, F.; Haruki, H.; Frequency-hybrid vector control for sensorless induction motor and its application to electric vehicle drive, *Applied Power Electronics Conference and Exposition, 2001. APEC 2001. Sixteenth Annual IEEE*, Volume 1, 4-8 March 2001 Page(s):32 - 39 vol.1
- [21] Capecchi, E.; Guglielmi, P.; Pastorelli, M.; Vagati, A.; Position sensorless control of transverse-laminated synchronous reluctance motors, *Industry Applications Conference, 2000. Conference Record of the 2000 IEEE*, Volume 3, 8-12 Oct. 2000 Page(s):1766 - 1773 vol.3
- [22] Mizutani, R.; Takeshita, T.; Matsui, N.; Current model-based sensorless drives of salient-pole PMSM at low speed and standstill, *Industry Applications, IEEE Transactions on* Volume 34, Issue 4, July-Aug. 1998 Page(s):841 – 846
- [23] Maes, J.; Melkebeek, J.A.; Speed-sensorless direct torque control of induction motors using an adaptive flux observer, *Industry Applications, IEEE Transactions on*, Volume 36, Issue 3, May-June 2000 Page(s):778 – 785
- [24] Hyunbae Kim; Lorenz, R.D.; Carrier signal injection based sensorless control methods for IPM synchronous machine drives, *Industry Applications Conference, 2004. 39th IAS Annual Meeting. Conference Record of the 2004 IEEE*, Volume 2, 3-7 Oct. 2004 Page(s):977 - 984 vol.2

- [25] Corley, M.J.; Lorenz, R.D.; Rotor position and velocity estimation for a salient-pole permanent magnet synchronous machine at standstill and high speeds, *Industry Applications, IEEE Transactions on*, Volume 34, Issue 4, July-Aug. 1998 Page(s):784 – 789
- [26] Hyunbae Kim; Harke, M.C.; Lorenz, R.D.; Sensorless control of interior permanent magnet machine drives with zero-phase-lag position estimation, *Industry Applications Conference, 2002. 37th IAS Annual Meeting. Conference Record of the*, Volume 3, 13-18 Oct. 2002 Page(s):1661 - 1667 vol.3
- [27] Davis, R.I.; Lorenz, R.D.; Engine torque ripple cancellation with an integrated starter alternator in a hybrid electric vehicle: implementation and control, *Industry Applications Conference, 2002. 37th IAS Annual Meeting. Conference Record of the*, Volume 3, 13-18 Oct. 2002 Page(s):2016 - 2021 vol.3
- [28] Hyunbae Kim; Lorenz, R.D.; Improved current regulators for IPM machine drives using on-line parameter estimation, *Industry Applications Conference, 2002. 37th IAS Annual Meeting. Conference Record of the*, Volume 1, 13-18 Oct. 2002 Page(s):86 - 91 vol.1
- [29] Hyunbae Kim; Kum-Kang Huh; Lorenz, R.D.; Jahns, T.M.; A novel method for initial rotor position estimation for IPM synchronous machine drives, *Industry Applications Conference, 2003. 38th IAS Annual Meeting. Conference Record of the*, Volume 2, 12-16 Oct. 2003 Page(s):1173 - 1180 vol.2
- [30] Jeong, Y.; Lorenz, R.D.; Jahns, T.M.; Sul, S.; Initial rotor position estimation of an interior permanent magnet synchronous machine using carrier-frequency injection methods, *Electric Machines and Drives Conference, 2003. IEMDC'03. IEEE International*, Volume 2, 1-4 June 2003 Page(s):1218 - 1223 vol.2
- [31] Briz, F.; Degner, M.W.; Garcia, P.; Lorenz, R.D.; Comparison of saliency-based sensorless control techniques for AC machines, *Industry Applications, IEEE Transactions on*, Volume 40, Issue 4, July-Aug. 2004 Page(s):1107 – 1115.
- [32] Vadstrup, P.; Lorenz, R.D.; Robust estimator design for signal injection-based IPM synchronous machine drives, *Industry Applications Conference, 2004. 39th IAS Annual Meeting. Conference Record of the 2004 IEEE*, Volume 2, 3-7 Oct. 2004 Page(s):957 - 963 vol.2
- [33] Hinkkanen, M.; Luomi, J.; Modified integrator for voltage model flux estimation of induction motors, *Industrial Electronics, IEEE Transactions on*, Volume 50, Issue 4, Aug. 2003 Page(s):818 – 820
- [34] Freitas, M.A.A.; Andrade, D.A.; de Paula, H.; Domingos, J.L.; A novel rotor flux estimator for vector-controlled induction motor drives, *Industrial Electronics Society, 2003. IECON '03. The 29th Annual Conference of the IEEE*, Volume 1, 2-6 Nov. 2003 Page(s):156 - 161 vol.1

- [35] Habetler, T.G.; Profumo, F.; Griva, G.; Pastorelli, M.; Bettini, A.; Stator resistance tuning in a stator-flux field-oriented drive using an instantaneous hybrid flux estimator, *Power Electronics, IEEE Transactions on*, Volume 13, Issue 1, Jan. 1998 Page(s):125 – 133
- [36] Lascu, C.; Boldea, I.; Blaabjerg, F.; A modified direct torque control for induction motor sensorless drive, *Industry Applications, IEEE Transactions on*, Volume 36, Issue 1, Jan.-Feb. 2000 Page(s):122 – 130

Chapter VI

Conclusion and contributions

6.1. Conclusion

The thesis was dedicated to the advanced drives with synchronous machines for mild hybrid vehicles.

The thesis presents a high performance drive – starting with the motor design, prototype and latest control strategy for hybrid (mild hybrid) vehicles applications. This is a complete solution of design and control for reluctance synchronous motor assisted by permanent magnets backed up by strong experimental results. The thesis represents an approach, based on permanent magnets assisted reluctance synchronous motor with a 48 V inverter fed by a battery stand, to electrical systems for traction applications in mild hybrid vehicle technology.

The thesis focused on several major topics like:

- hybrid vehicles – the electrical system;
- designing the proper electrical machine for the application (hybrid technology – the traction system);
- synchronous machines with permanent magnets;
- improvement of the design using finite element simulations;
- the behavior of the permanent magnets assisted reluctance synchronous machine (PMRSM) at standstill and generating – the parameters determination;
- the behavior of the synchronous machines in a direct torque and flux control drive;
- sensorless drive with PM-RSM at 48 V – for the trend vehicles technology (with a dual voltage system);
- experimental motoring and generating characteristics with the DTF control;
- Experimental new state observers and sensorless control of the PM-RSM.

6.2. Original contributions

The presented thesis includes, from the author point of view, the following original contributions:

- Presents a state of the art in the hybrid systems, including the different technologies used by the biggest car manufacturers, but also the electric drives included. There is also an overview of the storage systems and the starter/alternators functionalities;
- Designing of a PM assisted RSM able of high peak torque densities (4.33 N/cm^2 and 16 A/mm^2) and with the efficiency at maximum speed - 90 % and 73 % above 500 rpm – characteristics needed for the demanding automotive industry;
- Finite elements simulations on the designed machine, with the validation of the analytical model;
- Prototype manufacturing of the PM assisted RSM;
- Development of a series of tests to identify the parameters and energy conversion performance - standstill dc decay tests and generating tests (with capacitors at terminals) - efficiency above 80 % was proven from 3 kW to 6.5 kW output at 1370 rpm;
- Development and simulation in MATLAB[®]/Simulink of a robust control - a direct torque and flux control (DTFC) with space vector modulation (SVM) for synchronous machines with permanent magnets.
- Implementation of the sensorless DTFC-SVM for interior permanent magnets synchronous machines (IPMSM) – using a dSpace DS 1103 system – with results as:
 - DTFC with SVM for IPMSM is shown capable of 1750 rpm to 1

- rpm** speed range full loaded in motion-sensorless implementation with signal injection used for rotor position estimation up to 30 rpm only.
- Fast torque response has been demonstrated both in motoring and generating mode.
 - The compensation of SVM dead time and other inverter nonlinearities lead, also for DTFC (as they do for vector control) to smooth current ripple with reasonable torque ripple especially at very low speed
- Development of the same DTFC–SVM – without motion sensor – for the designed permanent magnets assisted reluctance synchronous starter/alternator.
 - Implementation of control – using the dSpace system – with a Sauer Danfoss 48V, 350A inverter, with experimental results as:
 - A stator flux observer that uses a combined current-voltage models with PI compensator for low speed below 50 rpm, and only the voltage model in PI closed loop for medium-high speed
 - A speed and position observer with fusion strategy that employs signal injection and only one D-module vector filter in stator reference for low speed below 50 rpm, corroborated with a speed observer from stator flux vector estimation for medium-high speed
 - Extensive experimental test results on a laboratory prototype focused on very low speed to high speed sensorless operation for motoring and generating, including artificial loading, prove the effectiveness of the proposed solution

Appendix

The used Space Vector Modulation (SVM) program (s-function implemented in MATLAB[®]/Simulink) – created by Assist. Prof. Dr. **Cristian Lascu**.

“svmtmpl.c” file

- * Space Vector Modulation S-Function Template
- * Project: PMSM Sensorless DTC drive
- * Autor: **Cristian Lascu**, 2004
- * Continut: Space Vector Modulation S-Function template for Simulink
- * Input: Us.alfa, Us.beta, Vdc
- * Output: Da, Db, Dc

```
#define S_FUNCTION_NAME svmtmpl
#define S_FUNCTION_LEVEL 2

#include "simstruc.h"
#include "svm.c"

static void mdlInitializeSizes(SimStruct *S)
{
    ssSetNumSFcnParams(S, 1); /* Number of expected parameters */
    if (ssGetNumSFcnParams(S) != ssGetSFcnParamsCount(S)) {
        /* Return if number of expected != number of actual parameters */
        return;
    }
    ssSetNumContStates(S, 0);
    ssSetNumDiscStates(S, 0);

    if (!ssSetNumInputPorts(S, 2)) return;
    ssSetInputPortWidth(S, 0, 3);
    ssSetInputPortDirectFeedThrough(S, 0, 1);
    ssSetInputPortWidth(S, 1, 3);
    ssSetInputPortDirectFeedThrough(S, 1, 1);

    if (!ssSetNumOutputPorts(S, 2)) return;
```

```

    ssSetOutputPortWidth(S, 0, 3);
    ssSetOutputPortWidth(S, 1, 2);
    ssSetNumSampleTimes(S, 1);

    /* Take care when specifying exception free code - see sfuntmpl.doc */
    ssSetOptions(S, SS_OPTION_EXCEPTION_FREE_CODE);
//  ssSetOptions(S, 0);
}
static void mdlInitializeSampleTimes(SimStruct *S)
{
//  ssSetSampleTime(S, 0, CONTINUOUS_SAMPLE_TIME);
    ssSetSampleTime(S, 0, INHERITED_SAMPLE_TIME);
    ssSetOffsetTime(S, 0, 0.0);
}
static void mdlOutputs(SimStruct *S, int_T tid)
{
    InputRealPtrsType uPtr = ssGetInputPortRealSignalPtrs(S,0);
    InputRealPtrsType iPtr = ssGetInputPortRealSignalPtrs(S,1);
    real_T          *d = ssGetOutputPortRealSignal(S,0);
    real_T          *y = ssGetOutputPortRealSignal(S,1);
    real_T          *k = mxGetPr(ssGetSFcnParam(S,0));
    real_T u[3],i[3];
    u[0]=*uPtr[0];
    u[1]=*uPtr[1];
    u[2]=*uPtr[2];
    i[0]=*iPtr[0];
    i[1]=*iPtr[1];
    i[2]=*iPtr[2];
    SVM(u,i,d,y,k);
}
static void mdlTerminate(SimStruct *S)
#ifdef MATLAB_MEX_FILE /* Is this file being compiled as a MEX-file? */
#include "simulink.c" /* MEX-file interface mechanism */
#else
#include "cg_sfun.h" /* Code generation registration function */
#endif

```

"svm.c" file

```

* Space Vector Modulation
* Proiect: PMSM Sensorless DTC drive
* Autor: Cristian Lascu, 2004
* Continut: Space Vector Modulation
* Input: Us.alfa, Us.beta, Vdc
* Output: Da, Db, Dc
*****

#include <math.h>
#include "vector.h"
#define R3 1.732051
#define Dmax 0.98
#define Dmin 0.02
// Space Vector Modulation
void SVM(real_T *u, real_T *i, real_T *d, real_T *y, real_T *k)
{
    struct Vector{float alfa,beta;} Us;
    float K=(*k)*tdead/h;
    float Umax=R3/u[0];
    float Da,Db,Dc;
    float T1,T2;
    int sector;
    Us.alfa = R3*Umax*u[1]; //normalizare - Holtz
    Us.beta = Umax*u[2];

    // Sectorul tensiunii si timpii de modulare
    if (Us.beta>0)
        if (Us.alfa>Us.beta)
            {
                sector=0;
                T1=0.5*(Us.alfa-Us.beta);
                T2=Us.beta;
            }
        else if (-Us.alfa<Us.beta)
            {
                sector=1;
                T1=0.5*(Us.alfa+Us.beta);
                T2=0.5*(Us.beta-Us.alfa);
            }
}

```

```

        else
        {
            sector=2;
            T1=Us.beta;
            T2=-0.5*(Us.alfa+Us.beta);
        }
else if (Us.alfa<Us.beta)
    {
        sector=3;
        T1=0.5*(Us.beta-Us.alfa);
        T2=-Us.beta;
    }
else if (-Us.alfa>Us.beta)
    {
        sector=4;
        T1=-0.5*(Us.alfa+Us.beta);
        T2=0.5*(Us.alfa-Us.beta);
    }
else
    {
        sector=5;
        T1=-Us.beta;
        T2=0.5*(Us.alfa+Us.beta);
    }

// Supramodularea Holtz
if (T1>1.0) T1=1.0,T2=0.0; //bang-bang
else if (T2>1.0) T2=1.0,T1=0.0; //bang-bang
else if (T1+T2>1.0) if (T1>T2) T2=1.0-T1; else T1=1.0-T2;//OVM

// Factorii de umplere - SVM
switch (sector) {
case 0: Da=0.5*(1.0+T1+T2);
        Db=0.5*(1.0-T1+T2);
        Dc=0.5*(1.0-T1-T2);
        break;
case 1: Da=0.5*(1.0+T1-T2);
        Db=0.5*(1.0+T1+T2);

```

```

        Dc=0.5*(1.0-T1-T2);
        break;
case 2: Da=0.5*(1.0-T1-T2);
        Db=0.5*(1.0+T1+T2);
        Dc=0.5*(1.0-T1+T2);
        break;
case 3: Da=0.5*(1.0-T1-T2);
        Db=0.5*(1.0+T1-T2);
        Dc=0.5*(1.0+T1+T2);
        break;
case 4: Da=0.5*(1.0-T1+T2);
        Db=0.5*(1.0-T1-T2);
        Dc=0.5*(1.0+T1+T2);
        break;
case 5: Da=0.5*(1.0+T1+T2);
        Db=0.5*(1.0-T1-T2);
        Dc=0.5*(1.0+T1-T2);
        break;
default:
    Da=0.0;Db=0.0;Dc=0.0;
}
// Stator voltage
y[0] = u[0]*(2.0*Da-Db-Dc)/3.0;
y[1] = u[0]*(Db-Dc)/R3;
// Dead-time compensation
Da = Da + K*sat(i[0],zone);
Db = Db + K*sat(i[1],zone);
Dc = Dc + K*sat(i[2],zone);
// Pulse drop
if (Da>Dmax) Da=1.0; else if (Da<Dmin) Da=0.0;
if (Db>Dmax) Db=1.0; else if (Db<Dmin) Db=0.0;
if (Dc>Dmax) Dc=1.0; else if (Dc<Dmin) Dc=0.0;
// Duty cycles
d[0] = Da;
d[1] = Db;
d[2] = Dc;
}

```

“vector.h” file

- * Global Variables and Constant Definitions
- * Project: PMSM Sensorless DTC drive
- * Autor: Cristian Lascu, 2004
- * Continut: Global Variables and Constant Definitions

```
#ifndef VECTOR
#define VECTOR
// Sampling time
const float h=0.0001; // [s]
// SVM parameters
const float tdead = 2e-6; // dead time [s]
const float zone = 1.0; // linear zone [A]
// Constante matematice
const float pi=3.1415926;
// Saturation function
float sat(real_T x, real_T z)
{
    if (x>z) return 1.0;
    else if (x<=-z) return -1.0;
    else return x/z;
}
#endif
```

Summary in Romanian

Sumar

Teza prezinta o actionare performanta – incepand cu proiectarea motorului electric, manufacturarea unui prototip si implementarea unei strategii de control pentru tehnologia vehiculelor hibride. Este o solutie completa de proiectare si control a masinilor sincrone reactive asistate de magneti permanenti, validata de o serie completa de rezultate experimentale. Teza prezinta o actionare, bazata pe masini sincrone reactive cu magneti permanenti cu invertor de 48 V alimentat de la un stand de baterii, care poate fi folosita in sistemele de tractiune electrice din aplicatiile de vehicule usor hibride.

Background

Cresterea cerintei pentru performante superioare, o cat mai insemnata economie de combustibili si reducerea emisiilor poluante in atmosfera a fortat cercetarea in industria de autovehicule pentru dezvoltarea unor solutii alternative ale sistemelor de propulsie. Pentru a indeplinii aceste cerinte, companiile producatoare de autovehicule investigheaza tot felul de accesorii cum ar fi: valve electro-mecanice, directie asistata electric, sisteme de suspensie active si sisteme de incalzire electrice. Aceasta crestere dramatica a sistemelor electrice are nevoie de o schimbare substantiala in generarea si distributia energiei electrice in autovehicule.

Autovehiculele electrice si hibride sunt doua sisteme care au captat din ce in ce mai multa atentie in ultimii ani.

Vehiculele electrice si vehiculele hibrid – electrice au avantajul unic fata de sistemele clasice de propulsie de a poseda o arhitectura prin care isi pot adapta mediul de operare in zona in care eficienta energetica este maxima, aceasta coroborata cu o reducere insemnata a emisiilor de gaze (chiar pana la eliminarea acestora). In traficul urban, datorita efectului benefic asupra mediului incojurator, vehiculele electrice sunt un factor important in imbunatatirea traficului si, in particular, creerea unui mediu inconjurator mai sanatos.

Obiectivul principal al acestei teze este de a oferi noi solutii pentru sistemele electrice din vehiculele hibrid–electrice – domeniu care a luat proportii immense in ultimii ani.

Obiectivele tezei

Obiectivele principale ale tezei sunt:

Prezentarea solutiilor existente in domeniul tractiunii hibrid – electrice si a autovehiculelor in care au fost implementate, aceasta incluzand companiile producatoare, configuratiile vehiculelor acestora, tipuri de motoare electrice, de inmagazinare a energiei electrice si functionalitatile starter-alternatorului.

Alegerea celui mai bun motor electric care sa indeplineasca normele dure impuse de tractiunea auto, incluzand caracteristicile vehiculelor putin hibride.

Dezvoltarea, dupa ce au fost fixate specificatiile, unui program de proiectare pentru motorul electric ales.

Dupa ce au fost fixate dimensiunile masinii electrice, simularea cu un program de elemente finite este necesara pentru validarea si corectarea programului analitic.

Pentru a demonstra corectitudinea programului analitic si al simularii cu elemente finite, construirea unui prototip al masinii electrice este necesara.

Urmatoarea etapa este aceea de a determina parametrii masinii electrice prin probe de standstill si caracteristici de generator – un pas foarte important pentru implementarea unui control foarte robust.

Urmatorul pas, avand masina electrica si parametrii acesteia, este dezvoltarea unui control foarte robust.

Prin intelegerea si invatarea montajelor din laborator si, in special a sistemului dSpace, premisele implementarii controlului motorului electric pentru vehicule putin hibride cu ajutorul invertorului de 48 V de la Sauer-Danfoss, sunt indeplinite.

Cu rezultatele masuratorilor din testele de generator si toti parametrii bine cunoscuti, este necesara alegerea unui control potrivit pentru aceasta aplicatie. Deoarece controlul direct de flux si cuplu, cu si fara senzori de miscare, s-a demonstrat a avea success pentru masina de inductie de la viteze foarte joase si robust in fenomenele tranzitorii, vom incerca sa adaptam acest control si masinii sincrone reactive asistata de magneti permanenti in aceasta aplicatie pretentioasa de starter-alternator, unde specificatiile sunt mult mai dure decat in majoritatea industriilor, pentru ca siguranta in autovehicul este pe primul plan.

Organizarea tezei

Teza este organizata in sase capitole care urmeaza linia obiectivelor precedent prezentate.

In *primul capitol* este prezentata starea actuala in domeniul vehiculelor hibrid-electrice. La inceput sunt prezentate topologiile vehiculelor electrice si hibride, urmate de cele mai bune vehicule hibride de pe piata auto, apoi sunt caracterizate sistemele electrice din vehiculele hibride si, la sfarsit, inceputul contributiei la acest domeniu, alegerea unui motor electric care sa indeplineasca cerintele acestui domeniu.

In cel de-*al doilea capitol*, este prezentat un program de design – dupa ce au fost determinate specificatiile, asistat de simulari cu un program de elemente finite. Apoi sunt aratate rezultatele simularilor cu elemente finite – cu validarea cuplului electromagnetic. La finalul capitolului, este aratat un exemplu de program de proiectare pentru masina sincrona cu reluctanta asistata de magneti permanenti.

In cel de-*al treilea capitol* este introdusa o serie de teste pentru determinarea parametrilor si a eficientei in regim de generator. Aceste teste constau in probe de repaos - stingere de current si regim de generator in gol si cu incarcare.

Cel de-*al patrulea capitol* prezinta implementarea unui control intr-o gama larga de turatii, fara senzori de miscare, pentru masini sincrone cu magneti permanenti interiori, prin controlul direct de flux si cuplu. Injectia de semnal impreuna cu observator de pozitie este folosit la viteze foarte joase pentru a fi inclus in observatorul de flux si, respectiv, pentru bucla de viteza. Un observator bazat pe un model combinat de curent-tensiune este introdus pentru a acoperi toata gama de turatii – modelul de curent micșorandu-si aportul in timp ce viteza creste. Compensarea neliniaritatilor introduse de PWM si inverter asigura o forma sinusoidala a curentului chiar si la viteze foarte joase.

Al cincilea capitol introduce controlul de flux si cuplu pentru masina sincrona asistata de magneti permanenti pentru vehicule hibride, fara senzori de miscare de la viteza zero. Controlul propus este descris si implementat pe un system dSpace DS 1103 cu un convertor cu MOSFETuri de 350 A, conectat la un stand de baterii de 48 V dc, 55 Ah. In final sunt prezentate rezultatele la diferite viteze in regim de motor si generator – rezultate foarte incurajatoare.

Cel de-*al saselea capitol* prezinta concluziile si contributiile acestei teze.

Contributii originale

Dupa parerea autorului, teza contine urmatoarele contributii originale:

- ofera o privire de ansamblu asupra sistemelor hibride actuale, incluzand diferitele topologii implementate de cele mai renumite companii producatoare de autovehicule, dar si tipurile de actionari electrice folosite. Mai sunt prezentate si trendurile actuale in sistemele de inmagazinare a energiei in autovehicule;
- Proiectarea unei masini sincrone asistata de magneti permaneti capabila de densitati de cuplu mari (4.33 N/cm^2 and 16 A/mm^2) si cu randamentul la viteza maxima de cel putin 90 % (si peste 73% la turatia de baza) – caracteristici necesare industriei de autovehicule;
- Simulari cu elemente finite pe masina proiectata, cu validarea modelului analitic;
- Fabricarea unui prototip al masinii sincrone reactive cu magneti permanenti;
- Dezvoltarea unei serii de teste pentru identificarea parametrilor si a performantelor in conversia energiei – stingere curentului si teste de generator (cu capacitoare la borne) – teste care au demonstrat randament de 80% de la 3.5kW la 6.5kW la o turatie de 1370 rpm;
- Dezvoltarea si simularea in MATLAB®/Simulink a unui control robust – un control direct de flux si cuplu pentru masinile sincrone cu magneti permanenti;
- Implementarea unui control direct de flux si cuplu fara senzori de miscare pentru masini sincrone cu magneti permanenti interiori, folosind un sistem dSpace DS 1103 – cu rezultate cum ar fi:
 - Capabilitatea unei game de turatii de la 1750 rpm pana la **1 rpm** cu incarcare nominala – intr-o implementare fara senzori de

- miscare cu injectie de semnal folosita pentru determinarea pozitiei rotorului;
- Raspuns prompt in cuplu a fost demonstrat atat in regim de motor, cat si de generator;
 - Compensarea timpului mort si a celorlalte neliniaritati introduse de inverter, conduc la o forma sinusoidala a curentului – rezultand pulsatii rezonabile in cuplu, in special la viteze foarte joase;
 - Dezvoltarea aceluasi control fara senzori de miscare pentru masina sincrona cu magneti permanenti proiectata ca starter/alternator;
 - Implementarea controlului folosind sistemul dSpace DS 1103 si inverterul de 48V, 350A de la Sauer Danfoss, cu rezultate experimentale si contributii cum ar fi:
 - Un observator de flux statoric care foloseste un model combinat de tensiune si curent, cu compensare (PI) – la viteze mici (sub 50 rpm) si numai model de tensiune in bucla inchisa pentru viteze medii si mari;
 - Un observator de viteza si pozitie bazat pe injectia de semnal pentru viteze sub 50 rpm, alaturat unui observator de viteza din estimarea vectorului flux statoric pentru viteze medii si mari;
 - Teste experimentale pe un prototip de laborator focusate pe conducerea fara senzori de miscare de la viteze foarte joase pana la viteze ridicate, operand atat in generator, cat si in motor, incluzand incarcarea artificiala – dovedesc eficienta solutiei propuse pentru aceasta aplicatie.

Curriculum vitae

Cristian Ilie Pitic

Office

SiemensVDO Automotive SRL

Calea Martirilor 1989, nr. 1

300724 Timisoara

Romania

Tel. +40 256 251 930

Fax +40 256 294 441

E-Mail:pitic.cristian@siemensvdo.com

Home

Turnatorului 5/7

331016 Hunedoara

Romania

Tel. +40 254 713 646

Mobile +40 744 772 867

E-Mail:piticcristian@yahoo.com

Education

2000-2005 PhD student at "Politehnica" University of Timisoara

2000 Dipl. degree in Electrical Engineering

1995-2000 University "Politehnica" of Timisoara, Timisoara, Romania
Department of Electrical Engineering

1995-2000 Theoretical high school Iancu de Hunedoara, Hunedoara, Romania

Professional Experience

3 month in 2004 Guest Researcher in Institute of Energy technology,
Aalborg University, Denmark;

From 15.04.2005 SiemensVDO Automotive SRL, SV P ED DT F4

Personal Information

Born: December 18th, 1976

Family: Unmarried

Author's papers related to the Ph. D. thesis

- Ion Boldea, Lucian Tutelea, Cristian Ilie Pitic, "PM – assisted Reluctance Synchronous motor / generator (PM - RSM) for mild hybrid vehicles", OPTIM 2002, Poiana Brasov, Romania
- Ion Boldea, Lucian Tutelea, Cristian Ilie Pitic, "PM-Assisted Reluctance Synchronous Motor/Generator (PM-RSM) for Mild Hybrid Vehicles: Electromagnetic Design", IEEE Transactions on Industry Applications, Vol. 40, No. 2, March/April 2004, pp. 492 – 498.
- Boldea, L.Tutelea, C.I. Pitic, "PM – assisted Reluctance Synchronous starter/generator (PM-RSM): generator experimental characterization", OPTIM 2004, Brasov, Romania.
- Boldea, L.Tutelea, C.I. Pitic, "PM – assisted Reluctance Synchronous starter/generator (PM-RSM): generator experimental characterization", Journal of Electrical Engineering, No.1, Vol 5, 2005, (<http://www.jee.ro/>);
- Cristian Ilie Pitic, G.D. Andreescu, F. Blaabjerg, I. Boldea, "IPMSM Motion-Sensorless Direct Torque and Flux Control", IECON 2005 – accepted – will be published.
- Ion Boldea, Cristian Ilie Pitic, Cristian Lascu, Gheorghe-Daniel Andreescu, Lucian Tutelea, Frede Blaabjerg, Per Sandholdt, "DTFC-SVM Motion-Sensorless Control of PM-Assisted Reluctance Synchronous Machine as Starter-Alternator for Hybrid Electric Vehicles" – passed the first review at IEEE PE.

PM – assisted Reluctance Synchronous motor / generator (PM - RSM) for mild hybrid vehicles

Ion Boldea, Lucian Tutelea, Cristian Ilie Pitic

Department of Electrical Machines and Drives, University Politehnica of Timisoara, V.Parvan 2,
RO - 1900 Timisoara, Romania, Tel.+40-56-204402, email: boldea@lselinux.utt.ro,
luci@lselinux.utt.ro, pitic.c@lselinux.utt.ro

ABSTRACT

The present paper introduces the conceptual design and FEM analysis of PM – assisted reluctance synchronous motor / generator (PM - RSM) for mild hybrid vehicles where a large constant power speed range (6:1) is required and machine volume and converter peak KVA, batteries size are main constraints.

Careful flux – barrier and PM sizing, high magnetic saturation and current density are main requirements for maximum torque production with constraint volume.

Voltage management provides for the 6:1 constant speed power range. A peak torque density of $4.33 \text{ N} / \text{cm}^2$ is obtained. Rated (continuous) power-battery limited- is 2.5KW at 42Vdc. from 1000rpm to 6000 rpm. The peak torque of 140 Nm is obtained at 257 A (RMS / phase) and can be secured up to 500 rpm. Peak power is still 7.85 kW at 6000 rpm at 42 V dc with an efficiency of 90 %.

I. INTRODUCTION

The new commercial hybrid vehicles of Toyota and Honda have proven a 30 – 35 % fuel saving in town driving in comparison with equivalent gasoline – only cars.

This is spectacular progress but it comes with rather large additional electric equipments (3000 USD or so), for the high voltage power battery life of 5 years.

While most prototypes already have adopted the induction machine as motor / generator the dispute over the best solution is far from over.

Quite recently rather complete studies [1 - 6] and comparison between induction [12], PM synchronous [3], reluctance synchronous, switched reluctance [4, 5], PM – assisted reluctance synchronous, PM transverse flux machine [6] have led to the conclusion that the induction motor has two strong competitors in terms of losses and motor weight: the PM - assisted Reluctance Synchronous (PM - RSM) [7 - 8] and the PM transverse flux machines [9] and the PM – RSM in terms of maximum peak converter KVA and total equipment costs.

Costs are important but are subject to change when high numbers of vehicles are fabricated under modern auto motion manufacturing auspices.

Machine volume, losses, maximum converter KVA and total loss capitalized costs lead to a multi-objective non-linear problem.

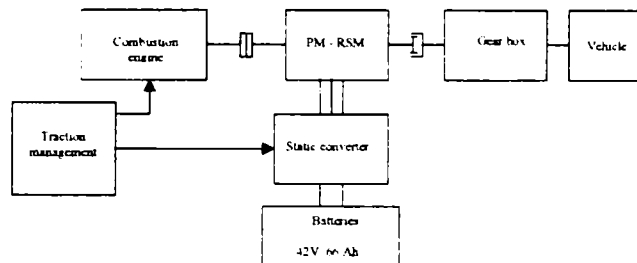


Figure 1. Mild hybrid vehicle diagram block.

Though Refs [7 - 9] do present results that suggest the PM – RSM as a better solution than the IM, a realistic approach to PM – RSM modelling, conceptual design and FEM analysis is apparently missing yet, for heavy electrical and magnetic loadings.

So the main goals of this paper is to settle on a practical topology, develop conceptual design for heavy saturation, FEM thorough analysis and verification, mainly in terms of torque versus i_d , i_q currents. Torque, currents, voltage, efficiency for motoring and generating versus speed are given that match very challenging design specifications.

II. TYPICAL SPECIFICATIONS

The mild hybrid vehicle block diagram is presented in figure 1. This topology contains the combustion engine, the electric motor (integrated starter – generator: ISG), the 42 V battery pack and the power electronic system. The traction system contains also the gearbox. The main advantage of an ISG system over a conventional starter motor can be found in the fast engine stop / start behaviour and the potential of reduced Noise, Vibration and Harshness during actively controlled engine start-up and shutdown procedures. During launch assist, the storage system must deliver high power to the ISG system. In the last few years the need for more power introduced the new 42 V systems instead of the actual 14 V [10, 11, 12, 13]. A mild hybrid vehicle should use this 42 V dc power bus (3 standard 14 V dc batteries in series) only, for ISG.

Typical specifications for a hybrid (or electric) vehicle application are related to:

- peak torque versus speed envelope;
- continuous constant power speed range;

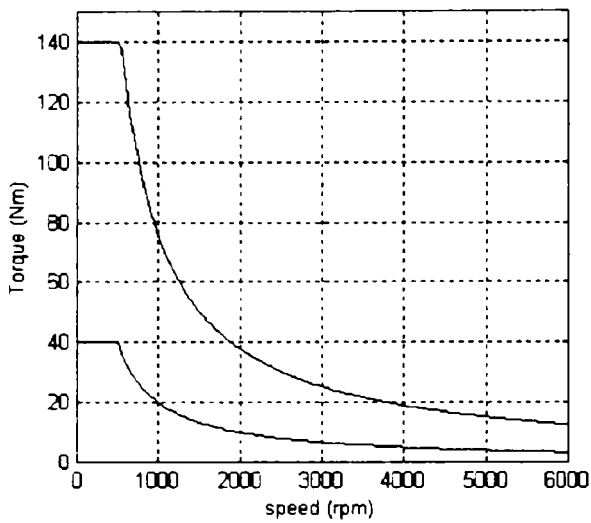


Figure 2. Torque and power versus speed

- maximum current for given d.c. link voltage and V_{dc} given maximum emf at maximum speed E_0 (in the d.c. link);
- maximum current density j (A / mm^2);
- losses versus speed for given torque – speed envelope;
- peak torque / kg of active materials;

A typical wide power speed range for continuous 2.5 KW from 1000 rpm (idle engine speed) to 6000 rpm (direct on the crankshaft drive) is shown on Figure 2. The unusually large constant power speed range is typical for crankshaft motor / generator. The elimination of any additional transmission is thus paid for. The solution is volume (weight) constraint also and, consequently, for the maximum torque (developed below base speed, a torque density in range of 15 – 20 Nm / kg of active materials stator and rotor is required.

On top of that the maximum phase current (RMS) for maximum torque has to be limited to cut the costs of the converter. Also the machine has to be able to deliver constant power over a 6:1 speed range.

To meet these contradictory specifications a bit of machine oversizing is required, in spite of heavy electrical and magnetic design loadings, together with some inverter oversizing as the voltage required at base speed is notably lower than maximum voltage available. While a rather complete mathematical approach of these aspects is in principle possible, we will adopt here an engineering, more practical approach starting with a practical PM – RSM configuration and conceptual design for heavy electrical and magnetic loadings.

III. THE PRACTICAL CONFIGURATION AND CONCEPTUAL DESIGN ASPECTS

In Figure 3 the design configuration for the permanent magnets assisted reluctance synchronous machine is presented.

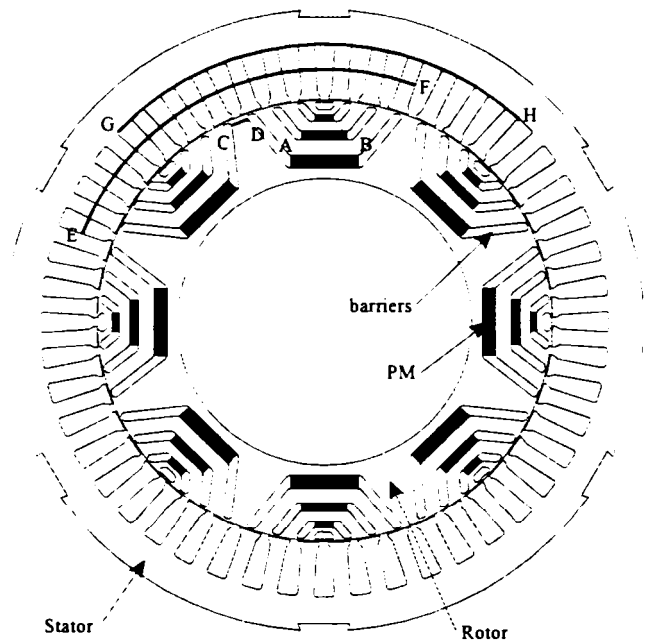


Figure 3. The PM – RSM machine

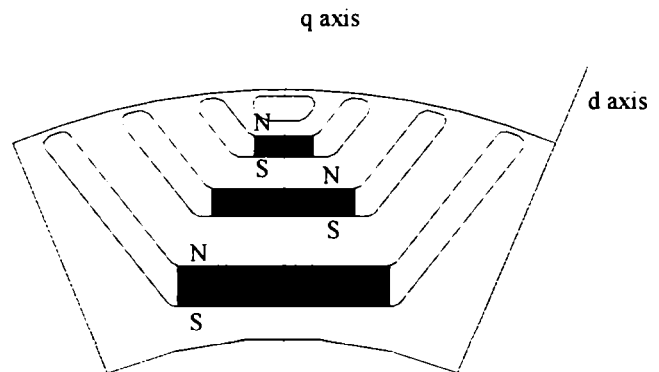


Figure 4. Rotor design and PM's polarity.

Table 1

Geometric parameters		Value
Stator outer diameter	SOD	245.2 mm
Rotor outer diameter	ROD	174.2 mm
Rotor inner diameter	RID	113 mm
Airgap	g	0.4 mm
Stack length	l_{stack}	68 mm
PM parameters at 20 °C	B_r	0.87 T
	H_c	660000 A/m

The stator laminations were chosen from an existing motor in order to lower the costs of the prototype. The rotor topology and the polarisation of the magnets is presented in figure 4. The rotor design (the permanent magnet dimensions) was made with FEM assistance. For the PM flux, we first calculate the rated RMS phase voltage with V_0 (dc voltage):

$$V_1 = k_{\max} \cdot V_0 \cdot \frac{\sqrt{2}}{\pi}$$

k_{\max} - voltage utilisation;

The max allowable emf E_0 means, E_1 [V] is:

$$E_1 = V_1 \cdot \frac{E_0}{V_0}$$

This value is obtained at max speed. The RSM flux linkage per pole in the airgap produced by the PM should be:

$$\Psi_{PMRMS} = \frac{E_1}{2 \cdot p \cdot \pi \cdot n_{\max}}$$

p - number of poles pairs ($2p = 8$);

n_{\max} - maximum speed;

The iron bridges in the rotor should not consume more than $k_{\text{bridge}} = 0.2$ of PM flux to saturate heavily. Consequently the PM airgap flux density is:

$$n_c B_{gPM} = \frac{\Psi_{PMRMS} \cdot \sqrt{2}}{k_{w1} \cdot 2 \cdot p \cdot q \cdot \tau \cdot l_{\text{stack}} \frac{1 - k_{\text{bridge}}}{\pi \cdot a}}$$

n_c - number of turns per coil;

B_{gPM} - PM's flux density;

k_{w1} - windings factor;

q - the number of slot / pole / phase ($q = 2$);

τ - the pole pitch;

k_{bridge} - rotor core bridge PM flux linkage ratio;

l_{stack} - stack length;

a - current path count;

This is the maximum product of n_c and B_{gPM} ,

$$n_c = \text{round} \left(\frac{n_c B_{gPM}}{B_{gPM}} \right)$$

The value of B_{gPM} is realized by changing the length of various PMs in the flux barriers with FEM check.

Rotor iron bridge thickness w_b is:

$$w_b = \frac{k_{\text{bridge}} \cdot \Psi_{PMRMS} \cdot \sqrt{6}}{4 \cdot l_{\text{stack}} \cdot B_{\text{bridge}} \cdot q \cdot n_c \frac{2 \cdot p \cdot k_{w1}}{a}}$$

B_{bridge} - rotor iron bridge saturation flux density;

The magnetic saturation acts along both axes. We suppose that the airgap flux density in fact counts and it has a given value B_g . Then we calculate the saturation factors k_{sd} and k_{sq} considering that the stator core saturation corresponds to the resultant airgap flux density.

The I_d and I_q currents can be calculated as:

$$I_d = \frac{a}{n_c} B_{gd} \pi \cdot k_c \cdot g \frac{1 + k_{sd}}{4.2426 \cdot \mu_0 \cdot 2 \cdot q \cdot k_{dm} \cdot k_{w1}}$$

$$I_q = k_i \cdot \left[\frac{B_{gPM}}{B_{gd}} - \sqrt{\left(\frac{B_g}{B_{gd}} \right)^2 - 1} \right] \cdot \frac{k_{dm} \cdot (1 + k_{sq})}{k_{qm} \cdot (1 + k_{sd})}$$

k_{dm}, k_{qm} - unsaturated coefficient for L_{dm} and L_{qm} [13];

The I_s current results as:

$$I_s = \sqrt{I_d^2 + I_q^2}$$

$$T = 3 \cdot p \cdot I_d \cdot$$

$$\cdot \left[\Psi_{PMRMS} \cdot (1 - k_{\text{bridge}}) + I_q \cdot \left(\frac{L_m \cdot k_{dm}}{1 + k_{sd}} - \frac{L_m \cdot k_{qm}}{1 + k_{sq}} \right) \right]$$

The efficiency of the motor is:

$$\eta = \frac{P_m - P_{mec}}{P_m + P_{copper} + P_{iron}}$$

In Figure 5, with FEM support the torque values on different rotor positions are shown. As we can see the maximum torque is obtained at 11.5 mechanical degree (140 Nm).

In Figure 6 the permanent magnets flux lines are shown. Figures 7 and 8 present the PM airgap flux and flux density. The PM flux density in the airgap is approximately 0.3 T.

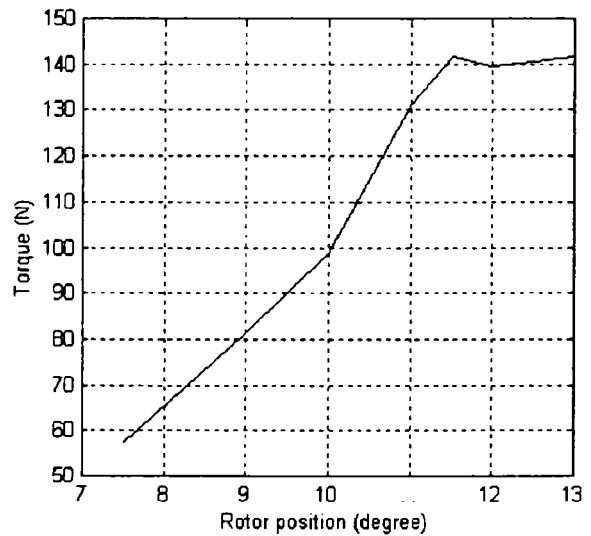


Figure 5. The FEM torque versus rotor position (max. current)

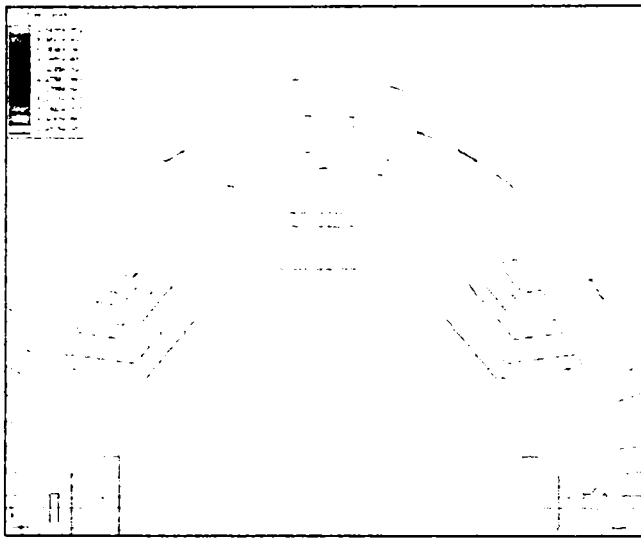


Figure 6. The PM flux lines in the machine

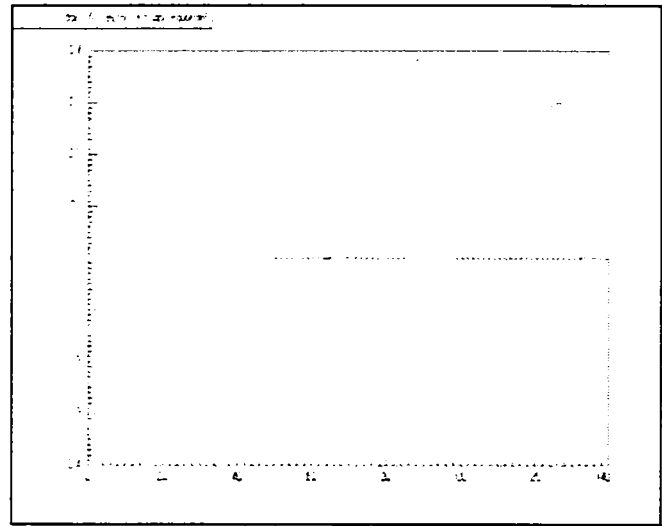


Figure 8. The PM airgap flux density

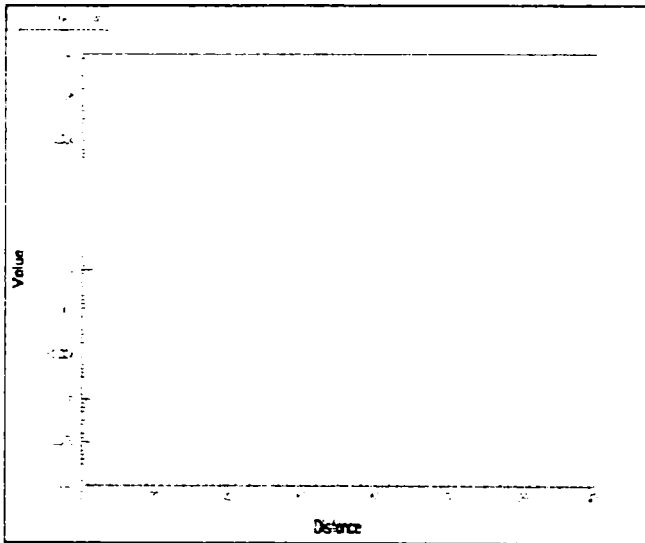


Figure 7. The PM airgap flux distribution

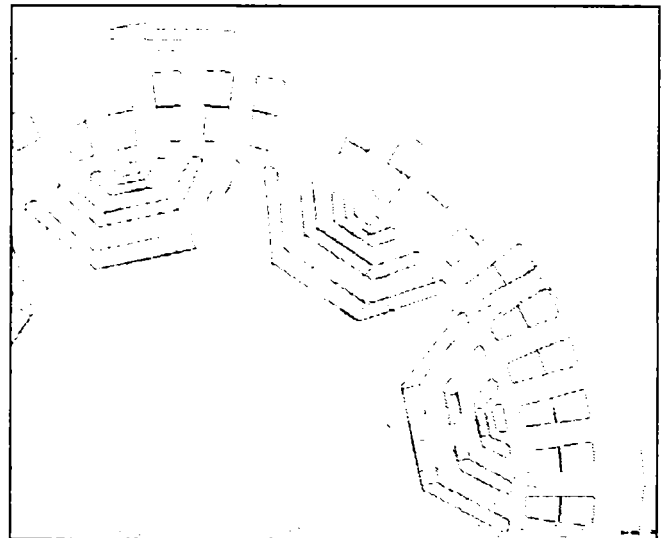


Figure 9. The flux lines for the maximum torque (140 Nm)

The flux distribution for the maximum obtained torque (140 Nm) is shown on Figure 9, and the Figure 10 and 11 represent the flux and flux density in the machine.

With FEM assistance and a Matlab programme (an iterative computation procedure to account for the wildly variable saturation level with speed) we estimated the torque and dc voltage (Figure 12) and the efficiency (Figure 13) versus speed. The magnetic material load of is also checked using FEM simulations. Figure 14 shows the flux density distribution at peak torque on PM surface along contour (AB) marked on fig. 3. The flux density distribution at peak torque in Rotor inter – barriers, contour (CD) is shown in Figure 15. Stator tooth and slot flux density at peak torque is shown along middle of teeth, contour (EF), in figure 16 and along bases of teeth, contour (GH), in figure 17.

The PM assisted reluctance synchronous motor is good performance with good values for both torque density and kVA.

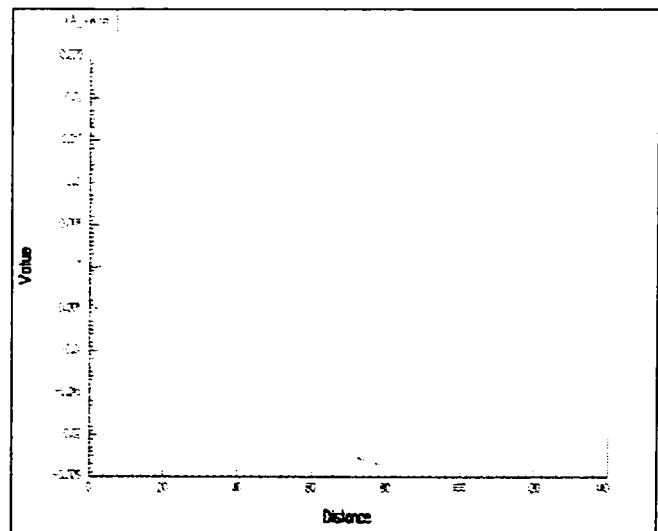


Figure 10. The airgap flux for the maximum torque

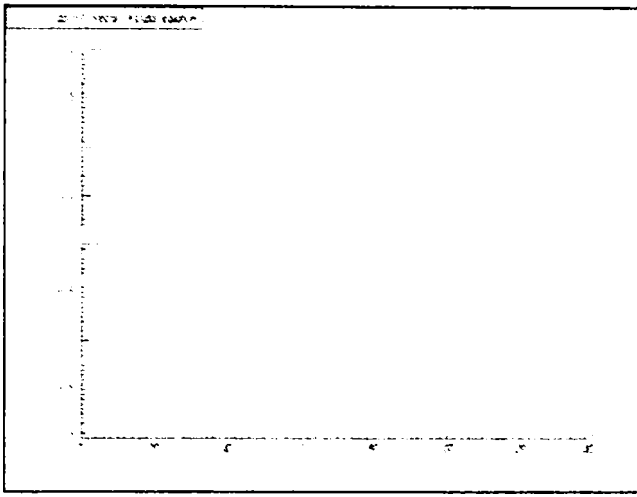


Figure 11. The airgap flux density for the maximum torque

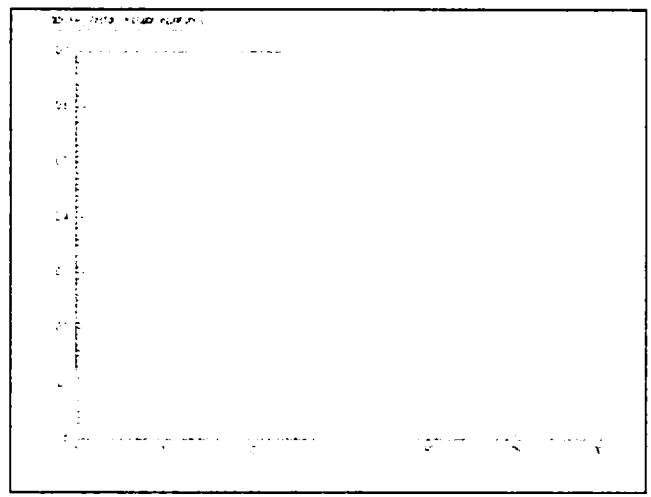


Figure 14. PM surface flux density distribution at peak torque along contour (AB)

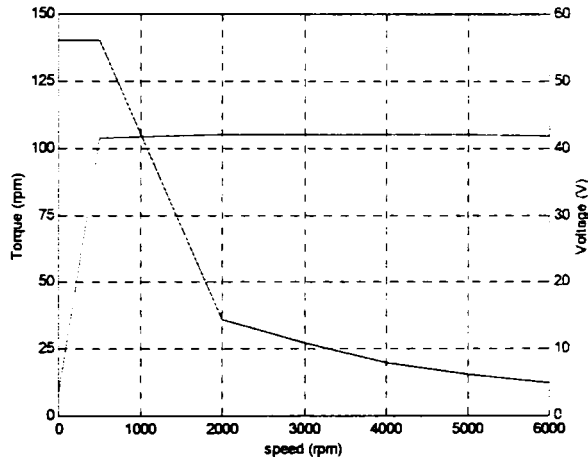


Figure 12. Peak torque and Voltage versus speed

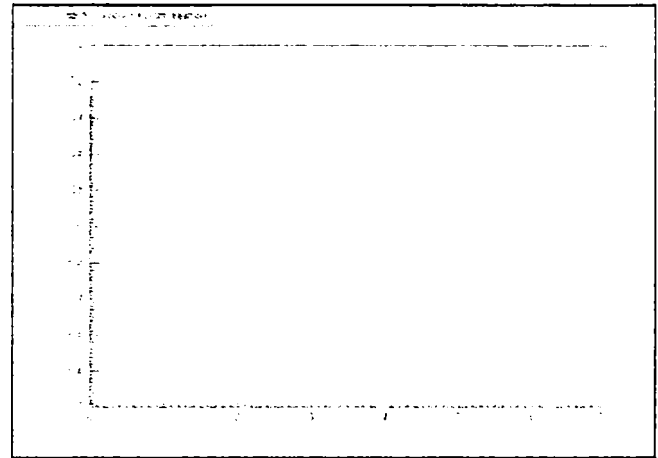


Figure 15. Rotor inter-barriers flux density distribution at peak torque along contour (CD)



Figure 13. Efficiency versus speed at peak torque

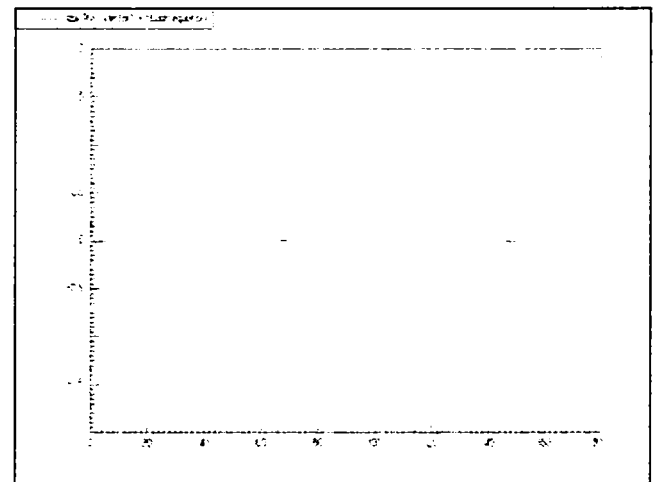


Figure 16. Stator tooth / slot flux density at peak torque along contour (EF)

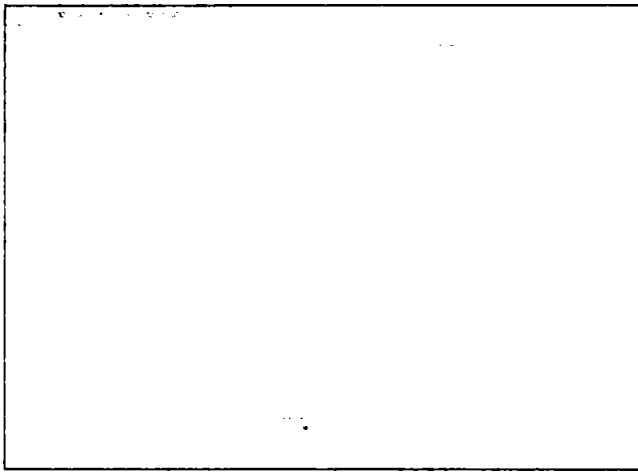


Figure 17. Stator tooth slot flux density distribution at peak torque along contour (GH)

IV DISCUSSION AND CONCLUSION

The sample numerical results obtained so far warrant conclusion such as:

- the PM assisted RSM is able of high peak torque densities (4.33 N/mm^2 and 16 A/mm^2).
- the magnetic saturation level is moderately large as documented with airgap, stator teeth, core and rotor iron flux densities values.
- at peak torque the PMs do not demagnetise as the flux density does not change sign along contour AB.
- the efficiency at maximum speed is 90 % while it is more than 73 % above 500 rpm.
- The peak kW / design (peak) kVA ratio, 0.568, is quite good for the application.

A test rig is under way with results due soon.

REFERENCES

[1] P.J.McCleer, I.Miller, A.R.Gale, M.W. Degner, F. Leonardi, „Nonlinear model and momentary performance capability of a cage induction machine as an automotive starter - alternator“, Record of IEEE – IAS – 1999 Annual Meeting.

[2] G. Alenbernd, H. Schafer, L. Wahner, „Vector controlled crankshaft starter generator for Motor vehicle“, Record of ICEM 2000, 28 – 30 August, Espoo, Finland, vol. 3, pp. 1549 – 1553.

[3] M. Paul, W. Hofmann, D. Bochinia, „Design of permanent magnet motors for a hybrid electric vehicle“, Record of ICEM – 2000, 28 - 30 August, Espoo, Finland, vol. 3, pp. 1535 – 1539.

[4] H. Bausch, A. Graaf, A.B.A. Nickel, „A switched reluctance and an induction machine in a drive train for an electrical vehicle under the conditions of car application“, Record of ICEM – 2000, 28 - 30 August, Espoo, Finland, vol. 3, pp. 1313 – 1316.

[5] M. Bebes, M. Gabbi, E. Hoang, M. Lecrivani, B. Grioni, C. Plante, „SRM design for Starter – Alternator system“, IBID, vol. 3, pp. 1931 - 1935.

[6] R. Blissenbach, G. Henneberger, U. Schafer, W. Hackmann, „Development of a transverse flux traction motor in a direct drive system“, IBID, vol. 3, pp. 1457 – 1460.

[7] E.C. Lovelace, T.M. Iahns, I.L. Kirtley jr., I.M. Lang, „An interior PM Starter / Alternator for automotive applications“, Record of ICEM – 1998, Istanbul, Turkey, vol. 3, pp. 1801 – 1808.

[8] A. Vagati, A. Fratta, P. Gaglielani, G. Franchi, F. Villata, „Comparison of a.c. motor based drives for electric vehicle application“, Record of PCIM – intelligent motion, June 1999, pp. 173 – 181.

[9] A. Lange, W.R. Canders, F. Laube, H. Mosebach, „Comparison of different drive systems for a 75 KW electrical vehicle drive“.

[10] J.G. Kassakian, J.M. Miller, N. Traub, “Automotive electronics power up”, IEEE Spectrum, May 2000

[11] J.G. Kassakian, H.C. Wolf, J.M. Miller, C.J. Hurton, “Automotive electrical systems circa 2005”, IEEE Spectrum, August 1996.

[12] R.Blumel, “Asymmetrical three level converter feeding a 42 / 14 V automobile network”, Intelligent motion, June 1997.

[13] D. Kok, E. Spijker, A. Seibertz, S. Buller, “42 V Energy Storage Systems for Stop – Start Applications in Hybrid Vehicles”, RVS 18, Berlin 2001.

[14] I. Boldea, “Reluctance synchronous machines and drives”, (book), OUP 1996.

PM-Assisted Reluctance Synchronous Motor/Generator (PM-RSM) for Mild Hybrid Vehicles: Electromagnetic Design

Ion Boldea, *Fellow, IEEE*, Lucian Tutelea, and Cristian Ilie Pitic

Abstract—This paper introduces the conceptual design and finite-element method analysis of a permanent-magnet-assisted reluctance synchronous motor/generator for mild hybrid vehicles where a large constant power speed range (6:1) is required and machine volume, converter peak kVA, and battery size are the main constraints. Careful flux-barrier and permanent-magnet sizing, high magnetic saturation, and current density are the main requirements for maximum torque production with constraint obtained. A rated (continuous) power-battery limited is 2.5 kW at 42 V dc, from 1000 to 6000 r/min. The peak torque of 140 N·m is obtained at 202 A (rms/phase) and can be secured up to 500 r/min. Peak power is still 7.85 kW at 6000 r/min at 42 V dc with an efficiency of 90%. Preliminary results on a prototype are also available.

Index Terms—Hybrid vehicle, permanent magnet (PM), reluctance synchronous machine (RSM).

I. INTRODUCTION

THE newly commercial full hybrid vehicles of Toyota and Honda have proven a 40%–50% fuel saving in town driving in comparison with equivalent gasoline-only cars.

This is spectacular progress but it comes with rather large additional electric equipment (\$3000 (U.S.) or so), for the high-voltage power battery life of five years.

Also, the mild hybrid from Toyota makes use of a 42-V battery and a claw-pole generator/motor [1] and produces about 20%–25% fuel saving in town driving while the extra equipment cost is around \$1000 (U.S.).

While many hybrid vehicle prototypes already have adopted the induction machine as motor/generator the dispute over the best solution is far from over.

Quite recently, rather complete studies [2]–[7] and comparisons between induction [8], permanent-magnet (PM) synchronous [4], reluctance synchronous, switched reluctance [5], [6], PM-assisted reluctance synchronous, and PM transverse flux machines [7] have led to the conclusion that the induction motor (IM) has two strong competitors in terms of losses and motor weight: the PM-assisted reluctance syn-

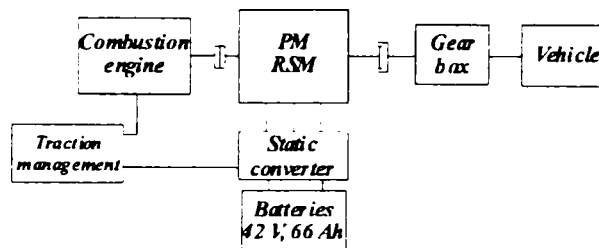


Fig. 1. Mild hybrid vehicle diagram block.

chronous (PM-RSM) [9], [10] and the PM transverse flux machines [11], and the PM-RSM in terms of maximum peak converter kVA at lower total equipment costs and total system losses.

Cost is important but is subject to change when high numbers of vehicles are fabricated under modern automotive manufacturing auspices.

Machine volume, losses, maximum converter kVA, and total loss capitalized costs lead to a multi-objective nonlinear problem.

References [9]–[11] do present results that suggest the PM-RSM is a better solution than the IM, but without a realistic approach to PM-RSM modeling and conceptual design with finite-element method (FEM) analysis. Design aspects, such as the analytical saturation model of [12], or a design method from inverter data [13] and required constant power–speed range to calculate synchronous inductances and electromotive force (EMF), do not yet constitute a rather coherent dimensioning process.

The main goals of this paper are to settle on a practical topology, develop conceptual design for heavy saturation, FEM thorough analysis and verification, mainly in terms of torque versus i_d , i_q currents. Torque, current, voltage, and efficiency for motoring and generating versus speed are given to match very challenging design specifications. Preliminary test results on a prototype are also available.

II. TYPICAL SPECIFICATIONS

The parallel mild hybrid vehicle block diagram is presented in Fig. 1. This topology contains the combustion engine, the electric motor [integrated starter–generator (ISG)], the 42-V battery pack and the power electronics system. The traction system also contains the gearbox.

The main advantage of an ISG system over a conventional starter motor can be found in the fast engine stop/start behavior

Paper IPCSD 03–130, presented at OPTIM 2002, Braşov, Romania, May 16–17, and approved for publication in the IEEE TRANSACTIONS ON INDUSTRY APPLICATIONS by the Electric Machines Committee of the IEEE Industry Applications Society. Manuscript submitted for review November 29, 2002 and released for publication January 20, 2004.

The authors are with the Department of Electrical Machines and Drives, University Politehnica of Timisoara, RO-1900 Timisoara, Romania (e-mail: boldea@lselinux.utt.ro; luci@lselinux.utt.ro; pitic.c@lselinux.utt.ro).

Digital Object Identifier 10.1109/TIA.2004.824434

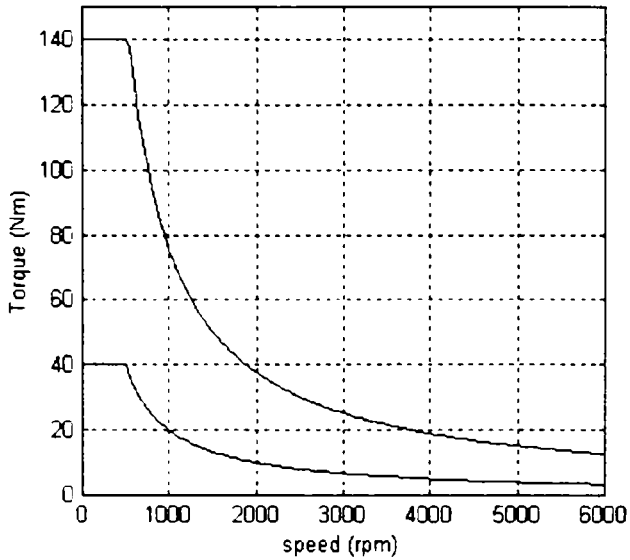


Fig. 2. Torque and power versus speed.

and the potential of electric drive, vibration, and noise during actively controlled engine start-up and shut-down procedures. During launch-assist, the storage system must deliver high power to the ISG system. In the last few years the need for more power led to the new 42-V dc systems instead of an actual 14-V dc [8], [14]–[16]. A mild hybrid vehicle uses this 42-V dc system (three 14-V dc batteries in series) only, for ISG.

Typical specifications for a hybrid (or electric) vehicle application are related to:

- peak torque versus speed envelope;
- continuous constant power speed range;
- maximum current for given dc-link voltage V_{dc} and given maximum EMF at maximum speed, E_1 per phase rms or as seen at battery terminals: E_0 ;
- maximum current density j (A/mm^2);
- losses versus speed for given torque–speed envelope;
- peak torque/kg of active materials;
- total system cost.

A typical wide power speed range for continuous 2.5 kW from 1000 (idle engine speed) to 6000 r/min (direct on the crankshaft drive) is shown in Fig. 2.

The unusually large constant power speed range is typical for a crankshaft motor/generator. The elimination of any additional transmission is, thus, paid for.

The solution is volume (weight) constraint, also, and, consequently, for the maximum torque (developed below base speed) a torque density in the range of 15–20 N·m/kg of active materials (stator and rotor) is required.

On top of that, the maximum phase current (rms) for maximum torque has to be limited, to cut the costs of the converter, for constant power over a 6:1 speed range.

To meet these contradictory specifications a bit of machine oversizing is required, in spite of heavy electrical and magnetic design loadings, together with some inverter oversizing as the voltage required at base speed is notably lower than maximum voltage available. While a simplified analytical mathematical approach of these aspects is, in principle, possible [12], we will adopt here an engineering approach, starting with a practical

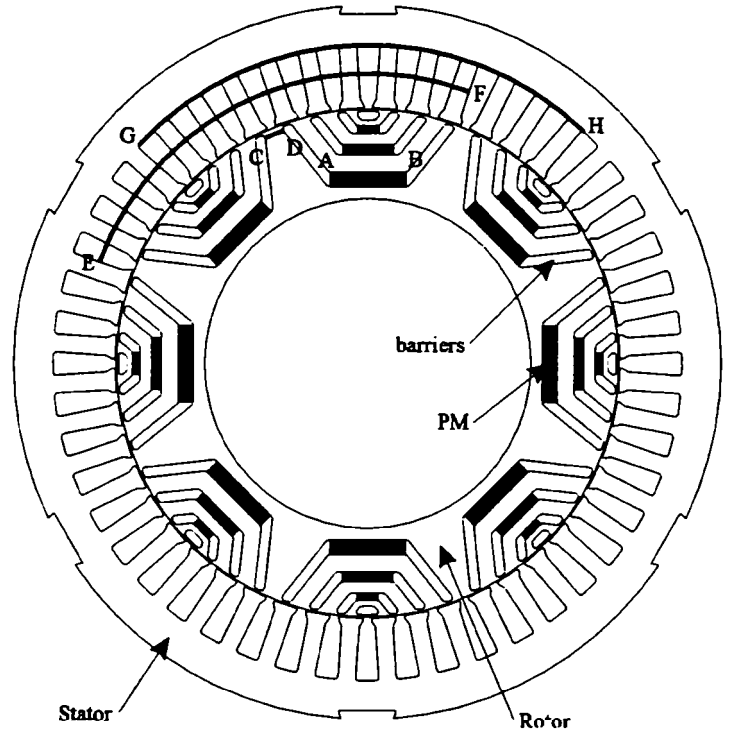


Fig. 3. PM-RSM machine.

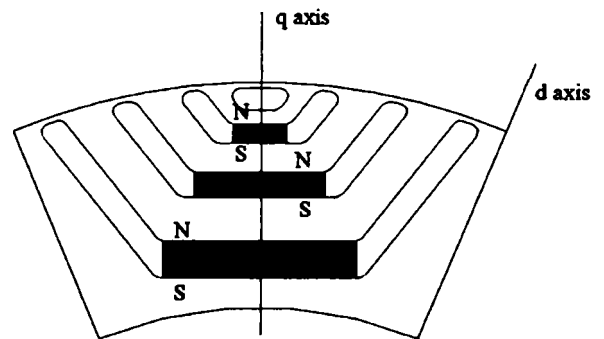


Fig. 4. Rotor design and PMs polarity.

PM-RSM configuration and conceptual design for heavy electrical and magnetic loadings.

III. PRACTICAL CONFIGURATION AND CONCEPTUAL DESIGN ASPECTS

In Fig. 3, the design configuration for the PM-RSM machine is presented. The stator laminations were chosen from a suitable existing motor in order to lower the costs of the prototype.

The rotor topology and the polarization of the magnets are presented in Fig. 4. The rotor design (the PM dimensions) was made with FEM assistance, by trial and error with seven flux bridges per pole to increase saliency and reduce cogging torque as the common lowest multiplier of $N_s = 48$ slots and 56 rotor bridges (virtual slots) is large enough.

Also, attempts have been made to reduce the PM flux density harmonics in the air gap by increasing the PM radial dimension of flux barriers toward the shaft.

In what follows we describe in sequence the equations that provide the most important variables in the analytical design.

The number of poles has been chosen at $2p = 8$. Also, the tangential shear stress f_{tk} corresponding to peak torque T_{ek} was chosen as $f_{tk} \approx 4 \text{ N/cm}^2$.

The ratio λ of stack length l_{stack} is chosen with respect to stator bore diameter D_{is} : $l_{\text{stack}}/D_{\text{is}} \approx 2$. This way D_{is} comes from

$$f_{tk} = T_{ck} \cdot \frac{2}{D_{\text{is}}} \cdot \frac{1}{\pi \cdot D_{\text{is}}^2 \cdot \lambda}, \quad \lambda = \frac{l_{\text{stack}}}{D_{\text{is}}} \quad (1)$$

For the PM flux, we first calculate the rated rms phase voltage for given V_0 (dc battery voltage)

$$V_1 = k_{\text{max}} \cdot V_0 \cdot \frac{\sqrt{2}}{\pi} \quad (2)$$

where k_{max} is voltage utilization and V_0 is battery voltage.

The maximum allowable PM EMF, E_1 , at maximum speed, is limited to

$$E_1 = V_1 \times (1.3 \div 1.5). \quad (3)$$

Once E_1 is known the rms value of flux linkage per pole in the air gap produced by the PM should be

$$\Psi_{\text{PMRMS}} = \frac{E_1}{2 \cdot p \cdot \pi \cdot n_{\text{max}}} \quad (4)$$

where p is the number of poles pairs ($2p = 8$) and n_{max} is the maximum speed.

The iron bridges in the rotor (above the flux barriers) should not consume more than $k_{\text{bridge}} = 0.2$ of PM flux to saturate heavily. Consequently, the PM air-gap flux density B_{gPM} multiplied by the turns per coil is

$$n_c B_{\text{gPM}} = \frac{\Psi_{\text{PMRMS}} \cdot \sqrt{2}}{k_{w1} \cdot 2 \cdot p \cdot q \cdot \tau \cdot l_{\text{stack}} \frac{1-k_{\text{bridge}}}{\pi \cdot a}} \quad (5)$$

where

n_c	number of turns per coil;
B_{gPM}	PMs flux density;
k_{w1}	windings factor;
q	number of slots/pole/phase ($q = 2$);
τ	pole pitch;
k_{bridge}	rotor core bridge PM flux linkage ratio;
l_{stack}	stack length;
a	current path count.

This is the maximum product of n_c and B_{gPM} , and in our design $B_{\text{gPM}} = 0.3$ T,

$$n_c = \text{round} \left(\frac{n_c B_{\text{gPM}}}{B_{\text{gPM}}} \right) \frac{\text{turns}}{\text{coil}} \quad (6)$$

For the case in point $n_c = 14$ turns/coil and $a = 8$ current paths. The value of B_{gPM} is chosen and then realized by changing the length of various PMs in the flux barriers with FEM checks. Rotor iron bridge thickness w_b is

$$w_b = \frac{k_{\text{bridge}} \cdot \Psi_{\text{PMRMS}} \cdot \sqrt{6}}{4 \cdot l_{\text{stack}} \cdot B_{\text{bridge}} \cdot q \cdot n_c \frac{2 \cdot p \cdot k_{w1}}{a}} \quad (7)$$

where B_{bridge} is the rotor iron bridge saturation flux density.

The magnetic saturation acts along both axes. We suppose that the air-gap flux density in fact counts and it has a given value B_g . Then, we calculate the saturation factors k_{sd} and k_{sq} considering that the stator core saturation corresponds to the

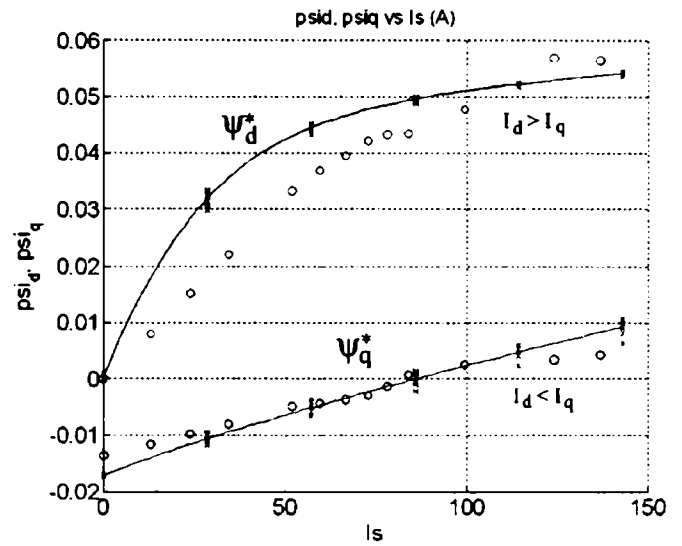


Fig. 5. FEM—extracted magnetization curves and from standstill current decay tests (o: test points).

resultant air-gap flux density. At start k_{sd} and k_{sq} are adopted and then checked and corrected after FEM calculations.

The I_d and I_q currents can be calculated as

$$I_d = \frac{a}{n_c} B_{gd} \pi \cdot \frac{k_c \cdot g \cdot (1 + k_{sd})}{4.2426 \cdot \mu_0 \cdot 2 \cdot q \cdot k_{dm} \cdot k_{w1}} \quad (8)$$

$$I_q = k_i \cdot \left[\frac{B_{\text{gPM}}}{B_{gd}} - \sqrt{\left(\frac{B_g}{B_{gd}} \right)^2 - 1} \right] \cdot \frac{k_{dm} \cdot (1 + k_{sq})}{k_{qm} \cdot (1 + k_{sd})} \quad (9)$$

where k_{dm} and k_{qm} are unsaturated coefficients for L_{dm} and L_{qm} [13].

The I_s current results as

$$I_s = \sqrt{I_d^2 + I_q^2} \quad (10)$$

$$T = 3 \cdot p \cdot I_d \cdot \left[\Psi_{\text{PMRMS}} \cdot (1 - k_{\text{bridge}}) + I_q \cdot \left(\frac{L_m \cdot k_{dm}}{1 + k_{sd}} - \frac{L_m \cdot k_{qm}}{1 + k_{sq}} \right) \right] \quad (11)$$

The iron losses are calculated with the standard analytical formulas accounting for single-value flux densities in stator teeth and back iron and including both eddy-current and hysteresis losses [17], [18].

The phase current was maximum in phase A and -50% of it in phases B and C and the rotor was placed in various positions (θ_{er}) and then the flux linkage in all coils of phases A , B , and C , has been calculated through FEM. By Park transformation, Ψ_d and Ψ_q have been calculated for different values of I_s and θ_{er} .

The resulting magnetization curves $\Psi_d(I_s)$ and $\Psi_q(I_s)$ gathering all these are shown in Fig. 5 and they demonstrate the existence of some cross-coupling saturation. However, still, for various combinations, $I_d > I_q$, there is a unique magnetization curve along axis d , $\Psi_d^* = f(I_m)$, and also for $I_q > I_d$ a unique magnetization curve for axis q exists. Both are functions

TABLE I
PM-RSM MAIN PARAMETERS

Geometric parameters		Value
Stator outer diameter	SOD	245.2 mm
Rotor outer diameter	ROD	174.2 mm
Rotor inner diameter	RID	113 mm
Airgap	g	0.4 mm
Stack length	l_{stack}	68 mm
PM parameters at 20 °C	B_r	0.87 T
	H_c	660000 A/m
Current path	a	8
Turns per coil	n_c	14
Current density at peak torque	J_{Comax}	16 A/mm ²
Stator phase resistance	R_s	0.039 Ω

of total magnetization current I_s . The actual $\Psi_d = L_d(I_s)I_d$ and $\Psi_q = L_q(I_s)I_q - \Psi_{PM}$ while from the magnetization curves on Fig. 5, $L_d(I_s) = \Psi_d * / I_s$ and $L_q(I_s) = (\Psi_q * + \Psi_{PM}) / I_s$.

Choosing the value of air-gap flux density in (9) we consider that cross coupling is sufficiently illustrated by assuming that the saturation factors k_{sd} and k_{sq} depend only on the chosen resultant air-gap flux density fundamental B_g . Then, for a given B_g , given torque, k_{sd} , k_{sq} , from (8)–(10), the values of d – q currents I_d and I_q and flux density along d axis B_{gd} are calculated iteratively. Then, the stator winding losses are calculated and then B_g is modified until the winding losses or other optimization criterion is satisfied. For the peak torque, the minimum of winding losses is targeted. Based on the above methodology, a MATLAB program was built and used repeatedly. Through the FEM it was then corrected in torque production.

Finally, based on the above rationale the chosen main dimensions are given in Table I, for $T_{ek} = 140 \text{ N} \cdot \text{m}$.

Finally, for the peak torque, the maximum phase rms current is $I_{phk} = 202 \text{ A}$ for a peak current density $J_{Comax} = 16 \text{ A/mm}^2$.

The peak kW/kVA design ratio was calculated at 0.658. These findings are considered satisfactory for the application.

The efficiency of the motor is

$$\eta = \frac{P_m - P_{mec}}{P_m + p_{copper} + p_{iron}} \quad (12)$$

In Fig. 6, with FEM support, the torque values for different rotor positions are shown. The maximum torque (140 N·m) is obtained at 11.75 mechanical degrees. This means 47 electrical degrees.

In Fig. 7, the PM flux lines are shown. Figs. 8 and 9 present the PM air-gap flux and flux density. The PM flux density in the air gap is approximately 0.3 T and its distribution is remarkably uniform.

The flux lines for the maximum obtained torque (140 N·m) are shown in Fig. 10, and Figs. 11 and 12 represent the resultant air-gap flux and flux density in the machine.

With FEM corrections for torque, the above described design method, instrumented by the mentioned Matlab program, which also includes the standard d – q voltage equations of the machine, was used to estimate the torque, phase voltage (rms), battery current (Fig. 13), and efficiency (Fig. 14) versus speed. The magnetic material loading is also checked using FEM simulations.

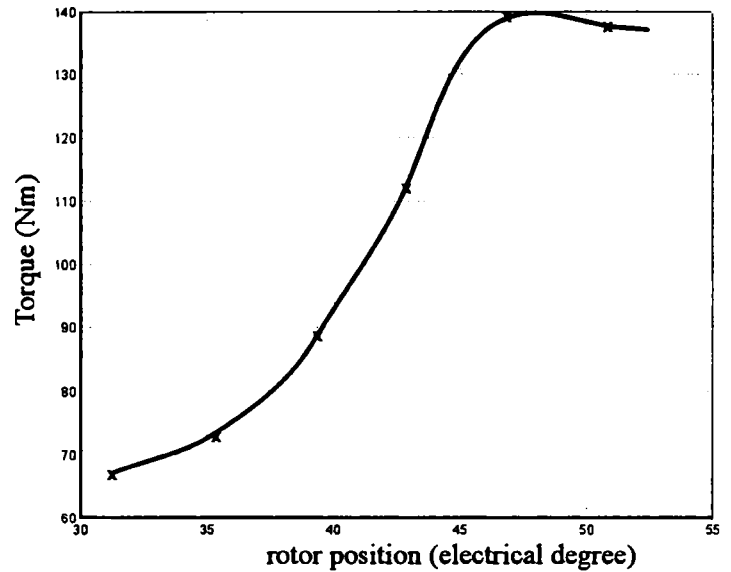


Fig. 6. FEM torque versus rotor position (maximum current).

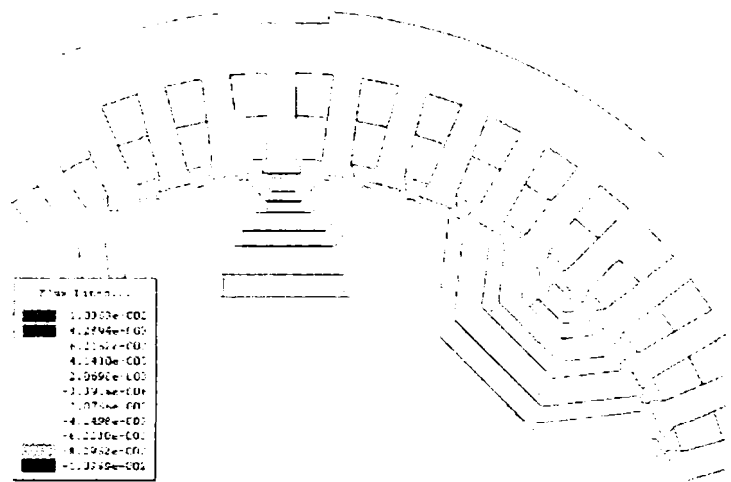


Fig. 7. PM flux lines in the machine.

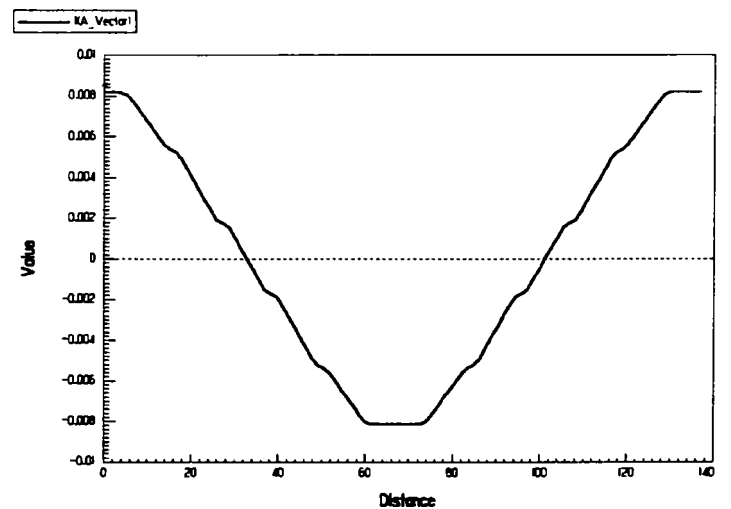


Fig. 8. PM air-gap flux distribution.

Fig. 15 shows the flux density distribution at peak torque on the PM surface along contour (AB) marked in Fig. 3. The flux density distribution at peak torque in rotor inter-barriers, contour (CD), is shown in Fig. 16. Stator tooth and slot flux density at peak torque are shown along the middle of the teeth, contour

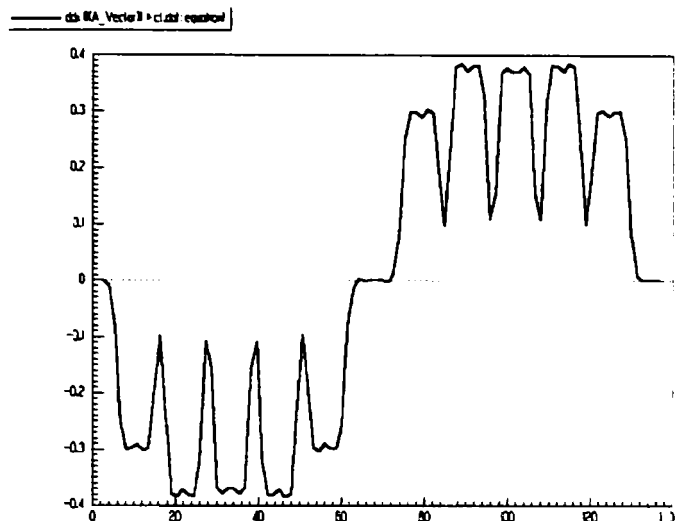


Fig. 9. PM air-gap flux density.

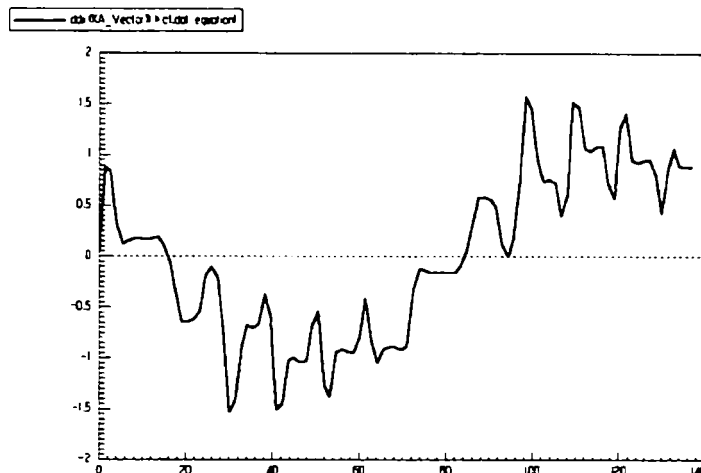


Fig. 12. Air-gap flux density for maximum torque.

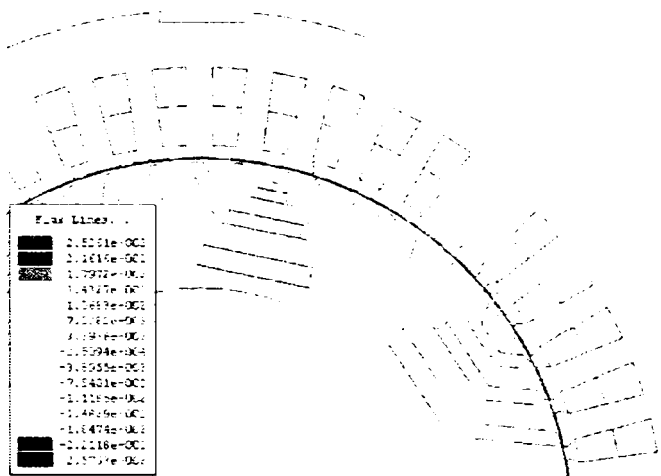


Fig. 10. Flux lines for maximum torque (140 N·m).

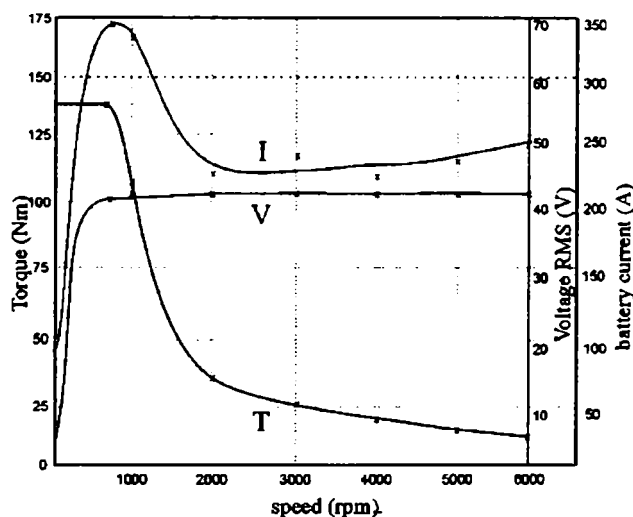


Fig. 13. Peak torque, voltage rms, and battery current versus speed (from FEM—corrected analytical model).

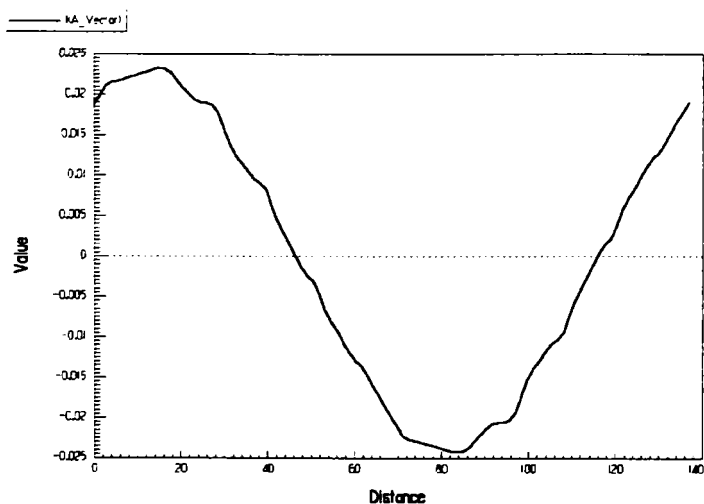


Fig. 11. Air-gap flux for maximum torque.

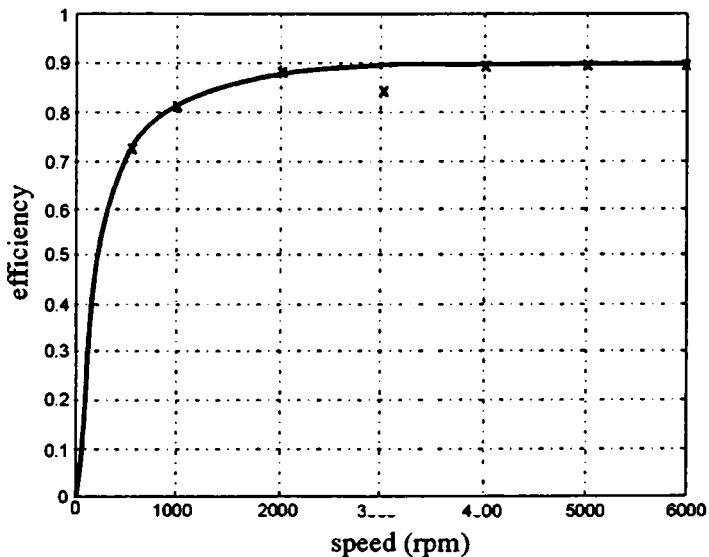


Fig. 14. Efficiency versus speed at peak torque (from FEM—corrected analytical model).

(EF), in Fig. 17 and along the bases of the teeth, contour (GH), in Fig. 18.

It may be concluded that the PM-assisted reluctance synchronous motor gives good performance with good values for both torque density and kVA.

IV. EXPERIMENTAL WORK

A prototype based on the above design has been built and some experiments have been run to feel more confident

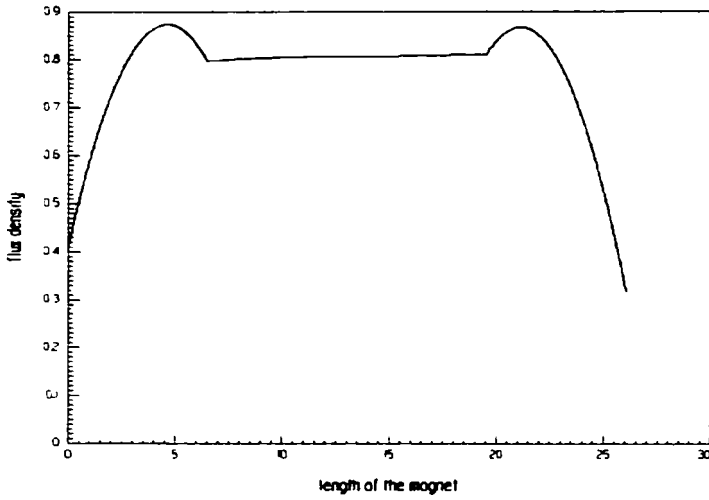


Fig. 15. PM surface flux density distribution at peak torque along contour (AB).

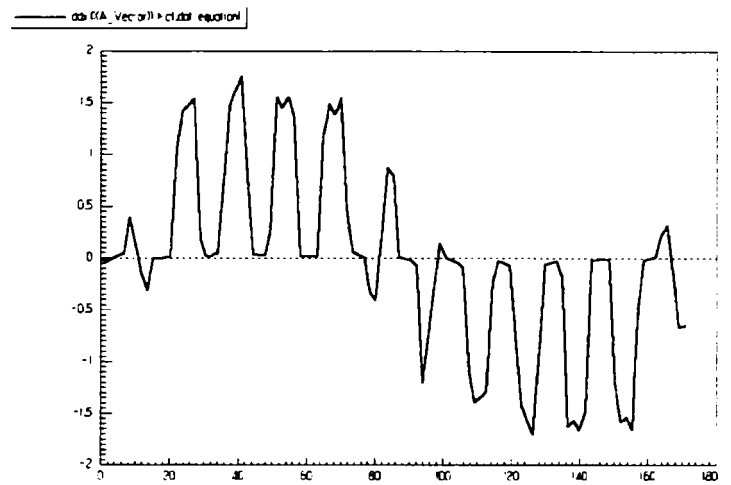


Fig. 18. Stator tooth slot flux density distribution at peak torque along contour (GH).

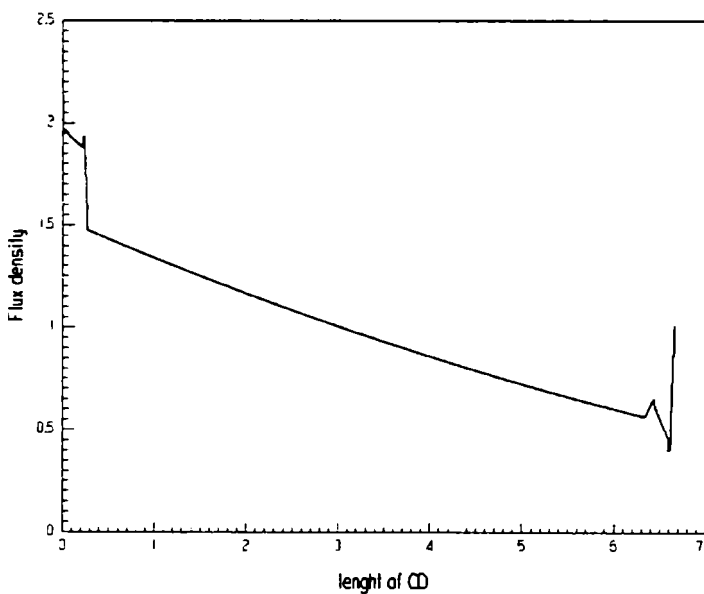


Fig. 16. Rotor inter-barriers flux density distribution at peak torque along contour (CD).

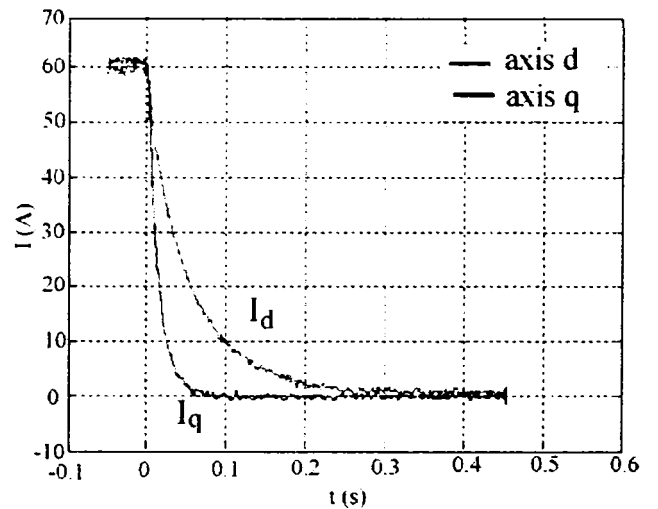


Fig. 19. Sample dc current decay at standstill in *d* and *q* axes.

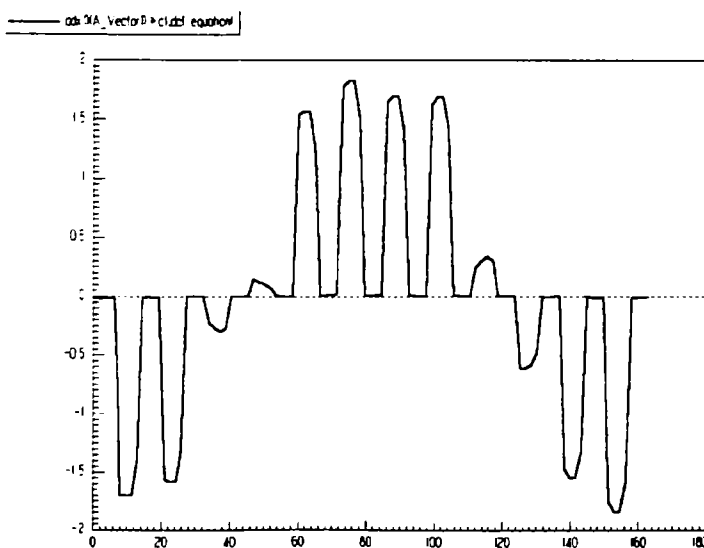


Fig. 17. Stator tooth/slot flux density at peak torque along contour (EF).

regarding the design procedure. First, from no-load tests, the PM flux linkage Ψ_{PM} was calculated as $\Psi_{PM} = 0.027$ Wb. Fig. 5 shows $\Psi_{PMFEM} = 0.03$ Wb (at $I_s = 0$ in axis *q*). The 10% difference may come from the fact that the actual PMs are thinner than the designed ones by 10%–15%. Then, it was decided that the *d*–*q*–axes magnetization curves are key verification performance indexes and, to validate them, standstill dc current decay tests in axes *d* and *q* have been run. A PWM inverter was used for the scope. Sample current decays in axes *d* and *q* are shown in Fig. 19. The complete dc current decay experimental results are visible in Fig. 5 as small circles. Although the stator leakage inductance flux has been subtracted from the experimental results, after measuring the leakage inductance as the homopolar inductance, there is still notable discrepancy between theory and tests, mainly along *d* axis ($L_d > L_q$). Looking for answers we did notice that the air gap in the real machine is larger than the 0.4 mm value considered in the calculations by as much as about 0.12 mm. On the other hand, the rotor back iron of the prototype is much larger than in the design, which may explain why, when the machine is oversaturated, the measured flux is higher than the calculated one in axis *d*.

V. DISCUSSION AND CONCLUSION

The sample numerical results obtained with FEM backup warrant conclusions such as the following.

- The PM-assisted RSM is capable of high peak tangential force densities (4.33 N/cm^2 at 16 A/mm^2).
- The magnetic saturation level is moderately large as documented by air-gap, stator teeth, core, and rotor iron flux densities values.
- At peak torque, the PMs do not demagnetize as the flux density does not change sign along contour AB (Fig. 15).
- The efficiency at maximum speed is 90% while it is more than 73% above 500 r/min.
- The peak kW/design (peak) kVA ratio of 0.568 is quite good for the application.

Preliminary no-load and standstill dc current decay tests results on a full-scale prototype partially validate the theory of the paper.

More work seems needed to fully validate the design methodology in this highly saturated machine.

REFERENCES

- [1] T. Teratani, K. Kuramochi, H. Nakao, T. Tachibana, K. Yagi, and S. Abou, "Development of toyota hybrid system (THS-M) with 42V powernet," in *Proc. IEMDC*, vol. 1, Madison, WI, June 1–4, 2003, pp. 3–10.
- [2] P. J. McCleer, I. Miller, A. R. Gale, M. W. Degner, and F. Leonardi, "Nonlinear model and momentary performance capability of a cage rotor induction machine used as an automotive combined starter-alternator," in *Conf. Rec. IEEE-IAS Annu. Meeting*, vol. 1, 1999, pp. 502–508.
- [3] G. Alenbernd, H. Schafer, and L. Wahner, "Vector controlled crankshaft starter generator for motor vehicle," in *Proc. ICEM 2000*, vol. 3, Espoo, Finland, Aug. 28–30, 2000, pp. 1549–1553.
- [4] M. Paul, W. Hofmann, and D. Bochinia, "Design of permanent magnet motors for a hybrid electric vehicle," in *Proc. ICEM 2000*, vol. 3, Espoo, Finland, Aug. 28–30, 2000, pp. 1535–1539.
- [5] H. Bausch, A. Graaf, and A. B. A. Nickel, "A switched reluctance and permanent magnet torque converter for electric car application," in *Proc. ICEM 2000*, vol. 3, Espoo, Finland, Aug. 28–30, 2000, pp. 1313–1316.
- [6] M. Bebes, M. Gabbi, E. Hoang, M. Lecrivain, B. Grioni, and C. Plasse, "SRM design for starter-alternator system," in *Proc. ICEM 2000*, vol. 3, Espoo, Finland, Aug. 28–30, 2000, pp. 1931–1935.
- [7] R. Blissenbach, G. Henneberger, U. Schafer, and W. Hackmann, "Development of a transverse flux traction motor in a direct drive system," in *Proc. ICEM 2000*, vol. 3, Espoo, Finland, Aug. 28–30, 2000, pp. 1457–1460.
- [8] R. Blumel, "Asymmetrical three level converter feeding a 42/14 V automobile network," in *Proc. PCIM—Intelligent Motion*, June 1997, pp. 233–242.
- [9] E. C. Lovelace, T. M. Jahns, I. L. Kirtley jr, and I. M. Lang, "An interior PM starter/alternator for automotive applications," in *Proc. ICEM'98*, vol. 3, Istanbul, Turkey, 1998, pp. 1801–1808.
- [10] A. Vagati, A. Fratta, P. Gaglielani, G. Franchi, and F. Villata, "Comparison of a.c. motor based drives for electric vehicle application," in *Proc. PCIM—Intelligent Motion*, June 1999, pp. 173–181.
- [11] A. Lange, W. R. Canders, F. Laube, and H. Mosebach, "Comparison of different drive systems for a 75 kW electrical vehicle drive," in *Proc. ICEM 2000*, vol. 3, Espoo, Finland, Aug. 28–30, 2000, pp. 1308–1312.
- [12] E. C. Lovelace, T. M. Jahns, and J. H. Lang, "A saturating lumped-parameter model for an interior PM synchronous machine," *IEEE Trans. Ind. Applicat.*, vol. 38, pp. 645–650, May/June 2002.
- [13] B.-H. Bae and S.-K. Sul, "Practical design criteria of permanent magnet synchronous motor for 42V integrated starter-generator," in *Proc. IEMDC 2003*, vol. 2, Madison, WI, June 1–4, 2003, pp. 656–662.
- [14] J. G. Kassakian, J. M. Miller, and N. Traub, "Automotive electronics power up," *IEEE Spectr.*, vol. 37, pp. 34–39, May 2000.
- [15] G. Kassakian, H. C. Wolf, J. M. Miller, and C. J. Hurton, "Automotive electrical systems circa 2005," *IEEE Spectr.*, vol. 33, pp. 22–27, Aug. 1996.
- [16] D. Kok, E. Spijker, A. Seibertz, and S. Buller, "42 V energy storage systems for stop-start applications in hybrid vehicles," in *Proc. EVS 18*, Berlin, Germany, 2001.
- [17] Boldea and S. A. Nasar, *The Induction Machine Handbook*. Boca Raton, FL: CRC Press, 2002.
- [18] Boldea, *Reluctance Synchronous Machines and Drives*. London, U.K.: Oxford Univ. Press, 1996.



Ion Boldea (M'77–SM'87–F'00) received the M.S. and Ph.D. degrees in electrical engineering from the University Politehnica of Timisoara, Timisoara, Romania, in 1967 and 1973, respectively.

He is currently a full Professor at the University Politehnica of Timisoara. He has visited universities in the U.S. and the U.K. repeatedly and has published extensively on linear and rotary electric machines, drives and power electronics. His latest books (with S.A. Nasar) are *Induction Machine Handbook* (Boca Raton, FL: CRC Press, 2001) and *Linear Motion Electromagnetic Devices* (London, U.K.: Taylor & Francis, 2001). He is an Associate Editor of *Electric Power Components and Systems* and Director of the *Internet-only Journal of Electric Engineering* (www.jee.ro). He has presented keynote addresses and intensive courses and works as a Consultancy in the U.S., Europe, and Asia.

Prof. Boldea is a member of the Industrial Drives and the Electric Machines Committees of the IEEE Industry Applications Society (IAS) and was Co-Chairman of the OPTIM International Conferences (IAS sponsored) in 1996, 1998, 2000, and 2002.



Lucian Tuole was born in A.B., Romania. He received the B.E. and Ph.D. degrees in electrical engineering from the University Politehnica of Timisoara, Timisoara, Romania, in 1989 and 1997, respectively.

He is currently an Assistant Professor at the University Politehnica of Timisoara in the Department of Electric Drives and Power Electronics. His research interests include design and control of electrical machines and drives.



Cristian Ilie Pitic was born in Hunedoara, Romania. He received the B.E. degree in electrical engineering from the Faculty of Engineering of Hunedoara, Hunedoara, Romania, in 2000. He is currently working toward his Ph.D. degree in the Department of Electric Drives and Power Electronics, University Politehnica of Timisoara, Timisoara, Romania.

His research interests include design, testing, and control of permanent-magnet-assisted reluctance synchronous motors for electric and hybrid vehicles.

The PM – Assisted Reluctance Synchronous Starter / Generator (PM – RSM): Generator Experimental Characterization

Cristian Ilie Pitic¹, Lucian Tutelea¹, Ion Boldea¹, Frede Blaabjerg²

¹Department of Electrical Machines and Drives, University Politehnica of Timisoara, V.Parvan 2, RO - 300223 Timisoara, Romania, Tel. +40-56-204402, email: pitic.c@lselinux.utt.ro, luci@lselinux.utt.ro, boldea@lselinux.utt.ro

²Institute of Energy Technology, Aalborg University, Pontoppidanstraede 101, 9220 Aalborg East – Denmark, Tel: +4596359254, email: fbl@iet.auc.dk

Abstract – Permanent Magnet – assisted Reluctance Synchronous Machines (PM - RSM) are well known for their lower initial costs and losses in a very wide constant power – speed characteristic. Therefore they are very suitable for hybrid or electrical vehicles. In this application a very good torque control is needed and the parameters of the machine have to be known precisely.

The present paper introduces a series of the tests for parameters and efficiency determination of a PM - assisted RSM in the generator mode. The testing methods consist of standstill tests (dc decay), generator no load testing with capacitor and on load ac and diode-rectifier dc tests. Satisfactory results are obtained but some unresolved questions are also raised.

Keywords – permanent magnets, reluctance synchronous machine, parameter determination.

I. INTRODUCTION

There is a continuous demand for better performance, lower emissions, and improved fuel economy in today's vehicles. Therefore, the manufacturers are investigating all kind of feature (electric power steering, electromechanical valves, etc) for the scope.

In order to meet this need for power a practical idea is considered – to be replacing the starter and the alternator in a vehicle with an electronically controlled very competitive electrical machine. Such a machine, mounted on the crankshaft, offers a compact package and a fast response in matter of transmitting the torque to the shaft.

The interior PM assisted Reluctance Synchronous Machine can be used for the scope. The need for a good efficiency in a very wide power-speed range of 6:1 in a hybrid electric vehicle can be accomplished by using this kind of machine when it operates at high flux densities [6, 12].

Because a very fast, robust and precise torque and power control is required, the parameters of the machine have to be known very well.

According to [2], the parameters cannot be determined by IEC Standard recommendations, therefore in this paper a combination of methods is proposed.

The following testing methods are considered in the paper:

- Standstill tests for parameters - flux decay response;
- No load (with capacitors) and short circuit testing;
- On load ac and dc testing with capacitor excitation and resistive load.

The flux decay responses at standstill provide full information about the magnetic saturation in the machine, which is heavy for peak torque in axis d and small in axis q (with PM). The noload generator test with capacitors at terminals perform at various speeds is used both to separate the core losses and to reassess the magnetic saturation with the machine in motion. Finally, the onload ac and dc testing is used not only for efficiency computation, but also for internal angle and L_d , L_q estimation on load. The corroboration of the proposed tests hopefully leads to comprehensive characterisation of PM – RSM. Capacitor excitation test on noload and onload are claimed to be novel in our approach.

II. PM-RSM PROTOTYPE SPECIFICATIONS

A photograph of the PM - RSM prototype is presented in Figure 1, and the configuration of the rotor lamination, with the marks for the PM's, appears in Figure 2.

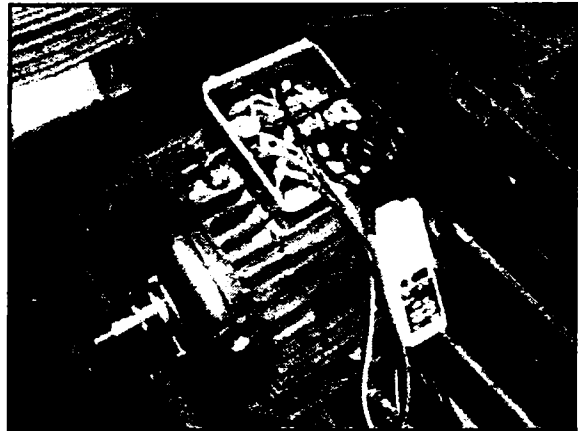


Figure 1. Permanent Magnet – Reluctance Synchronous Machine (PM – RSM) prototype.

The main dimensions of prototype are presented in Table 1. The experimental setup contains a belt transmission 10 / 13 kW (1500 / 3000 rpm) and an induction motor driven by an ACS 600 inverter (Figure 3).

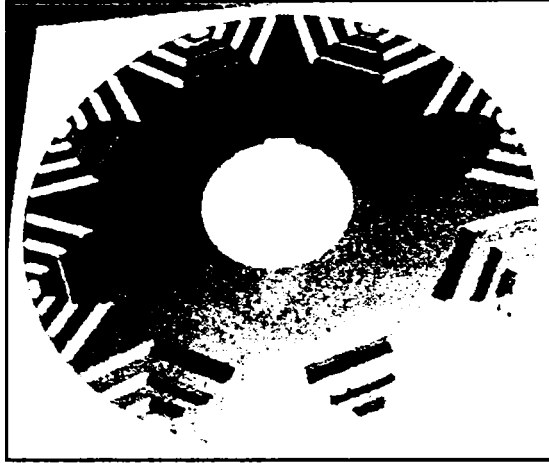


Figure 2. Reluctance Synchronous Machine lamination with permanent magnets

TABLE 1
Design output data of the developed prototype

Geometric parameters		Value
Stator outer diameter	SOD	245.2 mm
Rotor outer diameter	ROD	174.2 mm
Rotor inner diameter	RID	113 mm
Airgap	g	0.4 mm
Stack length	l_{stack}	68 mm
Number of slot/pole/phase	q	2
PM parameters at 20 °C	B_r	0.87 T
	H_c	660000 A/m
Current path	a	8 / 4 *
Number of stator slots	N_s	48
Peak torque in motoring	T_{ek}	140 Nm
Current density at peak torque	J_{Comax}	16 A / mm ²

* Though the machine was designed for 8 current paths, for generating two 4 path connections in series have been used for convenience.

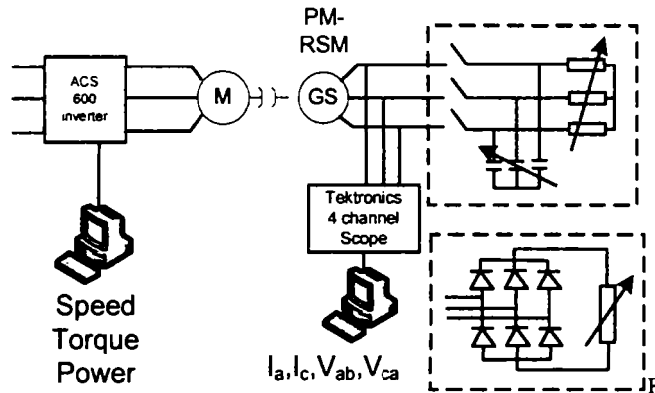


Figure 3. The experimental setup with the belt transmission induction motor driven by an ACS 600 inverter and the ac and diode rectifier dc resistive load.

A. Model description of the PM - RSM:

The d - q model steady state equations are [12]:

$$\begin{aligned} i_q \cdot R_s + V_q &= \omega_r \cdot \Psi_d \\ i_d \cdot R_s + V_d &= -\omega_r \cdot \Psi_q \\ \Psi_q &= L_q \cdot i_q - \Psi_{PM} \\ \Psi_d &= L_d \cdot i_d \\ V_d &= -V_s \cdot \cos\delta_v \\ V_q &= -V_s \cdot \sin\delta_v \\ 0 < \delta_v < 90^\circ \end{aligned} \quad (1)$$

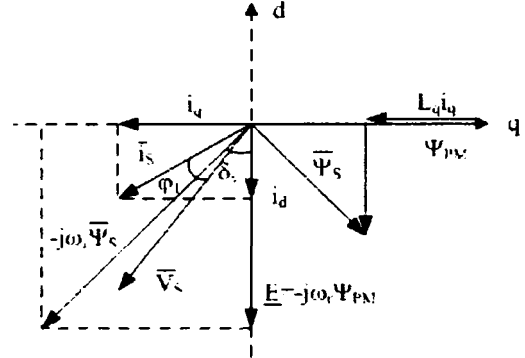


Figure 4. Vector diagram of PM - RSM for generating operation

$$\begin{aligned} I_q &= -I_s \cdot \sin(\delta_v + \phi_1) & I_s &= I_1 \sqrt{2} \\ I_d &= -I_s \cdot \cos(\delta_v + \phi_1) & V_s &= V_1 \sqrt{2} \end{aligned} \quad (3)$$

$$\Psi_d = \frac{-V_s \cos\delta_v - R_s I_s \cos(\delta_v + \phi_1)}{\omega_r} \quad (4)$$

$$\Psi_q = \frac{V_s \sin\delta_v + R_s I_s \sin(\delta_v + \phi_1)}{\omega_r}$$

See Figure 4 for visualization of the different components.

The torque in the machine can be estimated by:

$$T = \frac{3}{2} p_1 (\Psi_{PM} + (L_d - L_q) \cdot I_q) \cdot I_d \quad (5)$$

The copper and iron losses can be written:

$$\begin{aligned} P_{Cu} &= \frac{3}{2} R_s \cdot (I_d^2 + I_q^2) \\ P_{fe} &= \frac{3}{2} \frac{\omega_r^2}{R_{iron}} \left[(L_q I_q - \Psi_{PM})^2 + (L_d I_d)^2 \right] \end{aligned} \quad (6)$$

B. Permanent magnets flux (Ψ_{PM}):

The PM's flux is considered to be constant and can be calculated from no-load test's with:

$$\Psi_{PM} = \frac{V_0 \cdot \sqrt{2}}{2 \cdot \pi \cdot p_1 \cdot n} \quad (7)$$

Where: V_0 - no-load voltage;

III. STANDSTILL TESTING

The d – q inductances L_d and L_q are first measured in a standstill test. In this method the machine is set in d - axis (by feeding it with 5 V ac and moving the rotor until the current is minimum). With the experimental setup in Figure 5 we can determine $L_d = f(I_d)$. Then, changing the connections – in q - axis – the measurements are repeated and $L_q = f(I_q)$ is obtained.

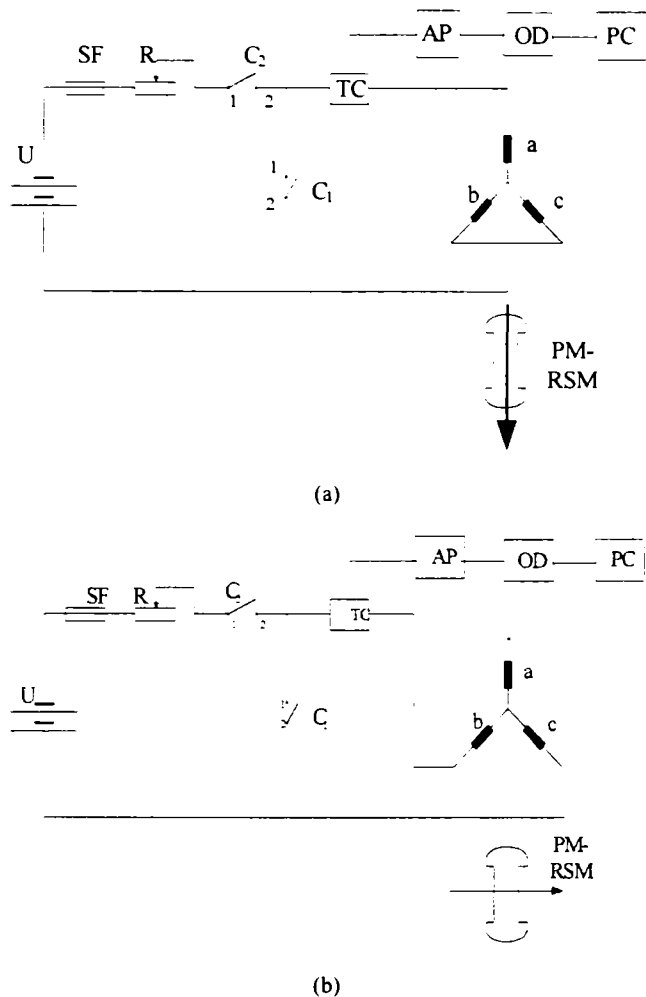


Figure 5. Experimental setup for dc decay tests of PM - RSM: (a) - in d axis, (b) – in q axis.

In figure 5:

- SF – fuse (63 A);
- R – variable resistor ($I = 7 \div 63$ A);
- U – battery voltage;
- AP – adapter (for the visualisation of the current on the oscilloscope);
- OD – Tektronix 4 channel oscilloscope.

The current decay is acquired in d - and q - axes and shown in Figure 6. The stator resistance was calculated to be 0.039Ω .

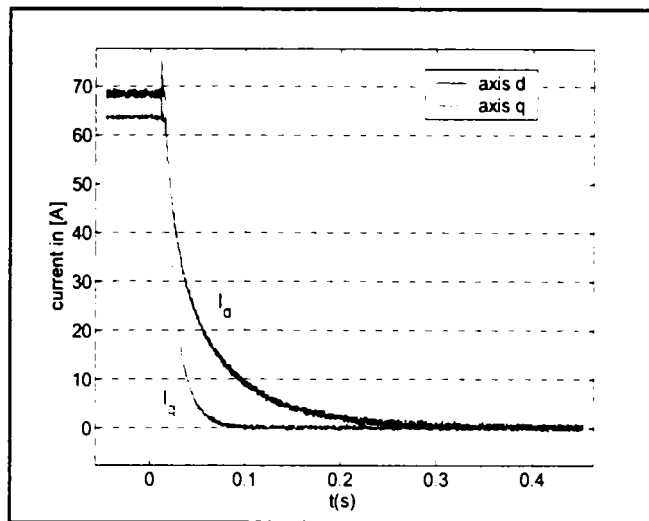


Figure 6. Dc current decay at standstill in the d - and q – axis

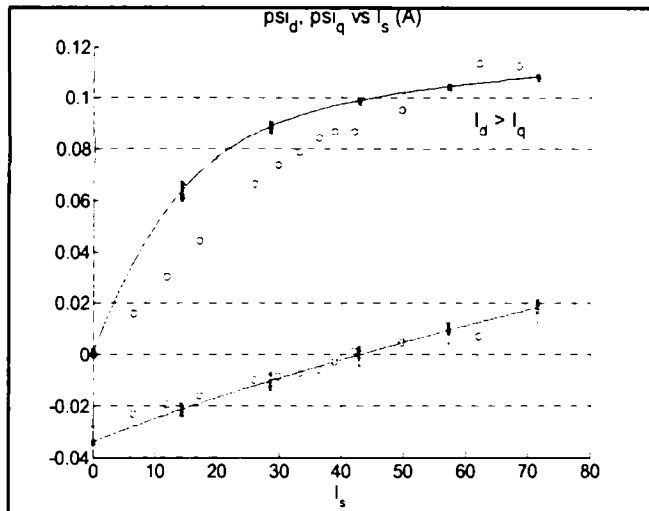


Figure 7. Magnetization curves of Ψ_d , Ψ_q versus I_s in PM-RSM x – FEM [1], o – dc decay tests

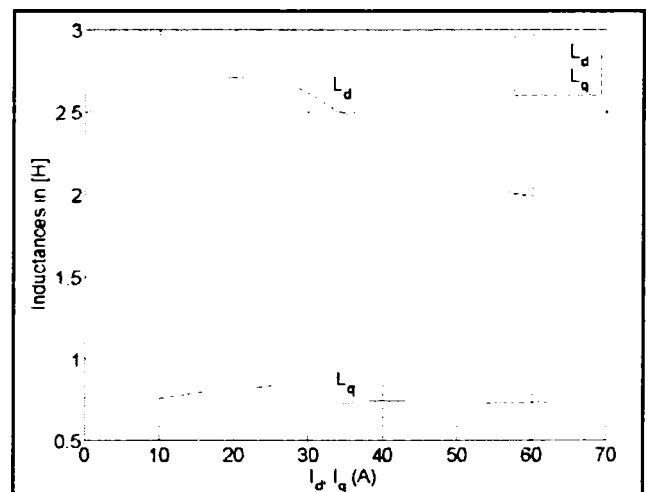


Figure 8. L_d , L_q vs I_d , I_q from dc decay tests

The results of the standstill tests in terms of magnetisation curves are presented in Figure 7 together with the theoretical ones (from the [1]). The differences for the d - axis (where the saturation is high) can be due to the manufacturing causes (the difference between the

0.4 mm theoretical airgap and $0.4_{-0}^{+0.12}$ mm of the prototype).

The d – q - inductances are extracted from the standstill test and they are shown in Figure 8.

It should be noticed that the FEM curves in Figure 7 have been obtained for the machine in different positions with respect to d – axis, and represented with respect to the total (magnetization) current.

The rather unique magnetization curves with various (I_d , I_q) components in the FEM calculations, along d - and q – axis reflect a mild cross-coupling effect [1].

IV. NO LOAD AND SHORTCIRCUIT TESTING

The no load voltage is shown in Figure 9 and the variation of no load voltage with frequency for the fundamental and harmonics appears in Figure 10.

The value of Ψ_{PMq} was calculated to 0.02355 Wb.

The harmonics in the no load voltage are due to the slotting for a small airgap and a full pitch double layer winding without skewing.

Further on the short - circuit testing was performed at various speed.

The short - circuit current shape and its peak value versus frequency are shown in Figure 10 and Figure 11.

From no load and short - circuit tests the value of L_q inductance is obtained from:

$$Z_q = V_{\text{no load}} / I_{\text{sc}} \quad (8)$$

$$X_q = \sqrt{Z_q^2 - R_1^2} \quad (9)$$

$$L_q = \frac{X_q}{2 \cdot \pi \cdot f_1} \quad (10)$$

$$\Rightarrow L_q = 0.67655 \text{ mH}$$

The value of L_q was not dependent on the current (or speed) as a low level of magnetic saturation was present.

V. CAPACITOR – ONLY LOAD TESTS

In an effort to segregate mechanical and core losses capacitor only load testing was performed.

From the load tests with capacitors the mechanical and iron losses were obtained (Figure 13) and with the stator resistance already found, the efficiency could be calculated from losses segregation and also from the drive data (by acquiring the torque and speed from the ACS 600 inverter).

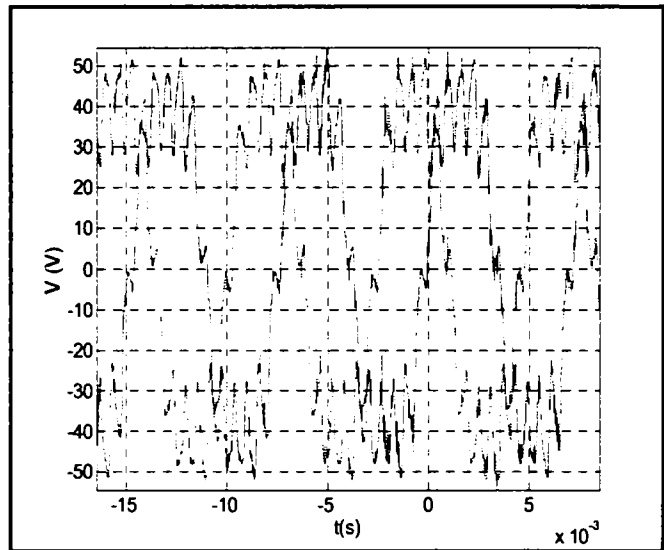


Figure 9. No load - phase voltage at 2000 rpm.

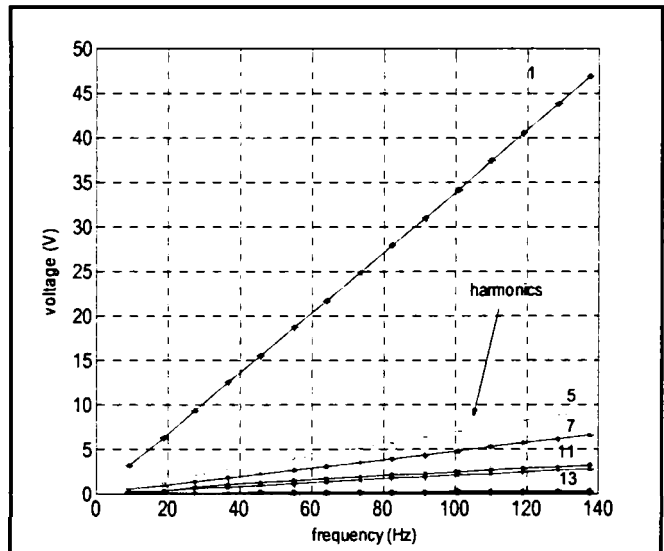


Figure 10. No load voltage fundamental and harmonics, versus frequency.

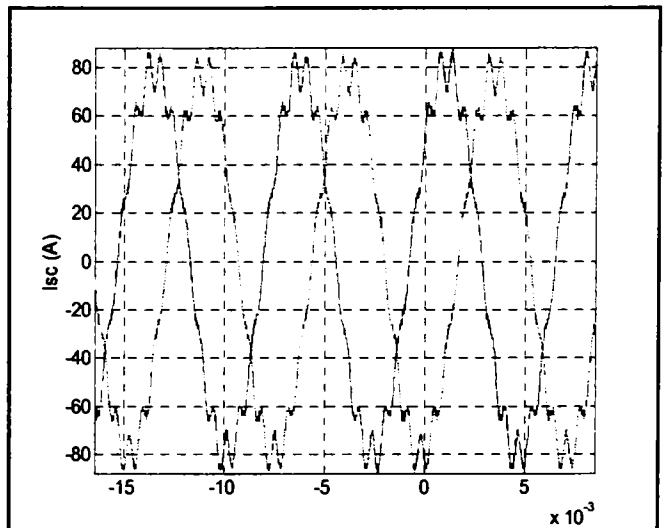


Figure 11. Short-circuit - phase currents at 2000 rpm.

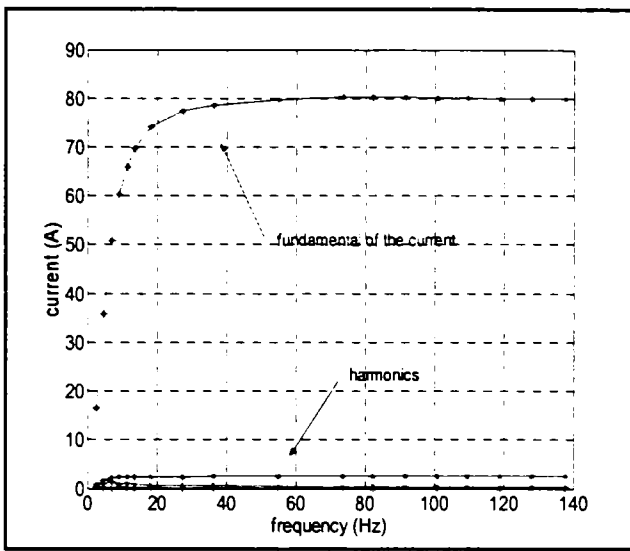


Figure 12. Short-circuit current versus frequency

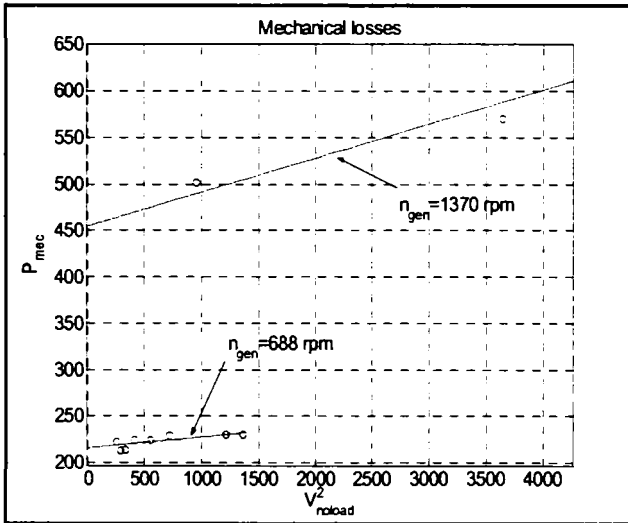


Figure 13. The mechanical losses versus squared voltage for two generator speed (1370 rpm and 688 rpm).

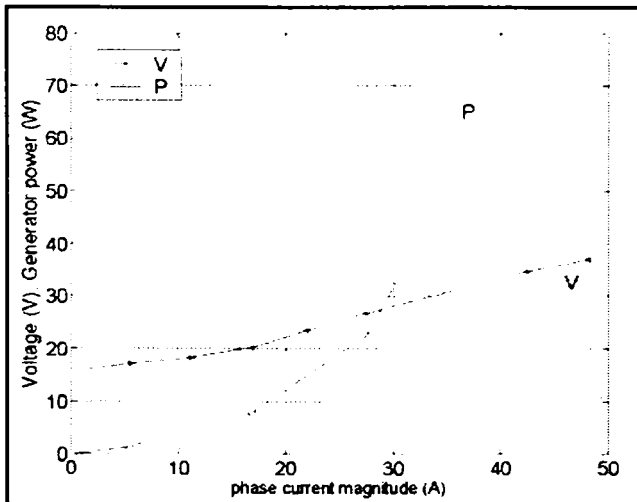


Figure 14. Voltage and generator (capacitor) power versus current with capacitor only load.

The terminal voltage and the phase current (peak current) for capacitor only load are shown in Figure 14 versus the input (mechanical) power.

The core and mechanical losses are represented in Figure 13 as a function of terminal voltage squared for two speeds. The mechanical losses represent, in fact the PM-RSM plus the transmission and drive mechanical losses. The input power to the generator was calculated from the estimated value of torque and speed of the DTC induction motor drive.

VI. ON LOAD A.C. TESTING WITH CAPACITOR EXCITATION

The load testing with resistive and with capacitive-resistive ac or dc (with a diode rectifier) load was used to validate the power capability and efficiency computed with the losses segregation.

The measured generator phase current and voltage with resistive load and capacitor excitation appear in Figure 15 while load ac resistance test results with and without capacitor excitation are visible in Figure 16 and Figure 17. The surplus in efficiency from segregated losses in Figure 17 is due to stray load losses.

By measuring V_1 , I_1 and $\cos\phi_1$ in the d-q flux equations, Ψ_d , Ψ_q and δ_v remain as unknowns.

$$P_1 = 3I_1 V_1 \cos\phi_1 \Rightarrow \cos\phi_1 \quad (11)$$

I_1 – phase current (A);

V_1 – voltage (V);

Because the magnetic saturation is small along the q - axis, L_q can be considered constant.

The value of L_q found from (8) - (10) is considered valid for the load tests as the cross-coupling influence is small (Figure 7).

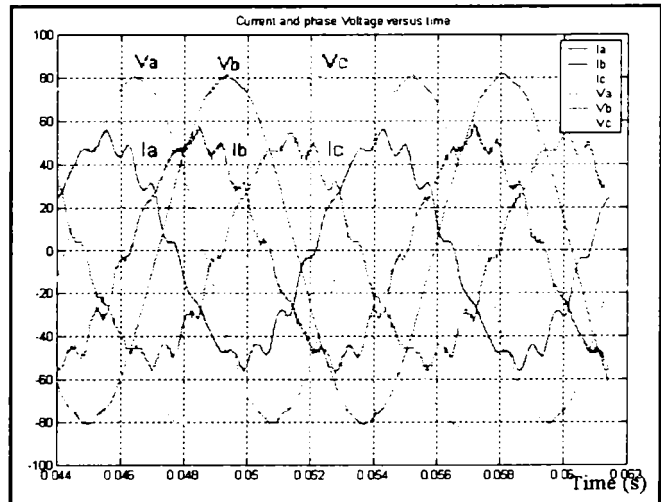


Figure 15. Current and voltage versus time at ac load (1370rpm).

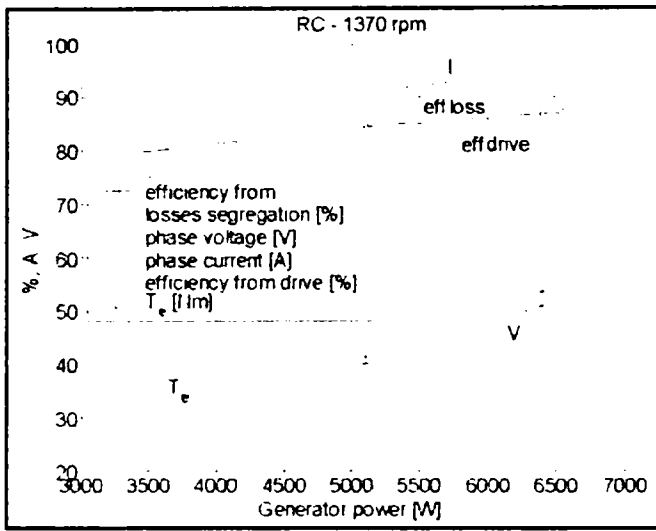


Figure 16. The characteristics for 1370 rpm with resistive load and capacitor excitation.

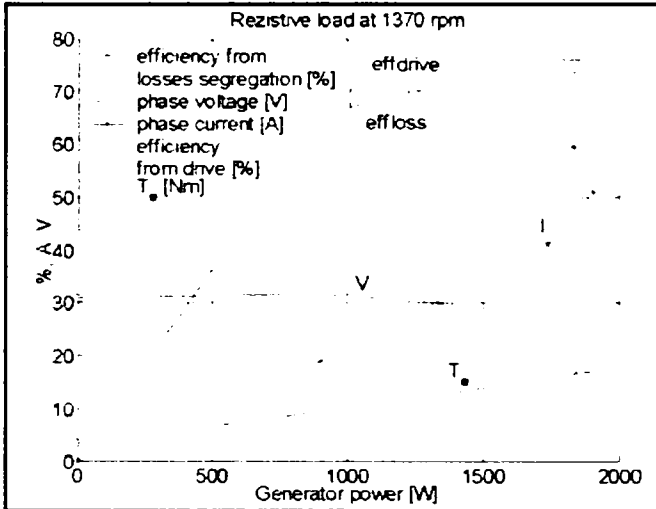


Figure 17 The characteristics for 1370 rpm with resistive load, without capacitor excitation

Many attempts to calculate the internal angle from the load tests have been made, with the mathematical computations [3].

Based on the vector diagram in this case [3]:

$$-X_d \cdot I_d = V_d \quad (12)$$

$$-V_{PM} + X_q \cdot I_q = V_q$$

$$V_d = V_{e1} \cdot \cos \delta$$

$$V_q = V_{e1} \cdot \sin \delta$$

$$I_d = I_{s1} \cdot \sin(\delta + \phi_1) \quad (13)$$

$$I_q = I_{s1} \cdot \cos(\delta + \phi_1)$$

$$\underline{V}_{e1} = \underline{V}_1 - R \cdot \underline{I}_{s1} \quad (14)$$

$$\phi_1 = \text{angle}(\underline{I}_{s1} \cdot \underline{V}'_{e1})$$

$$-V_{PM} + X_q \cdot I_{s1} \cdot \cos(\delta + \phi_1) = V_{e1} \cdot \sin \delta \quad (15)$$

The only unknown in eqn (15) is the power angle δ_v :

$$\delta_v = a_1 \tan 2(a_1, b_1) \pm a_1 \cos \frac{V_{PM}}{\sqrt{a_1^2 + b_1^2}} \quad (16)$$

With
$$a_1 = -V_{e1} - X_q \cdot I_{s1} \cdot \sin \phi_1 \quad (17)$$

$$b_1 = X_q \cdot I_{s1} \cdot \cos \phi_1$$

Consequently the power angle is directly computable. In this equation the sign in (16) is chosen for L_d to be positive and greater than L_q .

$$L_d = -\frac{V_d}{\omega_1 \cdot I_d} \quad (18)$$

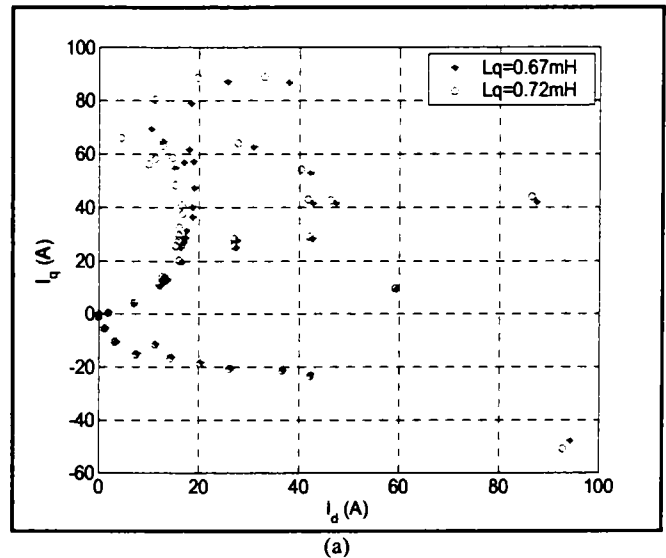
For 1370 rpm, with resistive load and capacitor excitation, a torque of 57 Nm has been obtained (Figure 16). The peak torque (for motoring) in the design was 140 Nm [1].

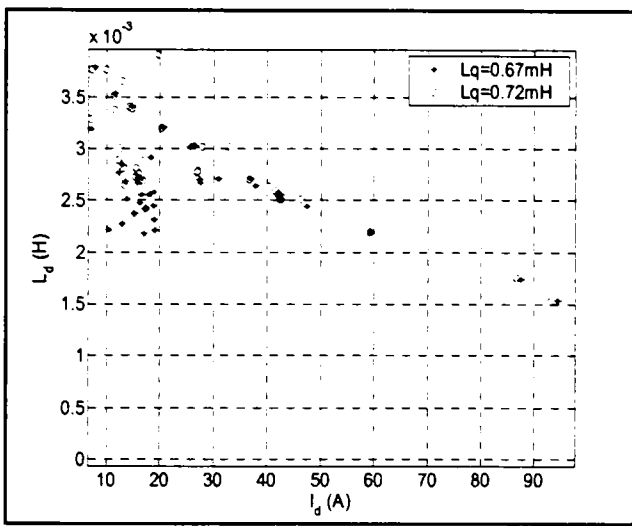
The I_q , L_d , δ_v (I_d) curve obtained from load tests as indicated above is shown in Figure 18 (a, b, c). Comparing with results in Figure 8 differences up to 20% can be seen which are thought to be due to heavy saturation in d - axis and due to errors in the measurements. The various power angles and L_q - values in Figure 18 suggest a wide range of load conditions.

VII. ON LOAD TESTING WITH DIODE RECTIFIER

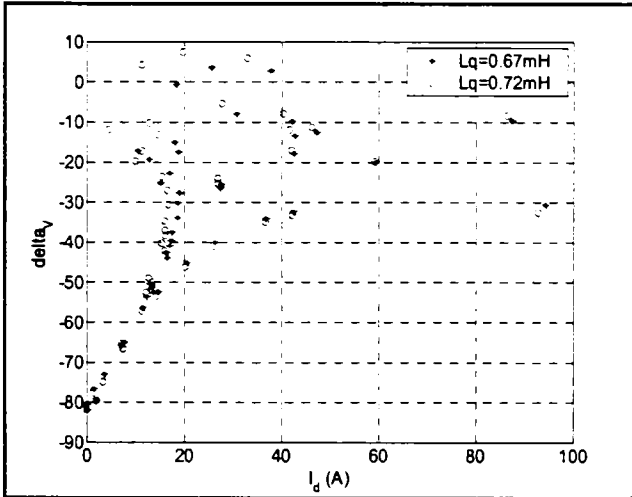
Some tests have been performed with a diode rectifier and resistive load. No capacitors have been present at generator terminals. (Tests with capacitor excitation diode rectifier and a 42 V dc battery are due soon).

The low level of delivered power is explained by the small contribution of PM to the machine torque (power) in Figure 19.





(b)



(c)

Figure 18. Determination of I_d (a), L_d (b) and δ_d (c) from on load ac tests – for both L_q calculated from standstill ($L_q = 0.72$ mH) and from no load + shortcircuit ($L_q = 0.67$ mH).

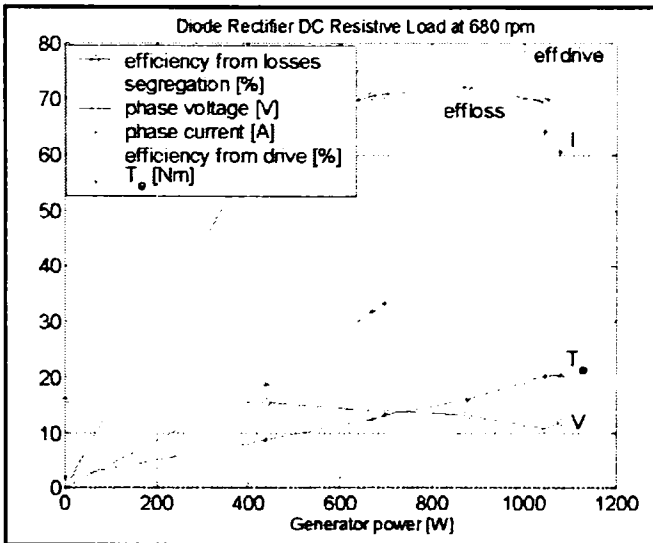


Figure 19. The characteristics for diode rectifier DC resistive loads at 680 rpm.

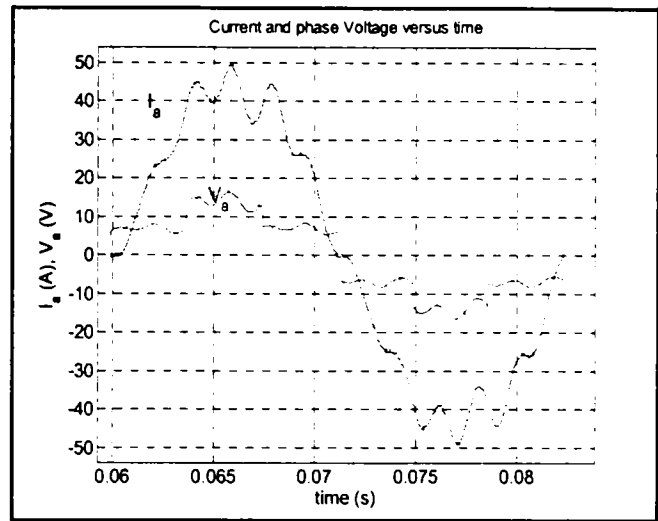


Figure 20 Measured I_{phase} , V_{phase} with diode rectifier dc load at 680 rpm ($V_{dc} = 20.86$ V, $I_{dc} = 42$ A)

The typical phase voltage and rather sinusoidal phase current with diode rectifier dc load is clearly visible at 680 rpm in Figure 20.

VIII. CONCLUSION

The paper introduces a series of tests for the PM – assisted RSM in the generator regime to identify the parameters and energy conversion performance.

The standstill dc decay tests have produced coherent unique magnetization curves along d - axis (high permeance) and q axis (low permeance).

The q - axis inductance (along the PM axis) was proven rather constant also from no load and short-circuit tests.

Capacitors were connected at machine terminals for generator loss segregation.

With capacitors at the terminals, resistive symmetric load was applied to the load the generator and determining the efficiency. Efficiency above 80 % was proven from 3 kW to 6.5 kW output at 1370 rpm.

By segregation of losses higher efficiencies were found. The stray load losses are the cause of this difference.

TABLE II
Experimental and simulation results

	Experimental	Simulation
R_s	0.039 Ω	-
L_q	0.67 mH (dc decay test)	1 mH
	0.72 mH (noload + SC tests)	
L_d	2.8 mH (dc decay test)	3.4 mH
Ψ_{PMq}	0.02355 Wb	0.027 Wb

This concluded that the proposed generator series of tests proved rather successful in characterizing the machine.

REFERENCES

- [1] I. Boldea, L. Tutelea, C. I. Pitic, "PM – assisted Reluctance Synchronous motor / generator (PM-RSM) for mild hybrid vehicle", Proc of OPTIM 2002, 16 – 17 May, 2002, Brasov, Romania, pp. 383-388
- [2] F.F. Bernal, A.G. Cerrada, R. Faure, "Determination of Parameters in Interior Permanent – Magnet Synchronous Motors With Iron Losses Without Torque Measurement", IEEE Transactions on Industry Applications, Vol. 37, No.5, September / October 2001, pp. 1265-1272.
- [3] H.P. Nee, L. Lefevre, P. Thelin, J. Soulard, "Determination of d - and q - Reactances of Permanent-Magnet Synchronous Motor Without Measurement of the Rotor Position", IEEE Transactions on Industry Applications, Vol. 36, No. 5, September - October 2000, pp. 1330-1335
- [4] T. Senjyu, A. Omoda, K. Uezato, "Parameter measurement for synchronous reluctance motors considering stator and rotor iron loss", Proc. of IEMDC '99, 9-12 May 1999, pp. 126 -128.
- [5] A. Kiltbau, J.M. Pacas, "Measurement of the parameters of the synchronous reluctance machine including cross saturation", Proc of EPE 2001, Graz.
- [6] M. Comanescu, A. Keyhani, M. Dai, "Design and analysis of 42-V Permanent-Magnet Generator for Automotive Applications", IEEE Transactions on Energy Conversion, Vol. 18, No. 1, March 2003, pp. 107 - 112.
- [7] J.H. Lee, J.C. Kim, D.S. Hyun, "Effect Analysis of Magnet on L_d and L_q inductance of permanent magnet assisted synchronous reluctance motor using finite element method", IEEE Transaction on Magnetics, Vol. 35, No. 3, May 1999, pp. 1199- 1202.
- [8] S. Chen, B. Lequesne, R.R. Henry, Y. Xue, J.J. Ronning, "Design and testing of a belt-driven induction starter-generator", IEEE Transaction on Industry applications, Vol. 38, No. 6, November - December 2002, pp. 1525 - 1533.
- [9] J.R. Melgoza, G.T. Heydt, A. Keyhani, B.L. Agrawal, D. Selin, "Synchronous Machine parameter estimation using the Hartley series", IEEE Transaction on Energy Conversion, vol. 16, no. 1, March 2001, pp. 49 – 54.
- [10] K. Yamazaki, "Torque and efficiency calculation of an interior permanent magnet motor considering harmonic iron losses of both the stator and rotor", IEEE Transaction on Magnetics, vol. 39, Issue 3, May 2003, pp. 1460 - 1463.
- [11] E.C. Lovelace et al, "Design and experimental verification of a direct-drive interior PM synchronous machine using a saturable lumped-parameter model", 2002, Record of the 37th IAS Annual Meeting. Conference, Vol. 4, 13 – 18 Oct.2002, pp: 2486 - 2492.
- [12] I. Boldea, "Reluctance synchronous machines and drives", (book), OUP 1996.

IPMSM Motion-Sensorless Direct Torque and Flux Control

Cristian Ilie Pitic¹, Gheorghe-Daniel Andreescu², Frede Blaabjerg³, Ion Boldea¹

¹Department of Electrical Machines and Drives, ²Department of Automation and Applied Informatics, University Politehnica of Timisoara, 2 Vasile Parvan Blvd., 300223 Timisoara, ROMANIA

³Institute of Energy Technology, Aalborg University, 101 Pontoppidanstraede, 9220 Aalborg East, DENMARK
pitic.c@lselinux.utt.ro, dandre@aut.utt.ro, fbl@iet.aau.dk, boldea@lselinux.utt.ro

Abstract – The paper presents a rather comprehensive implementation of a wide speed motion-sensorless control of IPMSM drives via direct torque and flux control (DTFC) with space vector modulation (SVM). Signal injection with only one D-module vector filter and phase-locked loop (PLL) observer is used at low speeds to estimate the rotor position and speed, to be used in the stator flux observer and, respectively, as speed feedback. A combined voltage-current model flux observer suits the whole speed range, while the current model fades away as speed increases. PWM and inverter nonlinearities compensation provides for a smooth current waveform even at 1 rpm. The paper demonstrates through ample experiments a 1750 rpm / 1 rpm speed range full-loaded with sensorless DTFC-SVM.

I. INTRODUCTION

Interior PM synchronous motor (IPMSM) drives are becoming more and more favored in wide speed range applications. Eliminating the shaft position sensor is welcome, based on cost and reliability constraints. Motion-sensorless control methods of PMSM fall into two main categories: 1) emf tracking based on the fundamental model, that fails at zero and very low speed, and 2) signal injection methods, which work from standstill but should be dropped at a certain low speed in favor of emf tracking methods.

The IPMSM is blessed with d - q saliency, which is tracked for rotor position estimation. Persistent high-frequency carrier-voltage ($\omega_c = 300$ - 1000 Hz, $V_c = 1$ - 10 V) [1-6], or discrete voltage pulses [2] can be injected in machine for the rotor position tracking. The resultant carrier-current harmonics contains the rotor position information. While a low pass filter (LPF) separates the fundamental current, a band pass filter (BPF) in a specific reference selects the targeted carrier-current harmonic. The BPF is complemented by a phase-locked loop (PLL) tracking observer that extracts the rotor speed and position.

After reviewing saliency-tracking estimators [1-4, 6] and the mirror-phase estimator [5], a simplified estimator with only one D-module vector filter (compared with two in mirror-phase) is used to estimate the rotor position & speed.

A hybrid voltage-current model closed-loop flux observer takes the rotor position into its current model at low speed, and uses only the voltage model at medium-high speed.

In contrast to the vector control, the direct torque and flux control (DTFC), used in this paper, does not need the rotor position in decoupling networks, and thus the use of DTFC should be beneficially in motion-sensorless implementations.

However, to reduce torque pulsations, the space vector modulation (SVM) is applied. Finally, dead time and other nonlinearities in the PWM converter are compensated to further smooth up current waveform at very low speed.

A detailed presentation of the proposed drive with ample experimental results follows.

II. IMPLEMENTED MOTION-SENSORLESS DTFC-SVM SYSTEM AT A GLANCE

The space vector IPMSM model includes: the voltage model in the general reference frame, rotating with ω speed (1); the current model in dq rotor reference (2); the electromagnetic torque T_e computed in $\alpha\beta$ stator reference (3). The magnetic saturation was considered rather constant and a small saliency rotor was used.

$$\underline{v} = R_s \underline{i} + d\underline{\lambda} / dt + j\omega \underline{\lambda} \quad (1)$$

$$\underline{\lambda} = (L_d \underline{i}_d + \lambda_{PM}) + jL_q \underline{i}_q \quad (2)$$

$$T_e = 1.5p(\lambda_{\alpha} i_{\beta} - \lambda_{\beta} i_{\alpha}) \quad (3)$$

where: \underline{v} , \underline{i} and $\underline{\lambda}$ are the stator voltage, current and flux vector, respectively; R_s is the stator phase resistance; L_d and L_q are the dq inductances; λ_{PM} is the PM flux; p is the pair pole number. Table I shows IPMSM specifications.

The proposed sensorless DTFC-SVM system for IPMSM is introduced in Fig. 1. It mainly contains: DTFC-SVM, flux and torque observer, position-speed estimator with signal injection, and a relay that inhibits the signal injection beyond ± 30 rpm. The DTFC uses the voltage model (1) in stator flux reference with the flux position $\hat{\theta}_\lambda$ in dq - $\alpha\beta$ transformation.

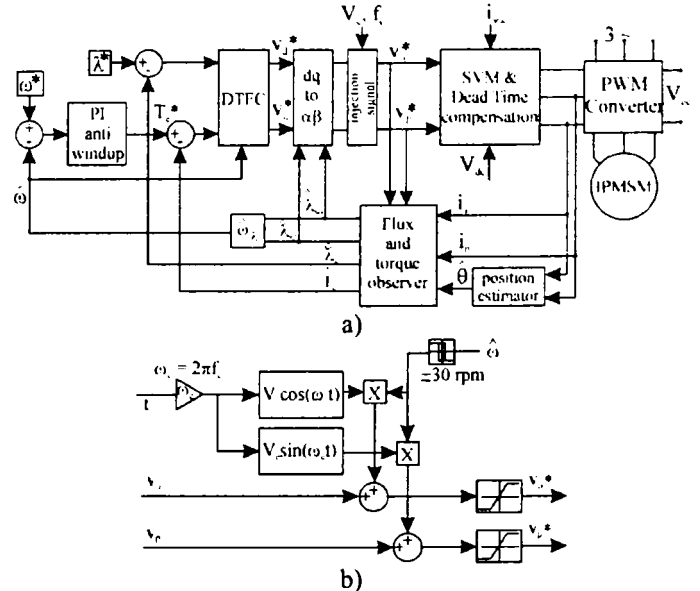


Fig. 1. a) The proposed sensorless DTFC-SVM for IPMSM, b) injection signal with $\omega_c = 2\pi 500$ rad/s for position estimation

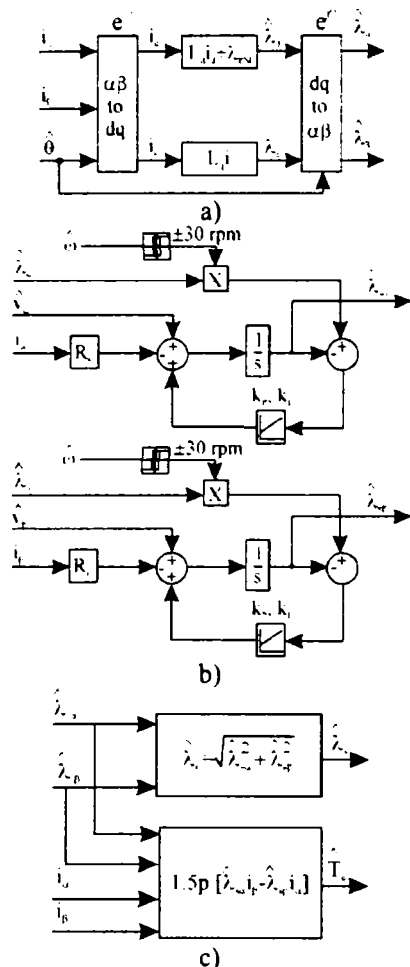


Fig. 2. Flux and torque observer with combined voltage-current models

The hybrid voltage-current model structure of the flux observer is visible in Fig. 2. It is based on (1)-(3) with the voltage model in $\alpha\beta$ stator reference ($\omega = 0$). The PI compensator makes the current model prevail at low speed, and the voltage model at medium-high speed, with a smooth transition between them. The current model (Fig. 2a) output is inhibited by a relay above ± 30 rpm, where the position estimation is neither available nor necessary for DTFC. Only the speed feedback is required above ± 30 rpm. The speed of stator flux vector was finally used for speed feedback.

The realization example for a 3rd-order filtering with the inverse D-module $D^{-1}(s, \omega_c)$ [5, 7] is shown in Fig. 3. This kind of vector filter discriminates for the phase-polarity and rejects the dc-offset originating in stator current acquisition process. If the scalar (single-input/output) filter $F(s)$ (as in Fig. 4a) is designed as a low-pass filter (LPF) with the bandwidth B , then the associated vector (two-input/output) filter in D-module $F(D(s, -\omega_c))$ is a band-pass filter (BPF) with the central frequency ω_c and same bandwidth B [7].

The position estimation with signal injection includes: 1) a BPF (Fig. 4a) with only one vector filter using inverse D-module realization (Fig. 4b) to select the 1st carrier-current negative-sequence harmonic from the stator current

$$i_c = I_c \exp\{j(-\theta_c + 2\theta + \pi/2)\}, I_c \approx V_c (L_d - L_q) / (2\omega_c L_d L_q) \quad (4)$$

with $\theta_c = \omega_c t$, that contains the rotor position θ , and 2) a PLL

tracking observer to extract $\hat{\theta}$, $\hat{\omega}$ from the i_c phase (Fig. 4c).

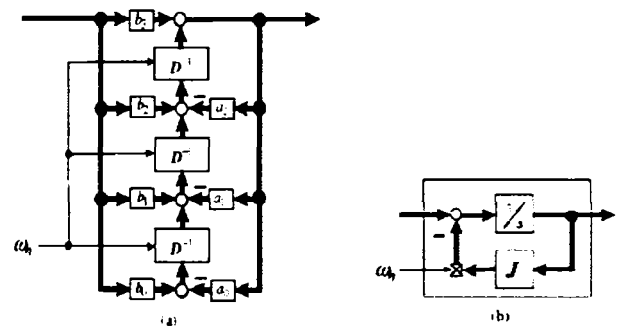
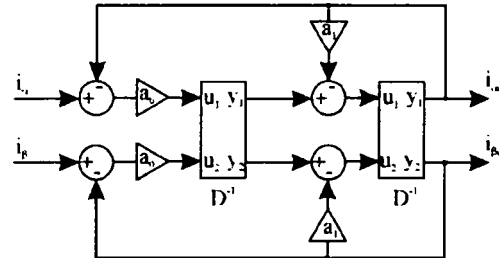


Fig. 3. a) Realization example for 3rd-order filtering, b) inverse D-module



$$F(s) = \frac{a_0}{s^2 + a_1 s + a_0}$$

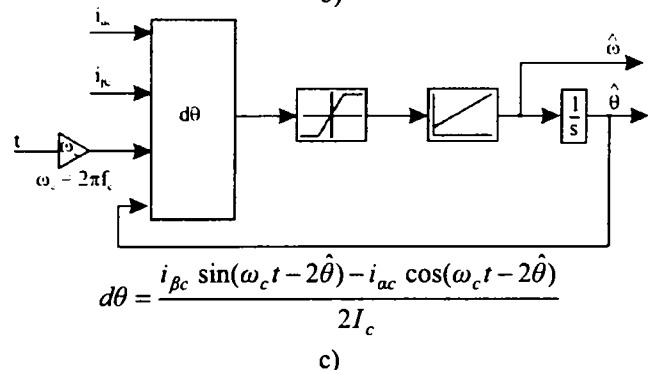
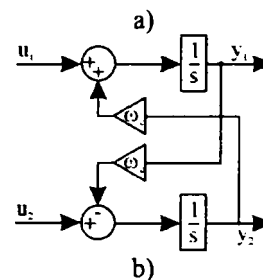


Fig. 4. Position estimation: a) 2nd-order vector BPF with D-module, b) D^{-1} realization, c) PLL for position estimation with $d\theta$ PLL error

To improve dynamic estimations, an extended Luenberger observer with zero-phase lag [1] could be used in PLL.

The initial rotor position is correctly estimated at standstill in $(-\pi/2, \pi/2)$ radians range. For the full angle range, an uncertainty of π radians appears that could be discriminated by the magnet polarity detection using other information as the 2nd-order carrier-current harmonics [4].

This rotor position / speed estimation with signal injection is very robust, independently of IPMSM parameters.

The configuration in Fig. 4 is believed to be less intensive in terms of online computation, in comparison with existing implementations of equivalent performance.

III. DIGITAL SIMULATION SAMPLE RESULTS

Digital simulations have been processed in MATLAB[®]/Simulink package for an easy translation into the dSpace system for the experiments.

Sample simulation results for the motor specified in Table I, with speed reversal for full load (12 Nm) at ± 1 rpm and ± 5 rpm, are shown in Figs. 5, 6 and 7.

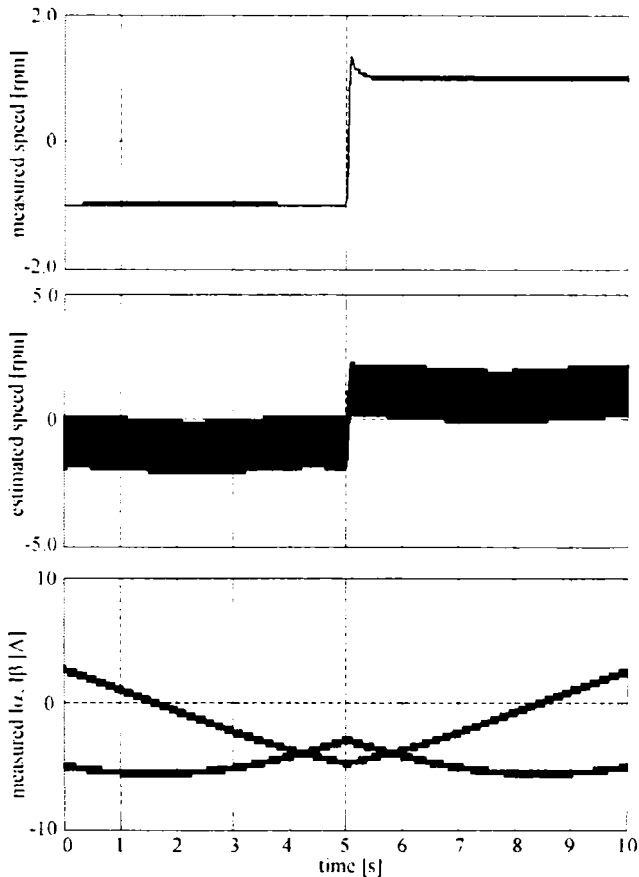


Fig. 5. Simulation results at -1 to 1 rpm reversal speed for full load (12 Nm): measured speed, estimated speed and measured current i_a , i_b

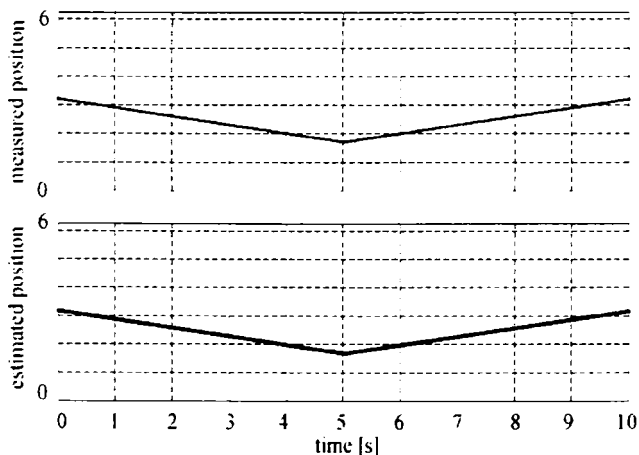


Fig. 6. Simulation results at -1 to 1 rpm reversal speed for full load: measured and estimated position

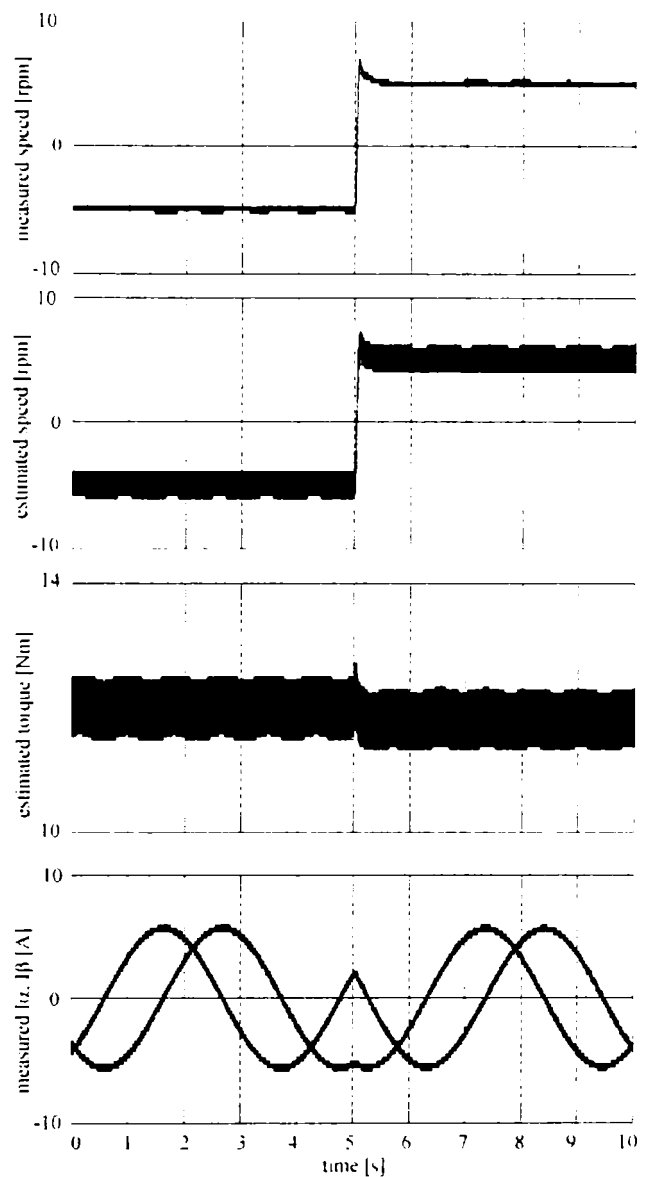


Fig. 7. Simulation results at -5 to 5 rpm reversal speed for full load: measured speed, estimated speed, estimated torque and measured current components i_a , i_b

The measured speed is also given for reference. About 1 rpm speed ripple is visible in the estimated speed. The position estimation during ± 1 rpm reversal speed transients is quite reliable and the SVM yields good current waveforms.

No-load startup transients from zero to 1750 rpm with full step load at 1.5 seconds (Fig. 8), and on-load starting to 1750 rpm with generating (full load) at 2 seconds (Fig. 9) show smooth performance with quick speed recovery.

Once, the digital simulations seem to give confidence into the proposed sensorless DTFC-SVM system for IPMSM drive, the experimental work was pursued.

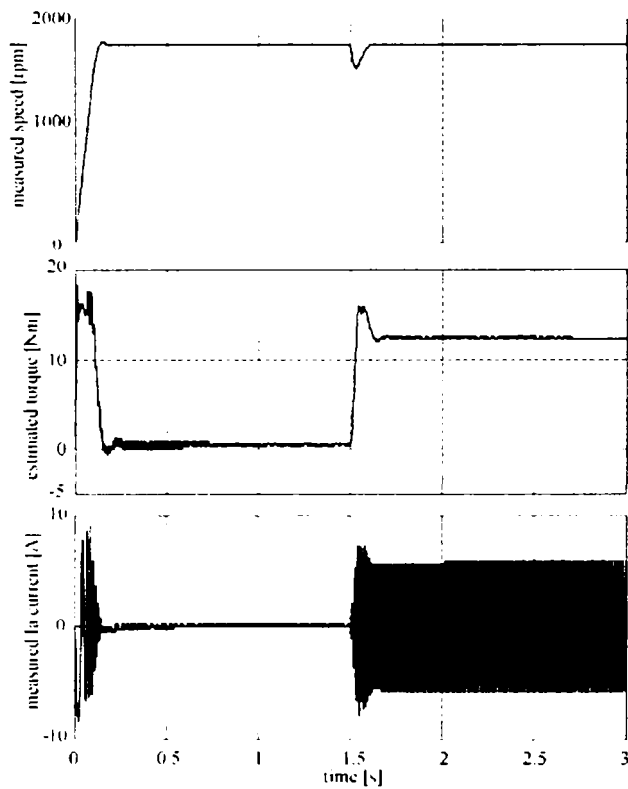


Fig. 8. Start-up transients (0 to 1750 rpm) with full load applied at 1.5 s: measured speed, estimated torque and measured current - simulation results

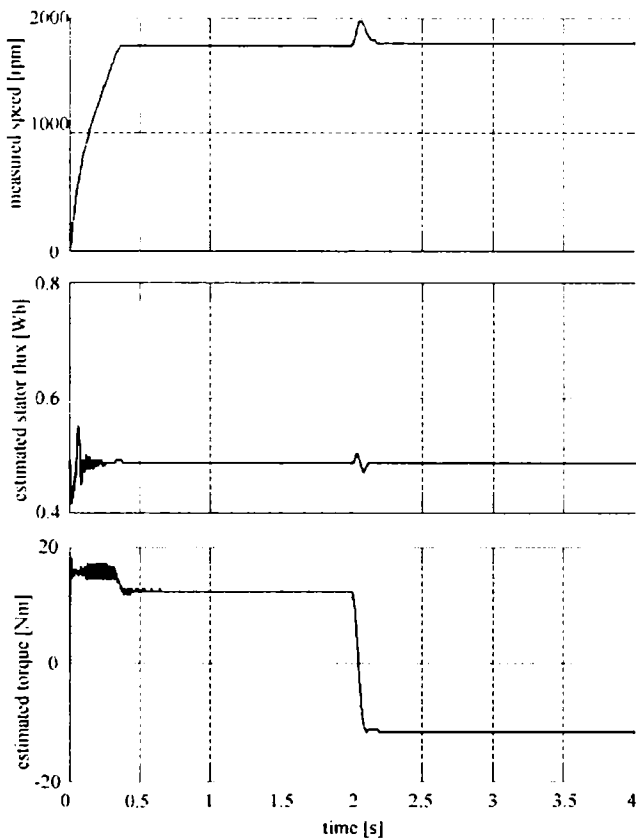


Fig. 9. Start-up with full torque and motoring to generating crossing at 2 s: measured speed, estimated flux and estimated torque - simulation results

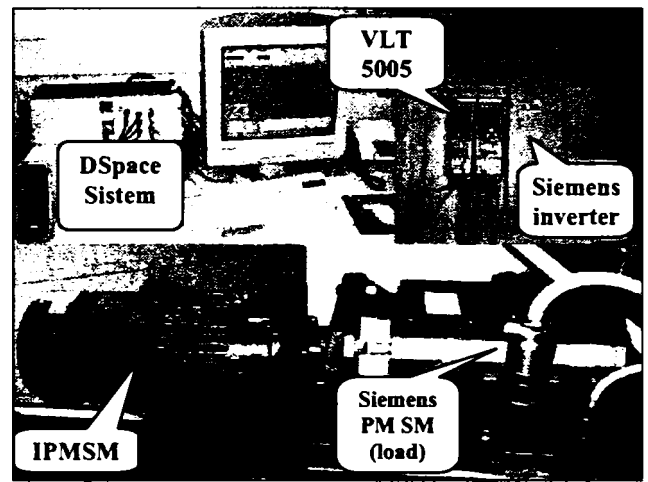


Fig. 10. Experimental setup

TABLE I
IPMSM SPECIFICATIONS

Number of pole pairs (p)	3
Rated power	2.2 kW
Rated speed	1750 rpm
Rated frequency	87.5 Hz
Rated torque	12 Nm
Rated phase to phase voltage	380 V(rms)
Rated phase current	4.1 A(rms)
Stator resistance per phase (R_s)	3.3 Ω
d-axis inductance (L_d)	41.59 mH
q-axis inductance (L_q)	57.06 mH
Rotor permanent-magnet flux (λ_{PM})	0.4832 V s rad ⁻¹
Inertia of the rotating system (J)	10.07 $\cdot 10^{-3}$ kgm ²
Viscous friction coefficient (B_m)	20.44 $\cdot 10^{-4}$ Nms/rad ⁻¹

IV. EXPERIMENTAL SYSTEM AND SAMPLE RESULTS

The testing setup consists in a IPMSM of 12 Nm rated torque driven by a Danfoss VLT 5005 and a Siemens SIMOVERT MASTERDRIVE as load (Fig. 10).

To check the lowest speed limit, operation at 120% load and 1 rpm has been tested with results in Fig. 11. The torque pulsations are there but they are reasonable. The measured rotor position (Fig. 11) is closed to the estimated one.

A speed ripple of ± 5 rpm was investigated experimentally with quite good results (Fig. 12). The estimated speed is smooth, but the measured one has notable pulsations as in Fig. 11.

Acceleration transients to 1750 rpm on no-load are shown in Fig. 13. The torque goes back to almost zero, with reasonable ripple, while the estimated flux hodograph comes very close to a circle, as it should be (flux weakening has not been reached).

Fast torque loading (from generating to motoring) at 1750 rpm is demonstrated in Fig. 14, where swift speed recovery occurs, with small undershooting.

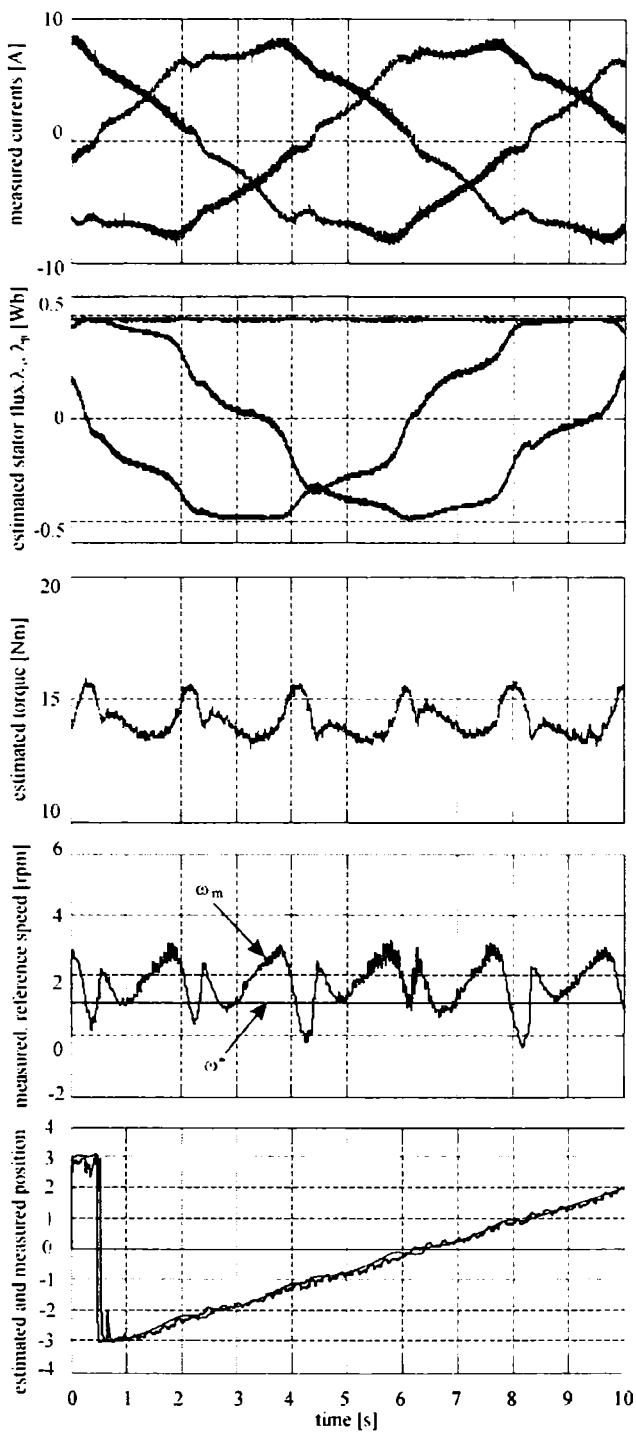


Fig. 11. 1 rpm at 120 % of nominal torque: measured currents, estimated flux and its components (λ_s , λ_α , λ_β), estimated torque, measured and reference speed, estimated and measured position

V. CONCLUSION

The present paper results warrant remarks such as:

- DTFC with SVM for IPMSM is shown capable of 1750 rpm to 1 rpm speed range full loaded in motion-sensorless implementation with signal injection used for rotor position estimation up to 30 rpm only.

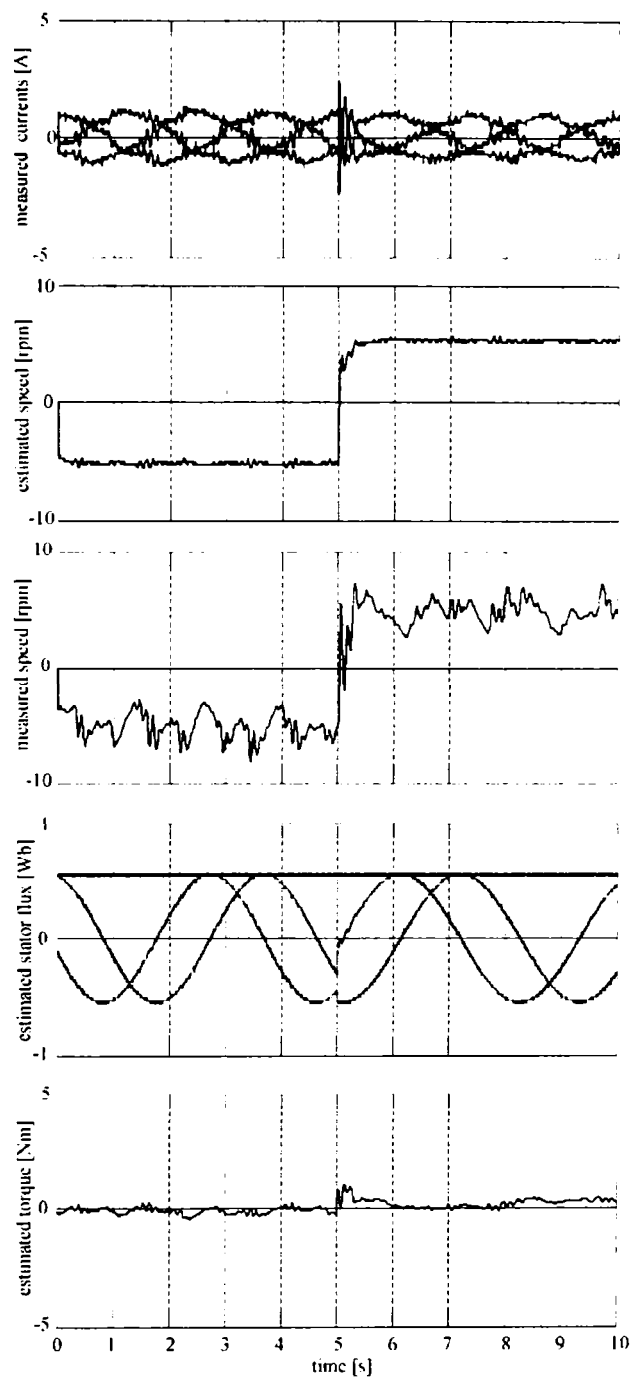


Fig. 12. No-load speed reversal at ± 5 rpm: measured currents, estimated speed, measured speed, estimated stator flux and its components (λ_s , λ_α , λ_β), and estimated torque

- Fast torque response has been demonstrated both in motoring and generating mode.
- The compensation of SVM dead time and other inverter nonlinearities lead, also for DTFC (as they do for vector control) to smooth current ripple with reasonable torque ripple especially at very low speed.

Initial online rotor position estimation in full range, and flux weakening (for even wider speed range) are due in the near future.

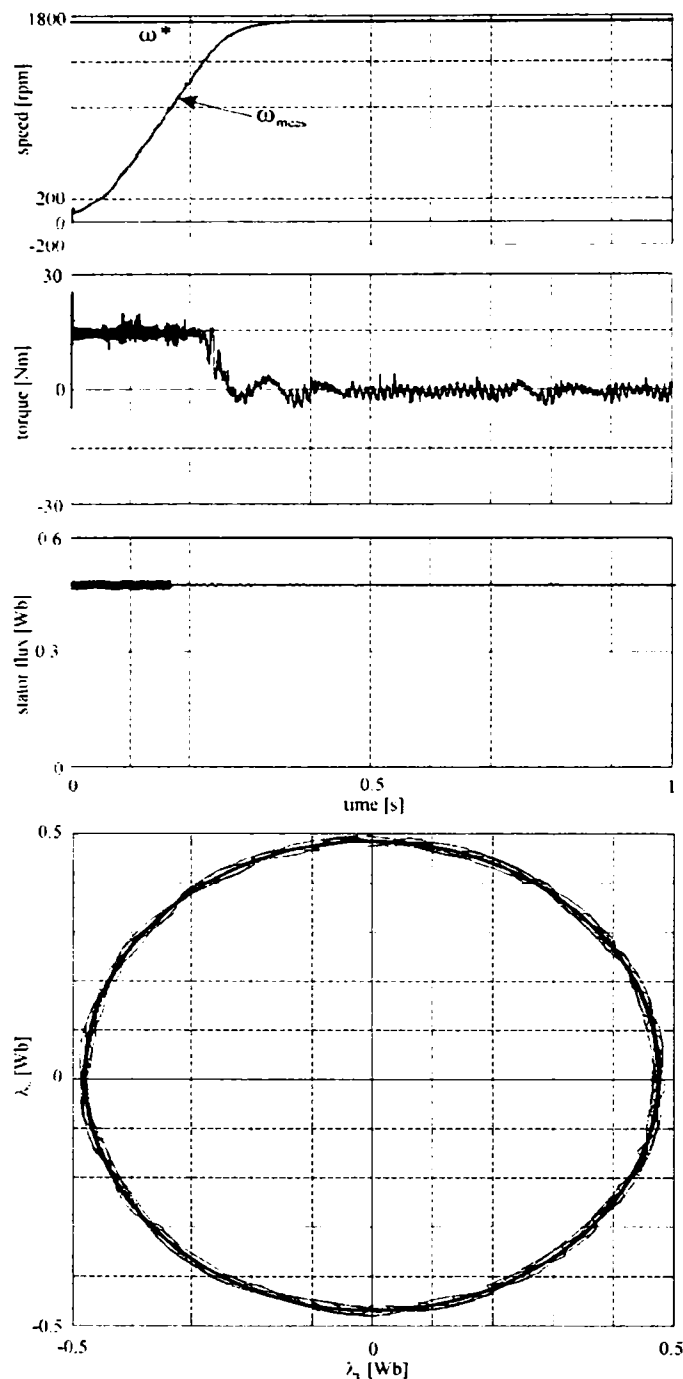


Fig. 13. Start-up response from 0 to 1750 rpm: reference and measured speed, estimated torque, estimated stator flux, λ_a versus λ_b hodograph

REFERENCES

[1] M.W. Degner and R.D. Lorenz, "Using multiple saliencies for the estimation of flux, position, and velocity in ac machines," *IEEE Trans. Ind. Appl.*, vol. 34, no. 5, Sept./Oct. 1998, pp. 1097-1104.

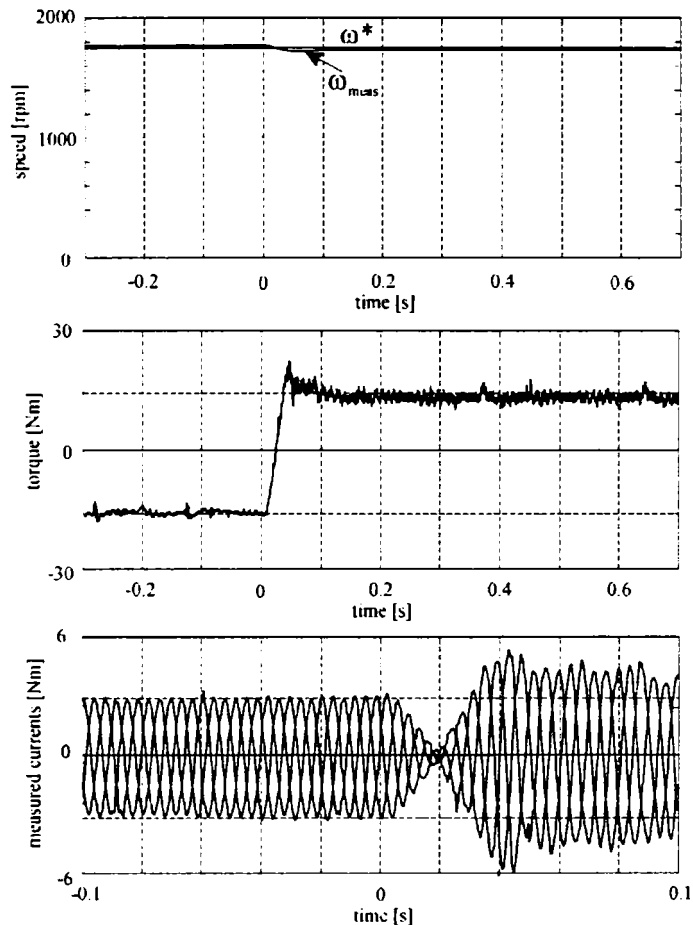


Fig. 14. Torque transient response (from -15 to 15 Nm) at nominal speed: measured and reference speed, estimated torque and measured currents

[2] M. Linke, R. Kennel and J. Holtz, "Sensorless speed and position control of synchronous machines using alternating carrier injection," in *Proc. IEEE-IEMDC'03*, Madison, WI, USA, vol. 2, June 2003, pp. 1211-1217.

[3] C. Silva, G.M. Asher, M. Summer and K.L. Bradley, "Sensorless rotor position control in surface mounted PM machine using hf voltage injection," in *Record of EPE-PEMC 2002*, Dubrovnik, Croatia, Sept. 2002.

[4] H. Kim, K.-K. Huh, M. Harke, J. Wai, R.D. Lorenz and T.M. Jahns, "Initial rotor position estimation for an integrated starter alternator IPM synchronous machine," in *Record of EPE 2003*, Toulouse, France, Sept. 2003.

[5] S. Shinnaka, "New "mirror-phase vector control" for sensorless drive of IPMSM," in *Proc. IEEE-IEMDC'03*, Madison, WI, USA, vol. 3, June 2003, pp. 1875-1881.

[6] G.D. Andreescu and I. Boldea, "Integrated sensors for rotor position and speed based on signal injection for IPMSM drives," in *Proc. IEEE-INES 2004*, Cluj-Napoca, Romania, Sept. 2004, pp. 371-375.

[7] S. Shinnaka, "A new characteristics-variable two-input/output filter in D-module - Designs, realizations and equivalences", *IEEE Trans. Ind. Appl.*, vol. 38, no. 5, Sept./Oct. 2002, pp. 1290-1296.

Ion Boldea¹, Cristian Ilie Pitic¹, Cristian Lascu¹, Gheorghe-Daniel Andreescu²,

Lucian Tutelea¹, Frede Blaabjerg³ and Per Sandholdt⁴

¹Department of Electrical Machines and Drives, ²Department of Automation and Applied Informatics, University Politehnica of Timisoara, 2 Vasile Parvan Blvd., 300223 Timisoara, Romania, *boldea@lselinux.utt.ro, pitic.c@lselinux.utt.ro, cristi@et.utt.ro, daniel.andreescu@aut.upt.ro, luci@lselinux.utt.ro*

³Institute of Energy Technology, Aalborg University, 101 Pontoppidanstraede, 9220 Aalborg East, Denmark, *fbl@iet.aau.dk*

⁴Sauer-Danfoss ApS, 81 Nordborgvej, 6430 Nordborg, Denmark, *per.sandholdt@sauer-danfoss.dk*

Abstract – PM-assisted reluctance synchronous (PM-RSM) starter alternator systems are credited with good performance for wide speed range in hybrid electric vehicles (HEV). This paper proposes a motion-sensorless motor/ generator control of PM-RSM from zero speed up to maximum speed, using direct torque and flux control (DTFC) with space vector modulation (SVM). A quasi-optimal stator flux reference with a flux versus torque functional is proposed. A stator flux observer in a wide speed range uses combined voltage-current models for low speed, and only voltage model for medium to high speed, both in PI closed loops. A novel rotor speed and position observer with a fusion strategy employs signal injection and only one D-module vector filter in stator reference - for low speed, combined with a speed observer from the stator flux vector estimation - for medium-high speed. The proposed system is introduced piece by piece and then implemented on a dSpace 1103 control board with a 350A MOSFET-PWM converter connected to a 42 Vdc, 55 Ah battery, and a 140 Nm peak torque PM-RSM. Extensive experimental results from very low speed to high speed, regarding observers and drive responses, including artificial loading (motoring and generating), seem very encouraging for future starter-alternator systems.

Corresponding author: Cristian Ilie Pitic, Department of Electrical Machines and Drives, University Politehnica of Timisoara, 2 Vasile Parvan Blvd., 300223 Timisoara, Romania, Tel. +40256-403463, Fax: +40256 403452, E-mail: pitic.c@lselinux.utt.ro

I. INTRODUCTION

The integrated starter-alternators (ISA) topic represents a hot subject for internal combustion engines (ICE) and hybrid electric vehicles (HEV). Typical specifications for ISAs depend on the degree of vehicle electrification (% E) [1]:

$$\%E = \frac{\textit{peak electric power} \times 100}{\textit{peak electric power} + \textit{peak ICE power}}. \quad (1)$$

% E varies from less than 10% in conventional ICE vehicles to 10-25% in mild hybrid vehicles, 25-50% in full parallel hybrid vehicles, and 100% in series hybrid and fully electric vehicles. In all cases a wide constant power-speed range (from 4:1 to 12:1) is beneficial. From this point of view, corroborated with low inverter kVA and low total system losses, the permanent magnet reluctance synchronous motor (PM-RSM) seems to be one of the best [2], together with the electrically dc-excited claw-pole [3], or standard rotor synchronous machines [4]. Quite a few research teams have recently investigated in depth the design, performance [5-8] and vector-control [5] of PM-RSM.

Sensorless vector-control for internal permanent magnet synchronous motors (IPMSM) [9-11] close to PM-RSM [5] has been presented with rather comprehensive solutions containing initial position estimation for non-hesitant starting via signal injection methods. As the PM-RSM has notable saliency that is strongly influenced by magnetic saturation, the vector-control has to account for it explicitly both in the stator flux observers and in the control itself (in sensorless operation), especially as speed increases above the base speed and the stator flux is weakened due to battery dc voltage limitation.

Sensorless direct torque and flux control with space vector modulation (DTFC-SVM) for induction machines has been successfully proven, from very low speed with robust dynamics, in a sliding-mode approach [12]. It has been applied also to reluctance synchronous motors [13]. The direct torque control (DTC) for PMSM has been reported recently [14], but not in

the motion-sensorless SVM implementation, and not for ISA where the specifications are much tougher than for industrial drives.

The present paper develops a complete solution for sensorless DTFC-SVM of PM-RSM drive for integrated starter-alternator in mild hybrid electric vehicles, from zero speed to wide speed range for motor/ generator control. A stator flux reference with a quasi-optimal flux versus torque functional is proposed. Stator flux observers in wide speed range employing combined voltage-current models for low speed and only the voltage model for medium-high speed in PI closed loops, are developed. A novel rotor speed and position observer with fusion strategy employs signal injection and only one D-module vector filter in stator reference - for low speed, corroborated with a speed observer from the stator flux vector estimation - for medium-high speed. The effectiveness of this solution has been confirmed by extensive experimental test results in wide speed range including artificial loading.

II. TYPICAL INTEGRATED STARTER-ALTERNATOR SPECIFICATIONS

The ISA has to perform (at most): 1) Motoring: for vehicle self-starting (in torque control mode) and for auxiliaries driving during ICE shut-off (in speed control mode). 2) Generating: for vehicle regenerative braking and for battery recharge during exclusive ICE running. In essence, for both motoring and generating regime, the electromagnetic torque (T_e) versus speed (positive or negative) envelopes are given in Fig. 1.

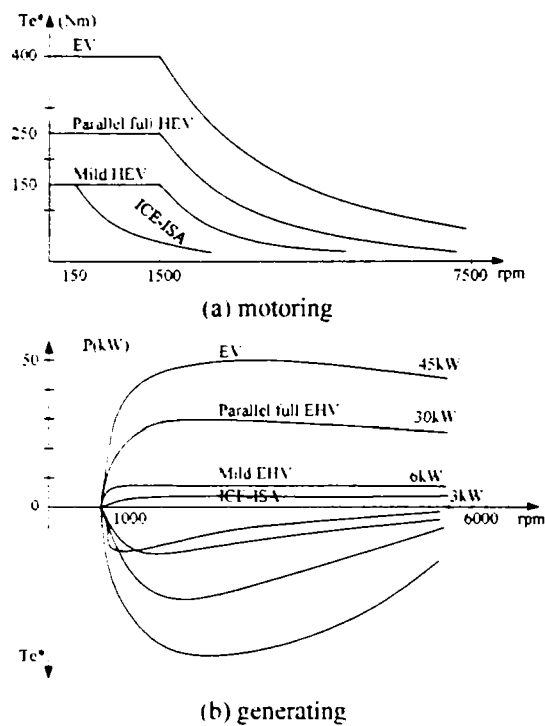


Fig. 1 Typical integrated starter-alternator requirements: a) electric torque (T_e) versus speed at crankshaft for motoring, and b) electric power (P) versus speed for generating, with various degrees of vehicle electrification.

These envelopes have to be tempered further by the battery state of charge (accessibility) both in motoring and generating. The division of torque between ICE and PM-RSM may also be decided by the optimum gas-mileage or lowest pollution criteria for the ICE.

Further on, we will just retain the fact that: 1) the torque closed-loop control is mandatory, and 2) an external power control-loop may be required for generating. As the battery power flow can be easily measured ($V_{dc} I_{dc}$), this fact seems to be a good way to go.

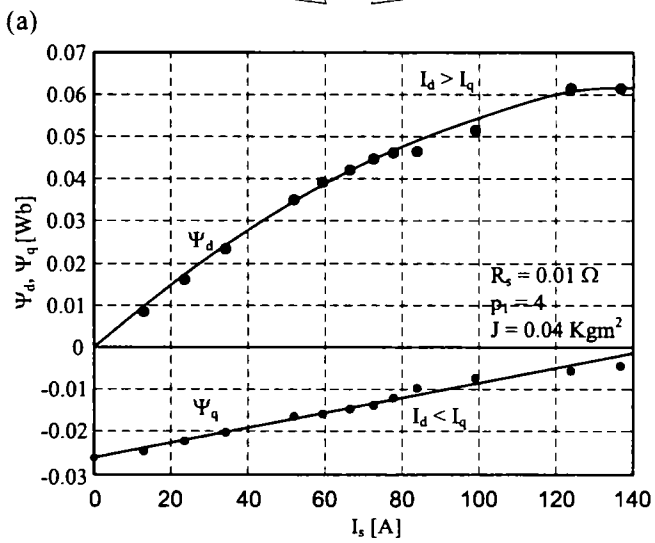
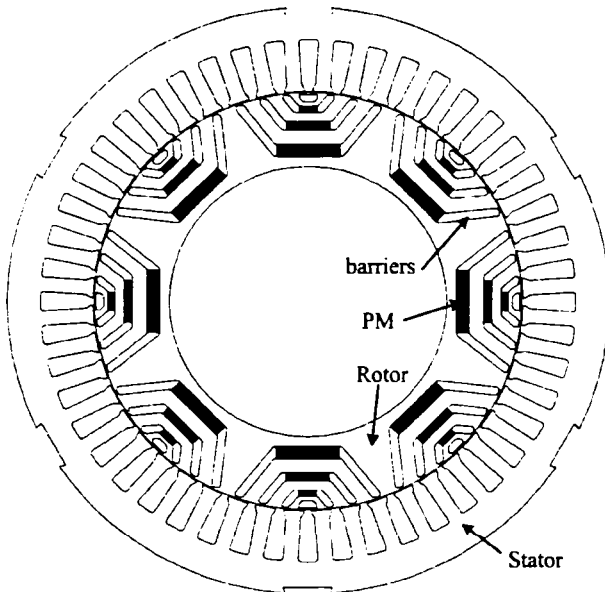
III. FLUX REFERENCE

In what follows, the PM RSM is presented, with the novel stator flux referencer for the starter-alternator applications (for better performances in a high speed range).

A. PM-RSM Model

The PM-RSM is a rather good saliency interior PM rotor synchronous machine (Fig. 2) [7]. The rotor contains a multiple flux barrier structure with PMs placed on the bottom of flux barriers. The PM flux (Ψ_{PMq}) produces a limited electromotive force (emf), of 150-200% at

highest speed, to limit the inverter switches voltage rating (and costs). The PMs are placed in the q -axis, while the d -axis shows higher magnetic permeance ($L_d > L_q$).



(b)
Fig. 2 (a) Permanent magnet reluctance synchronous motor cross section; (b) Measured magnetization curves $\Psi_d(I_s)$, $\Psi_q(I_s)$ [Wb], I_s [A].

The PM-RSM model in dq -rotor reference, considering the emf and inductances that vary sinusoidally with the rotor position, is given by:

$$\begin{aligned} \frac{d\underline{\Psi}_s}{dt} &= -j\omega_r \underline{\Psi}_s - \underline{I}_s R_s + \underline{V}_s \\ \underline{\Psi}_s &= L_d I_d + j(L_q I_q - \Psi_{PMq}) \\ T_e &= 3/2 p_1 [\Psi_{PMq} + (L_d - L_q) I_q] I_d = 3/2 p_1 \text{Im}(\underline{\Psi}_s^* \underline{I}_s) \end{aligned} \quad (2)$$

where: $\underline{\Psi}_s$, \underline{I}_s (I_d, I_q) and \underline{V}_s are the stator flux, current and voltage vector, respectively; R_s is the stator resistance; ω_r is the electrical rotor speed; L_d, L_q are the d, q inductances; p_1 is the

pole-pair number; and $\#$ means the conjugate vector operator. The magnetic saturation is considered only in the d -axis $L_d(I_d)$, with $L_q = \text{constant}$, and cross-coupling saturation effects are neglected.

B. Flux Reference

In DTFC, the stator flux reference (Ψ_s^*) is coordinated with the torque reference (T_e^*) to produce the required (below maximum) torque for a given speed. The problem is that for a given flux Ψ_s^* and torque T_e^* there are two current pairs (I_d, I_q) that can produce them:

$$\Psi_s = \sqrt{(L_d I_d)^2 + (L_q I_q - \Psi_{PMq})^2}. \quad (3)$$

The torque equation from (2) shows clearly that a specific torque T_e can be obtained with $I_{d1}, I_{d2} > 0$, when $\Psi_q = L_q I_q - \Psi_{PMq} \neq 0$, for a given stator flux Ψ_s . An example is shown in the vector diagram in Fig. 3, based on the 2nd equation from (2).

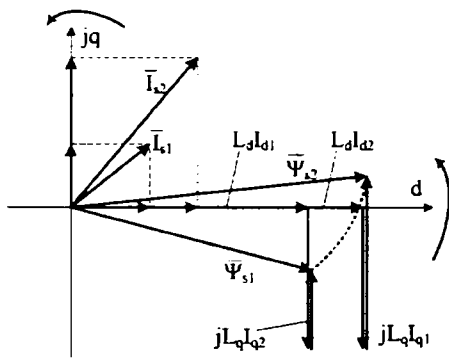


Fig. 3 Two stator current pairs (I_d, I_q) for a given torque T_e^* and flux Ψ_s^* .

The $\underline{I}_{s1}, \underline{\Psi}_{s1}$ couple is better because the current amplitude is smaller, and also the PM is less stressed ($\Psi_q < 0$). Thus, the control should make sure that the flux vector $\underline{\Psi}_s$ is always in the 4th quadrant for positive torque, or in the 3rd quadrant for negative torque. One possibility to realize this fact in DTFC is to make the reference flux $\Psi_s^* = \Psi_{PMq}$ for zero torque (point 0' in Fig. 4), which guaranties zero stator current ($I_d = I_q = 0$) for zero torque, and then the control starts from there to travel the reference flux Ψ_s^* functional, depending on the reference torque T_e^* (Fig. 4).

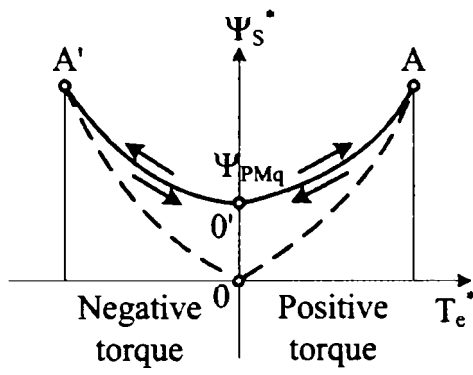


Fig. 4 Flux-torque functional $\Psi_s^*(T_e^*)$ from zero to base speed for the PM-RSM.

On the other hand, for fast torque response in a machine which works mostly under heavy load and in flux weakening, the control goes to around zero stator flux at zero torque (point 0 in Fig. 4), when:

$$I_{q\max} = \Psi_{PMq} / L_q. \quad (4)$$

When the maximum torque/ speed envelope is required, $I_{q\max}$ is applied and therefore:

$$T_{e\max}^* = 3/2 p_1 \Psi_d I_{q\max}, \quad \text{and thus } (\Psi_s^*)_{T_{e\max}} = \frac{2T_{e\max}^* L_q}{3 p_1 \Psi_{PMq}}. \quad (5)$$

$$\begin{aligned} (\Psi_s^*)_{T_{e\max}} &\approx K_{MG} \frac{V_{sb}}{\omega_b} = \Psi_{s0}; \quad \text{for } \omega_r < \omega_b \\ \text{Also:} & \\ (\Psi_s^*)_{T_{e\max}} &\approx \Psi_{s0} \frac{\omega_r}{\omega_b}; \quad \text{for } \omega_r \geq \omega_b \end{aligned} \quad (6)$$

where: K_{MG} is a coefficient in the range of 0.95-0.97 for motoring, and 1.03-1.07 for generating; ω_b is the electrical rotor base speed; V_{sb} is the stator voltage at base speed. In this way, the functional (limiters) $\Psi_{s\max}^*(\omega_r)$ and $T_{e\max}^*(\omega_r)$ are provided for.

Whenever the required torque at a certain speed is smaller than the available (maximum) $T_{e\max}^*(\omega_r)$ value, the control may relax the I_q^* value by maintaining the latter positive:

$$I_q^* = \frac{\Psi_{PMq}^*}{L_q} \sqrt{\frac{|T_e^*|}{|T_{e\max}^*|}}; \quad \Psi_q^* = L_q I_q^* - \Psi_{PMq}. \quad (7)$$

model prevails at medium-high speed with a smooth transition between them depending on speed. Two flux observers have been used for comparison.

The serial observer (Fig. 6a) contains the voltage model in stator reference serially connected with the current model in the rotor reference frame, using a PI compensator driven by the current estimation error. Both models are enclosed within the correction loop. The parallel observer (Fig. 6b) contains the same models but connected in parallel and using the flux estimation error. This time, the PI correction loop encloses only the voltage model, while the current model is open loop operated.

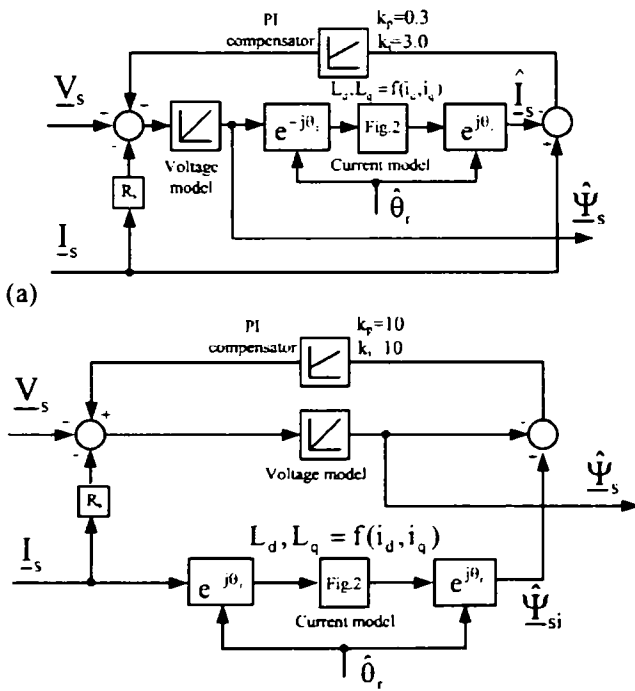


Fig. 6 Stator flux observers with combined voltage-current models: (a) serial observer; (b) parallel observer.

With accurate stator flux estimation and measured currents, the torque estimation is simply calculated in $\alpha\beta$ -stator reference as:

$$\hat{T}_e = 3/2 p_1 (\hat{\Psi}_\alpha I_\beta - \hat{\Psi}_\beta I_\alpha). \quad (8)$$

The rotor position estimation $\hat{\theta}_r$ is required in the current model within the flux observer – but only at low speed, below 50rpm, because at medium-high speed the voltage model becomes dominant and the signal injection (which gives $\hat{\theta}_r$) discontinuation does not produce

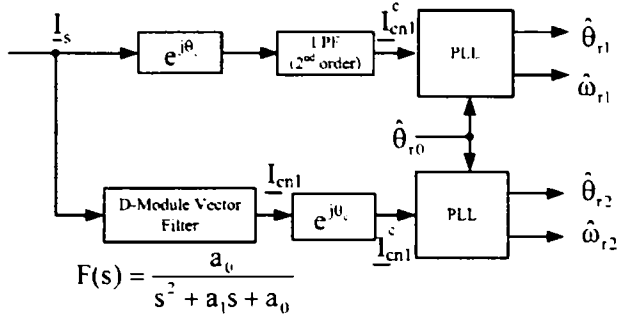
a notable influence on the flux observer. The rotor speed estimation $\hat{\omega}_r$ in the whole speed range is required in the flux (and torque) referencer, and accurately – in the speed controller.

B. Speed and Position Observers with Signal Injection

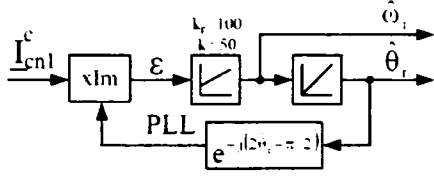
For low speed operation a speed observer using signal injection has been implemented as shown in Fig. 7. A rotating carrier-voltage $\underline{V}_c = V_c \exp(j\omega_c t)$ with $V_c = 1\text{V}$ and $\omega_c = 500\text{ Hz}$ is injected in the stator superimposing on top of driving fundamental stator-voltage \underline{V}_s . The resulting stator current \underline{I}_s , modulated by the position dependent inductances with magnetic saliency, contains carrier-current harmonics with rotor position information θ_r . Usually, the negative 1st order sequence carrier harmonic $\underline{I}_{cn1} = I_{cn1} \exp\{j(-\theta_c + 2\theta_r + \pi/2)\}$ with $\theta_c = \omega_c t$ [9] is selected from the measured stator current.

Two schemes have been tested: 1) Observer with synchronous low-pass filter (LPF) in carrier reference (upper part of Fig. 7a) [10]. 2) Novel observer with vector filter in D-module in stator reference as band-pass filter (BPF) with central frequency ω_c and phase-sign discrimination (lower part of Fig. 7a). Both observers select the \underline{I}_{cn1} harmonic. A phase-locked loop (PLL) tracking observer shown in Fig. 7b extracts the estimation of rotor speed $\hat{\omega}_r$ and position $\hat{\theta}_r$ from the phase of \underline{I}_{cn1} harmonic in carrier reference, with PLL error $\sigma \sim 2I_{cn1} (\theta_r - \hat{\theta}_r)$. During the experiments it was noticed that both observers in Fig. 7a have similar behavior, with very robust estimation, almost independent of machine parameters.

The initial rotor position $\hat{\theta}_{r,0}$ is correctly identified at standstill by both observers in the range of $(-\pi/2, \pi/2)$ radians. For full angle range, an uncertainty of π radians appears, and this is discriminated by the magnet polarity detection using the 2nd order harmonics [9-10].



(a)



(b)

Fig. 7 Speed and position observers with signal injection: (a) Observers with synchronous low-pass filter and with vector filter in D-module; (b) PLL used in (a).

C. Speed Estimation from Stator Flux

For medium-high speed operation, above 50 rpm, the signal injection is disabled to reduce losses, and thus the associated speed and position observer from Fig. 7 is also inhibited. Now, additional speed estimation is required, with a smooth transition between the two of them.

The proposed solution estimates the rotor speed $\hat{\omega}_r$ from the estimated stator flux vector $\hat{\underline{\psi}}_s$:

$$\hat{\omega}_r = \hat{\omega}_{\psi_s} + \frac{d\hat{\theta}_{\psi_{dq}}}{dt}; \quad \hat{\omega}_{\psi_s} = \frac{d\hat{\theta}_{\psi_s}}{dt} \quad (9)$$

where $\hat{\omega}_{\psi_s}$ and $\hat{\theta}_{\psi_s}$ are the estimated speed and position of $\hat{\underline{\psi}}_s$ in $\alpha\beta$ -stator reference, which is given by the stator flux observer in Fig. 6; $\hat{\theta}_{\psi_{dq}}$ is the estimated position of $\hat{\underline{\psi}}_s$ in dq -rotor reference (Fig. 3).

The 1st main component of the rotor speed in (9), i.e., $\hat{\omega}_{\psi_s}$ is extracted together with $\hat{\theta}_{\psi_s}$ from the $\hat{\underline{\psi}}_s$ phase by a PLL observer similarly as in Fig. 7b. The 2nd component, living only in transient regimes, is obtained from the electric torque expression that can be derived as:

$$\hat{T}_e = \frac{3}{2} p_1 \frac{\hat{\Psi}_s \Psi_{PMq}}{L_q} \cos \hat{\theta}_{\psi_{dq}} + \frac{3}{2} p_1 \frac{\hat{\Psi}_s^2}{2} \left(\frac{1}{L_q} - \frac{1}{L_d} \right) \sin 2\hat{\theta}_{\psi_{dq}}. \quad (10)$$

The angle $\hat{\theta}_{\psi_{dq}}(\hat{T}_e, \hat{\Psi}_s)$ is extracted from a look-up table with linear interpolation based on (10) using \hat{T}_e (8) and $\hat{\Psi}_s$ from Fig. 6, with an average value for L_d , because magnetic saturation is not so important. Then $d\hat{\theta}_{\psi_{dq}}/dt$ is calculated to finally decide $\hat{\omega}_r$ in (9).

Note: As the torque and flux response of the machine is faster than the speed response in automotive applications, the angle $\hat{\theta}_{\psi_{dq}}$ may alternatively be calculated as:

$$\sin\hat{\theta}_{\psi_{dq}} = \hat{\Psi}_q^*/\hat{\Psi}_s^*; \quad \cos\hat{\theta}_{\psi_{dq}} = \hat{\Psi}_d^*/\hat{\Psi}_s^* \quad (11)$$

from the flux referencer in Fig. 5, provided that the flux and torque references do not experience step variations, or some filtering is applied.

D. DTFC-SVM Motion-Sensorless Control System

Now that the proposed flux/torque referencers and the comprehensive state observers have been introduced, the proposed sensorless DTFC-SVM system for PM-RSM is illustrated in Fig. 8 with the main components discussed above.

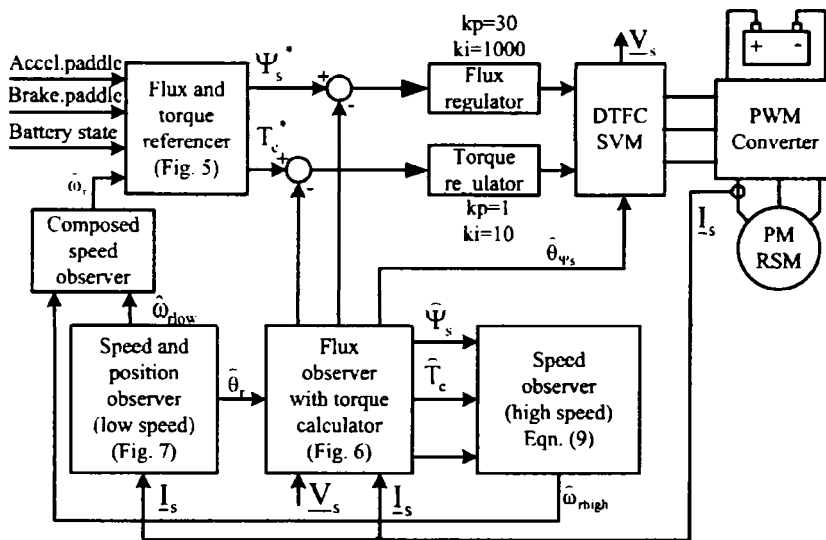


Fig. 8 DTFC-SVM motion-sensorless control of PM-RSM.

Only the PI flux and torque regulators of DTFC-SVM have not been detailed so far. Their design is presented in [12], and is thus skipped here. In what follows, the digital implementation and the experimental results with the proposed DTFC-SVM system will be tackled directly.

V. EXPERIMENTAL RESULTS

The experimental setup for the sensorless DTFC-SVM of PM-RSM (Fig. 9) contains a belt transmission 10/13 kW (1500/3000 rpm) with an induction motor driven by an ABB ACS600 bidirectional inverter. The 140 Nm peak torque PM-RSM is fed through a 48Vdc, 350A inverter from 48V, 55Ah battery pack. The simulations (cut out from lack of space) have been managed in Matlab/Simulink, and implemented on a dSpace 1103 control board.

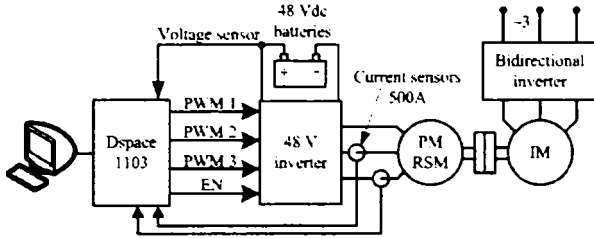


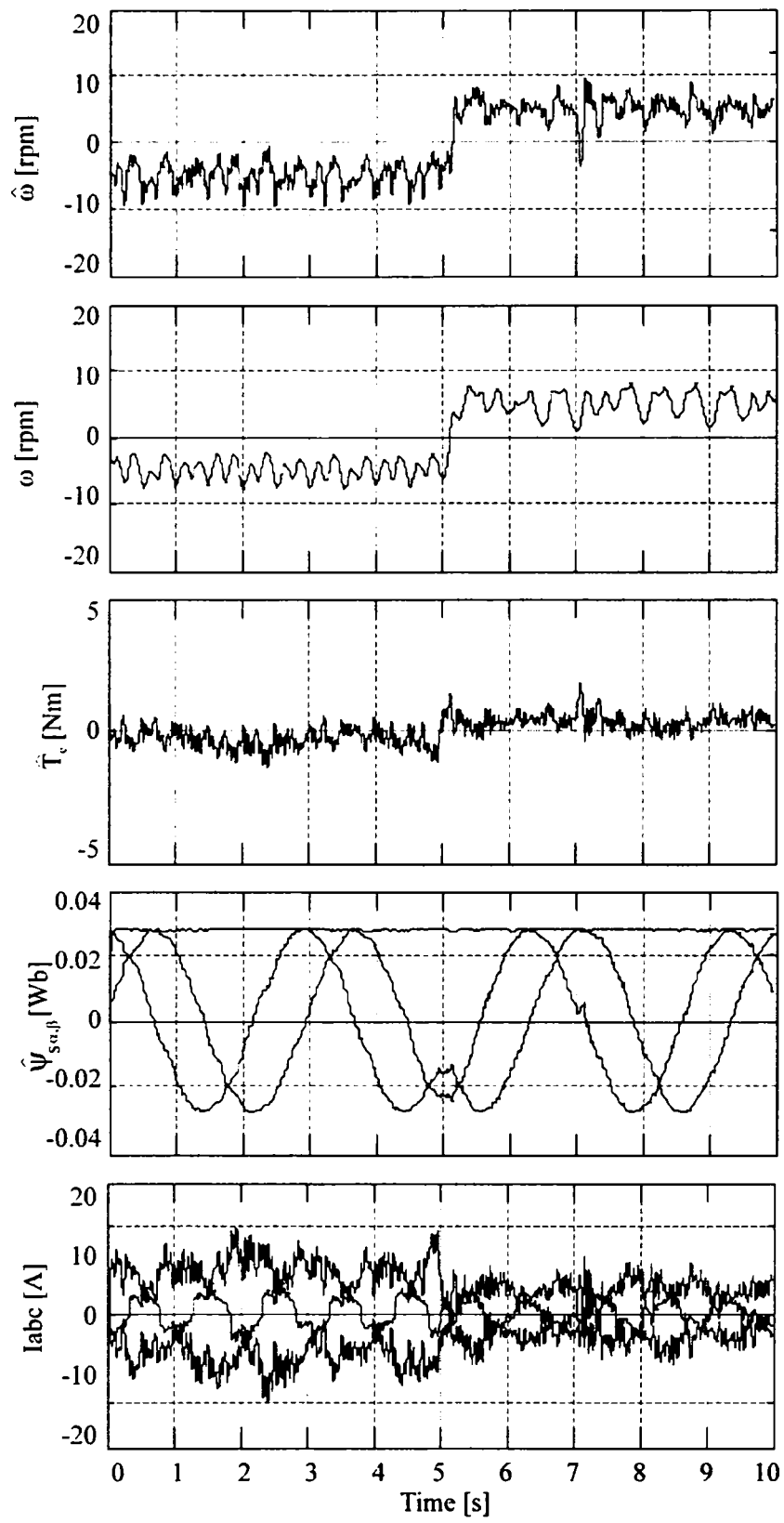
Fig. 9 Experimental setup for sensorless DTFC-SVM of PM-RSM.

A series of experiments have been processed to test the behavior of the proposed sensorless DTFC-SVM of PM-RSM. Two stator flux observers (Fig. 6), and two rotor speed/position observers with signal injection (Fig. 7) have been tested.

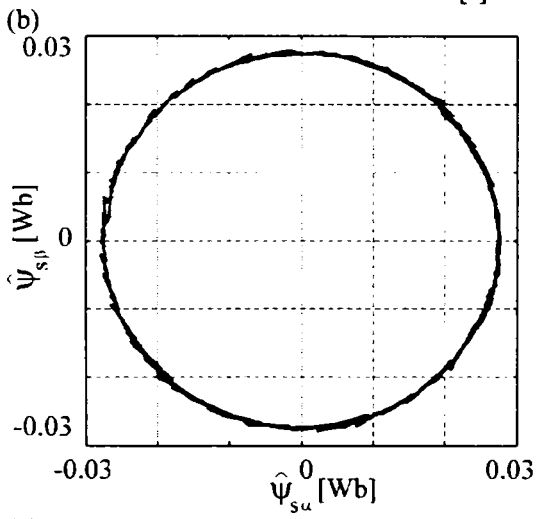
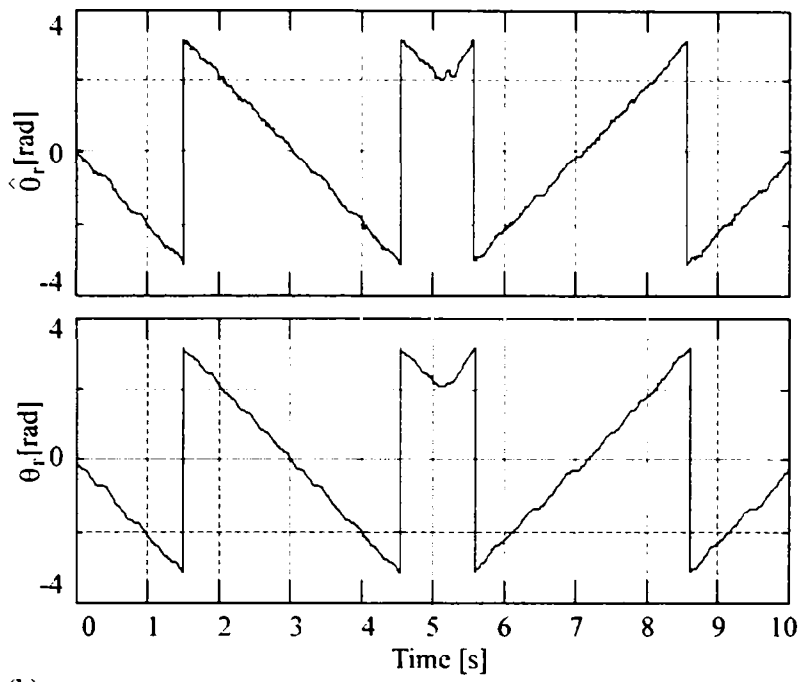
The experimental test results at low and high speeds are shown. A fusion strategy (Fig. 8) is proposed using the speed/position observer with signal injection for low-speed, and the speed estimation from stator flux for medium-high speed.

Fig. 10 shows the no-load speed reversal at very low speed: from -5 rpm to 5 rpm. The flux hodograph is almost circular (Fig. 10c), the position estimation is very good (Fig. 10b) and the speed estimation is acceptable. The use of SVM in DTFC has made a smooth operation possible at 5 rpm. Fig. 11 shows the no-load start from zero to 10 rpm, again with good results.

The speed reversal at high speed from -750 rpm to 750 rpm, which requires the transition of the speed observer from signal injection at low-speed to estimation from stator flux at high-speed, is illustrated in Fig. 12 with good results.



(a)



(c)
 Fig. 10 Test results at ± 5 rpm speed reversal without load: (a) from top to bottom: estimated speed ($\hat{\omega}$), measured speed (ω), estimated torque (\hat{T}_e), estimated flux components ($\hat{\Psi}_s$), and measured currents (I_{abc}); (b) estimated and measured rotor position (θ_r); (c) estimated flux in $\alpha\beta$ -plane $\hat{\Psi}_{s\alpha}$ ($\hat{\Psi}_{s\beta}$) [Wb].

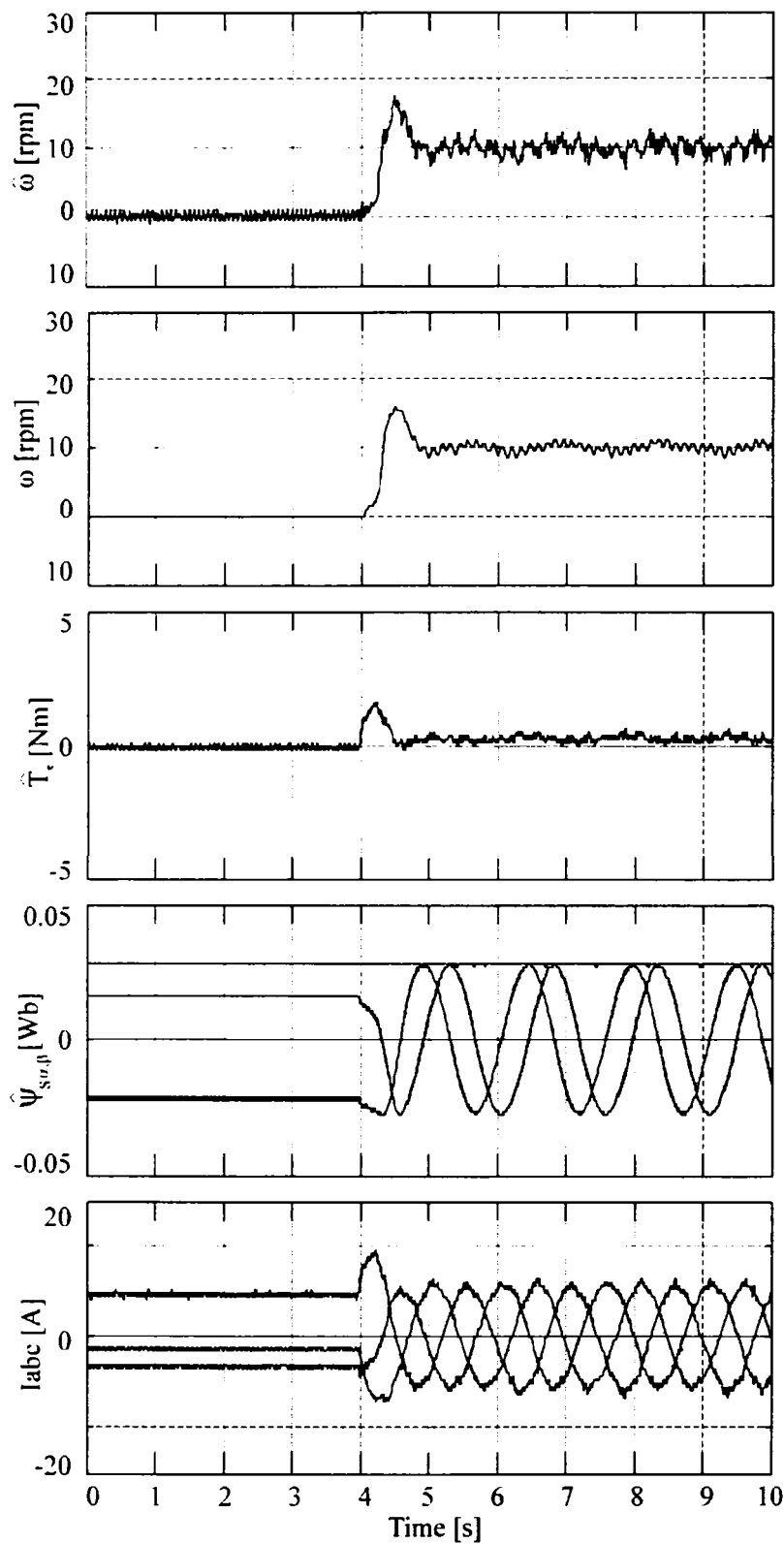


Fig. 11 Test results at start-up to 10 rpm without load; from top to bottom: estimated speed ($\hat{\omega}$), measured speed (ω), estimated torque (\hat{T}_e), estimated flux components ($\hat{\Psi}_s$), and measured currents (I_{abc}).

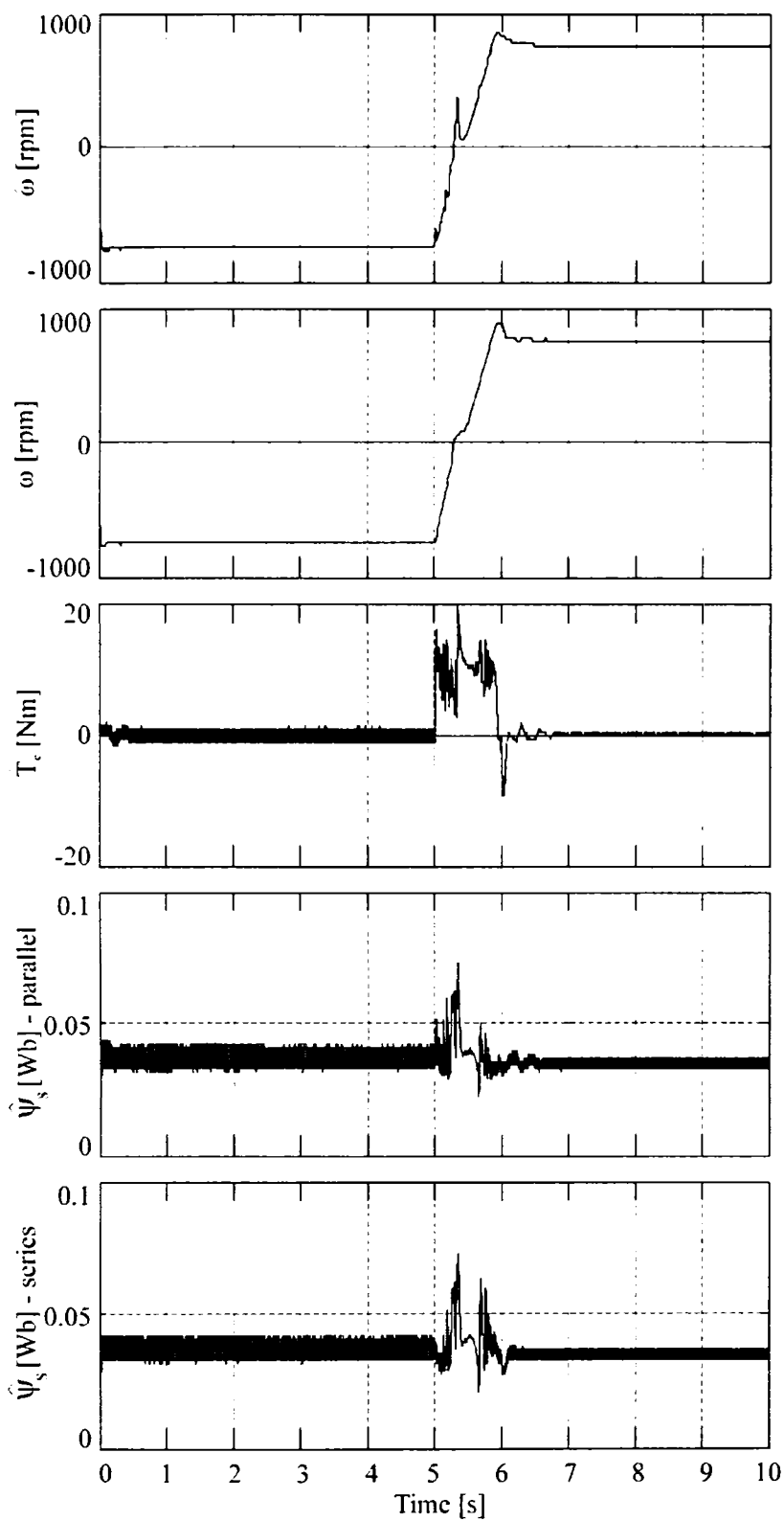


Fig. 12 Test results at ± 750 rpm speed reversal without load; from top to bottom: estimated speed ($\hat{\omega}$) and measured speed (ω) (estimated from the stator flux and from signal injection at low speeds until 50 rpm), estimated torque (\hat{T}_e), estimated flux magnitude ($\hat{\Psi}_s$) - from serial and parallel observers.

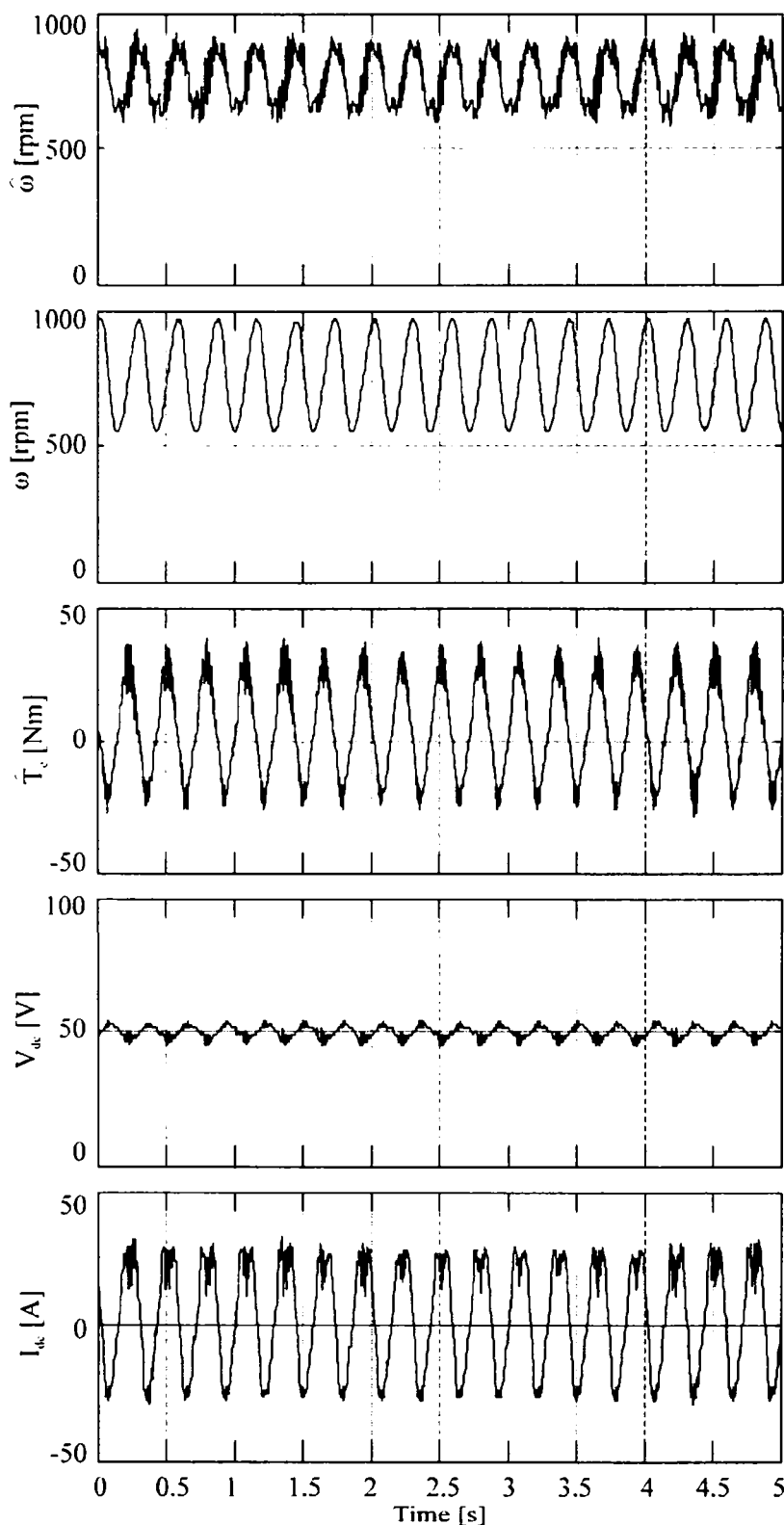


Fig. 13 Artificial loading with fast switching from motoring to generating: estimated speed ($\hat{\omega}$), measured speed (ω), estimated torque (\hat{T}_e), measured battery voltage (V_{dc}), measured battery current (I_{dc}).

The switching from motoring to generating - as in artificial loading [15], by pulsating the speed reference, is shown in Fig. 13, where the battery current changes sign with fast response. This artificial loading has allowed for to reach 35 Nm peak torque with substantial battery charging (negative) current.

VI. CONCLUSION

The proposed sensorless DTFC-SVM of PM-RSM includes the following contributions:

- A quasi-optimal flux referencer to optimize the energy consumption in wide speed range, with a flux versus torque functional leading to unique flux and torque reference values;
- A stator flux observer that uses a combined current-voltage models with PI compensator for low speed below 50 rpm, and only the voltage model in PI closed loop for medium-high speed.
- A speed and position observer with fusion strategy that employs signal injection and only one D-module vector filter in stator reference for low speed below 50 rpm, corroborated with a speed observer from stator flux vector estimation for medium-high speed.
- Extensive experimental test results on a laboratory prototype focused on very low speed to high speed sensorless operation for motoring and generating, including artificial loading, prove the effectiveness of the proposed solution.

Further investigations on on-line initial position estimation in full range, generator and motor heavy loading over the entire speed range are still to be added to take full advantage of the sensorless DTFC-SVM robust control capabilities.

REFERENCES

- [1] J. M. Miller, V. R. Stefanovic, and E. Levi, "Prognosis for integrated starter alternator systems in automotive applications," in *Proc. 10th Int. Power Electronics and Motion Control Conf. EPE-PEMC 2002*, Cartat & Dubrovnik, Croatia, Sept. 2002, CDROM T5-001.pdf, pp. 1-15.
- [2] A. Vagati, A. Fratta, P. Guglielmi, G. Franchi, and F. Villata, "Comparison of ac motor based drives for electric vehicles," in *Proc. Power Conversion & Intelligent Motion, PCIM'99 Europe*, Nuremberg, Germany, Vol. I, June 1999, pp. 173-180.
- [3] T. Teratani, K. Kuramochi, H. Nakao, T. Tachibana, K. Yagi, and S. Abou, "Development of Toyota mild hybrid system (THS-M) with 42V power-net," in *Proc.*

IEEE Int. Electric Machines and Drives Conf. IEMDC'03, Madison, WI, vol. 1, June 2003, pp. 3-10.

- [4] A. Lange, W.-R. Canders, F. Laube, and H. Mosebach, "Comparisons of different drive systems for a 75 kW electrical vehicle drive," in *Proc. Int. Conf. on Electrical Machines ICEM 2000*, Espoo, Finland, Vol. 3, Aug. 2000, pp. 1308-1312.
- [5] P. Guglielmi, M. Pastorelli, G. Pellegrino, and A Vagati, "Position-sensorless control of permanent-magnet-assisted synchronous reluctance motor," *IEEE Trans. Ind. Appl.*, Vol. 40, no. 2, pp. 615-622, Mar./Apr. 2004.
- [6] E. C. Lovelace, T. Keim, J. H. Lang, D. D. Wentzloff, T. M. Jahns, J. Way, and P. J. McCleer "Design and experimental verification of a direct-drive interior PM synchronous machine using a saturable lumped-parameter model," in *Proc. 37th IEEE Industry Applications Conf. IEEE-IAS 2002*, Pittsburgh, PA, vol. 4, Oct. 2002, pp. 2486-2492.
- [7] I. Boldea, L. Tutelea, and C. I. Pitic, "PM-assisted reluctance synchronous motor/generator (PM-RSM) for mild hybrid vehicles: electromagnetic design," *IEEE Trans. Ind. Appl.*, Vol. 40, no. 2, pp. 492-498, Mar./Apr. 2004.
- [8] B. A. Welchko, T. M. Jahns, W. L. Soong, and J. A. Nagashima, "IPM synchronous machine drive response to symmetrical and asymmetrical short circuit faults," *IEEE Trans. Energy Convers.*, Vol. 18, no. 2, pp. 291-298, June 2003.
- [9] H. Kim, K.-K. Huh, R. D. Lorenz, and T. M. Jahns, "A novel method for initial rotor position estimation for IPM synchronous machine drives," *IEEE Trans. Ind. Appl.*, Vol. 40, no. 5, pp. 1369-1378, Sept./Oct. 2004.
- [10] Y. Jeong, R. D. Lorenz, T. M. Jahns, and S. Sul, "Initial rotor position estimation of an interior permanent magnet synchronous machine using carrier-frequency injection methods," in *Proc. IEEE Int. Electric Machines and Drives Conf. IEMDC'03*, Madison, WI, Vol. 2, June 2003, pp. 1218-1223.

- [11] S. Shinnaka, "New "mirror-phase vector control" for sensorless drive of permanent-magnet synchronous motor with pole saliency," *IEEE Trans. Ind. Appl.*, Vol. 40, no. 2, pp. 599-606, Mar./Apr. 2004.
- [12] C. Lascu, I. Boldea, and F. Blaabjerg, "Direct torque control of sensorless induction motor drives: a sliding-mode approach," *IEEE Trans. Ind. Appl.*, Vol. 40, no. 2, pp. 582-590, Mar./Apr. 2004.
- [13] I. Boldea, L. Janosi, and F. Blaabjerg, "A modified direct torque control (DTC) of reluctance synchronous motor sensorless drive," *Electr. Mach. Pow. Syst.*, Vol. 28, no. 2, pp. 115-128, Feb. 2000.
- [14] M. F. Rahman, M. E. Haque, L. Tang, and L. Zhong, "Problems associated with the direct torque control of an interior permanent-magnet synchronous motor drive and their remedies," *IEEE Trans. Ind. Electron.*, Vol. 51, no. 4, pp. 799-809, July/Aug. 2004.
- [15] L. Tutelea, I. Boldea, E. Ritchie, P. Sandholdt, F. Blaabjerg, "Thermal testing for inverter-fed induction machines using mixed frequency method", Record of ICEM-1998, Istanbul, Turkey, Vol. 1, pp.248-253.